Mineral dust mobilisation, transport, and deposition in different climate epochs

Dissertation
zur Erlangung des Grades
“Doktor
der Naturwissenschaften”

am Fachbereich Physik, Mathematik und Informatik
der Johannes Gutenberg-Universität
in Mainz

GREGOR GLÄSER
geb. am 27. März 1984
in Limburg a. d. Lahn

Mainz, den 30. November 2012

Tag der Promotion: 25. Januar 2013

D77 - Mainzer Dissertation

Contents

Abstract vii

Zusammenfassung ix

1 Introduction and objectives 1

2 The ECHAM5/MESSy Atmospheric Chemistry model system . . 9

2.1 ECHAM5 – General model description 9

2.2 MESSy – The concept of modularisation 10

2.3 Mineral dust emission parametrisation 11

2.3.1 The emission scheme of Balkanski et al. 2004 12

2.3.2 The emission scheme of Tegen et al. 2002 12

2.3.3 Comparison of the two dust emission schemes 13

2.4 Mineral dust deposition processes 14

2.5 Model setup 15

3 Sensitivity of the mineral dust cycle to the spectral resolution and the dust emission scheme 17

3.1 Introduction 17

3.2 Comparison data sets 19

3.2.1 Long-term in situ measurements 19

3.2.2 Satellite-based aerosol mass concentration measurements 19

3.2.3 The Saharan Mineral Dust Experiment SAMUM 20

3.2.4 Measurements at Kleiner Feldberg, Germany 20
3.2.5 Satellite-based infrared dust composites 20
3.2.6 Regional dust model forecasts 20
3.3 Evaluation of five-year time slice simulations 21
3.3.1 Comparison with dust measurements 21
3.3.2 Global dust budget 22
3.3.3 Geographical dust distribution 25
3.3.4 Seasonal cycle and regional considerations 25
3.3.5 Selection of the preferable model configuration 31
3.4 Simulation of two single dust episodes 31
3.4.1 May/June 2006: SAMUM 32
3.4.2 May/June 2008: Kleiner Feldberg 38
3.5 Summary 41

4 Transatlantic transport of Saharan dust 43
4.1 Introduction 43
4.2 Methodology 44
4.2.1 Euler vs. Lagrange: two philosophies, one intention 44
4.2.2 Trajectory initialisation 45
4.3 Eulerian time series 46
4.4 Transport time scales 50
4.4.1 Eulerian approach 50
4.4.2 Eulerian vs. Lagrangian approaches 52
4.5 Transport pathways 54
4.5.1 Total number of trajectories 54
4.5.2 Trajectory characteristics 57
4.5.3 Vertical structure 60
4.5.4 Dust gain and loss during the transport 66
4.6 Source regions of dust reaching the Americas 70

4.7 Summary . . . 74

5 The mineral dust cycle during the Little Ice Age (LIA) . . . 77

5.1 Introduction . . . 77

5.2 Methodology . . . 79

5.2.1 Forcing factors for LIA simulations . . . 79

5.2.2 Setup of LIA simulations . . . 80

5.3 Results . . . 80

5.3.1 Model spin up during the LIA . . . 80

5.3.2 Model evaluation . . . 83

5.3.3 Climatic differences within the “dust belt” . . . 90

5.3.4 Climatic differences of the transatlantic transport . . . 103

5.4 Summary . . . 115

6 Conclusion . . . 117

6.1 Discussion of the results . . . 117

6.2 Outlook . . . 120

A MECCA reaction tables . . . 123

B MESSy submodels used in this thesis . . . 127

C Dust measurements . . . 131

D Abbreviations and units . . . 135

References . . . 139

Danksagung . . . 155

Abstract

Mineral dust is an important component of the Earth's climate system and provides essential nutrients to oceans and rain forests. During atmospheric transport, dust particles directly and indirectly influence weather and climate. The strength of dust sources and characteristics of the transport, in turn, might be subject to climatic changes. Earth system models help for a better understanding of these complex mechanisms.

This thesis applies the global climate model ECHAM5/MESSy Atmospheric Chemistry (EMAC) for simulations of the mineral dust cycle under different climatic conditions. The prerequisite for suitable model results is the determination of the model setup reproducing the most realistic dust cycle in the recent climate. Simulations with this setup are used to gain new insights into properties of the transatlantic dust transport from Africa to the Americas and adaptations of the model's climate forcing factors allow for investigations of the impact of climatic changes on the dust cycle.

In the first part, the most appropriate model setup is determined through a number of sensitivity experiments. It uses the dust emission parametrisation from Tegen et al. (2002) and a spectral resolution of T85, corresponding to a horizontal grid spacing of about 155 km. Coarser resolutions are not able to accurately reproduce emissions from important source regions such as the Bodélé Depression in Chad or the Taklamakan Desert in Central Asia. Furthermore, the representation of ageing and wet deposition of dust particles in the model requires a basic sulphur chemical mechanism. This setup is recommended for future simulations with EMAC focusing on mineral dust.

One major branch of the global dust cycle is the long-range transport from the world's largest dust source, the Sahara, across the Atlantic Ocean. Seasonal variations of the main transport pathways to the Amazon Basin in boreal winter and to the Caribbean during summer are well known and understood, and corroborated in this thesis. Both Eulerian and Lagrangian methods give estimates on the typical transport times from the source regions to the deposition on the order of nine to

ten days. Previously, a huge proportion of the dust transported across the Atlantic Ocean has been attributed to emissions from the Bodélé Depression. However, the contribution of this hot spot to the total transport is very low in the present results, although the overall emissions from this region are comparable. Both model results and data sets analysed earlier, such as satellite products, involve uncertainties and this controversy about dust transport from the Bodélé Depression calls for future investigations and clarification.

Aforementioned characteristics of the transatlantic dust transport just slightly change in simulations representing climatic conditions of the Little Ice Age in the middle of the last millennium with mean near-surface cooling of 0.5 to 1 K. However, intensification of the West African summer monsoon during the Little Ice Age is associated with higher dust emissions from North African source regions and wetter conditions in the Sahel. Furthermore, the Indian Monsoon and dust emissions from the Arabian Peninsula, which are affected by this circulation, are intensified during the Little Ice Age, whereas the annual global dust budget is similar in both climate epochs. Simulated dust emission fluxes are particularly influenced by the surface parameters. Modifications of the model do not affect those in this thesis, to be able to ascribe all differences in the results to changed forcing factors, such as greenhouse gas concentrations. Due to meagre comparison data sets, the verification of results presented here is problematic. Deeper knowledge about the dust cycle during the Little Ice Age can be obtained by future simulations, based on this work, and additionally using improved reconstructions of surface parameters. Better evaluation of such simulations would be possible by refining the temporal resolution of reconstructed dust deposition fluxes from existing ice and marine sediment cores.

Zusammenfassung

Mineralstaub stellt eine bedeutende Nährstoffquelle für die Ökosysteme der Ozeane und Regenwälder dar. Weiterhin nimmt er während des atmosphärischen Transports direkt und indirekt Einfluss auf Wetter und Klima. Die Intensität von Staubemissionen und Eigenschaften des Transports können ihrerseits unter verschiedenen klimatischen Bedingungen variieren. Zu einem besseren Verständnis dieser komplexen Mechanismen können Erdsystem-Modelle beitragen.

In dieser Arbeit wird der Mineralstaubzyklus anhand von Simulationen mit dem globalen Klimamodell ECHAM5/MESSy Atmospheric Chemistry (EMAC) in verschiedenen Klimaepochen untersucht. Um sinnvolle Ergebnisse zu erhalten muss zunächst das Modellsetup bestimmt werden, welches den Staubzyklus im heutigen Klima am besten reproduziert. Simulationen mit diesem Setup sollen neue Erkenntnisse über die Charakteristiken des transatlantischen Transport von Staub aus Nordafrika nach Süd- und Mittelamerika liefern. Des Weiteren wird durch Anpassen der klimatischen Randbedingungen des Modells untersucht, inwiefern der Mineralstaubzyklus von Veränderungen des Klimas abhängt.

Im ersten Teil dieser Arbeit wird mit Hilfe diverser Sensitivitätsstudien das optimale Modellsetup festgelegt. Es verwendet die Staubemissions-Parametrisierung von Tegen et al. (2002) und die spektrale Auflösung T85, was einem horizontalen Gitterpunktabstand von etwa 155 km entspricht. Emissionen von bedeutenden Staubquellen wie der Bodélé-Senke in Tschad oder der Taklamakan-Wüste in Zentralasien können mit gröberen Auflösungen nicht richtig wiedergegeben werden. Darüber hinaus ist ein Chemiemechanismus nötig, der den Schwefelkreislauf realistisch simuliert, um chemisches Prozessieren und somit das Auswaschen von Staubpartikeln aus der Atmosphäre richtig abzubilden. Für künftige Simulationen des Staubzyklus mit EMAC wird dieses Modellsetup empfohlen.

Der Staubtransport aus der größten Emissionsregion der Welt, der Sahara, über den Atlantik stellt einen Hauptbestandteil des globalen Staubkreislaufs dar. Die bekannte saisonale Variation des Transports nach Südamerika im Winter und in die Karibik im Sommer kann in dieser Arbeit bestätigt werden. Für die Dauer des Transports

von den Emissionsregionen bis zur Deposition werden anhand von Eulerschen und Lagrangeschen Methoden typische Zeitskalen von neun bis zehn Tagen bestimmt. Für Staub, der über den Atlantik transportiert wird, wurde in früheren Studien die Bodélé-Senke als eines der größten Herkunftsgebiete angesehen. Obwohl die absoluten Emissionen in dieser Region vergleichbar sind, ist der Beitrag von Staub aus der Bodélé-Senke am transatlantischen Transport in den vorliegenden Ergebnissen gering. Dieser Widerspruch kann hier nicht aufgeklärt werden und bedarf weiterer Untersuchungen, da sowohl die Modellresultate als auch die Grundlage bisheriger Analysen, wie Satellitendaten, mit Unsicherheiten behaftet sind.

Die genannten Eigenschaften des transatlantischen Transports ändern sich nur geringfügig in Simulationen, welche die Verhältnisse während der Kleinen Eiszeit in der Mitte des vergangenen Jahrtausends, mit einer durchschnittlichen bodennahen Abkühlung von 0,5 bis 1 K, wiedergeben. Allerdings bewirkt die Intensivierung des Westafrikanischen Monsuns während der Kleinen Eiszeit im Sommer höhere Staubemissionen in Nordafrika, sowie feuchtere Bedingungen in der Sahelzone. Auch der Indische Monsun und die von dieser Zirkulation beeinflussten Staubemissionen auf der Arabischen Halbinsel sind während der Kleinen Eiszeit verstärkt. Das Jahresmittel des globalen Staubbudgets hingegen zeigt nur schwache klimatische Abhängigkeit. Änderungen des Mineralstaubzyklus sollen in dieser Arbeit auf klimatische Einflussfaktoren wie Treibhausgaskonzentrationen zurückgeführt werden können, weshalb die Bodenparameter des Modells, von denen die Staubemission ebenfalls abhängt, nicht variiert werden. Die Verifikation der vorliegenden Resultate ist aufgrund einer geringen Anzahl an Vergleichsdatensätzen problematisch. Künftige Simulationen, die auf den Ergebnissen dieser Arbeit aufbauen und auch verbesserte Rekonstruktionen der Bodenparameter berücksichtigen, können das Wissen über den Staubzyklus in vergangenen Klimaepochen weiter vertiefen. Höhere zeitliche Auflösungen von Zeitreihen der Staubdeposition aus existierenden Eis- und Sedimentbohrkernen würden eine präzisere Evaluation solcher Modellstudien ermöglichen.

1

Introduction and objectives

Due to the debate on anthropogenic climate change the global climate system moved into the focus of public attention during past decades. While most of the public discussions deal with the human impact on the climate due to greenhouse gas emissions, it is also important to improve the understanding of natural climate forcing factors. In addition to solar and volcanic activity, aerosol particles are a considerable natural forcing factor for the climate system. About 40% of the global atmospheric aerosol mass consist of mineral dust (Seinfeld and Pandis 1997). Airborne mineral dust particles have the potential to influence regional and global climate. Dust aerosol directly changes the radiation budget by scattering and absorption (Haywood et al. 2001, DeMott et al. 2003b). Dust particles also very efficiently act as ice nuclei (IN) causing indirect radiative effects by impacting ice clouds (Zuberi et al. 2002, DeMott et al. 2003a, b, Sassen et al. 2003). Despite great scientific efforts during the past years, there are still huge uncertainties about the magnitude of these direct and indirect effects on the global climate (IPCC 2007), calling for further research on this topic. Global in-situ measurements of dust concentrations and deposition fluxes are as important as the numerical simulation of the dust cycle.

Due to uncertainties in the source and sink processes of the mineral dust cycle, Global Chemistry Climate Models (GCCMs) cover a very wide range of values for global dust emission and deposition fluxes, the total dust burden and its atmospheric life time. In the AEROCOM project (Aerosol Comparisons between Observations and Models, http://nansen.ipsl.jussieu.fr/AEROCOM/) results of several GCCMs have been compared with each other and with observations. For example, global dust emission and deposition fluxes vary from model to model within the range of one order of magnitude (Textor et al. 2006, Huneeus et al. 2011). This thesis presents the first detailed analysis and evaluation of the mineral dust cycle in the ECHAM5/MESSy Atmospheric Chemistry (EMAC) GCCM (http://www.messy-interface.org). This model system is described in detail in chapter 2.

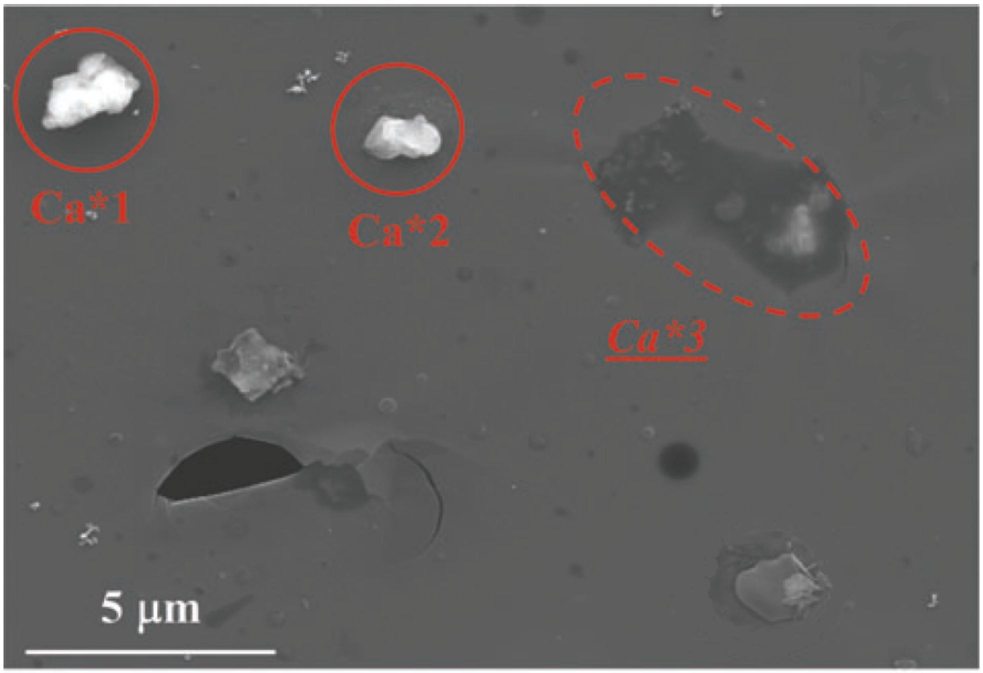

Fig. 1.1: Sample of unprocessed, non-hygroscopic (Ca*1, Ca*2) and processed, hygroscopic (Ca*3) mineral dust particles, collected at Shoresh, Israel in February 2004 (modified from Laskin et al. 2005).

Freshly emitted dust particles are typically water insoluble (Aquila et al. 2011). By coagulation with other particles having a soluble fraction or by condensation of gaseous acids, like nitric or sulphuric acid, the dust particles become soluble. This irreversible ageing or processing of dust was measured by Laskin et al. (2005). An example of unprocessed and processed particles is shown in Fig. 1.1. In this case the solid calcium carbonate of the dust particles reacted with gaseous nitric acid to form aqueous calcium nitrate, water and gaseous carbon dioxide. The properties of dust particles regarding their impact on radiative processes, cloud modification and heterogeneous chemistry may significantly change during the ageing (Laskin et al. 2005). This is indicated, e.g., by the much larger size of the processed particle compared to the unprocessed ones (see Fig. 1.1). The ageing of particles is also very important for the removal of dust from the atmosphere, as scavenging is much more efficient for soluble particles. For these reasons a suitable chemistry setup in the model (described in section 2.5) is required to realistically simulate the processing of dust particles.

It is known that Global Circulation Models (GCMs) can produce considerably different results in many respects depending on the model resolution. Affected are, for example, the characteristics of extratropical cyclones (Jung et al. 2006), storm-tracks and the North Atlantic Oscillation (NAO) (Marti et al. 2010), and variables as relative humidity and aerosol optical thickness (Bian et al. 2009). Therefore, the influence of the horizontal resolution on the dust cycle is investigated. For this, five-year time slice simulations with four different resolutions (T42 $\approx$ 2.8°, T63 $\approx$ 1.9°, T85 $\approx$ 1.4°, and T106 $\approx$ 1.1°) are considered in this study. The time slices are driven by constant boundary conditions, e.g., monthly values of the sea surface temperature (SST) and the emissions of chemical species, to enable the calculation of climatological means.

Furthermore, the effect of the dust emission scheme is analysed because this plays a decisive role for the simulation of the entire dust cycle (Kang et al. 2011). For each of the four model resolutions, simulations with two different emission schemes are conducted, namely, the schemes described in Balkanski et al. (2004) and in Tegen et al. (2002), which have been widely used in the literature. For instance, some of the models in the AEROCOM project also use these dust emission parametrisations (Huneeus et al. 2011). Both schemes calculate log-normal size distributed dust emission fluxes, depending on actual meteorological variables such as the 10-m wind speed. The scheme of Balkanski et al. (2004) provides a monomodal emission flux while the parametrisation of Tegen et al. (2002) calculates bimodal dust emissions, based on 192 internal size classes. The two schemes also differ in the description of surface parameters, which affect the emission flux. Further details are given in section 2.3.

In addition to the abovementioned effects on the global climate system, mineral dust influences another scope of the earth system. Dust deposition to oceans and rain forests provides nutrients as iron and phosphorous to these ecosystems (Martin and Fitzwater 1988, Swap et al. 1992, Chadwick et al. 1999). By changing the productivity of the oceans with regard to, e.g., dimethyl sulfide, Jickells et al. (2005) described a complex feedback mechanism between the mineral dust cycle and the global climate system. Development and growing of algae and phytoplankton blooms are associated with the input of mineral dust to the oceans (Ramos et al. 2005). The satellite image in Fig. 1.2 illustrates such a situation with dust from the Sahara over the eastern Atlantic Ocean and an algae bloom off the Portuguese coast.

An important branch of the global dust cycle constitutes the transatlantic transport of dust from North African source regions, across the ocean to the Americas. Investigations of the impact of mineral dust on the atmosphere over North Africa started as early as 1949 (ElFandy 1949). Junge (1956) found mineral dust particles as a “curiosity” in aerosol samples, taken in Florida in July and August 1954, and assumed that the dust was carried from West Africa across the Atlantic Ocean by easterly trade winds. Thenceforth, the transatlantic transport of mineral dust from the Sahara to the Americas has become a large area of research (see, e.g., Delany et al. 1967, Prospero et al. 1970, Carlson and Prospero 1972, Lushine 1975, Swap et al. 1992, Engelstaedter et al. 2009, Nowottnick et al. 2011). An exemplary case of

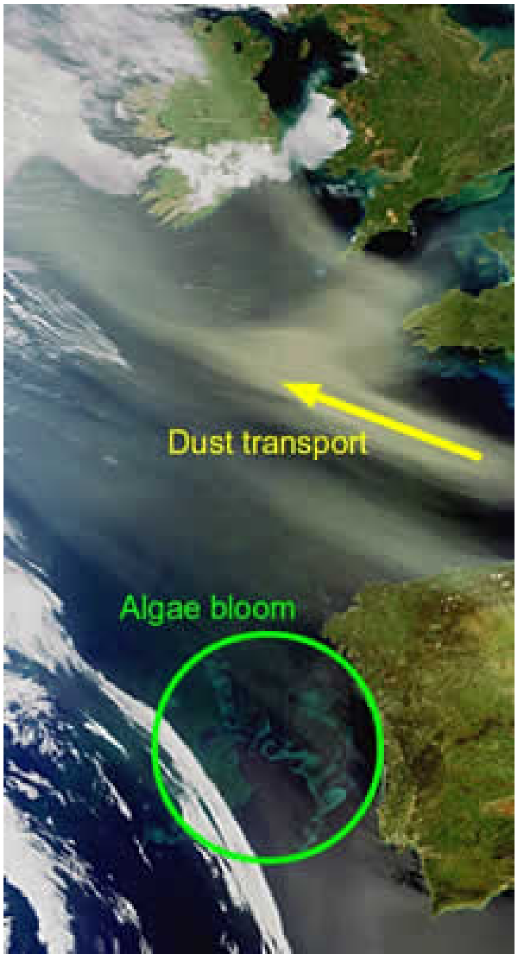

Fig. 1.2: Satellite image of a Saharan dust plume over the Bay of Biscay and surroundings and an algae bloom west of Portugal on 8 April 2011 (http://www.wmo.int/pages/prog/arep/wwrp/new/ocean.html, 27. 11. 2012).

a large-scale Saharan dust outbreak, which transported huge amounts of dust across the Atlantic Ocean, is shown in Fig. 1.3. In this situation, the dust could be traced in satellite imagery for several days from the Sahara all across the Atlantic Ocean. Several publications on this case (e.g., Knippertz and Fink 2006, Min et al. 2009, Shao et al. 2010, Mangold et al. 2011, Gläser et al. 2012a) and other significant Saharan dust outbreaks (e.g., Bencardino et al. 2011, Pan et al. 2011, Skonieczny et al. 2011, Kocha et al. 2012) appeared during the last years. In the present study the transatlantic dust transport is climatologically analysed on the basis of a five-year time slice simulation (see chapter 4). The focus will be on questions of transport time, seasonal variation of the spatial dust distribution, and main source regions for the transatlantic dust transport.

The third part of this thesis deals with the variations of the mineral dust cycle under different climatic conditions. To improve projections of future climate, it is essential

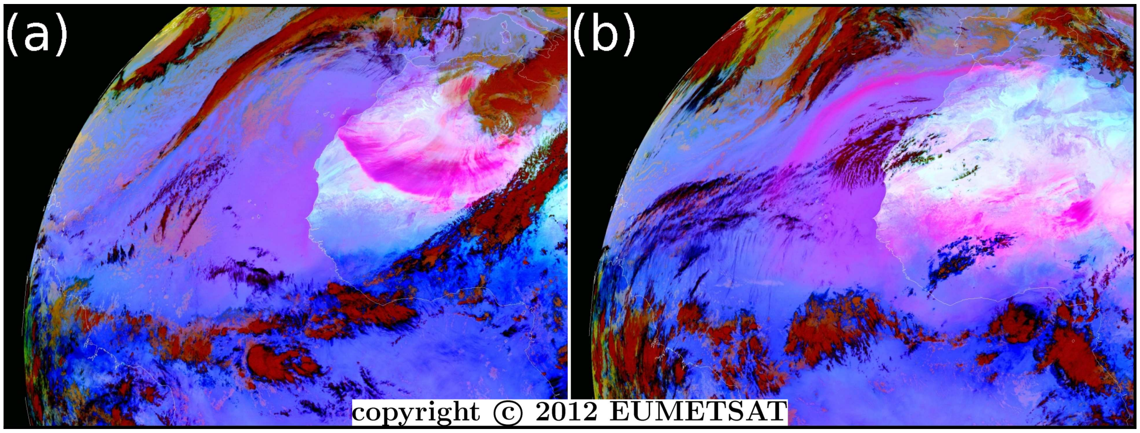

Fig. 1.3: European Organisation for the Exploitation of Meteorological Satellites (EUMETSAT) Meteosat Second Generation (MSG) dust red–green–blue (RGB) composite for (a) 3 and (b) 6 March 2004 12:00 UTC. Airborne dust is indicated by pinkish colours. The RGB composite is produced using the following MSG infrared channels: 12.0 µm - 10.8 µm (red), 10.8 µm - 8.7 µm (green), 10.8 µm (blue) (Gläser et al. 2012a).

to understand the impact of single climate forcing factors and potential feedback mechanisms between these forcings and other parameters they affect. Simulations of past climate epochs can be evaluated by comparing them with data from independent climate reconstructions. Although such a comparison is (i) subject to uncertainties in both the proxy and model data and (ii) usually only possible at specific sites, it is a necessary step in order to verify the model representation of the relevant processes and to enhance confidence in the results of future climate projections.

The mineral dust cycle is on the one hand influenced by climatic changes. On the other hand it feeds back on the global climate mainly due to the particles' impact on radiation and cloud microphysics. Data from ice cores and marine sediment records show up to 20 times higher dust deposition rates during the Last Glacial Maximum (LGM, about 20 000 BP) compared to the recent climate (see Fig. 1.4, Mahowald et al. 1999). In general, numerical simulations and data from ice cores indicate about 2.5 times higher atmospheric dust loadings and dust deposition fluxes during cold glacial periods than during interglacials (Petit et al. 1999, Winckler et al. 2008, Takemura et al. 2009, Maher et al. 2010, Lambert et al. 2012). These differences have been attributed to higher wind velocities, causing higher dust emissions, to a reduced intensity of the hydrological cycle, leading to a longer life time of dust particles in the atmosphere, and to an enlargement of the dust source regions due to reduced vegetation and soil moisture during the cold periods (Mahowald et al. 1999).

In this thesis the focus is on the mineral dust cycle during the Little Ice Age (LIA, 13th to 19th century). The climatic conditions of the LIA cannot be compared with those of the glacial periods, as the LGM. During the LGM global temperature was

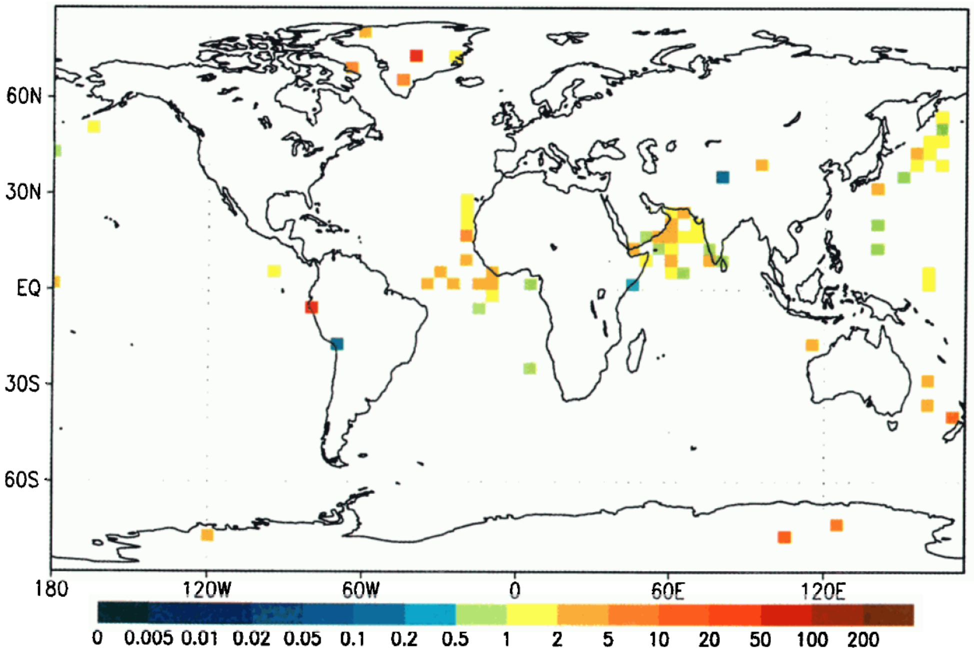

Fig. 1.4: Ratio of dust deposition fluxes during the LGM to the recent climate from ice cores and marine sediment cores and traps (Mahowald et al. 1999).

about 4–5 K colder than today (Smith and Gregory 2012), while the cooling during the LIA is on the order of 1 K (Hegerl et al. 2006, Christiansen and Ljungqvist 2012). Thus, the characteristics of the mineral dust cycle cannot be estimated from earlier reconstructions of glacial periods, which requires performing specific simulations of the dust cycle during the LIA (see chapter 5). New information on the atmospheric mineral dust cycle under LIA conditions potentially pave the way for further investigations on feedback mechanisms between dust and the earth system.

Moreover, besides the aforementioned specific objectives of this work, research on mineral dust is interesting for several other reasons, relating to human life. Dust particles, especially after passing industrialised regions where they could gather pollutants, might carry these over long distances. Weak evidence has been found for Asian dust impacting human health in Korea, Taiwan, and Beijing (Kwon et al. 2002, Chen et al. 2004, Zhao et al. 2007). Regarding the risk of infection with meningococcal meningitis in West Africa, Sultan et al. (2005) attributed catalytic effects to dust-laden winds. For Saharan dust and its impact on people in Europe, Karanasiou et al. (2012) summarised several studies on this topic. They concluded that so far no explicit answer can be given, requiring further exploration of the health impact of Saharan dust.

Severe dust storms have the potential to affect land, sea, and air traffic by requiring the closure of airports or causing accidents due to reduced visibility (Criado and Dorta, 2003, http://www.arabtimesonline.com/Portals/0/PDF_Files/pdf11/apr/05/03.pdf, http://thextremeweather.com/the-blogs/major-dust-storm-moves-through-arizona.pdf, 27. 11. 2012). This aspect, however, will not be considered in this global-scale study.

The remainder of this thesis is structured as follows: The model system EMAC in general and the applied model setups are described in chapter 2. The dependency of the dust cycle on the spectral model resolution and the dust emission scheme is analysed in chapter 3. This chapter additionally contains the investigation of two single dust storms, simulated with EMAC, in order to evaluate the performance of the model in reproducing distinct dust events. Chapter 4 addresses the transatlantic transport of dust from North Africa to the Americas. Impacts of changed climatic conditions on the mineral dust cycle during the LIA are presented in chapter 5, followed by a final discussion of the results and an outlook in chapter 6.

2

The ECHAM5/MESSy Atmospheric Chemistry model system (EMAC)[1]

The model system EMAC couples the Global Circulation Model (GCM) ECHAM to the Modular Earth Submodel System (MESSy). All simulations throughout this thesis are performed with the model version EMAC 2.40, comprising the version 5.3.02 of the ECHAM GCM, denoted as ECHAM5 from now on. In the following, a general overview about the GCM ECHAM5 (section 2.1) and the concept of MESSy (section 2.2) is given. Sections 2.3 and 2.4 contain a detailed description of the representation of mineral dust emission and deposition processes in the model, followed by the specification of the model setup in section 2.5.

2.1 ECHAM5 – General model description

The GCM ECHAM, based on a former version of the numerical weather prediction (NWP) model of the European Centre for Medium-range Weather Forecasts (ECMWF, Reading, United Kingdom), was developed at the Max Planck Institute for Meteorology (MPI-MET) in Hamburg, Germany. Its name is composed of the capitals of European Centre and the first syllable of Hamburg. At the MPI-MET the NWP model was modified to be suitable for climate simulations (Roeckner et al. 2003, 2006).

To describe the atmospheric circulation, numerical models have to solve the Navier-Stokes equations, a set of coupled differential equations. They assemble Newton's law of motion, conservation of mass, the first law of thermodynamics, and the ideal gas law. Prognostic variables of the ECHAM5 model are vorticity, divergence, temperature, the natural logarithm of surface pressure, and mixing ratios of different water species. For time integration a semi-implicit leapfrog scheme is used and a time filter inhibits the growth of numerical modes (Roeckner et al. 2003).

The ECHAM5 is based on a spectral dynamical, hydrostatic core. The Navier-Stokes equations are approximated in the horizontal by truncated series of spherical

---

[1] This chapter is based on the model description in Gläser et al. (2012b).

harmonics. Moisture variables constitute an exception, as they are represented in the grid point space. The spectral truncation represents the horizontal resolution of the model. Only triangular truncations are applicable in the ECHAM5 and some standard wave numbers for the truncation exist. There are the following typical truncations (associated number of Gaussian longitudes and latitudes): T21 (64×32), T31 (96×48), T42 (128×64), T63 (192×96), T85 (256×128), T106 (320×160), T159 (480×240) (Roeckner et al. 2003).

A hybrid pressure grid is applied as vertical coordinate, where terrain-following levels in the lower troposphere fade to constant pressure levels in the stratosphere. The most common vertical resolution for tropospheric simulations involves 31 layers, reaching up to 10 hPa. Further resolutions with top heights of 0.01 hPa use 87 or 90 layers.

A detailed description of the ECHAM5 model is provided in the Technical Report of Roeckner et al. (2003).

2.2 MESSy – The concept of modularisation

The MESSy project started in 2001 at the Max Planck Institute for Chemistry in Mainz, Germany. Today ten institutes apply this model system and many of them contribute to its further development. MESSy approaches the development of a comprehensive Earth System Model (Jöckel et al. 2005). The central idea is the consolidation of various, modularised processes via the MESSy interface (see Fig. 2.1).

MESSy consists of generic and regular submodels. Generic submodels provide the interface required for the interaction between the submodels, e.g., the data man-

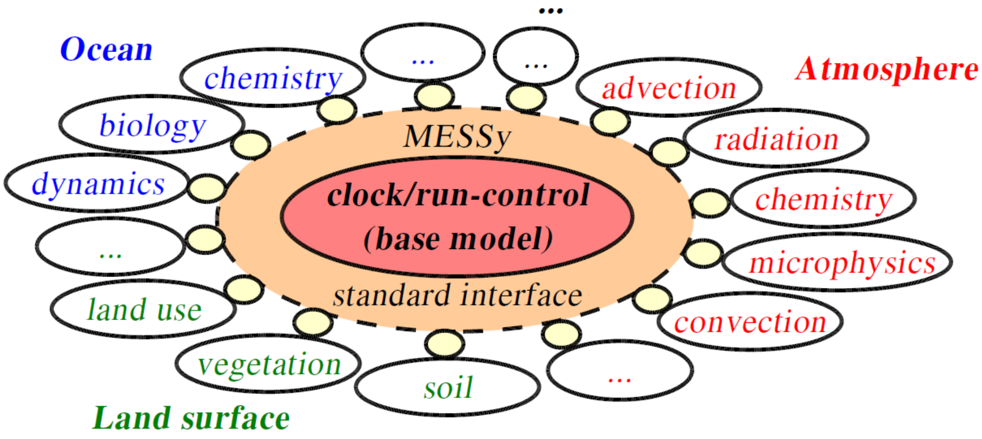

Fig. 2.1: Schematic illustration of the connection of different, modularised processes (outer ring) with each other and with a base model via the MESSy interface (Jöckel et al. 2005).

agement, the Input/Output facility, and a tracer interface. They enable the data exchange between the MESSy submodels and, if necessary, between the MESSy submodels and a base model, in case of EMAC this is the ECHAM5. Regular submodels, depicted as ellipses in the outer ring in Fig. 2.1, describe miscellaneous processes as radiation, cloud microphysics, atmospheric chemistry, or emission and deposition of tracers and aerosols or provide diagnostic tools. Different realisations of a single process, for example, the emission of mineral dust, can be chosen via namelist settings. No re-compilation is required for such changes, ensuring the reproducibility of the results. The following example illustrates this MESSy principle: The base model provides the near-surface wind velocity and the soil moisture. Via the MESSy interface these data are made available to the submodel that calculates the dust emission flux according to the parametrisation chosen via namelist switch. The dust flux is then accessible by other submodels that calculate, for instance, the chemical ageing or the deposition of the dust particles.

The functionality of MESSy as GCCM, comprising the ECHAM5 as base model, is well evaluated (Jöckel et al. 2006). For further information see Jöckel et al. (2010) and the MESSy website: http://www.messy-interface.org/.

2.3 Mineral dust emission parametrisation

Emissions of trace gases and aerosols that depend on the actual meteorological conditions, e.g., the 10-m wind velocity, are calculated by the submodel ONLEM, which stands for online-calculated emissions. In addition to mineral dust, ONLEM calculates the emission fluxes of sea salt, dimethyl sulfide, nitrogen oxides, and others (Kerkweg et al. 2006b). The default dust emission scheme in EMAC is described in Balkanski et al. (2004), which is called BK scheme from now on. Additionally, a second dust emission parametrisation has been implemented for this study to quantify the effect of the emission scheme. As second scheme the one by Tegen et al. (2002), in the following referred to as TG scheme, was chosen. Both parametrisations are also implemented in the ECHAM5-HAM model (Stier et al. 2005), where HAM stands for Hamburg Aerosol Module. Despite the fact that both models, EMAC and ECHAM5-HAM, are based on the same GCM (i.e., ECHAM5) they differ with respect to the implementation of the aerosol modifying processes, e.g., the removal processes (sedimentation, dry and wet deposition) and the chemistry. The two parametrisations calculate the dust emission online in every time step, i.e., in response to prognostic model variables. Details on both emission schemes and a first comparison of them is provided in the following.

2.3.1 The emission scheme of Balkanski et al. (2004)

The BK scheme requires three external input fields: threshold 10-m wind velocity (v_{thr}), source strength factor (SSF), and clay content (Kerkweg et al. 2006b). Balkanski et al. (2004) derived their parametrisation by using v_{thr} according to Marticorena and Bergametti (1995) and the database of soil types from the Food and Agricultural Organization of the United Nations (http://www.fao.org). Parameters were adjusted such that the simulated optical depth matches with the optical depth corrected from the Total Ozone Mapping Spectrometer (TOMS) aerosol index (Balkanski et al. 2004, Stier et al. 2005). No dust particles are emitted if the soil is too wet. The drying rate of soil is a function of recent precipitation, surface temperature, and the clay content, as clay retains water for a longer time than other soil types. Hence, the higher the clay content, the longer it takes the surface soil to dry. For each desert grid point, where the soil is dry enough, the vertical dust emission flux ($VDEF$) is calculated as a function of v_{thr}, SSF and, the 10-m wind velocity ($v_{\text{10-m}}$) according to:

$$VDEF = SSF \cdot (v_{\text{10-m}} - v_{thr}) \cdot (v_{\text{10-m}})^2 \quad . \tag{2.1}$$

The emitted dust aerosol is described as a log-normal size distribution with a mass mean radius (mmr) of 1.25 μm and a standard deviation (σ) of 2 μm.

2.3.2 The emission scheme of Tegen et al. (2002)

The TG scheme is much more complex (see Tegen et al. (2002), Stier et al. (2005), and Cheng et al. (2008) for details). In return, it provides more information about the dust emission, which is calculated from 192 internal dust size classes i ranging from 0.2 to 1300 μm in diameter. For each class an individual threshold friction velocity ($u_{*thr}(i)$) is specified. The soil of each dust source grid point consists of a varying portion of four soil types: clay, silt, medium/fine sand, and coarse sand. In addition, preferential source regions (dried palaeolake beds) are prescribed, which are particularly active for 10-m wind speeds above 10 m s^{-1}. From these soil texture classes, required as input fields, the relative surface area (s_i) covered by each dust size class i is computed. The horizontal particle flux (HPF) is then calculated for each size class as follows:

$$HPF(i) = \frac{\rho_a}{g} \cdot u_*^3 \cdot \left(1 + \frac{u_{*thr}(i)}{u_*}\right) \cdot \left(1 - \frac{u_{*thr}^2(i)}{u_*^2}\right) \cdot s_i$$

$$\text{if } u_* \geq u_{*thr}(i) \quad (HPF(i) = 0, \text{ otherwise}), \tag{2.2}$$

with ρ_a the air density, g the gravitational constant, and u_* the surface wind stress, which is calculated from the prognostic 10-m wind speed. The horizontal fluxes are turned into the respective vertical dust emission fluxes $VDEF$ by:

$$VDEF(i) = \alpha \cdot f(LAI) \cdot HPF(i) \cdot I_\Theta \quad , \tag{2.3}$$

where α describes the soil texture characteristics. For the Leaf Area Index (LAI) monthly mean values are prescribed. The LAI-dependent function takes into account that the flux increases or decreases depending on the vegetation. I_Θ is 0 if the ratio of prognostic soil moisture to the field capacity is higher than 0.99 and 1 otherwise (Tegen et al. 2002). The vertical emission fluxes of single size classes are summed up to get a bimodal dust emission with an insoluble accumulation mode (mmr = 0.37 µm, σ = 1.59 µm) and an insoluble coarse mode (mmr = 1.75 µm, σ = 2 µm) (Cheng et al. 2008).

2.3.3 Comparison of the two dust emission schemes

As an example for the different behaviour of the two dust emission schemes, the values of the input fields of two prominent dust source regions, the Bodélé Depression in Chad and the Thar Desert in Northwest India, are shown in Table 2.1. With the BK scheme 10-m wind speeds of more than 7.2 m s^{-1} are necessary to mobilise particles from the Bodélé Depression while only 6 m s^{-1} are required in the Thar Desert. The SSF is about 3.5 times higher in the Thar Desert than in the Bodélé Depression. With the TG scheme the 10-m threshold velocity is 6.2 m s^{-1} in both regions. The LAI for the TG scheme varies from 0.27 to 0.43 over the year in the Thar Desert where the soil mainly consists of medium-fine and medium particles.

Emission scheme	Parameter	Bodélé Depression	Thar Desert
Balkanski et al. (2004)	v_{thr}, m s^{-1}	7.2	6.0
	SSF	0.30×10^{-9}	1.08×10^{-9}
Tegen et al. (2002)	v_{thr}, m s^{-1}	6.2	6.2
	LAI	0.00 in each month	varies from 0.43 (Jan) to 0.27 (Jun, Jul, Aug)
	soil texture class:		
	Coarse	1.00	0.14
	Coarse-medium	0.00	0.06
	Medium	0.00	0.26
	Medium-fine	0.00	0.54
	Fine	0.00	0.00

Table 2.1: Input parameters for the dust emission schemes of Balkanski et al. (2004) and Tegen et al. (2002) for the Bodélé Depression and the Thar Desert.

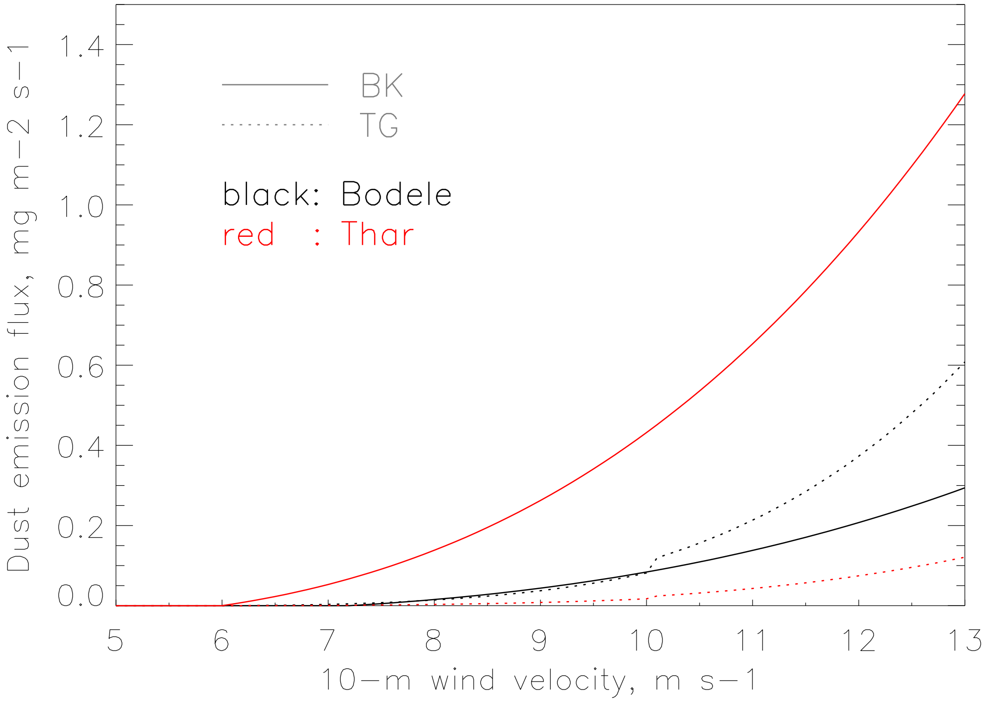

Fig. 2.2: Vertical dust emission flux (mg m^{-2} s^{-1}) vs. 10-m wind velocity (m s^{-1}) as simulated with the two dust emission schemes by Balkanski et al. (2004) (BK, solid lines) and Tegen et al. (2002) (TG, dotted lines) in the Bodélé Depression (black) and the Thar Desert (red).

In the Bodélé Depression the LAI is constantly 0 and the particles are assumed to be in the coarse texture class.

How these two very different schemes behave dependent on the region and the 10-m wind speed is shown in Fig. 2.2. For this example the soil moisture is set to 0. Both parametrisations produce similar fluxes in the Bodélé Depression for 10-m wind speeds up to 10 m s^{-1}. Higher velocities cause higher emissions with the TG scheme because the Bodélé Depression is a classic example of a palaeolake preferential dust source area (Tegen et al. 2002). The differences in the Thar Desert are enormous. The relatively low v_{thr} and the high SSF cause very strong emissions with the BK scheme.

2.4 Mineral dust deposition processes

The removal of mineral dust, other aerosol particles, and trace gases from the atmosphere is calculated in three submodels, treating different kinds of deposition processes. According to the process, these submodels are called SCAV for scavenging (Tost et al. 2006b), SEDI for sedimentation, and DRYDEP for dry deposition (Kerkweg et al. 2006a).

Wet removal processes are treated in the submodel SCAV, which distinguishes between nucleation scavenging and impaction scavenging. Soluble aerosol species, such as aged dust particles, can be the origin of a cloud droplet or can become part of a growing droplet. If the growth of such droplets results in precipitation formation, the involved dust particles are removed from the atmosphere by nucleation scavenging. Impaction scavenging of dust occurs if a dust particle is hit and taken up by a falling droplet. The efficiency of nucleation and impaction scavenging depends on the size of the aerosol particles and of the cloud or rain droplets (Tost et al. 2006b).

The sedimentation velocity of aerosol particles due to their mass is calculated in the submodel SEDI. It is based on the Stokes velocity, which depends on the size and the density of the particle and the air density. Multiplication of the Stokes velocity with the Cunningham-slip-flow factor takes into account that dust and other aerosol particles are no ideal spheres. For modal descriptions of aerosols, the sedimentation velocity has to be modified by another, the Slinn factor. It corrects for differences between the sedimentation velocity of a particle with the mean radius of a log-normal mode and the mean velocity of all particles of this mode, which is larger than the first-mentioned (Kerkweg et al. 2006a). The sedimentation of particles is calculated in each model layer. Only the loss from the lowermost layer describes the actual removal from the atmosphere.

In contrast to the sedimentation, dry deposition is only considered in the surface layer. The submodel DRYDEP covers the removal of aerosol particles and trace gases due to near-surface turbulence. The aerosol deposition fluxes are based on the 'big leaf approach' and depend on the properties of the particle and of the earth's surface, as the roughness length, surface resistances, etc. (Kerkweg et al. 2006a).

2.5 Model setup

The mineral dust cycle mainly takes place in the troposphere. Stratospheric processes are assumed to have only minor impact on the dust cycle. Therefore, all simulations presented in this study, independent of the horizontal resolution, employ a vertical resolution of 31 layers with the top layer at a height of 10 hPa. The impact of the horizontal model resolution on the mineral dust cycle is investigated using spectral resolutions of $T42 \approx 2.8°$, $T63 \approx 1.9°$, $T85 \approx 1.4°$, and $T106 \approx 1.1°$.

The entire dust cycle in the model crucially depends on the dust emission scheme. Two different parametrisations, which are implemented in ONLEM and used in this study, are described in detail in section 2.3. The removal processes of mineral dust and other aerosol species are calculated in the submodels DRYDEP, SCAV, and SEDI, as depicted in section 2.4.

The ageing processes of aerosol particles are simulated with the microphysical aerosol model M7 (Vignati et al. 2004), implemented as delineated by Kerkweg et al. (2008).

M7 describes the aerosol distribution by four soluble and three insoluble log-normal modes. Freshly emitted dust particles are assumed to be always insoluble and can belong to the accumulation and the coarse mode. They become soluble either by intermodal coagulation or due to the condensation of sulphuric acid. Wet deposition is an important removal process for dust. Soluble particles are more efficiently scavenged than insoluble ones. Thus, accurate sulphur chemistry is required to transfer dust particles from the insoluble modes to the respective soluble mode. A simulation without any sulphurous species produced an unrealistic, almost homogeneous global dust distribution. Hence, gas phase chemistry is simulated using the submodel MECCA (Module Efficiently Calculating the Chemistry of the Atmosphere, Sander et al. 2011). The hypothesis that not the most complex, and therefore computationally most expensive, chemistry setup is required to simulate a realistic global dust distribution was proven by further tests. These tests showed that the minimum requirements in terms of chemistry are to include basic sulphur chemistry in order to correctly represent the ageing processes of the dust particles. The chosen chemistry setup contains 44 gas phase and 13 photolysis reactions including HO_X, NO_X, and sulphur chemistry. These chemical equations are listed in appendix A. A complete list of all used submodels is given in appendix B.

3

Sensitivity of the mineral dust cycle to the spectral resolution and the dust emission scheme[1]

3.1 Introduction

The importance of mineral dust for the global climate system is widely delineated in the literature. Properties and direct and indirect effects of dust particles on the climate are described, for example, in Haywood et al. (2001), Zuberi et al. (2002), DeMott et al. (2003a, b), and Sassen et al. (2003), but the scientific knowledge about these effects needs to be deepened (IPCC 2007). In addition to the climate impact of airbourne mineral dust, the deposition of dust to oceans and rain forests fertilises these ecosystems (e.g., Martin and Fitzwater 1988, Swap et al. 1992, Chadwick et al. 1999). Moreover, dust particles might have negative impacts on human health (Kwon et al. 2002, Chen et al. 2004) and dust storms potentially affect land, sea, and air traffic (Criado and Dorta 2003). Numerical simulations of the mineral dust cycle can provide new insights about its impact on the earth system. However, model results involve uncertainties, as very wide ranges of global dust parameters in simulations of various model systems show. The AEROCOM project summarises results of 14 GCCMs, with global dust emission fluxes varying from 514 to 4 313 Tg yr^{-1} and deposition fluxes from 676 to 4 359 Tg yr^{-1}. Total dust burdens range from 6.8 to 29.5 Tg and life times vary between two and seven days (Huneeus et al. 2011).

The horizontal model resolution influences a model's results in many ways. For example, there are differences in the simulation of extratropical cyclones with the ECMWF Integrated Forecasting System (IFS) at various resolutions (Jung et al. 2006). The influence of the horizontal resolution on the dust cycle over West Africa in regional simulations with the UK Met Office Unified Model are shown by Marsham et al. (2011) and Heinold et al. (2012, submitted). Regarding dust emissions, they found severe differences between convection-permitting simulations with fine resolutions and convection-parametrising simulations with coarser resolutions. Marti et al. (2010) reported resolution sensitivity of storm-tracks, characteristics of the NAO and

---

[1] This chapter is based on the publication Gläser et al. (2012b).

Resolution	Number of grid boxes lon × lat	Approximated box width, degree	Approximated box width, km
T42	128 × 64	2.8	312
T63	192 × 96	1.9	208
T85	256 × 128	1.4	155
T106	320 × 160	1.1	125

Table 3.1: Grid box numbers in longitudinal (lon) and latitudinal (lat) direction and the approximated box widths of the spectral model resolutions T42, T63, T85, and T106.

inter-annual variability in the tropics with the IPSL (Institut Pierre Simon Laplace) coupled ocean-atmosphere GCM and Bian et al. (2009) found resolution effects in the simulation of relative humidity and aerosol optical thickness with the GMI CTM (Global Modeling Initiative, Chemistry Transport Model). Therefore, the impact of the horizontal resolution on the dust cycle in EMAC is investigated. Four different resolutions, namely T42, T63, T85, and T106 are considered in the present study. Characteristics of these resolutions are listed in Table 3.1.

The influence of the dust emission scheme is analysed because the entire dust cycle in the model crucially depends on the emission parametrisation (Kang et al. 2011). The two emission schemes by Balkanski et al. (2004) and by Tegen et al. (2002) are investigated and details about these parametrisations are provided in section 2.3.

All possible combinations of four spectral resolutions and two dust emission schemes yield eight different model setups. For each of them a time slice simulation is performed. Time slice simulations are intended for representing the possible climatic variability for boundary conditions of one specific year. Due to the dependency of the results on the initialisation of the model, several years with different initial conditions are simulated. Climate forcing factors such as greenhouse gas concentrations as well as boundary conditions, e.g., the SST, stay the same in each year. In this way, the natural variability of the climate system is considered in the results. All time slice simulations presented in this thesis cover a time span of five years. The results are evaluated by comparing them with several in situ dust measurements and the performance of the GCCMs of the AEROCOM project. The aim of the evaluation is to determine the most appropriate model setup for simulations of the mineral dust cycle with EMAC.

In addition to climatological analyses the ability of EMAC to reproduce single dust outbreaks is studied. With the most suitable model setup in terms of reproducing the main climatological aspects, two episodes are simulated and compared with observational data sets. The first episode in May and June 2006 coincides with SAMUM, the Saharan Mineral Dust Experiment, in South Morocco (Kandler et al.

2009). The second episode covers a dust outbreak from the Sahara to Central Europe in May and June 2008. An upper-level trough penetrated from the mid-latitudes into the North African continent. An associated surface low in the lee of the Atlas Mountains caused high near-surface wind speeds and dust emissions in the Sahara (Wiegand et al. 2011). The emerging dust plume was transported northwards and became apparent in measurements of the IN concentration at Kleiner Feldberg in Germany (Klein et al. 2010).

In section 3.2 various data sets that will be compared with the simulations are described. The analysis of the five-year time slice simulations is presented and discussed in section 3.3, followed by the investigation of the two abovementioned single dust episodes simulated with the most appropriate setup in section 3.4. Section 3.5 contains the summary.

3.2 Comparison data sets

The following observational and model data sets were used for validating the EMAC simulations.

3.2.1 Long-term in situ measurements

The results of the time slice simulations will be compared to measured dust deposition fluxes and surface dust concentrations at selected sites (see Tables C.1 and C.2 in the appendix). Deposition data are taken from Ginoux et al. (2001), Tegen et al. (2002), and Mahowald et al. (2009), surface dust concentrations from Stier et al. (2005) and Mahowald et al. (2009). The measurements from cruises, listed in Mahowald et al. (2009), are not considered here because they do not represent annual values. Also measurements of iron concentrations are omitted to avoid uncertainties from the assumption that dust contains 3.5% iron (Mahowald et al. 2009). All together, this provides deposition and concentration measurements at 91 and 47 sites, respectively, which will be compared to the simulated values at the grid box containing the measurement site in section 3.1.

3.2.2 Satellite-based aerosol mass concentration measurements

Fields of columnar aerosol mass concentrations measured by the Moderate Resolution Imaging Spectroradiometer (MODIS) with 1° × 1° grid spacing are provided via the web interface http://gdata1.sci.gsfc.nasa.gov/daac-bin/G3/gui.cgi?instance_id=MODIS_DAILY_L3. The retrieval algorithms are described by Remer et al. (2005). For the evaluation of the time slice simulations presented in this thesis, seasonal mean values of MODIS mass concentrations are calculated using data from 1 March 2000 to 28 February 2005.

3.2.3 The Saharan Mineral Dust Experiment SAMUM

During the SAMUM 2006 field campaign (see Heintzenberg (2009) and the special issue Tellus Ser. B-Chem. Phys. Meteorol., Vol. 61) physical and chemical properties of desert aerosols were measured in South Morocco near Tinfou (30° 14'N, 5° 36'W, 684 m a.s.l.) (Kandler et al. 2009, Knippertz et al. 2009). In section 3.4.1 measured concentrations of the total suspended particle matter (TSP, 12-hourly measurements most of the time) and of particles smaller than 10 μm (PM_{10}, daily measurements) are compared to simulated dust concentrations for the entire measurement period from 12 May to 6 June 2006.

3.2.4 Measurements at Kleiner Feldberg, Germany

Number concentrations of IN and PM_{10} concentrations have been measured since April 2008 at the Taunus Observatory of the Goethe-University of Frankfurt/Main at Kleiner Feldberg in Germany (50° 13'N, 8° 27'E, 825 m a.s.l.) (Klein et al. 2010). The authors suggested that ice nucleating aerosols in Central Europe may consist to a large extent of mineral dust. The comparison of the measurements with simulated dust concentrations is presented in section 3.4.2 for the period from 23 May to 4 June 2008, which contains the strongest event of Saharan dust advection to Germany during the years 2006 to 2010 (Klein et al. 2010).

3.2.5 Satellite-based infrared dust composites

Particular combinations of different channels of the MSG satellite allow for the visualisation of single atmospheric compounds. The RGB composite of the Spinning Enhanced Visible and InfraRed Imager (SEVIRI) IR8.7, IR10.8, and IR12.0 channels shows dust aerosol in magenta colours. Limitations and uncertainties of this satellite product are described by Brindley et al. (2012), who found the ability to identify airbourne dust to be dependent on, for example, the column water vapour or the temperature profile in the lower troposphere. More information about the MSG dust RGB composite can be found in the online documentation (http://oiswww.eumetsat.org/SDDI/html/doc/dust_interpretation.pdf, 27. 11. 2012). These images are used to evaluate the EMAC simulation of the SAMUM episode.

3.2.6 Regional dust model forecasts

Additionally, short-range forecasts of the Barcelona Supercomputing Center-Dust REgional Atmospheric Model (BSC-DREAM) are used for comparison with EMAC for the two episodes. DREAM simulates the atmospheric dust cycle with the emission scheme of Shao and Raupach (1993) modified by Janjic (1994) and Fécan et al.

(1999). The model version 8b has a horizontal resolution of 50 × 50 km and 24 layers extending up to 15 km. For further details see Nickovic et al. (2001), Pérez et al. (2006a, b), and http://www.bsc.es/plantillaH.php?cat_id=322 (27. 11. 2012).

3.3 Evaluation of five-year time slice simulations

In this section, the entire dust cycle of the five-year time slice simulations is analysed with respect to the horizontal model resolution (T42, T63, T85, and T106) and the dust emission scheme (BK and TG). The aim is to determine the model setup that produces the most accurate mineral dust cycle.

For simulations during the LIA (see chapter 5) no analysis data are available. To ensure comparability of the simulations in different climate epochs, no "nudging" towards realistic meteorology is applied in the simulations presented here.

3.3.1 Comparison with dust measurements

For the eight time slice simulations different skill scores determined by the measurements of dust deposition and surface dust concentration, described in section 2.2.1, are listed in Table 3.2. The bias, the mean normalised bias (MNB), the log-mean normalised bias (LMNB), and the normalised root mean square error (NRMS) are considered here and defined according to Lee et al. (2009) and Huneeus et al. (2011) as follows.

$$\text{Bias} = \frac{1}{n_{obs}} \cdot \sum_{i=1}^{n_{obs}} \left[X_{mod}(i) - X_{obs}(i)\right] \tag{3.1}$$

$$\text{MNB} = \frac{1}{n_{obs}} \cdot \sum_{i=1}^{n_{obs}} \left[\frac{X_{mod}(i) - X_{obs}(i)}{X_{obs}(i)}\right] \tag{3.2}$$

$$\text{LMNB} = \frac{1}{n_{obs}} \cdot \sum_{i=1}^{n_{obs}} \left[log_{10}\left(\frac{X_{mod}(i)}{X_{obs}(i)}\right)\right] \tag{3.3}$$

$$\text{NRMS} = \sqrt{\frac{1}{n_{obs}} \cdot \sum_{i=1}^{n_{obs}} \left[\frac{X_{mod}(i) - X_{obs}(i)}{X_{obs}(i)}\right]^2} \tag{3.4}$$

For the calculation of these skill scores the different observational data sets are treated as one concatenated data set. n_{obs} is the total number of measurements, X_{mod} and X_{obs} are the simulated and measured dust deposition or concentration values, respectively, and i is the running index.

The interpretation of Table 3.2 is not straight forward because different setups yield the best results for different skill scores. For example, T42BK is the worst setup with regard to the bias, but it is the best one considering the NRMS. The bias of all

	Bias	MNB	LMNB	NRMS
T42BK	−5.59	3.98	0.04	15.39
T63BK	−4.56	4.92	0.07	19.36
T85BK	−4.11	3.45	−0.08	15.51
T106BK	−4.05	7.13	−0.02	31.11
T42TG	−3.91	6.26	0.20	23.43
T63TG	−2.36	7.32	0.17	30.43
T85TG	−2.09	4.95	0.00	22.08
T106TG	1.95	7.00	0.14	29.25

Table 3.2: Skill scores according to Eqs. (3.1) – (3.4) resulting from the comparison of the eight time slice simulations with in situ measurements of dust deposition and surface dust concentration from Ginoux et al. (2001), Tegen et al. (2002), Stier et al. (2005), and Mahowald et al. (2009), listed in appendix C.

simulations using the BK scheme is worse compared to the simulations with the TG scheme but on average they perform better with regard to the MNB, the LMNB, and the NRMS. Hence, no final decision on the preferred dust emission scheme is made from this analysis alone. Additionally, a clear dependence of the results on the horizontal resolution is lacking. Because measurements at single stations are compared with grid box values here, it is possible that finer resolutions are subject to the double-penalty problem. Double-penalty is an inherent problem of grid point-based verifications, as discussed, e.g., for precipitation forecasts by Wernli et al. (2009). It means that, for instance, a displacement of a feature in a simulation is punished twice, namely for missing the observed feature and for simulating it at the wrong place. Among the simulations with the TG scheme, it is remarkable that T85 yields the best results for three of the four skill scores but from Table 3.2 alone no conclusion can be drawn which setup performs best.

A scatter plot of simulated versus measured values for the different setups (Fig. 3.1) brings about the decision neither. Dashed lines mark a discrepancy of a factor of ten between simulation and measurements. For all setups most of the values lie within this range. This is comparable to results of Huneeus et al. (2011), who compared the AEROCOM models with measurements from Ginoux et al. (2001), Mahowald et al. (2009), and others. One mentionable, resolution-dependent difference is the partly reduction of the overestimation of the lowest deposition measurements (green symbols in the lower left corner in Fig. 3.1). They represent data from the Southern Ocean and of ice cores from Antarctica. The finer resolutions T85 and T106 are able to reproduce some of these measurements better than T42 and T63.

3.3.2 Global dust budget

Table 3.3 shows five-year averages of the global dust emission, load, life time, total and wet deposition and the ratio of wet to total deposition as simulated by EMAC

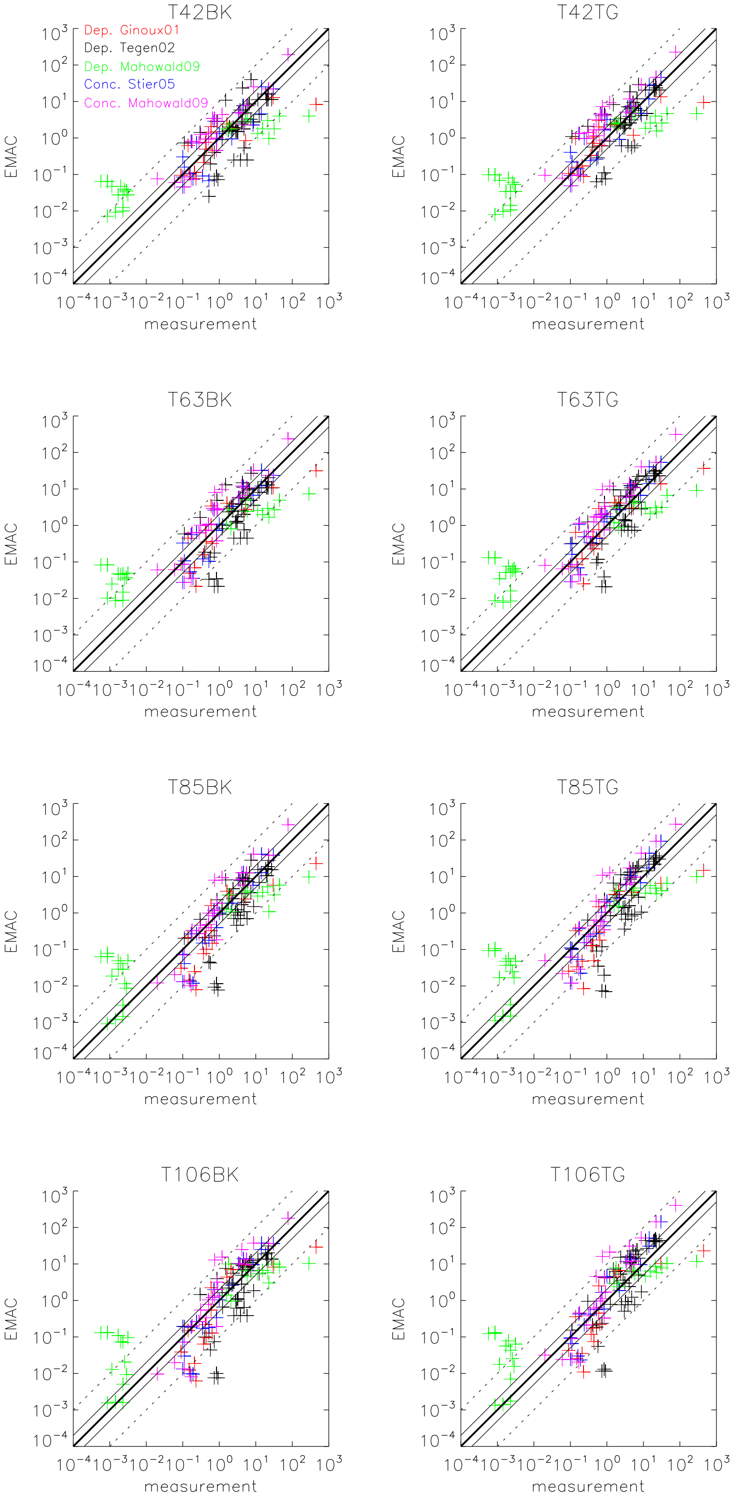

Fig. 3.1: Simulated versus measured dust deposition (g m^{-2} yr^{-1}) and surface dust concentration (μg m^{-3}). Measurements are described in section 2.2.1. Deposition: red: Ginoux et al. (2001), black: Tegen et al. (2002), green: Mahowald et al. (2009); Concentration: blue: Stier et al. (2005), magenta: Mahowald et al. (2009). The bold solid line indicates the 1:1 ratio, thin solid lines the 1:2 and 2:1 ratios, and dashed lines the 1:10 and 10:1 ratios.

	emission Tg yr^{-1}	load Tg	life time days	total dep. Tg yr^{-1}	wet dep. Tg yr^{-1}	$\frac{\text{wet}}{\text{total}}$ dep. %
T42BK	1 651	27.85	6.19	1 644	1 262	76.8
T63BK	2 704	36.20	4.91	2 693	2 096	77.9
T85BK	2 841	31.50	4.09	2 813	2 222	79.0
T106BK	3 238	34.92	3.98	3 208	2 557	79.7
T42TG	1 683	26.63	5.85	1 662	1 046	62.9
T63TG	1 975	27.34	5.12	1 953	1 174	60.1
T85TG	1 815	22.18	4.55	1 781	1 068	59.9
T106TG	2 673	31.55	4.41	2 615	1 588	60.7

Table 3.3: Five-year mean values of various dust parameters of the eight time slice simulations. Deposition is abbreviated as dep.

using T42, T63, T85, and T106 spectral resolutions. For each resolution the results with both implemented emission schemes (BK and TG) are listed. The total dust deposition does not deviate more than 2% from the emissions and there is no trend in the dust load over the five years, showing that the dust budget is closed. The life time is calculated as ratio of dust load to total dust deposition. For the eight different setups, the emissions range from 1 651 to 3 238 Tg yr^{-1}, the load from 22.18 to 36.20 Tg and the life time from 3.98 to 6.19 days. All values of the dust emission and life time are within the very wide range of earlier estimates based upon model simulations (AEROCOM: Textor et al. 2006, Huneeus et al. 2011). The dust load, however, exceeds this range in the T63BK, T85BK, T106BK, and T106TG simulations.

Some other interesting aspects can be obtained from Table 3.3. With the BK scheme, dust emissions increase and life times decrease with increasing model resolution. The dust load, however, is lower in T85BK and T106BK than in T63BK although the emissions are higher leading by definition to the shorter life times. With the TG scheme the life times show the same trend as with the BK scheme, the dust emissions also increase with finer resolution except in T85TG where the emission is lower than in T63TG. The same is true for the dust load, which is in T85TG even lower than in T42TG. One possible explanation for the decreasing life times from T42 to T106 is the increase in the maximum near surface wind speed in finer resolutions, which is associated with the emission of larger particles that settle faster. This is confirmed by the ratio "total deposition close to source regions" to "global total deposition" (not listed), which increases with finer resolution. With both emission schemes the wet-to-total deposition rate is hardly dependent on the resolution but it is generally higher with the BK scheme (≈ 78%) than with the TG scheme (≈ 60%). The BK scheme produces much higher dust emission fluxes in the Thar Desert in India than the TG scheme (see sections 2.3.3 and 3.3.3). These higher emissions lead to very strong wet deposition in the region around the Thar Desert in simulations with the BK scheme. This signal dominates when calculating the overall wet-to-total deposition rate. If the evaluation is limited to the domain outside the Thar region, simulations with the BK and the TG scheme produce both a similar fraction of wet deposition (60–70%). This indicates that wet deposition is particularly important for dust from certain emission regions, and consequently, that emission schemes with stronger emissions in these regions contribute to a larger wet-to-total deposition ratio.

3.3.3 Geographical dust distribution

The global distribution of dust emissions and loads of the eight experiments are illustrated in Figs. 3.2 and 3.3, respectively. At first sight, each setup produces reasonable distributions. A closer look at single regions reveals interesting differences. Independent of the model resolution the BK scheme simulates the global maximum of the emissions in Northwest India, leading to the global maximum in the loads in the same region (left column in Figs. 3.2 and 3.3). For the same location emissions of the TG scheme are in general much lower (right column in Fig. 3.2) and comparable to the values at other hot spots like the Bodélé Depression in Chad (middle column in Figs. 3.2 and 3.3). According to other studies, the Sahara is the largest dust source in the world (Prospero et al. 2002, Washington et al. 2003, Ginoux et al. 2004). The averaged dust emission of the four simulations with the BK scheme accounts for 608 Tg yr^{-1} in the Sahara (5°–36°N, 20°W–40°E) and 1 483 Tg yr^{-1} in India (20°–33°N, 65°–85°E). This means that the dust emissions in India are 2.4 times higher than in the Sahara, which is in clear contradiction to the abovementioned studies. Very strong emissions in India in the BK scheme result from a relatively low 10-m wind speed threshold and a rather high source strength factor in this region compared to values in the Sahara (see section 2.3.3, in particular the discussion of Fig. 2.2). The TG scheme on average simulates 925 Tg yr^{-1} in the Sahara and 169 Tg yr^{-1} in India. Stier et al. (2005) also mentioned the higher emissions in the Thar Desert with the BK scheme compared to the TG scheme.

3.3.4 Seasonal cycle and regional considerations

The seasonal comparison of simulated values of the dust column mass over the Indian subcontinent with MODIS aerosol column mass (not shown) reveals two problems of the BK scheme. Firstly, the simulations with the BK scheme strongly overestimate the column mass, especially during northern hemispheric summer[1]. MODIS measures 539 mg m^{-2} in JJA, 330 mg m^{-2} in MAM, 253 mg m^{-2} in SON, and 212 mg m^{-2} in DJF. T42BK overestimates the JJA value by a factor of 12

---

[1] "northern hemispheric" is abbreviated as NH from now on. Alternatively, seasons are shortened according to the capitals of the included months as DJF, MAM, JJA, and SON.

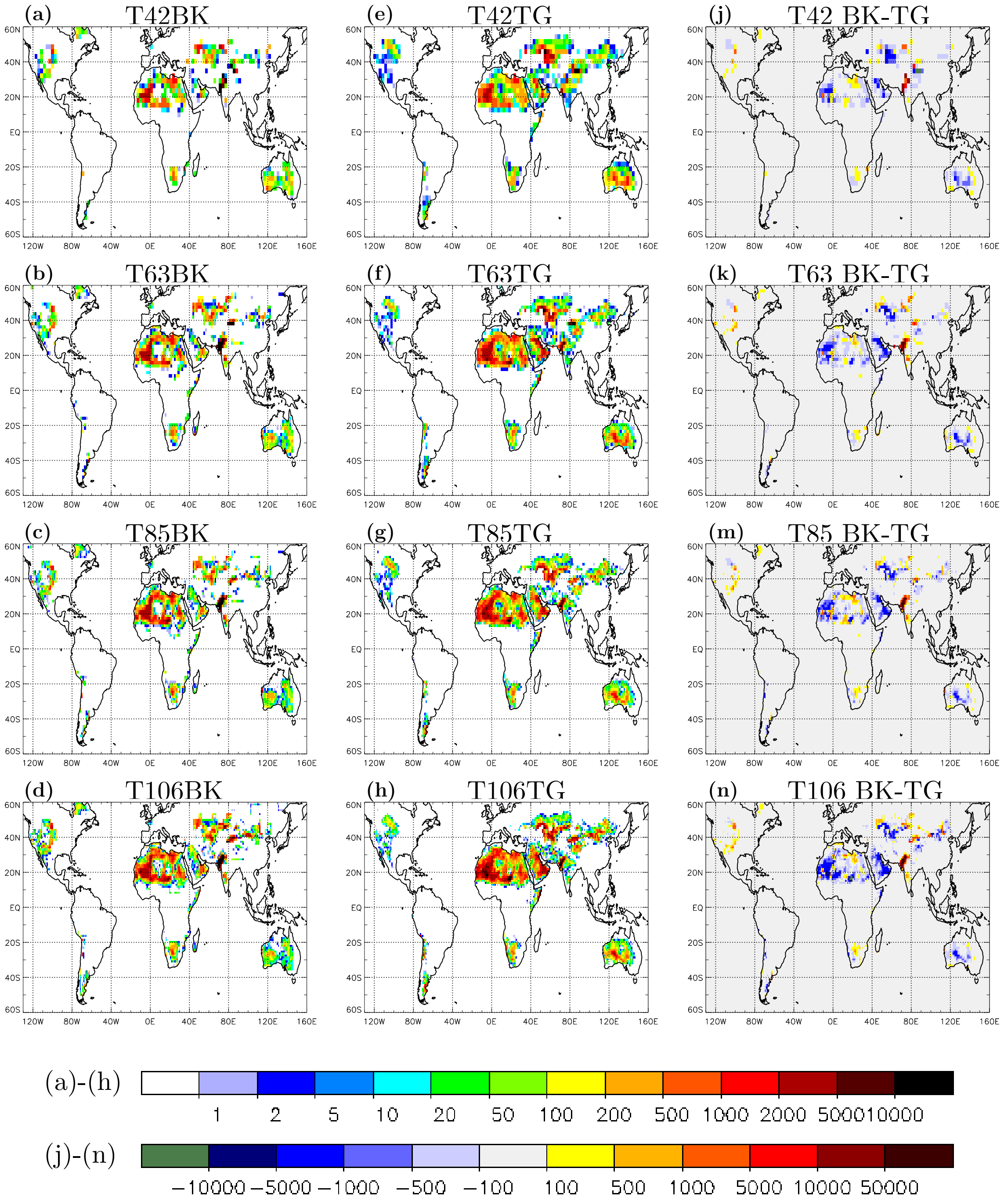

Fig. 3.2: Simulated five-year mean dust emission (kg ha^{-1} yr^{-1}) using the dust emission schemes of Balkanski et al. (2004) (left column) and Tegen et al. (2002) (middle column) and for the spectral model resolutions T42 (1st row), T63 (2nd row), T85 (3rd row), and T106 (4th row). Colours correspond to the upper colourbar. The right column shows the difference of the BK minus the TG scheme, according to the lower colourbar.

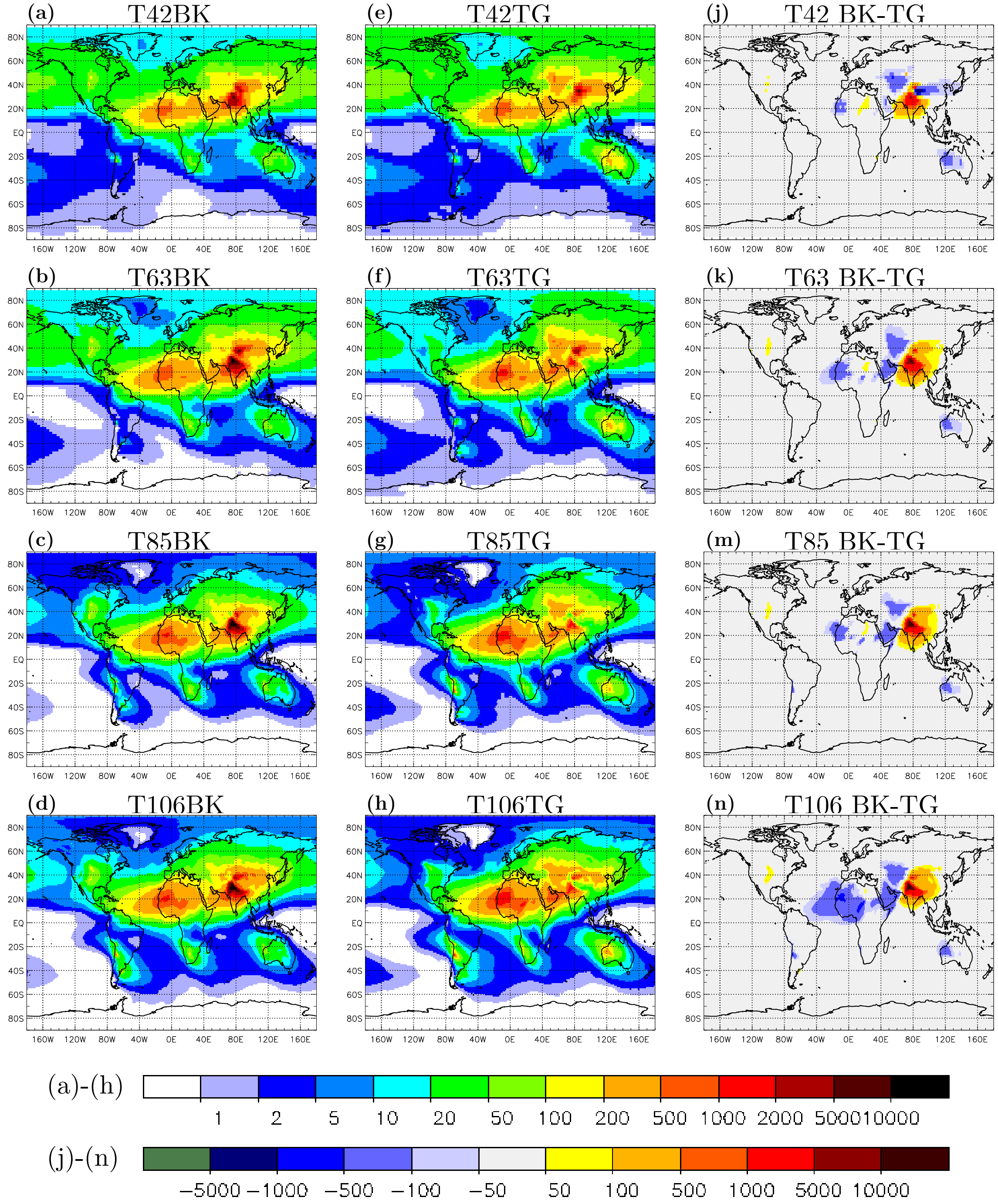

Fig. 3.3: Simulated five-year mean dust column mass (mg m^{-2}) using the dust emission schemes of Balkanski et al. (2004) (left column) and Tegen et al. (2002) (middle column) and for the spectral model resolutions T42 (1^{st} row), T63 (2^{nd} row), T85 (3^{rd} row), and T106 (4^{th} row). Colours correspond to the upper colourbar. The right column shows the difference of the BK minus the TG scheme, according to the lower colourbar.

and the finer resolutions even by a factor of about 20. Also in MAM and SON the simulations with the BK scheme overestimate the column mass by a factor of 3–4 while there is a slight underestimation during DJF. Secondly, the BK scheme simulations and the MODIS measurements differ with respect to the seasonal cycle. Except for the T106 resolution, each simulation shows the second highest column mass in SON, not in MAM like MODIS. The simulations with the TG scheme correctly reproduce the seasonal cycle, independent of the horizontal resolution. The simulated values in JJA are less than three times higher than the MODIS column mass. The detection of aerosols by MODIS is affected by clouds (Remer et al. 2005). Habib et al. (2006) showed for the TOMS aerosol index that the presence of clouds could obscure the aerosol detection in this region leading to an underestimation of the aerosol load during the monsoon period from June to September. This could explain why the simulated values with the TG scheme are higher than the MODIS values.

As an example for the seasonal variation of the dust cycle over the Indian subcontinent, Fig. 3.4 shows dust emission and deposition fluxes and the wind on the lowest model layer of the T85TG simulation. In NH-winter (Fig. 3.4a) the intertropical convergence zone (ITCZ) lies south of the equator and the wind arrows over the Indian Ocean illustrate the northeasterly trade winds. During this season there is almost no dust activity in this region. In NH-summer (Fig. 3.4b) the strong southwesterly trade winds mobilise a huge amount of dust when they make landfall in the region of the Thar Desert in the northwestern part of India. The dust particles get washed out by monsoon-related precipitation at the southern slope of the Himalayas. This effect generates the global maxima of the dust emission and deposition in this region in JJA.

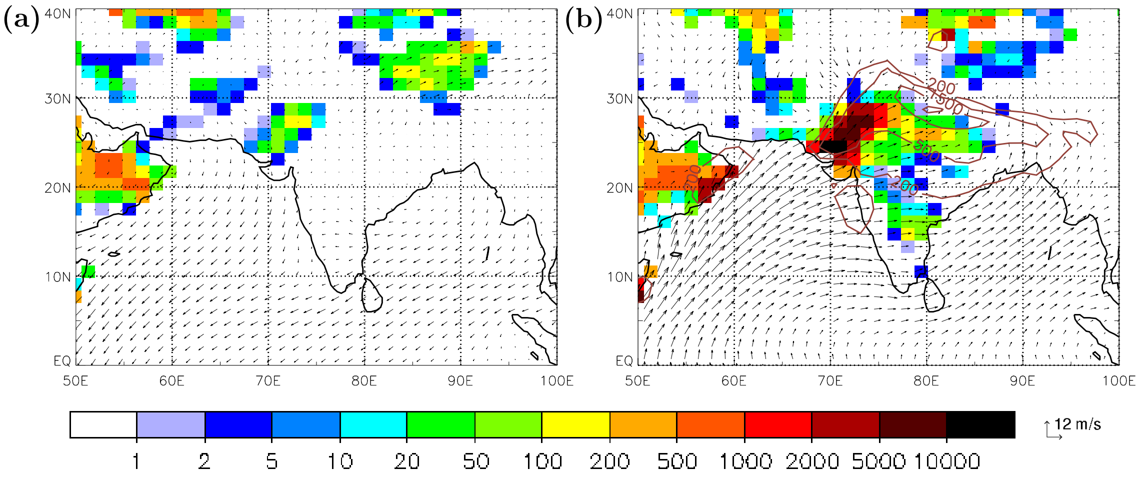

Fig. 3.4: Mean dust emission (kg ha^{-1}, shading), deposition (brown isolines for 200, 500, 1 500, and 3 000 kg ha^{-1}), and the wind on the lowest model layer (arrows) over the Indian subcontinent during DJF (a) and JJA (b) in the simulation T85TG.

Another region where the two dust emission schemes produce different emission fluxes is the northern part of Africa and the Arabian Peninsula. Here, on average, the TG scheme produces higher values (right column in Fig. 3.2). These higher emissions with the TG scheme, especially over Northwest Africa, cause higher dust column masses locally and over the adjacent Atlantic Ocean. The difference between the two emission schemes is strongest in the T106 simulations, but its magnitude is still ten times lower than the differences over the Indian subcontinent. The results for the Sahara dust emissions are within the wide span of published values for each of the time slices (Washington et al. 2003, Ginoux et al. 2004, Huneeus et al. 2011). Prospero et al. (2002) described the seasonal cycle of the transatlantic transport of dust from North Africa: It is highest in JJA and reaches the Caribbean, while during DJF the dust is transported to South America. These seasonal transport patterns are reproduced in each simulation. Figure 3.5 exemplarily illustrates this behaviour for the T42 resolution and both emission schemes, showing the mean dust column mass during DJF and JJA.

The Bodélé Depression in Chad is the world's most intense dust source and is active during the whole year (Prospero et al. 2002). The low-level jet over the Bodélé Depression is crucial for the dust emissions in this region. Orographic channelling and associated acceleration of the jet between the Tibesti and Ennedi Mountains increases the potential for dust emissions from the Bodélé Depression (Todd et al. 2008). However, the T42 simulations and T63BK do not show a distinct dust emission signal in this region (Figs. 3.2a,b,e), indicating insufficiently resolved orography in this region with these coarse model resolutions. Prospero et al. (2002) also showed that the dust activity in DJF in North Africa is greatest at the low latitudes and moves to higher latitudes during the year. This behaviour is reproduced by all setups. The centre of mass of the dust load is about 5° further south in DJF than during JJA and SON.

The above analyses reveal that the major difference between the two dust emission schemes is positioned in the Thar Desert, while variations in other parts of the world are much smaller. Due to the strong overestimation of emissions in India with the BK scheme, the TG scheme is overall regarded as the more reliable dust emission parametrisation for the EMAC model at resolutions between T42 and T106.

Both global mean values (Table 3.3) and the patterns of dust emissions and loads (Figs. 3.2 and 3.3) are influenced by the model resolution. In addition to the problems in the Bodélé Depression, another weakness of the coarse resolutions T42 and T63 arises in Central Asia. For both emission schemes T42 and T63 generate some grid points with quite high emissions in the area of the Taklamakan Desert in the Tarim Basin north of the Himalayas (Figs. 3.2a,b,e,f). The mean emission with T42 and T63 within the small box 34°–40°N, 75°–95°E is about half of the mean emission in entire North Africa. This causes very high dust loads in polar regions of

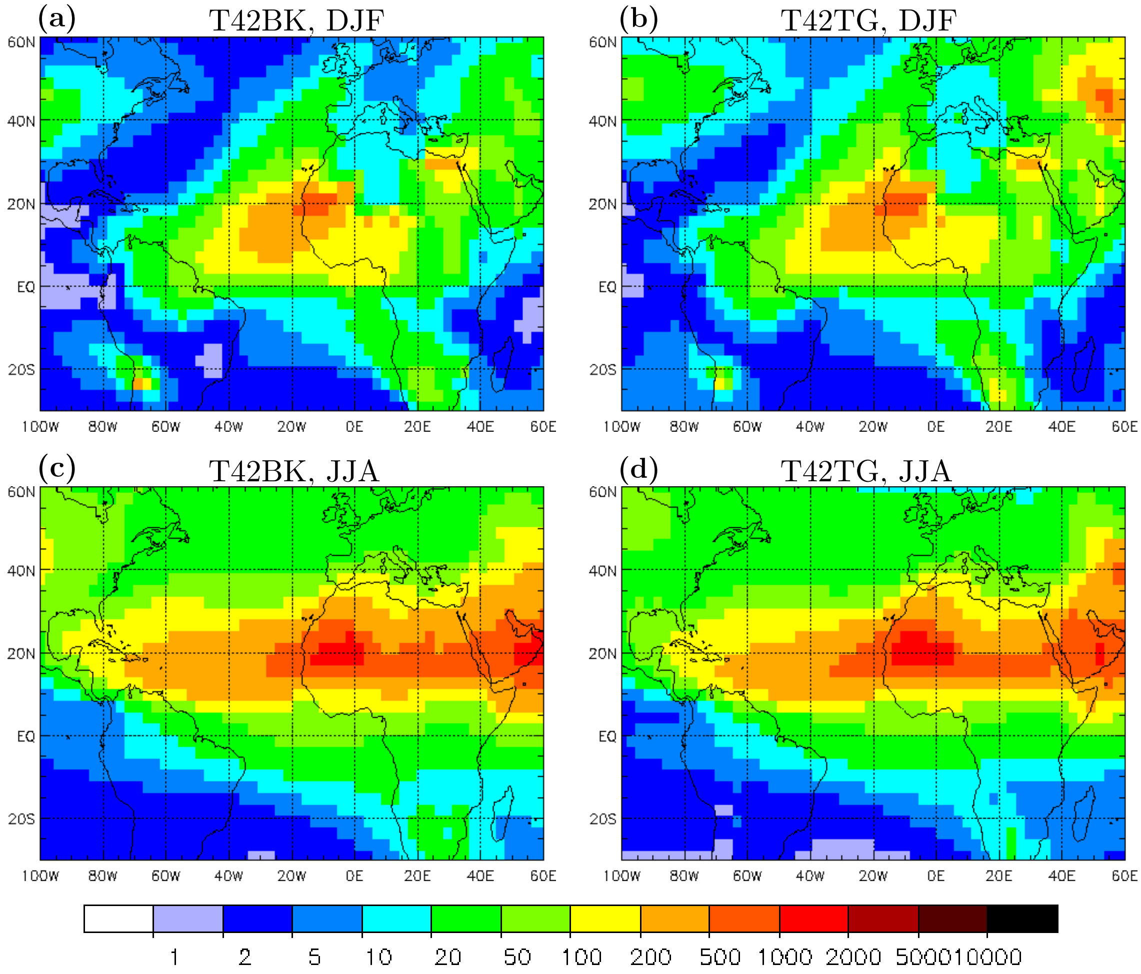

Fig. 3.5: Mean seasonal dust column mass (mg m^{-2}) using the spectral model resolution T42 and the dust emission schemes of Balkanski et al. (2004) (left panels) and Tegen et al. (2002) (right panels) during DJF (upper panels) and JJA (lower panels).

more than 10 mg m^{-2} north of 80°N (Figs. 3a,b,e,f). The mean load of all AEROCOM models is less than 5 mg m^{-2} in this region (http://dataipsl.ipsl.jussieu.fr/cgi-bin/AEROCOM/aerocom/surfobs_annualrs.pl, choose as Species: DUST and as Parameter: LOAD, 27. 11. 2012) but 10 mg m^{-2} is still within the wide range of the AEROCOM models. Comparison to the MODIS column mass provides strong evidence that the emissions in the Taklamakan Desert and column masses in high northern latitudes with T42 and T63 are too high. The dust sources in Central Asia are most active in NH-spring (Tegen et al. 2002, Geng et al. 2009). The mean value of the MODIS column mass in the region 35°–55°N, 50°–110°E accounts for 238 mg m^{-2} in MAM, 217 mg m^{-2} in JJA, 157 mg m^{-2} in DJF, and 150 mg m^{-2} in SON. Independent of the emission scheme the T42 and T63 simulations produce the maximum in JJA, with an overestimation of the column mass by a factor of 3–4.5. T85TG and T106TG correctly reproduce the seasonal cycle and the values do not deviate more than 50% from the MODIS column mass. T85BK and T106BK also simulate the maximum in MAM, followed by JJA. However, the minimum is produced in DJF with an underestimation of the MODIS values by a factor of 2–3. The strong emissions in the Taklamakan Desert with T42 and T63 occur due to a combination of an orographic effect and the coarse resolution. At the steep northern slope of the Himalayas the model produces very high near-surface wind velocities at elevated grid points. Due to the coarse resolution some of these grid points are preferential dust source regions. In T85 and T106 it becomes possible to distinguish between elevated grid points with high winds and those in the basin, which are the dust source grid points. Because of these deficiencies – unrealistically high emissions in the Tarim Basin, which cause too high dust loads in the Arctic – model simulations with T42 and T63 produce a less realistic global dust cycle than T85 and T106.

3.3.5 Selection of the preferable model configuration

So far, the analyses revealed some distinct shortcomings in simulating the global mineral dust cycle with each setup except T85TG and T106TG. However, the quantitative differences between T85 and T106 with the TG scheme are substantial: Mean dust emissions and loads are almost 50% higher in T106TG than in T85TG. The higher emissions are caused by differences in the 10-m wind velocities at dust source grid points, where the mean wind speed is on average 3.5% higher in T106TG than in T85TG. Nevertheless, the global distributions look quite similar (see Figs. 3.2g,h and 3.3g,h) and appear realistic, compared to the AEROCOM mean dust emission and column mass. Both simulations produce dust emissions and life times that are within the range of earlier estimates but the dust load of T106TG (31.6 Tg) exceeds the range of the AEROCOM models (6.8–29.5 Tg). Considering all this, and because of the better performance of T85TG in comparison with the measurements of dust deposition fluxes and surface concentrations (see Table 3.2), the T85 setup with the TG scheme is the one to prefer for long-term climate simulations with the EMAC model system.

3.4 Simulation of two single dust episodes

The intensity of dust emissions varies dependent on the meteorological situation. Single dust outbreaks, lasting a few days, can contribute a large amount to the annually emitted dust from a certain region. In this section the ability to reproduce such events with EMAC using the T85TG setup is investigated. To compare simulations with measurements the model was nudged to reanalysis data of the ECMWF. The nudging through Newtonian relaxation of four prognostic model variables, namely temperature, divergence, vorticity, and the logarithm of surface pressure is only applied in the free troposphere (Jöckel et al. 2006). The nudging has the potential to influence the climatological values of different model variables. For example, the 10-m wind speed distribution in the ECHAM4 model is shifted in a nudged simulation compared to a free running one, which causes a higher dust load and a shorter life time in the free running mode (Timmreck and Schulz 2004). It is highly probable that similar effects also occur in the EMAC model system. Therefore, the decision on the preferred model setup for climatological simulations of the mineral dust cycle with EMAC is not dependent on the results of nudged simulations.

3.4.1 May/June 2006: SAMUM

During the field campaign (SAMUM: Kandler et al. 2009, Knippertz et al. 2009) the mass concentrations of desert aerosols were measured near Tinfou (30° 14'N, 5° 36'W, 684 m a.s.l.) in South Morocco from 12 May to 6 June 2006. For this episode the period from 1 April to 30 June 2006 was simulated.

Figure 3.6 compares the simulated dust concentrations of the grid box containing the measurement site with the measured ones. The diameter of the largest emitted

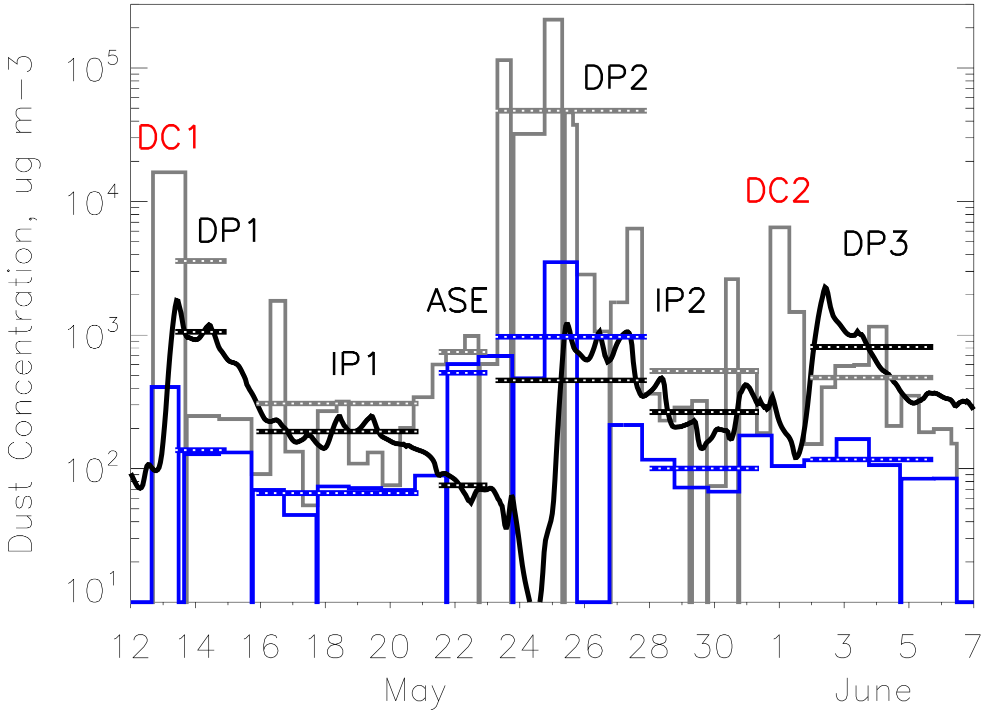

Fig. 3.6: Time series of measured TSP (grey) and PM_{10} (blue) concentrations at Tinfou, Morocco and simulated dust concentrations (black) in the grid box containing Tinfou with T85TG (µg m^{-3}). Horizontal bars with white dotted lines on it show the mean values for the periods defined by Kandler et al. (2009), DC1 and DC2 mark the two density currents, observed during SAMUM.

particles in the TG scheme is 15.88 μm. The simulated mean concentration is with 407 μg m^{-3} 37% higher than the PM_{10} measurements (291 μg m^{-3}) and much lower than the TSP values (9 742 μg m^{-3}). In the measurements particles larger than 10 μm in diameter account for more than 90% of the total airborne aerosol mass under high dust concentrations. Local wind speed observations indicate that large particles (diameter $>$ 10 μm) were locally emitted, while a significant portion of the smaller ones stems from remote sources and was advected to the measurement site (Kandler et al. 2009). This explains the difference between measured and simulated concentrations, especially during the local strong-wind period from 23 to 27 May. Due to its coarse horizontal resolution of about 155 km, EMAC is not able to produce strong local dust emission events that, e.g., result from channelling effects of the regional orography. A second reason for the differences of the concentration values during this period is that the TG scheme does not take the super-coarse mode into account. However, this mode contributes most to the observed total aerosol mass, as described above. Overall, it is a satisfying result that the mean value of the simulated dust concentration over the whole time series is higher than the measured PM_{10} and much lower than the TSP concentration.

Regional scale effects that are not captured by EMAC with the horizontal resolution T85 could lead to a time shift between measurements and the simulation. For example, there is a measured maximum on 1 June while a peak in the simulation occurs on 2 June. Therefore, mean values for six periods, named DP1, DP2, DP3, IP1, IP2, and "advection from southeast", as described by Kandler et al. (2009) and Knippertz et al. (2009) are considered, which are displayed in Fig. 3.6. DP and IP stand for dust and intermediate phase, respectively.

As described above, during DP1, IP1, and IP2 the simulated concentrations are higher than the PM_{10} and lower than the TSP measurements. The periods IP1 and IP2 represent desert background conditions, which are captured well by EMAC. Without freshly emitted, large particles the TSP concentrations are only slightly above the simulated ones. DP2 is the local strong-wind period discussed earlier. The concentrations for the period "advection from southeast" (abbreviated as ASE in Fig. 3.6) are underestimated by EMAC. This is due to relatively small discrepancies between the simulated and real flow patterns. At least the simulated concentration of soluble particles is one order of magnitude higher than the one of insoluble particles (not shown). This indicates that the dust has been advected to the measurement site because freshly emitted dust is assumed to be insoluble in the model. For DP3 the simulated concentrations are even higher than TSP. The periods "advection from southeast" and DP3 are further investigated later in this section.

In contrast to those longer periods, two density currents were observed during SAMUM, which generated high dust concentrations on 12 and 13 May (DC1) and on 31 May and 1 June (DC2) as discussed by Knippertz et al. (2007). Due to inevitable parametrisation of convection in global simulations, the model is not able to reproduce density currents (Heinold et al. 2012, submitted). However, a rapid increase of simulated concentrations of insoluble particles in the night from 12 to 13 May is visible in Fig. 3.6. In this case also the large-scale flow – nudged towards realistic meteorology in the model – advected dusty air from Algeria into Morocco (Knippertz et al. 2009), which is captured by the model. The simulated concentrations are quite low when DC2 was observed, showing that DC2 was missed in the simulation.

This analysis points out the limitations of the global model concerning the regional and temporal resolution of small-scale processes causing massive dust emission. To mention is also that a comparison between a global simulation and measurements at one station is problematic. The elevation of the Tinfou grid point in the model, for example, is about 200 m higher than in reality, because the model orography is dominated by the High Atlas in this region. A more equitable approach to evaluate EMAC is to validate the results on a larger scale, which is done in the following.

Figure 3.7 compares EMAC with the BSC-DREAM8b model and the MSG dust RGB composite at 12:00 UTC 1 June 2006. EMAC simulates dust concentrations higher than 5 000 μg m^{-3} on the lowest model layer in central Algeria. The forecast of the BSC-DREAM8b model for this time shows dust concentrations on the same order of magnitude in this region. The pinkish colours in the MSG composite corroborate a huge amount of airborne dust at the same place. Also in the southern part of Mauritania there are indications for dust in the satellite image and high concentrations in the EMAC results.

On several other days during this episode the MSG dust composite shows dust aerosol in single regions over North Africa (not shown). There is high qualitative agreement of the EMAC results with the satellite composites on days with strong signals in the MSG images, e.g., on 11 May in South Algeria and Niger, on 16 May in West Algeria, on 22 May in West Algeria, North Mali and North Mauritania, on 24 and 25 May in West Algeria and Mali, and on 29 May in West Mali and Southeast Mauritania.

The period “advection from southeast” on 21 and 22 May seemed not to be captured by the model at first sight. However, on 21 and 22 May the model simulates high dust emissions in Mali and West Algeria. This dust is transported northwards but not far enough to reach Tinfou. The comparison to MSG composites confirms that this event is reproduced quite well. Only a small displacement inhibits a better consistence with in situ measurements in this case.

During DP3 EMAC produces a higher dust concentration than observed. Satellite images and the 2D-fields of the simulated dust concentrations show a dust front evolving in North Algeria on 1 June, which spreads southwestwards on the following days. The large-scale circulation, dominated by an upper-level trough over

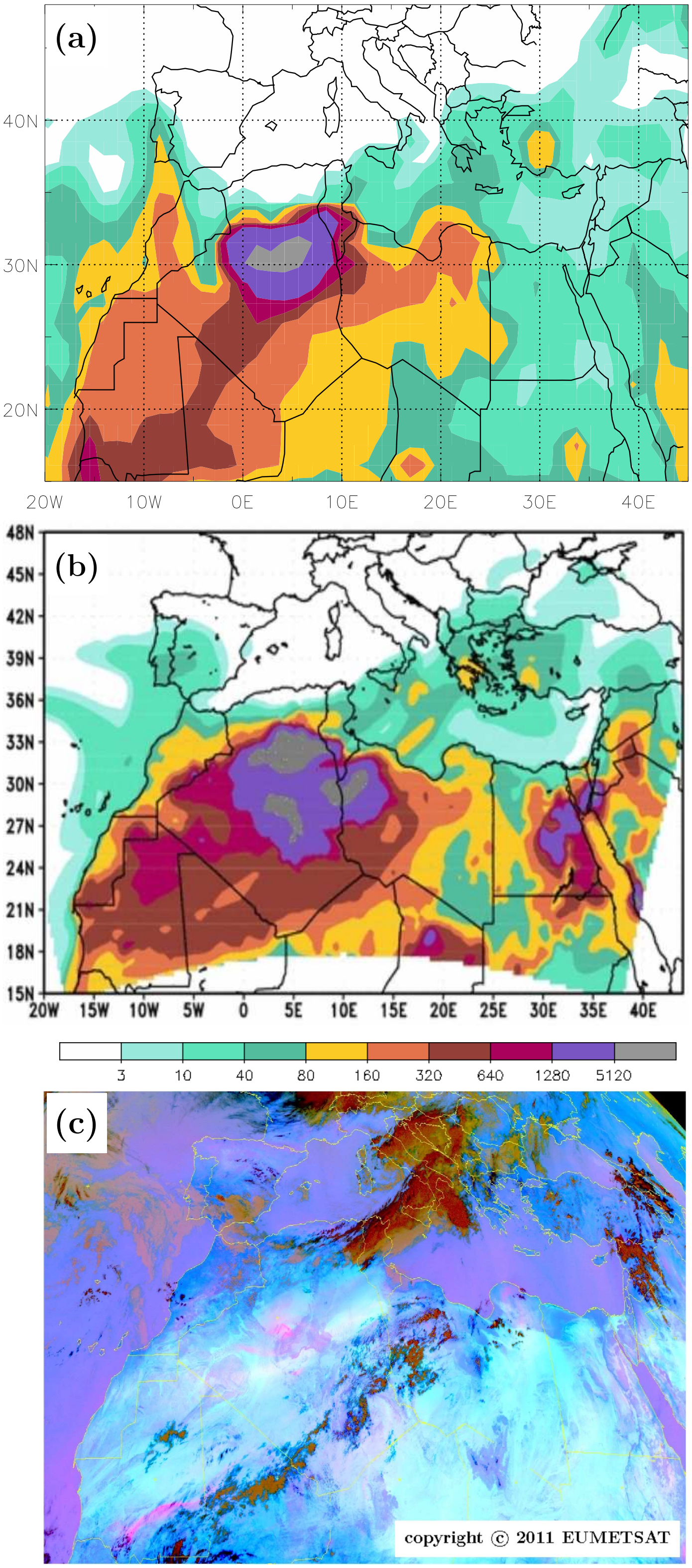

Fig. 3.7: Dust concentration (µg m^{-3}) on the lowest model layer of EMAC (a) and BSC-DREAM8b (b), respectively and MSG dust RGB composite (c) on 1 June 2006 12:00 UTC.

the central and Eastern Mediterranean during DP3 (Knippertz et al. 2009), is well reproduced in the nudged simulation. The MSG composites indicate a good representation of the location of the dust front by the model as well. However, EMAC overestimates the dust emission along the front leading to higher concentrations at the measurement station than observed, especially during the first stages of DP3 (Fig. 3.6).

Further insight into this episode can be obtained by trajectory analyses. Trajectories were calculated from five-hourly EMAC model output using the LAGRangian ANalysis TOol (LAGRANTO: Wernli and Davies 1997). Various model variables, e.g., the dust concentration and the surface dust emission from the Eulerian model output are traced along the trajectories. Here the simulated and observed peak in the dust concentrations at the SAMUM measurement site on 3 June is investigated. Eight-day backward trajectories starting from the three lowest model layers at the station show the simulated dust emission and concentration along the air parcel trajectories (Fig. 3.8). Strong emissions of more than 20 μg m^{-2} s^{-1} during 1 June (even 50–100 μg m^{-2} s^{-1} in the first hours of the day) lead to a rapid increase in the dust concentrations along the trajectories, when passing North Algeria. High concentrations can also be seen in the MSG dust composite in this region at 12:00 UTC 1 June (Fig. 3.7b). This reveals that the dust reaching Tinfou on 3 June was emitted on 1 June over the southern slope of the Atlas Mountains in Algeria.

Figure 3.9 shows the mean values of several variables along the trajectories. The very abrupt acceleration of the 10-m wind speed during the first hours of 1 June from 6 to 9 m s^{-1} causes strong dust emissions of about 100 μg m^{-2} s^{-1}, which again leads to an abrupt increase of the dust concentration from less than 100 to more than 4 000 μg m^{-3}. While the 10-m wind velocity and the emissions decrease during the following two days, the concentration stays on a high level. When the air reaches the measurement site on 3 June 00:00 UTC a value of about 1 700 μg m^{-3} is simulated.

Figure 3.9 shows high 10-m wind speeds also on 27, 28, and 30 May. The maximum on 27 May is associated with high dust emissions in central Algeria (see also Fig. 3.8). However, during this time the altitude of the trajectories is too high for the air parcels to be directly affected by these emissions. Therefore, freshly emitted dust does not reach the trajectories and the dust concentration does not increase. As averaged values smaller one of the Land-Sea-Mask show, the two peaks in the wind speed on 28 and 30 May occur when the trajectories cross the Mediterranean, where dust emission is impossible.

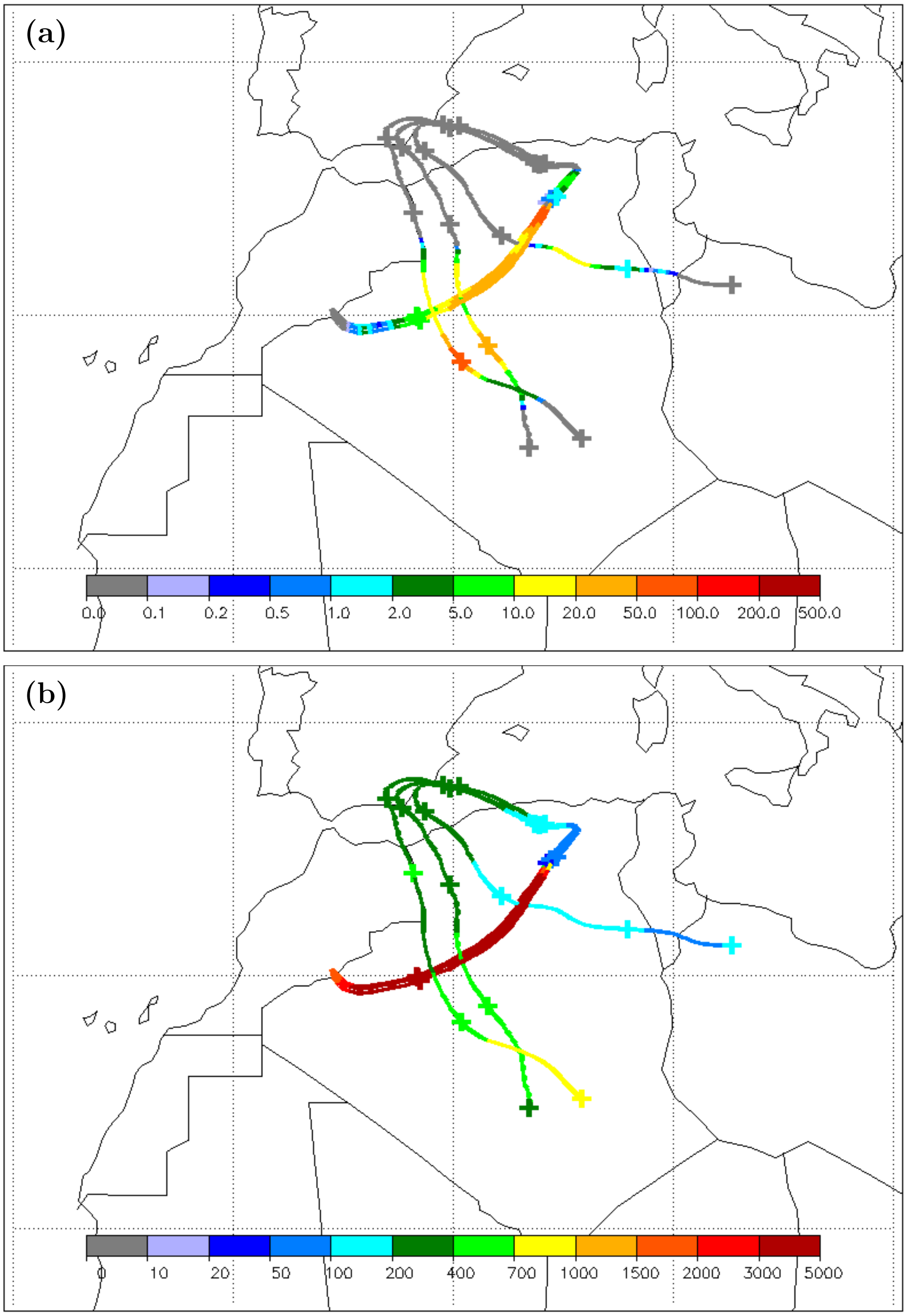

Fig. 3.8: Eight-day backward trajectories initialised on 3 June 2006 00:00 UTC starting from the three lowest model layers at Tinfou. A "+" is drawn every 24 hours. Coloured variables along the trajectories are (a) the dust emission (μg m^{-2} s^{-1}) and (b) the dust concentration (μg m^{-3}).

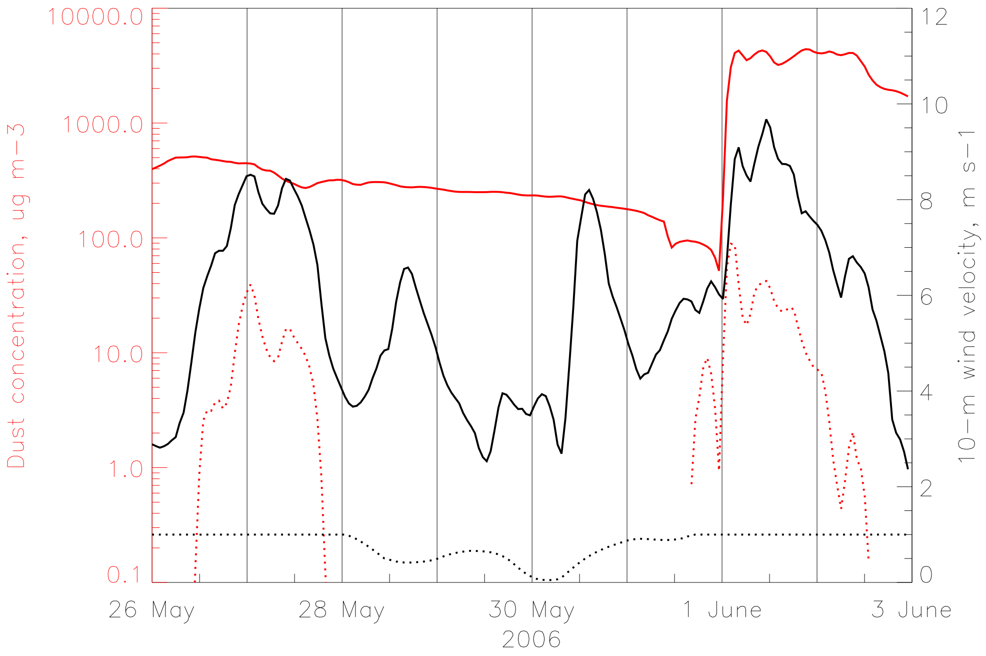

Fig. 3.9: Mean values along the trajectories illustrated in Fig. 3.8. According to the left axis: dust concentration (solid red line, µg m^{-3}), dust emission (dotted red line, µg m^{-2} s^{-1}); according to the right axis: 10-m wind velocity (solid black line, m s^{-1}), Land-Sea-Mask (dotted black line).

3.4.2 May/June 2008: Kleiner Feldberg

At the Taunus Observatory of the Goethe-University of Frankfurt/Main at Kleiner Feldberg in Germany (50° 13'N, 8° 27'E, 825 m a.s.l.) the number concentration of IN and PM_{10} concentrations have been measured since April 2008 (Klein et al. 2010). Here, a Sahara dust episode observed in May 2008 is considered. The EMAC simulation was performed from 1 April to 30 June 2008.

The measured concentrations of PM_{10} and IN, the simulated dust concentrations of BSC-DREAM8b, and the concentrations of the grid box containing the measurement site simulated by EMAC show peaks at the end of May 2008 (Fig. 3.10). The mean values from 24 May to 1 June are highest in the EMAC simulation with 54.84 µg m^{-3}, followed by BSC-DREAM8b with 43.38 µg m^{-3} and the PM_{10} measurements with 23.91 µg m^{-3}. This is a satisfying result because the maximum diameter of particles in EMAC is 15.88 µm (see section 3.4.1) while it is 12 µm in the BSC-DREAM8b data and, self-evident, 10 µm in the PM_{10} measurements.

The absolute maximum is simulated at the same time by EMAC and BSC-DREAM8b, i.e., in the afternoon hours of 28 May. It reaches values of 218 µg m^{-3} in EMAC and 196 µg m^{-3} in the BSC-DREAM8b simulation. The PM_{10} measurements show no distinct peak at this time, but one and two days later, when the simulated values decrease again. BSC-DREAM8b reproduces the observed peaks on 29 and 30 May, while the decline in EMAC is almost monotonous. Klein et al. (2010)

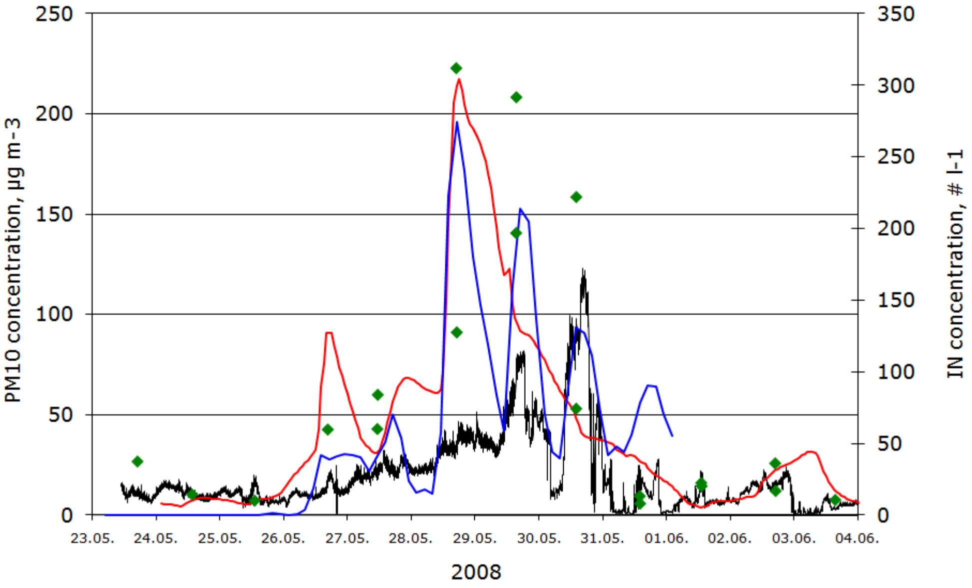

Fig. 3.10: According to the left axis: time series of the measured PM_{10} concentration (black line, µg m^{-3}) at Kleiner Feldberg, Germany and the simulated dust concentrations at Kleiner Feldberg of EMAC (red line) and BSC-DREAM8b (blue line). According to the right axis: measured number concentration of IN (green diamonds, number per litre [# l^{-1}]). Measurements are described in Klein et al. (2010).

assumed that the deviations on 28 and 29 May can be traced back to thunderstorm development over the Taunus hills, which is not represented in BSC-DREAM8b and EMAC because it is a sub-grid scale phenomenon. This could explain the much higher consistency between the two simulations compared to the one between the simulations and the PM_{10} measurements. Another effect that might reduce the comparability of these time series is the fact that many other species like soot, acids, and sea salt contribute to the PM_{10} measurements (Klein et al. 2010).

The correlation is higher between the simulated dust concentrations and the measured IN concentrations. Mineral dust particles very efficiently act as heterogeneous IN (Zuberi et al. 2002, DeMott et al. 2003a, b, Cziczo et al. 2004, Richardson et al. 2007). Linear regression of IN number concentration against simulated dust concentration yields correlation coefficients $R_{\mathrm{DREAM}} = 0.888$ and $R_{\mathrm{EMAC}} = 0.729$ for the BSC-DREAM8b and the EMAC simulation, respectively.

As before, for this episode the source region of the dust that reaches Central Europe can be identified by backward trajectories. Very strong dust emissions in Central Algeria of more than 200 µg m^{-2} s^{-1} on 26 May (Fig. 3.11a) lead to high dust concentrations along the trajectories. The concentrations decrease from more than 2 000 µg m^{-3} on 26 May to values of about 200 µg m^{-3} when the trajectories reach Kleiner Feldberg (Fig. 3.11b). Klein et al. (2010) showed backward trajectories calculated by the German Meteorological Service confirming the advection of air

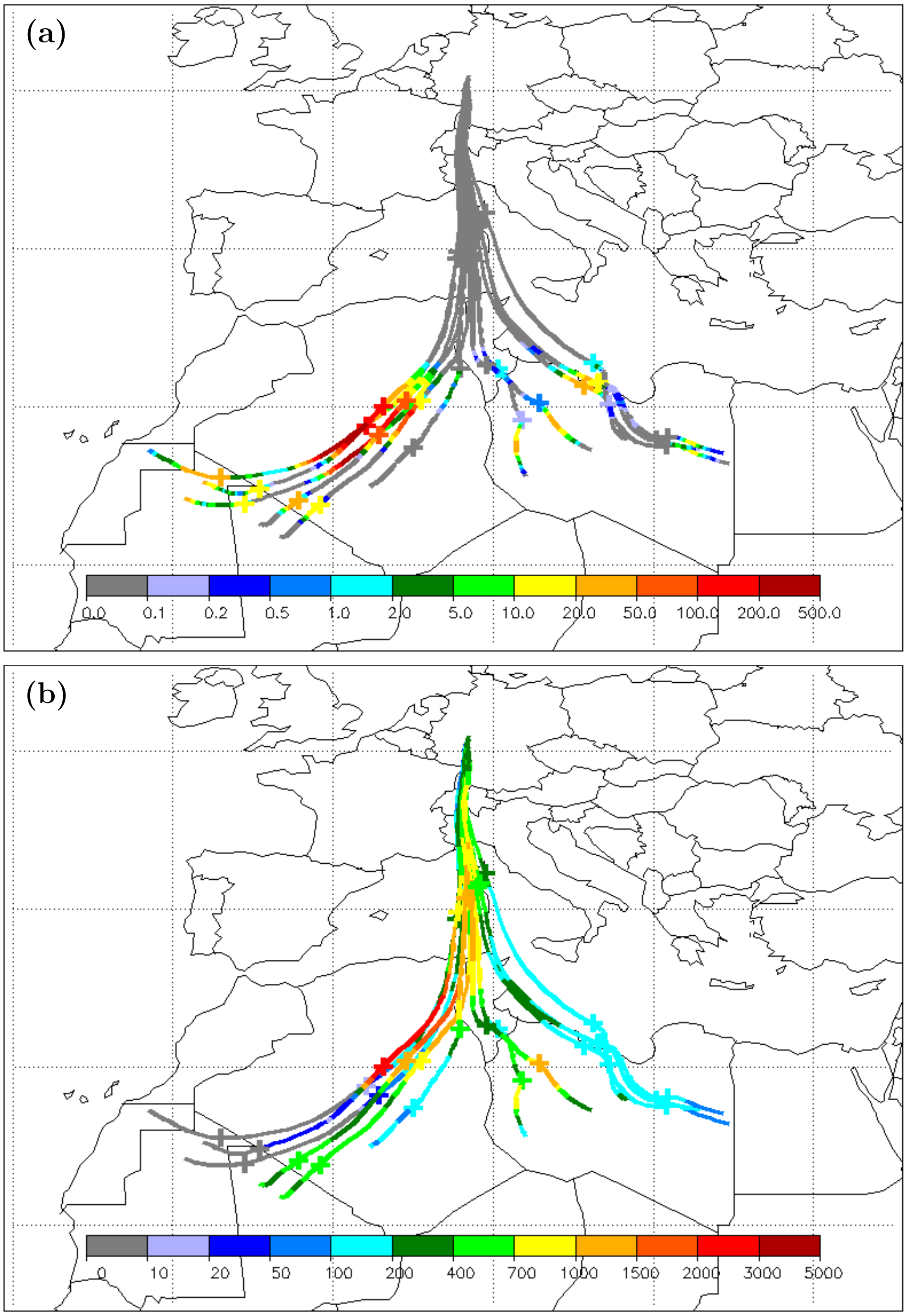

Fig. 3.11: 90-h backward trajectories initialised on 28 May 2008 18:00 UTC starting in intervals of 30 hPa from the surface to 350 hPa at Kleiner Feldberg. Only trajectories with northward displacement larger than 22° latitude are displayed. Coloured variables along the trajectories are (a) the dust emission (µg m^{-2} s^{-1}) and (b) the dust concentration (µg m^{-3}). A "+" is drawn every 24 hours.

from the Sahara to Central Europe. The EMAC results reveal that most of the dust was emitted in the afternoon of 26 May in the northeastern part of the province Adrar in central Algeria (Fig. 3.11a).

In terms of source region and the direct transport pattern across the Western Mediterranean, this event is comparable to the one studied by Sodemann et al. (2006) in October 2000.

3.5 Summary

The first objective of the present thesis is to determine the model setup of the GCCM EMAC that simulates the most realistic mineral dust cycle. Sensitivity studies were conducted with regard to the chemistry setup, the horizontal model resolution, and the dust emission scheme.

Freshly emitted dust particles are assumed to be insoluble. By coating of sulphate they become soluble and are much more efficiently scavenged from the atmosphere. Therefore, a basic sulphur chemistry is required to avoid an unrealistic, almost homogeneous distribution of the dust over the entire globe.

Results of five-year time slice simulations show in parts severe differences between the four horizontal resolutions considered here (T42, T63, T85, and T106) and the two implemented dust emission schemes (BK and TG). While the seasonality of the emission and the transatlantic transport of dust from North Africa is well reproduced in all simulations, the accentuation of the Bodélé Depression is not captured with the T42 and the T63BK setups. With the resolutions T42 and T63 there are some grid points at the northern slope of the Himalayas where on the one hand, high 10-m wind velocities are simulated because of high elevation, and on the other hand, these grid points belong to the Tarim Basin, which is a dust source region. Hence, T42 and T63 overestimate the dust emissions in this region, especially during NH-summer, leading to an erroneous annual cycle of Central Asian dust activity. The northward transport of this dust causes unrealistically high dust loads in the Arctic. With the resolutions T85 and T106 the elevated grid points and those in the basin can be distinguished leading to much lower emissions in the Tarim Basin and a more realistic dust burden in polar regions. This behaviour is independent of the dust emission scheme.

Independent of the model resolution the BK scheme produces too strong emissions in the Thar Desert in Northwest India. On average the emissions are 2.4 times higher in India than in the Sahara, which is in contradiction to current scientific knowledge, considering the Sahara to be the world's largest dust source. The annual cycle of the dust load over the Indian subcontinent is correctly reproduced only with T106BK and in the simulations with the TG scheme.

Finally, due to the better performance in the comparison to AEROCOM and in situ measurements of dust deposition and surface concentration, the T85TG setup is found to generate a more realistic global dust cycle than the T106TG simulation. T85TG is also able to fairly accurately simulate single dust episodes. The large-scale flow patterns are reproduced and the TG scheme generates dust emissions that lead to dust concentrations on the same order of magnitude as observed. Especially the transport pathways of dust are realistically simulated according to MSG images and results of the BSC-DREAM8b regional model. Nevertheless, the investigation of episodes points to the limitations of the GCCM EMAC, when it comes to resolving effects on small spatial and temporal scales, which cannot be represented by a GCCM. In addition, trajectory analyses allowed for a detailed investigation of the dust transport and of the processes that occur along the pathway. For both episodes the source regions of dust, reaching the measurement sites, could be identified.

Amongst all investigated model parameters, the setup with the horizontal resolution of T85, including a basic sulphur chemistry and using the dust emission scheme by Tegen et al. (2002) is found to reproduce the mineral dust cycle in the most accurate way. Deeper analyses in the following chapters are therefore based on the results of the T85TG five-year time slice simulation and this model setup is recommended for future investigations of the mineral dust cycle with the EMAC GCCM.

4

Transatlantic transport of Saharan dust

4.1 Introduction

Investigations of the transatlantic dust transport began with the publication of Junge in 1956. He detected mineral dust particles in aerosol samples, taken in Florida and ascribed them to African dust source regions. Today, African dust is known to be an important nutrient for the Amazon rain forest (Swap et al. 1992) and other marine and terrestrial ecosystems (e.g., Mahowald et al. 2005, Wang et al. 2012). It is also an important source of ice nuclei in the Amazon Basin during the wet season (Prenni et al. 2009) and the research interest has increased during the last years, resulting in a large number of publications on this topic (e.g., Schepanski et al. 2009, Engelstaedter et al. 2009, Ben-Ami et al. 2010, Huang et al. 2010, Prospero et al. 2010, Pan et al. 2011, Nowottnick et al. 2011, Ben-Ami et al. 2012) and *"The First International Workshop on the Long-Range Transport and Impacts of African Dust on the Americas"* in San Juan, Puerto Rico in October 2011.

Schepanski et al. (2009) described the large-scale flow patterns over North Africa in the context of the general circulation and with focus on mechanisms influencing the mineral dust emission and transport. They distinguished the conditions during boreal summer and winter: In NH-winter the Harmattan carries dust in western and southwestern directions within the trade wind layer, i.e., below 1.5–3 km. Higher insolation and the northward shift of the ITCZ during NH-summer cause a deeper boundary layer, leading to higher upward-mixing of dust. A combination of the southwesterly winds of the West African Monsoon (WAM) south of about 20°N and the Harmattan in the north generates a two-layer structure. Dust-laden Saharan air from the north, transported within the Harmattan at low levels, is lifted when reaching the denser air of the WAM in the south and of the subtropical Atlantic Ocean in the west (Knippertz and Todd 2012). This results in an elevated dust layer, the "Saharan Air Layer" (SAL), which, seasonally averaged, reaches its maximum at about 4 km above sea level (Schepanski et al. 2009). Not uncommonly, the SAL is present at altitudes of up to 6 km height (Knippertz and Todd 2012).

This chapter presents a climatological investigation of the transatlantic dust transport, using the results of the T85TG five-year time slice simulation. Based on Eulerian and Lagrangian methods, the seasonal variations of various characteristics of the transport are analysed. In particular, the following main questions will be addressed:

- What is the time scale the dust needs to cross the Atlantic Ocean?
- How does the spatial distribution of the transport vary in the course of the year?
- Which role do dry and wet deposition of dust play during the transport?
- Where are the main source regions of dust reaching the Americas?

At first, Eulerian and Lagrangian methods used in this study are described and discussed in section 4.2.1. The detailed description of the trajectory calculation and selection is then given in section 4.2.2. Eulerian time series are introduced and investigated in section 4.3, followed by the analysis of the transport time scales in section 4.4 and various methods to investigate the transport pathways in section 4.5. An objective connection between North African dust emission regions, called source regions from now on, and the dust deposition beyond the Atlantic Ocean is provided in section 4.6. This chapter ends with summarising remarks on the transatlantic transport in section 4.7.

4.2 Methodology

4.2.1 Euler vs. Lagrange: two philosophies, one intention

The investigation of the abovementioned issues is addressed by adopting Eulerian and Lagrangian approaches; benefits of both should complement each other. Eulerian methods consider the atmospheric state at separate time steps, while the Lagrangian concept is based on the temporal evolution of single air parcels, the trajectories. For climatological purposes a strength of the Eulerian method is the specification of annual or seasonal mean values of the simulated variables. Also the absolute values of, e.g., the yearly dust emission and deposition fluxes, are exactly described. To receive useful Lagrangian information out of the five-year data set, carefully chosen trajectories have to be considered. Then, valuable information on various processes during the transport can be gained, such as the dust concentration along the trajectories or the increase and decrease of dust. One must consider that a set of trajectories does not describe the entire atmosphere. Hence, the Lagrangian decrease of dust along trajectories, for example, does not necessarily coincide with the Eulerian deposition flux (see section 4.5.4). Furthermore, the transport time of dust from the emission regions to its deposition can be obtained by either Eulerian or Lagrangian calculations. For trajectories this is just the duration they need to travel from A to B. It is much more complicated to compute this from Eulerian data. One approach are time-lagged correlations of time series. Eulerian and Lagrangian results on transport time estimates are opposed in section 4.4.2. With Lagrangian methods it is also possible to consider dust only from specific source regions and to describe its transport pathways and characteristics separated from dust of other sources.

For a complete picture of the transatlantic dust transport a hybrid of Eulerian and Lagrangian analyses is presented, exploiting the advantages of both approaches.

4.2.2 Trajectory initialisation

Trajectories were calculated with LAGRANTO (Wernli and Davies 1997). 15-day forward trajectories are started from North Africa and the Arabian Peninsula (brown area in Fig. 4.1) at each grid box and at each simulation output time step if the local dust emission flux is greater than zero. Depending on meteorological conditions, e.g., boundary layer stability, the dust emission flux is distributed to the model levels inside the planetary boundary layer. In order to be sure to capture all grid boxes in the vertical where fresh dust is emitted, trajectories are initialised at each model layer from the surface to the top of the planetary boundary layer, which is available from model output. With this method, however, it cannot be distinguished between freshly emitted dust and the dust that was transported into the grid box. This is an element of uncertainty with regard to the comparison of Eulerian and Lagrangian results. To minimise double counting of dust, a weighting factor F_{EC}[1] is introduced for each grid point (i,j).

$$F_{EC}(i,j) = \begin{cases} 0 & \text{, if } M_{emi}(i,j) \leq 0 \\ 1 & \text{, if } M_{emi}(i,j) \geq M_{col}(i,j) \\ \dfrac{M_{emi}(i,j)}{M_{col}(i,j)} & \text{, else} \end{cases} \quad \text{, with} \tag{4.1}$$

$$M_{emi}(i,j) = [DEF(i,j) - DDF(i,j)] \cdot A(i,j) \cdot 18\,000\ \text{s} \quad \text{and} \tag{4.2}$$

$$M_{col}(i,j) = \sum_{k=1}^{k_{max}} DU_{conc}(i,j,k) \cdot V(i,j,k) \tag{4.3}$$

DEF (DDF) is the mean dust emission (deposition) flux in kg m^{-2} s^{-1} during the last five hours, i.e., one output time interval. To obtain the mass of dust, M_{emi}, that was emitted from grid point (i,j) during this time step, the net emission flux, i.e., $DEF - DDF$, is multiplied with the grid box area A and the time step of 18 000 s. M_{col} is the total mass of dust inside the boundary layer at the grid point

---

[1] Subscript EC refers to the dust *E*mission and *C*olumn mass, included in the calculation.

(i, j). It is calculated as the sum over all vertical levels from the surface ($k = 1$) to the planetary boundary layer height ($k = k_{max}$) of the dust concentration DU_{conc} times the volume V of grid box (i, j, k). If M_{emi} is less than 0, F_{EC} is set to 0, if M_{col} is less than M_{emi}, then F_{EC} is set to 1, so that F_{EC} is defined in the range from 0 to 1. Weighting the trajectories with F_{EC} prevents double counting of dust that was emitted from grid box (i_1, j_1) at time t_1 and transported within the boundary layer into grid box (i_2, j_2) at time t_2. Without this weighting factor, this dust would be considered a second time by a trajectory, initialised at (i_2, j_2, t_2), even though the emission flux at (i_2, j_2) at time t_2 might be very small. F_{EC} also inhibits that trajectories are considered that are initialised at grid points where the net dust emission flux is negative, i.e., the deposition flux is larger than the emission. All further trajectory calculations presented in this section consider the factor F_{EC}.

To separate the trajectories contributing to the transatlantic dust transport, the criterion of crossing 30°W between 20°S and 40°N has to be fulfilled (red line in Fig. 4.1). Different processes, which are not captured by the calculation of the trajectories, can cause increasing or decreasing dust concentrations in one air parcel, e.g., the gravitational settling of particles or numerical diffusion. These processes cause an exchange of dust from the trajectories considered here into air masses that are not captured by the trajectories, which leads to differences between the Eulerian and Lagrangian results.

To ensure that the hereby selected trajectories adequately represent the Eulerian data of the transatlantic dust transport, results of both methods are compared in several of the following sections (4.4.2, 4.5.3, 4.5.4).

4.3 Eulerian time series

From the Eulerian model output the time series of dust emission in North Africa and the Arabian Peninsula (henceforth abbreviated as EMI), dust transport across 30°W (TRA), the dust concentration arriving (ARR) in the Caribbean (CAR) and the Amazon region (AMA), the deposition (DEP) of dust in the same areas, and the precipitation (RR) over the arrival regions are calculated in the following way:

$$\begin{array}{lllll}
EMI &= \varnothing_{i,j} & \text{dust emission flux} & \forall i,j & \text{in North Africa} \\
TRA &= \varnothing_{j,k} & u \cdot \text{dust concentration} & \forall j,k & \text{at } 30^\circ\text{W} \\
ARR &= \varnothing_{i,j,k} & \text{dust concentration} & \forall i,j,k & \text{in CAR and AMA} \\
DEP &= \varnothing_{i,j} & \text{dust deposition flux} & \forall i,j & \text{in CAR and AMA} \\
RR &= \varnothing_{i,j} & \text{precipitation} & \forall i,j & \text{in CAR and AMA} \quad ,
\end{array} \tag{4.4}$$

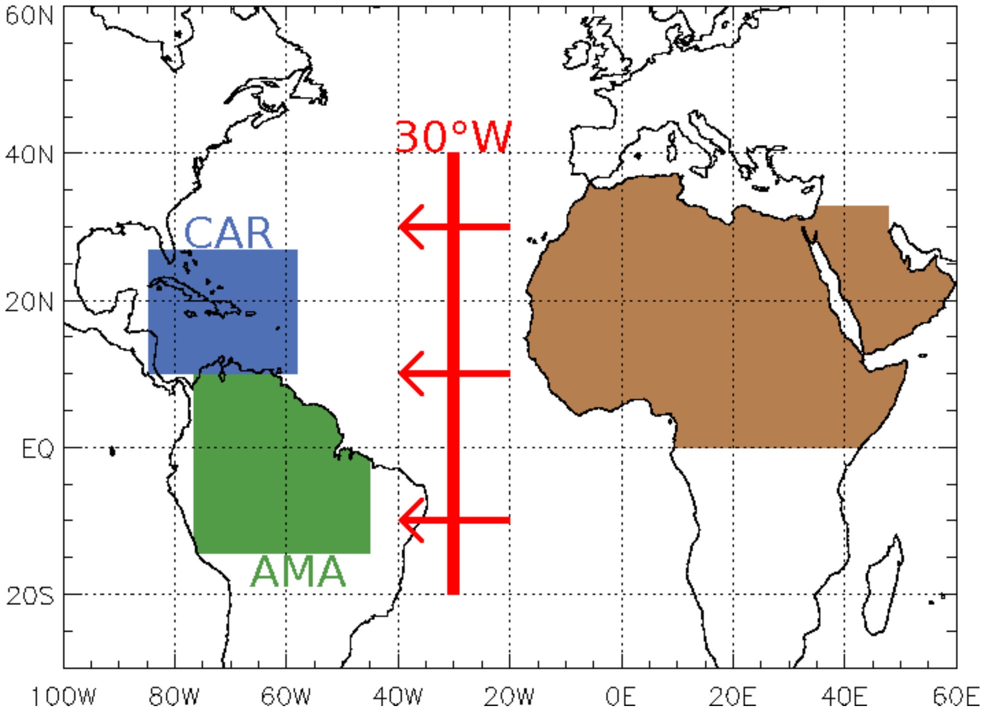

Fig. 4.1: Illustration of the different regions, considered in the analysis of the transatlantic transport of Saharan dust: North Africa and the Arabian Peninsula are the potential dust emission regions (brown), the Caribbean (CAR, blue) and the Amazon Basin (AMA, green) are the target regions, where the concentration and deposition of dust that was transported across 30°W between 20°S and 40°N (red line), are investigated.

where u denotes the zonal wind velocity and $\varnothing$ the spatial average over the respective subscripts, which are the longitudinal (i), the latitudinal (j) and the vertical (k) grid indices. The different regions are defined in Fig. 4.1.

Figures 4.2 and 4.3 depict these time series and their seasonal cycle, respectively. Here, the Amazon Basin is restricted to the green part in Fig. 4.1 located south of the equator (AMA-S) because it is well known that Saharan dust reaches the Caribbean mainly during the NH-summer months and the Amazon Basin in NH-winter. With the restriction to AMA-S, a clearer seasonal variation is obtained.

Single peaks in Figs. 4.2a,b illustrate the episodic character of the dust emission and the transport across 30°W. The emission in North Africa and the Arabian Peninsula reaches its maximum in JJA. During MAM the emission is about 30%, in DJF 40% and in SON more than 50% lower than in JJA (Fig. 4.3a). The transport is also strongest in JJA but only slightly weaker in DJF (about 80% of the JJA value), showing that in JJA a bigger portion of the emitted dust is transported towards other directions and/or deposited before reaching 30°W (Fig. 4.3b).

The ARR and DEP time series for AMA-S and CAR show marked peaks indicating isolated events of dust transport into these regions, and a strong seasonal variation

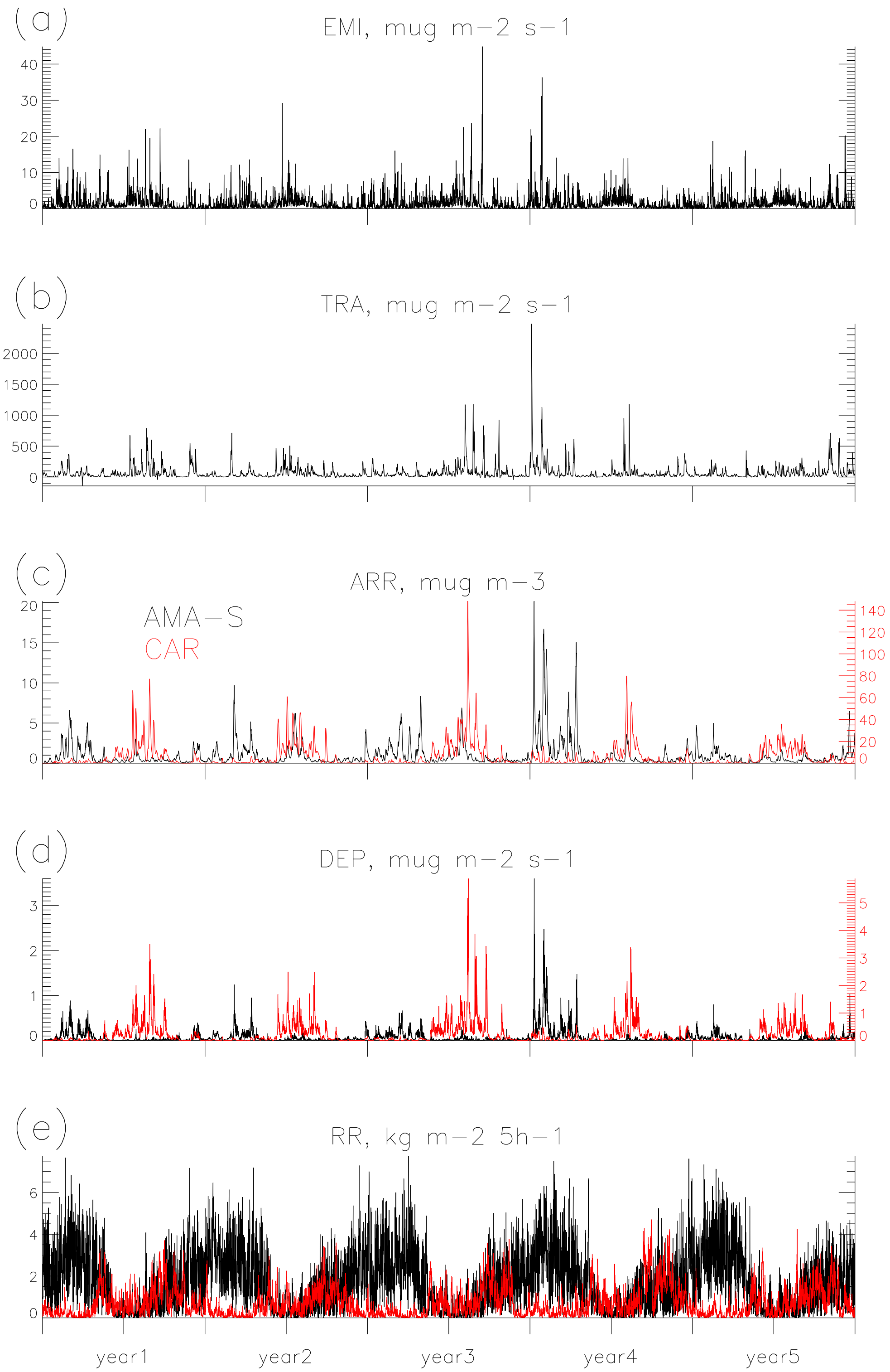

Fig. 4.2: Five-year time series according to Eq. (4.4). (c)–(e) show data for the Amazon Basin south of the equator (black) and the Caribbean (red). Note the different ordinates for AMA-S and CAR in (c) and (d). year1 to year5 on the abscissa denote the respective year of the time slice simulation.

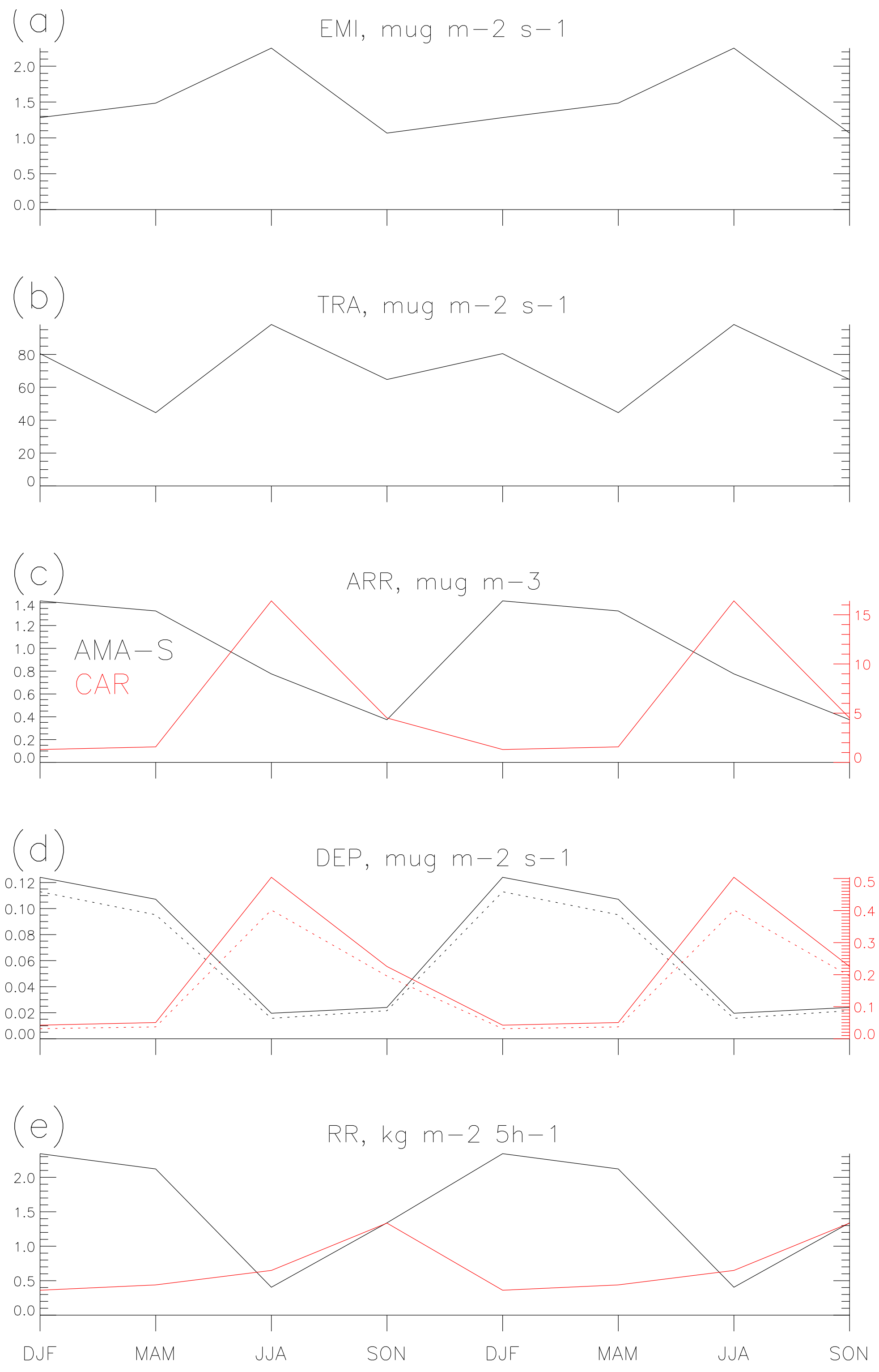

Fig. 4.3: Seasonal cycle of the parameters described in Eq. (4.4). For better visibility, the course of the year is shown consecutively twice on the abscissa. (c)–(e) show data for the Amazon Basin south of the equator (black) and the Caribbean (red). Note the different ordinates for AMA-S and CAR in (c) and (d). Dotted lines in (d) mark wet deposition.

(Figs. 4.2c,d). The latter is also evident in Figs. 4.3c,d. In the Caribbean the arrival and the deposition peak in JJA. They are much lower in SON and negligible in MAM and DJF. About 80% of the dust deposition are attributed to wet removal (Fig. 4.3d). The fact that the maximum of the arrival coincides with the rainy season in the Caribbean (from June to November) promotes the deposition during that time of the year. In AMA-S the percentage of the wet deposition is even higher with around 90%. Arrival and deposition reach their maximum in DJF and are somewhat lower in MAM. The arrival in JJA is about half of the DJF value and even reduced to 25% in SON. It is conspicuous that the deposition does not reflect this cycle. It is even lower during JJA than during SON. A likely explanation for this is the seasonality of the precipitation (Fig. 4.3e). The rainy season in the Amazon rain forest lasts from November to April. As wet deposition plays a decisive role in the dust cycle, the meagre precipitation in JJA might cause this minimum in the deposition during NH-summer. However, correlating the DEP and the RR time series does not yield an obvious connection of these two parameters, most likely because the precipitation is relatively constant during the rainy season while the dust deposition strongly depends on the episodic arrival. Therefore, RR is high and DEP is low at many times, causing a low correlation. Further analyses of correlations between the different time series are discussed in the next section 4.4.

4.4 Transport time scales

To determine the duration of the dust transport from the Sahara to the Americas, different approaches – one Eulerian and one Lagrangian – are considered and compared.

4.4.1 Eulerian approach

The transport time of dust from 30°W to the Caribbean and the Amazon region is derived by correlating the TRA time series with the temporally shifted ARR time series (see Eq. 4.4). The time shift Δt that yields the maximum correlation coefficient is assumed to represent the averaged transport time. The time shift is varied in five-hour steps from 0 to 200 hours. To obtain the time between the dust arrival in the region and its deposition, the time series of ARR and DEP are considered, with time lags varying from -100 to 100 hours. The duration of the transport of dust from the source regions in Africa to 30°W cannot be derived in this way, because the Eulerian data yield no information on which dust (i.e., from which source regions) actually reaches 30°W. This will only be investigated with the trajectories in section 4.4.2.

In the following the Amazon Basin is restricted to the part south of the equator – as in section 4.3 –, in order to get a clearer seasonal variation. Figure 4.4 shows

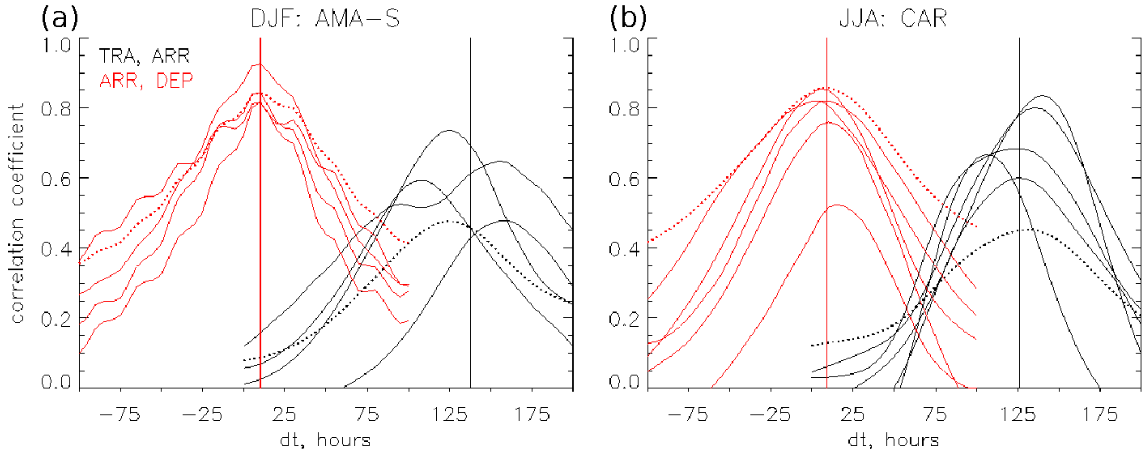

Fig. 4.4: Time lagged correlations of the time series TRA and ARR (black) and ARR and DEP (red). Solid lines show single seasons, i.e., DJF of year1/year2, ..., DJF of year4/year5 in (a) and JJA of year1, ..., JJA of year5 in (b). Dotted lines illustrate the time series of the entire five years from year1 to year5. Vertical lines mark the time shift of the maximum correlation, averaged over the the single seasons.

the correlation of the time series according to Eq. (4.4) for various time lags Δt for arrival and deposition in (a) the southern Amazon Basin in DJF and (b) the Caribbean in JJA.

In single seasons, the correlation between TRA and ARR reaches its maximum for Δt between 110 to 160 hours during DJF in AMA-S and 105 to 140 hours during JJA in CAR (see maxima of the solid black lines in Figs. 4.4a,b). Averaged over the single seasons, the maximum is reached for Δt = 137.5 hours = 5.73 days (DJF: AMA-S) and for Δt = 126 hours = 5.25 days (JJA: CAR), respectively (vertical black lines in Figs. 4.4a,b). Correlating the five-year time series, the maximum is reached for similar time shifts, but the correlation coefficient is generally lower than for single seasons (dotted black lines in Figs. 4.4a,b). The reason for the lower correlation is that the transport across 30°W is relatively constant over the year, while the arrival in CAR and AMA-S has a more distinct seasonal cycle. For example, during JJA large amounts of dust are transported across 30°W but this dust does not reach the Amazon Basin, reducing the correlation coefficient between the transport and the arrival in the Amazon region.

Red lines in Figs. 4.4a,b reveal a time shift of 10 (9) hours between the arrival and the deposition during DJF in AMA-S (JJA in CAR). During seasons with low dust transport into the respective regions, both the arrival and the deposition are low. This leads to higher correlation coefficients between ARR and DEP when considering the five-year time series. Only during DJF in AMA-S, one season has an even stronger correlation with values above 0.9.

From this Eulerian analysis the average transport time of dust from 30°W to the southern part of the Amazon Basin in DJF and to the Caribbean in JJA is found to be in the order of five to six days.

4.4.2 Eulerian vs. Lagrangian approaches

With the Lagrangian approach, the mean time is calculated that the trajectories need to reach 30°W and the target areas CAR and AMA-S. To reduce the impact of trajectories that transport only little amounts of dust, the average time of reaching 30°W ($\bar{\tau}_{30°\mathrm{W}}$) is weighted with the dust concentration at 30°W ($DU\_conc_{30°\mathrm{W}}$):

$$\bar{\tau}_{30°\mathrm{W}} = \frac{\sum_T \left[DU\_conc_{30°\mathrm{W}}(T) \cdot \tau(T)\right]}{\sum_T DU\_conc_{30°\mathrm{W}}(T)} \quad , \tag{4.5}$$

where T denotes a single trajectory and $\tau(T)$ the duration from the initialisation of trajectory T to its crossing of 30°W. As in all following trajectory calculations, the factor F_{EC} according to Eq. (4.1) is implicitly considered in the traced variables along the trajectories and does not appear in the equations. The average times of reaching CAR ($\bar{\tau}_{\mathrm{CAR}}$) and AMA-S ($\bar{\tau}_{\mathrm{AMA\text{-}S}}$) are calculated accordingly, but weighted with the dust concentration when reaching the respective region. The duration of the transport from 30°W to CAR and AMA-S is the difference $\bar{\tau}_{\mathrm{CAR}} - \bar{\tau}_{30°\mathrm{W}}$ and $\bar{\tau}_{\mathrm{AMA\text{-}S}} - \bar{\tau}_{30°\mathrm{W}}$, respectively. Note that it is not possible to determine the transport time from the source regions to 30°W with the Eulerian approach, as mentioned in the previous section.

Table 4.1 gives the seasonal transport durations derived from the Lagrangian (LAG) and the Eulerian (EUL) approaches. The transport time to 30°W varies from 4.62 days in DJF to 7.25 days in MAM. There are some discrepancies between the Eulerian and Lagrangian values for the transport from 30°W to CAR and AMA-S, respectively. Lagrangian values are in general lower than the Eulerian ones, which can be explained with the different methodologies. The arrival *ARR* in the Eulerian

	$\bar{\tau}_{30°\mathrm{W}}$	$\bar{\tau}_{\mathrm{CAR}} - \bar{\tau}_{30°\mathrm{W}}$		$\bar{\tau}_{\mathrm{AMA\text{-}S}} - \bar{\tau}_{30°\mathrm{W}}$	
	LAG	EUL	LAG	EUL	LAG
DJF	4.62	**4.53**	3.56	**5.73**	4.71
MAM	7.25	5.38	3.99	6.21	3.39
JJA	6.63	**5.25**	3.66	3.83	4.32
SON	5.79	5.63	4.34	4.75	5.16

Table 4.1: Transport time of dust from North African source regions to 30°W and from there to the target regions CAR and AMA-S in days. For the first part of the transport (to 30°W) only values from the Lagrangian approach are available. The Eulerian values are bold (grey) if the mean correlation coefficient is higher than 0.6 (lower than 0.4).

approach represents the mean dust concentration over the entire target region. In the Lagrangian approach, the mean time for reaching the border of the target region is calculated. Further penetration into the target region is not considered. Hence, the Lagrangian values give a lower limit for the transport time. Two exceptions, where the Eulerian time is shorter than the Lagrangian time, are the durations to reach AMA-S in JJA and SON. However, these Eulerian values result from the TRA and ARR time series that have the lowest correlation coefficients, so, the Lagrangian values are more reliable. The Lagrangian transport time from 30°W to CAR is in all seasons – and to AMA-S during DJF – less than two days shorter than the Eulerian one. This results from differences in the methodologies. Overall, the Lagrangian results corroborate the Eulerian time scales. Only in MAM the difference for the transport from 30°W to AMA-S amounts to almost three days.

It is worth mentioning that the mean correlation coefficient in the Eulerian calculation of the transport time from 30°W to CAR during DJF is higher than 0.6, although CAR is not the main target region of the dust that is transported across 30°W in this season. This shows that parts of the dust in DJF do reach CAR whereas the correlation coefficients in JJA and SON for AMA-S are very low. The ITCZ represents a clear barrier for the dust and almost no dust is transported to the southern part of the Amazon region when the ITCZ is located north of the equator.

The two approaches used here for determining the transport time of dust from North Africa to the Americas yield fairly coherent results. The sum of the Lagrangian values of $\bar{\tau}_{30°\mathrm{W}}$ plus the time from there to the target regions represents the overall transport time. It accounts for $4.62 + 4.71 = 9.33$ days for the transport to AMA-S in DJF and for $6.63 + 3.66 = 10.29$ days for the transport to CAR in JJA, which are the two most outstanding transport pathways.

Engelstaedter et al. (2009) calculated backward trajectories from Barbados on days with high surface dust concentrations. They only considered days in June between 1980 to 1992 and received transport times of about six days for the trajectories to reach the African coast. This is much faster than the result for the transport to CAR in JJA presented above. However, Engelstaedter et al. (2009) did not account for the time, it takes the dust from the source regions to the African coast. The Lagrangian transport time from 30°W to CAR amounts to 3.66 days. This distance is about two-thirds of the length from the African coast (around 15°W) to Barbados (59°W). Assuming similar transport velocities between the coast and 30°W and from there to CAR (eastern corner at 58°W), the Lagrangian method reveals a transport time of 5.75 days from the African coast to 59°W. This is in very good agreement with the result of Engelstaedter et al. (2009) and confirms that the selected trajectories (see section 4.2.2) describe the transatlantic dust transport in a plausible way.

4.5 Transport pathways

Former analyses of the transport pathways of dust across the Atlantic Ocean and especially the vertical distribution were restricted to short episodes, to measurements at single stations or to satellite retrievals. For example, Pierangelo et al. (2004) investigated mineral dust optical depth and altitude with satellite based measurements of the Advanced Infrared Radiation Sounder (AIRS) for the period from April to September 2003. Schepanski et al. (2009) used simulations with the regional model system LM-MUSCAT[1], for three monthly case studies in different seasons in March and July 2006 and in January 2007. Engelstaedter et al. (2009) analysed dust concentration measurements at Barbados between 1980 and 1992 and calculated back-trajectories from Barbados, driven by ERA-40[2] wind fields, without any information on the dust concentration and deposition during the transport.

The T85TG five-year time slice simulation provides a basis for Eulerian and Lagrangian climatological investigations of the horizontal and vertical structure of the dust transport and the processes influencing dust particles on their way from Africa to the Americas.

4.5.1 Total number of trajectories

Figure 4.5 illustrates the horizontal distribution of all trajectories starting from North African dust emission grid points and passing 30°W. During DJF the trajectory density is highest in a region stretching in southwest-northeastern direction from south of the equator in South America to the western part of the Sahara. During JJA the pattern is much more zonally orientated, reaching from the Caribbean to the Central Sahara. The absolute number of initialised trajectories is by far highest in JJA (257 403), followed by DJF (152 357), SON (143 331), and MAM (102 534) (see Table 4.3). Remember that trajectories are started at each model output time step and from each grid box within the planetary boundary layer if the surface dust emission flux is greater than zero. They are weighted with the factor F_{EC}, according to Eq. (4.1). In none of the seasons a clear signal is visible in the region of the Bodélé Depression in Chad (14°–18°N, 16°–20°E). This is surprising because the Bodélé Depression is an active dust source throughout the year (Prospero et al. 2002) and the most outstanding region with regard to dust emission in the T85TG simulation during DJF and MAM. In these seasons, Figs. 4.5a,b show only a little extension towards the Bodélé Depression, from 0°E eastwards, between 10° and 20°N. In general, there are more trajectories starting east of 0°E during JJA and SON than in the other seasons, including the Bodélé Depression. A certain

---

[1] Lokal Modell (Ger.: regional model) - MUlti-Scale Chemical Aerosol Transport

[2] ECMWF 40-year Re-analysis data set

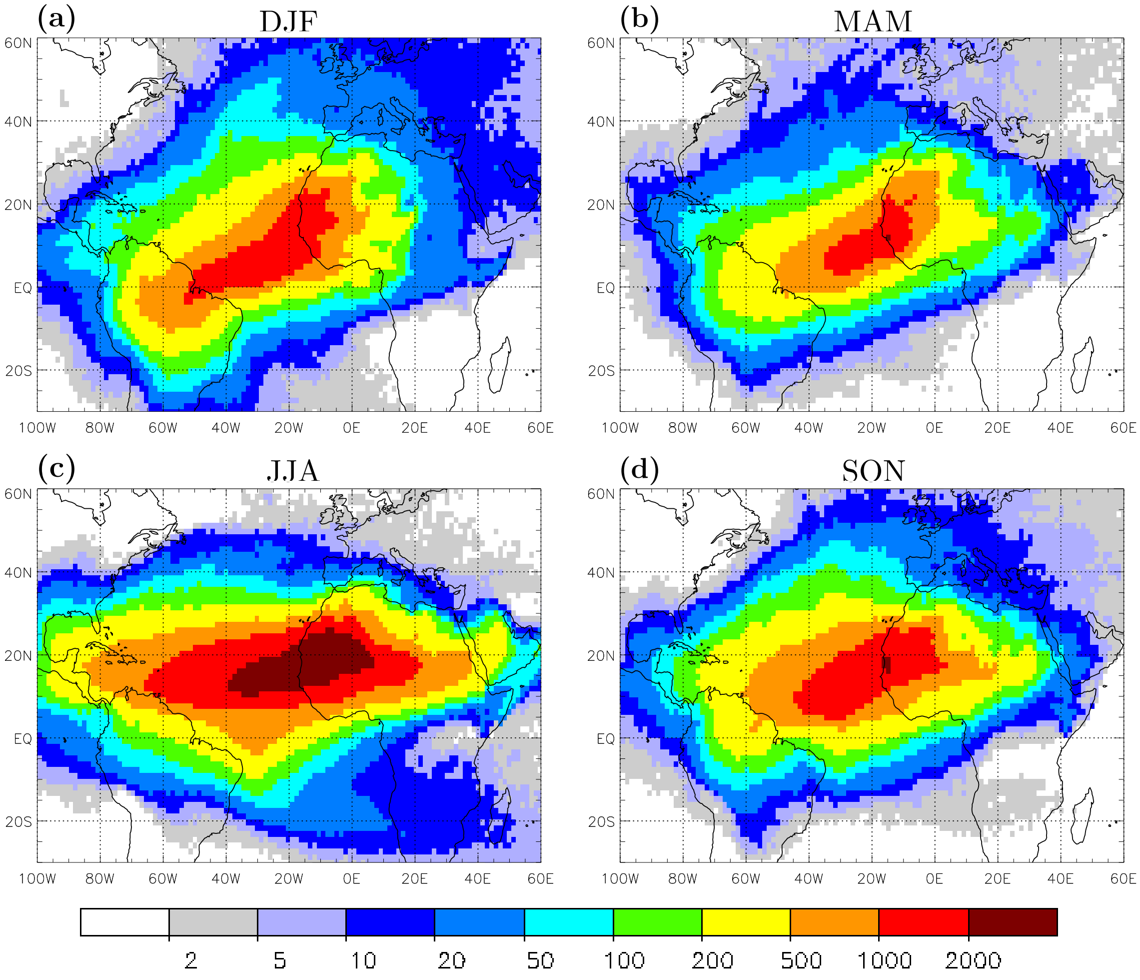

Fig. 4.5: Seasonal averaged number density (# per 10^4 km^2 per season) of all trajectories, initialised as described in section 4.2.2.

amount of trajectories starts from the Arabian Peninsula during JJA, in contrast to the rest of the year. During NH-summer the African easterly jet with maximum wind velocities of about 12.5 m s^{-1} between 600 and 700 hPa around 15°N is located over the Sahara (Thorncroft and Blackburn 1999). When the Arabian trajectories reach the Sahara they come under the influence of the African easterly jet. They are then transported further west fast enough to carry at least parts of their initial dust across 30°W, resulting in the signal over the Arabian Peninsula during JJA in Fig. 4.5c.

The mean dust concentration (DU_conc, in µg m^{-3}) along the trajectories, scaled with the number of trajectories (#) – i.e., $\overline{DU\_conc}$ according to the following equation – gives better insight into the distribution of airborne dust in single seasons and is illustrated in Fig. 4.6.

$$\overline{DU\_conc}_{i,j} = \frac{\varnothing_{n\in X} DU\_conc_{i,j,n} \cdot \sum_{n\in X} \#_{i,j,n}}{\sum_{n\in X} \sum_{i,j} \#_{i,j,n}} \quad , \tag{4.6}$$

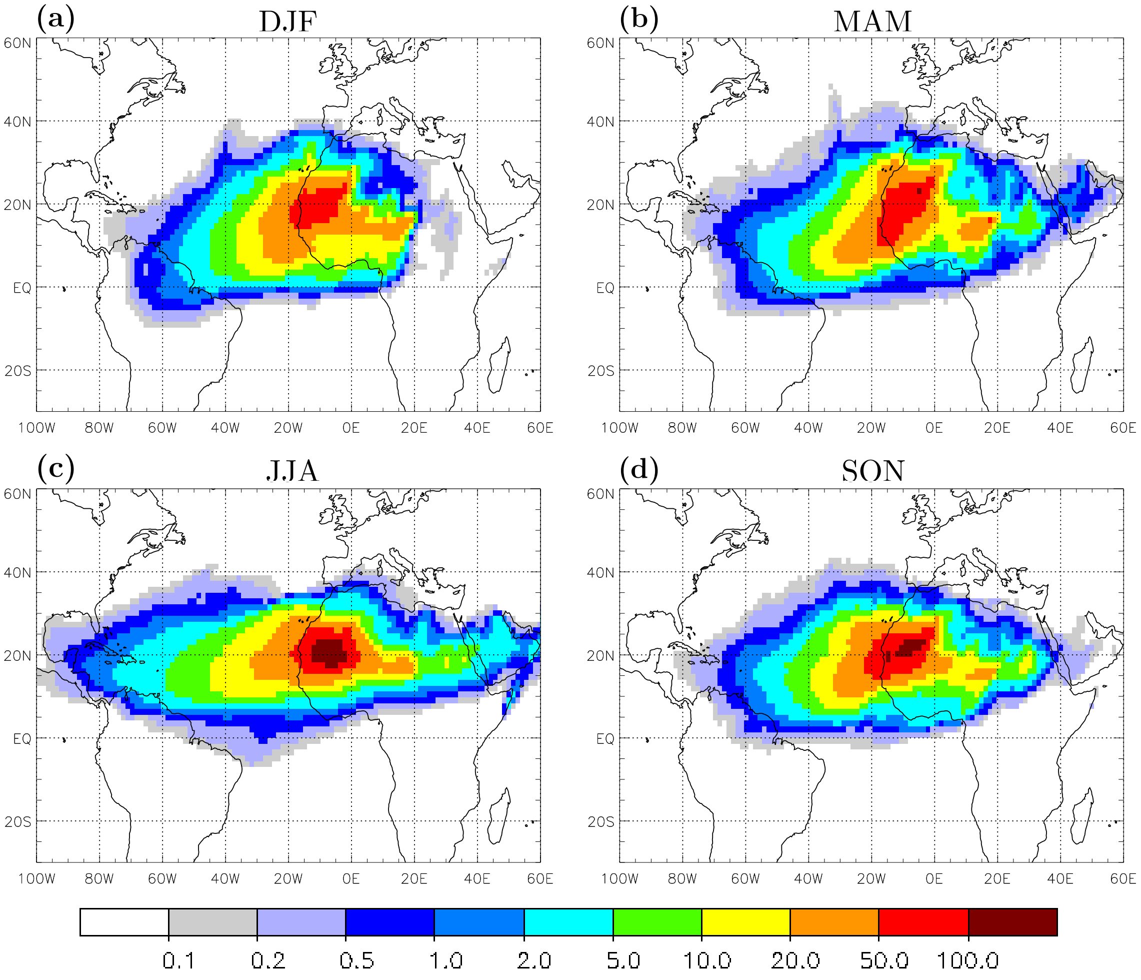

Fig. 4.6: Seasonal averaged mean dust concentration along the trajectories, scaled with the number of trajectories, i.e., $\overline{DU\_conc}$ according to Eq. 4.6.

where i, j are the horizontal grid indices, n the model output time steps, and X denotes the different seasons. The maximum of $\overline{DU\_conc}$ is positioned over the western part of North Africa around 20°N in each season. The transatlantic transport of dust shows a similar seasonal cycle as the trajectory density in Fig. 4.5, with transport in the southwestern direction towards South America in DJF and MAM and zonal transport towards the Caribbean mainly in JJA (Fig. 4.6). The Bodélé Depression is emphasised in each season and especially in MAM, when a local maximum occurs there. This indicates that the few trajectories starting from there have relatively high dust concentrations, compared to other regions. A detailed discussion of the contribution of single source regions to the dust deposition in Central and South America is provided in section 4.6.

4.5.2 Trajectory characteristics

For the following analyses three differently weighted averages over all trajectories, initialised as described in section 4.2.2, are calculated and handled as one trajectory each.

- One weighting factor is the traced dust mixing ratio, when the trajectories cross 30°W. The average, obtained with this weighting factor, gives information about the characteristics of trajectories contributing a lot to the transatlantic dust transport. This average is referred to as dusty trajectories from now on.
- The reciprocal of this factor is the weight for the calculation of the second average. It describes those trajectories carrying along only little amounts of dust when passing 30°W, called non-dusty trajectories in the following.
- The third average is just the non-weighted mean over all trajectories.

The pathways of the dusty, non-dusty, and non-weighted trajectories are shown in Fig. 4.7 during the different seasons. The pressure along the trajectories is shown in colours.

The mean starting point of the dusty trajectories is located in Southwest Algeria and its seasonal variation is small. Only in SON it is shifted slightly eastwards. The seasonal variation of the transatlantic transport is clearly visible, with the southwesterly transport towards South America in NH-winter (Fig. 4.7a) and in a more zonal direction to the Caribbean in NH-summer (Fig. 4.7c). During the transitional seasons (Figs. 4.7b,d) the pathways lie between the DJF and JJA routes.

The mean height of the dusty trajectories has also a strong seasonal cycle. In NH-winter they cross almost the entire Atlantic Ocean below 900 hPa (Fig. 4.7a). When rising to levels above 750 hPa off the northern tip of the Brazilian coast, they start curving to the east and rise up to 550 hPa. Here, they get influenced by the eastward subtropical jet stream. In JJA the dusty trajectories cross the Atlantic Ocean between 750 and 800 hPa and rise to 650 hPa after 15 days over the Caribbean (Fig. 4.7c). In MAM they pass 30°W at a height of 800 to 850 hPa and in SON around 900 hPa showing again the transitional character of these two seasons (Figs. 4.7b,d).

The mean position of the non-dusty trajectories is slightly further south compared to the dusty trajectories in each season. Only in JJA there is also a huge eastward displacement of the starting point of the non-dusty trajectories at 30°W, which originate in the region of the Bodélé Depression (Fig. 4.7c). This indicates strong dust source activity of the Bodélé Depression during NH-summer but also little contribution of this region to the transatlantic transport of dust, meaning that the trajectories from the Bodélé Depression lose their dust before reaching 30°W. During

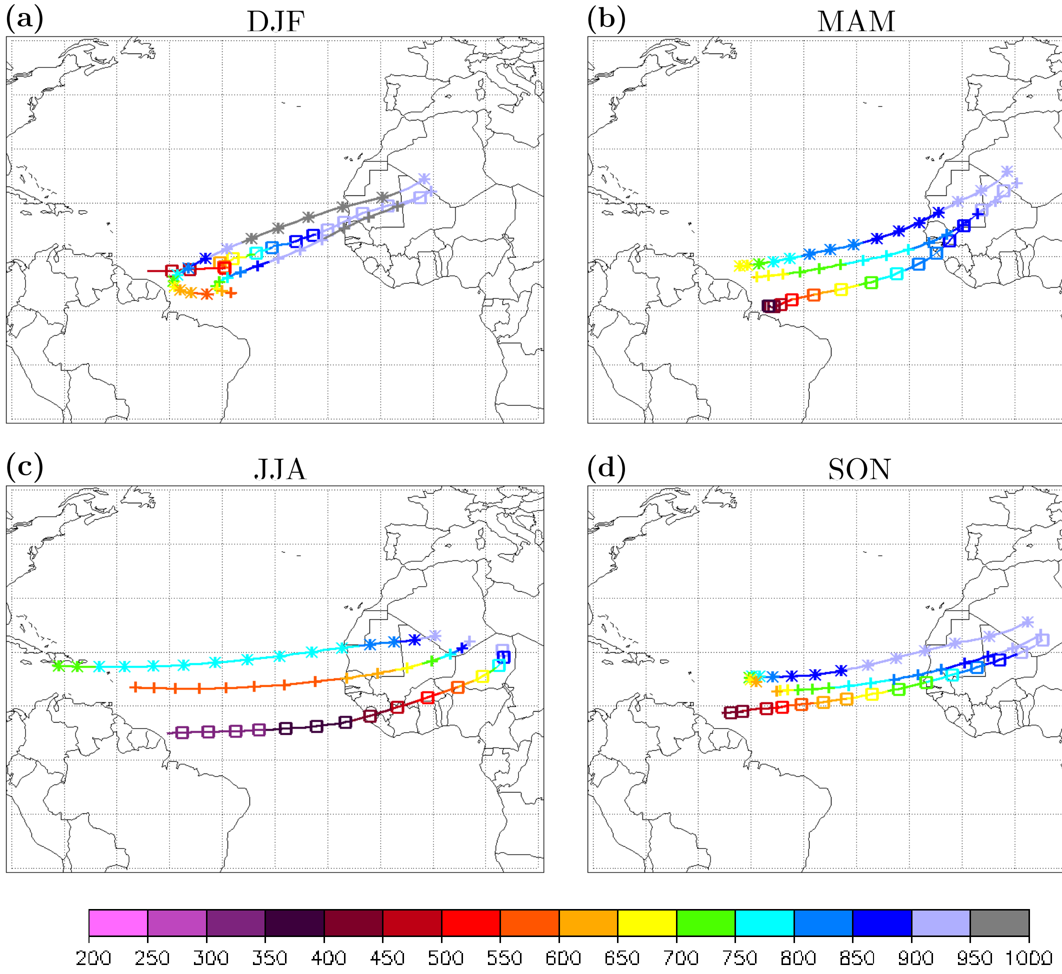

Fig. 4.7: Seasonal variation of the trajectory pathways. A symbol along the trajectories is drawn every 25 hours. “+” indicates the non-weighted average over all trajectories, “✳” the dusty trajectories, and “□” the non-dusty trajectories, according to the description in the beginning of section 4.5.2. The coloured variable along the trajectories is the pressure in hPa.

the whole year the non-dusty trajectories rise faster and further than the dusty ones, up to altitudes above 350 hPa in NH-summer.

The mean non-weighted trajectories show a mixture of the behaviour of the dusty and the non-dusty ones. Their characteristics, however, are closer to the dusty trajectories, indicating that there are more trajectories with high dust mixing ratios at 30°W than with low ones.

In Fig. 4.8 the coloured variable along the trajectories is the dust mixing ratio and the underlying contours show the ratio of the Eulerian wet-to-total dust deposition flux. Throughout the year a tongue with low wet-to-total deposition ratios stretches from North Africa westwards to the nearby Atlantic Ocean. This tongue is most distinct in DJF and MAM (Figs. 4.8a,b) and weakest in SON (Fig. 4.8d). In DJF wet deposition accounts for less than 10% of the total dust deposition flux almost

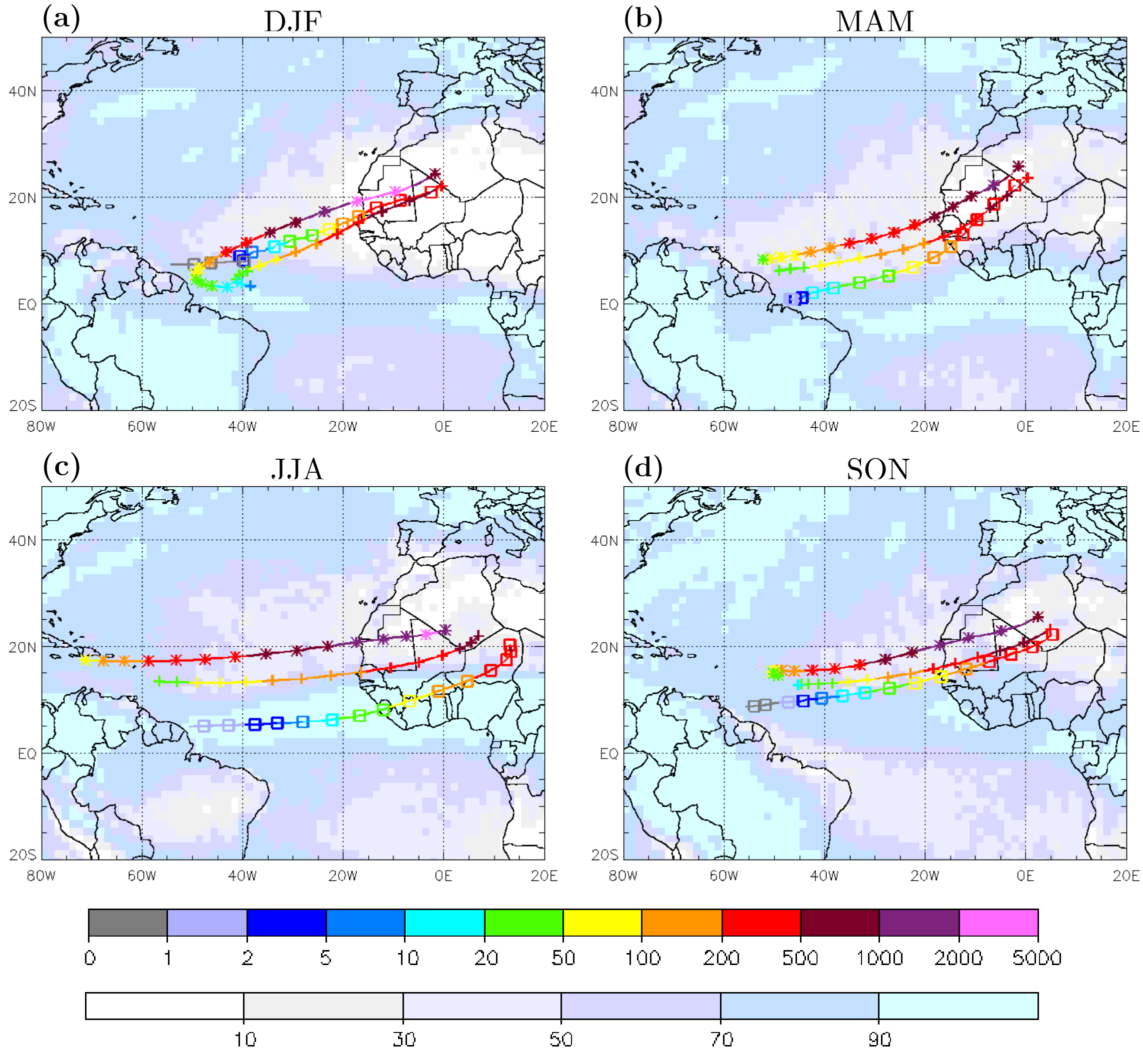

Fig. 4.8: Seasonal variation of the trajectory pathways. A symbol along the trajectories is drawn every 25 hours. “+” indicates the non-weighted average over all trajectories, “∗” the dusty trajectories, and “□” the non-dusty trajectories, according to the description in the beginning of section 4.5.2. The coloured variable along the trajectories is the dust mixing ratio in μg kg^{-1} (upper colourbar). The underlying contour shows the ratio of the Eulerian wet-to-total dust deposition flux in % (lower colourbar).

over entire North Africa and off the West African coast. South of the equator in South America, however, more than 70% or even 90% of the dust is scavenged when the dust arrives there in the rainy season in DJF and MAM. During JJA and SON (Figs. 4.8c,d) the ratio is much smaller but during the second half of the year only a small amount of dust is transported there. In the Caribbean the wet-to-total deposition ratio mostly lies between 70 and 90%. The importance of the wet deposition becomes clearly apparent in DJF and SON. When the dusty trajectories pass the 50% line, the dust mixing ratio abruptly decreases. Interesting seasonal differences occur in the non-dusty trajectories. In DJF and MAM they last in regions that are dominated by dry deposition for several days. Their dust mixing ratio is already very low when reaching wetter areas. In the rest of the year, especially in JJA, the dust deposition along the non-dusty trajectories is dominated by scavenging along the entire trajectory pathway.

4.5.3 Vertical structure

In the previous subsection the transport height of the trajectories was discussed considering the averaged pressure along the trajectories. The vertical structure is now analysed in more detail, with the aid of vertical cross sections of the zonal dust flux up to 400 hPa from 20°S to 40°N along 10°W, 30°W, and 50°W in the different seasons (Figs. 4.9 – 4.12). Again, the Eulerian (left columns) and the Lagrangian (right columns) results are compared.

Eulerian seasonal fluxes $DU\_flux^{X}_{\mathrm{EUL}}$, where X denotes the season, are calculated by multiplying the dust concentration with the zonal wind speed u at each model output time step n and computing the seasonal mean afterwards:

$$DU\_flux^{X}_{\mathrm{EUL}} = \varnothing_n \text{ dust concentration}(n) \cdot u(n) \quad \forall n \in X. \tag{4.7}$$

For the Lagrangian fluxes ($DU\_flux^{X}_{\mathrm{LAG}}$) the vertical cross section is subdivided in 5° latitude × 30 hPa boxes. The dust mixing ratio at the time when a trajectory crosses the respective longitude is multiplied with the trajectory mass m_T and divided by the area A of the 5° latitude × 30 hPa box that it passes through.

$$DU\_flux^{X}_{\mathrm{LAG}} = \sum_{\mathrm{Traj.}\in X} \frac{1}{A} \cdot m_T \cdot \text{ dust mixing ratio}\Big|_{Y} \tag{4.8}$$

$$\text{, with } Y = 10°\mathrm{W},\ 30°\mathrm{W},\ 50°\mathrm{W}$$

If one trajectory crosses one of the longitudes from west to east, the flux according to Eq. (4.8) is subtracted. In Figs. 4.9 – 4.12 positive (negative) values show fluxes in western (eastern) direction.

The overall fairly good agreement of the patterns and absolute values of $DU\_flux^{X}_{\mathrm{EUL}}$ and $DU\_flux^{X}_{\mathrm{LAG}}$ in all seasons and at all depicted longitudes shows that Eulerian zonal dust fluxes are well represented by the trajectories. The annual fluxes in Tg yr^{-1} across different longitudes, i.e., the vertically and latitudinally integrated values, are listed in Table 4.2, revealing some discrepancies between the different methods. At 10°W the Lagrangian fluxes are 1.5 times higher than the Eulerian ones. Further west the ratio of Lagrangian to Eulerian results decreases and the Lagrangian fluxes represent only half of the Eulerian transport at 50°W. The Eulerian values represent the actual transport as it is simulated in the model.

Higher Lagrangian values close to the source regions at 10 and 20°W arise from the criterion chosen for the trajectory selection. As trajectories are only initialised

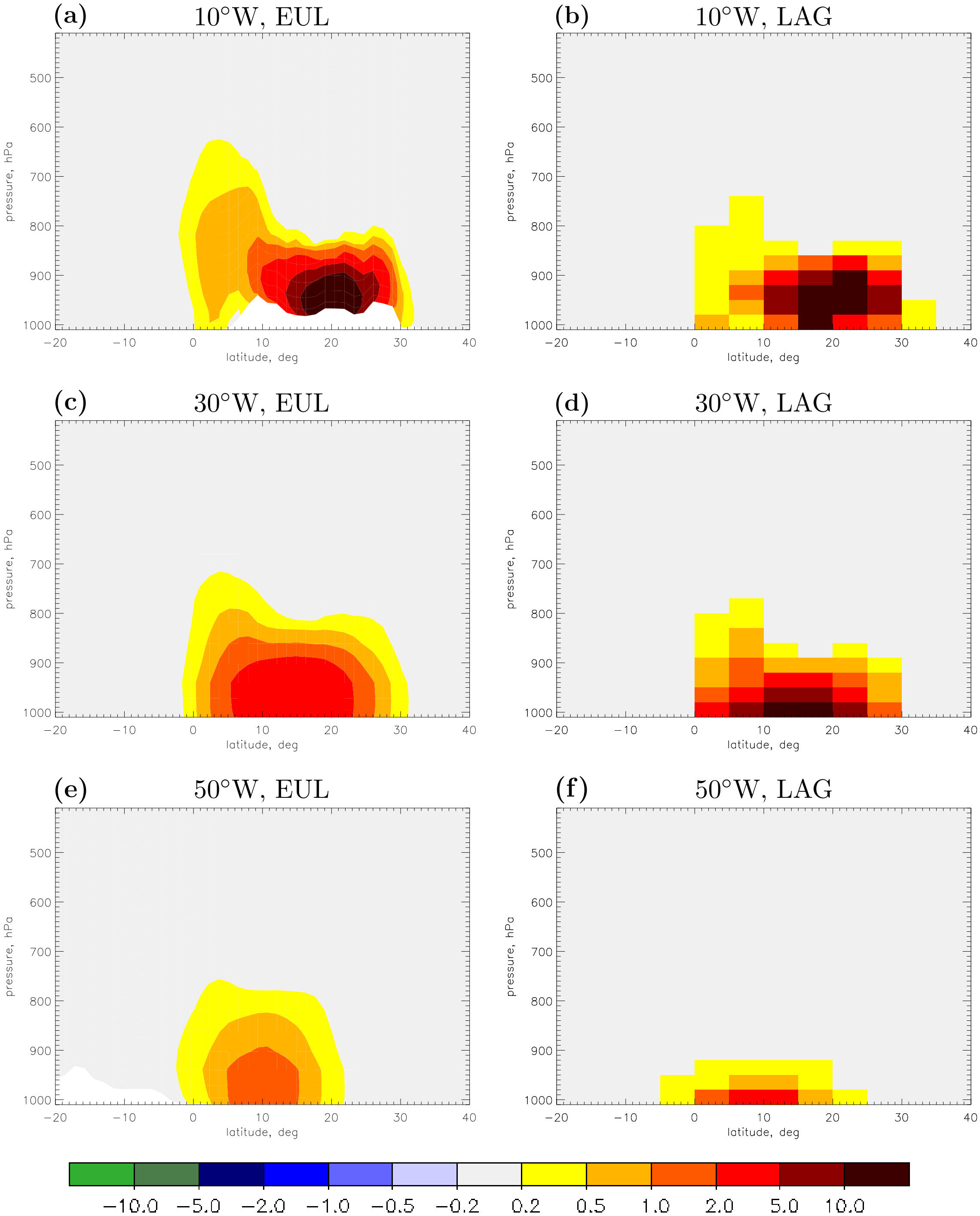

Fig. 4.9: Meridional cross sections of the DJF mean zonal dust flux of the Eulerian model output ($DU\_flux^{\mathrm{DJF}}_{\mathrm{EUL}}$ in kg m^{-2} per month according to Eq. 4.7, left column) and the Lagrangian trajectory data ($DU\_flux^{\mathrm{DJF}}_{\mathrm{LAG}}$ according to Eq. 4.8, right column) across 10°W (top), 30°W (middle), and 50°W (bottom). Positive (negative) values mark westward (eastward) fluxes. White areas at the bottom of panels (a) and (e) show the orography.

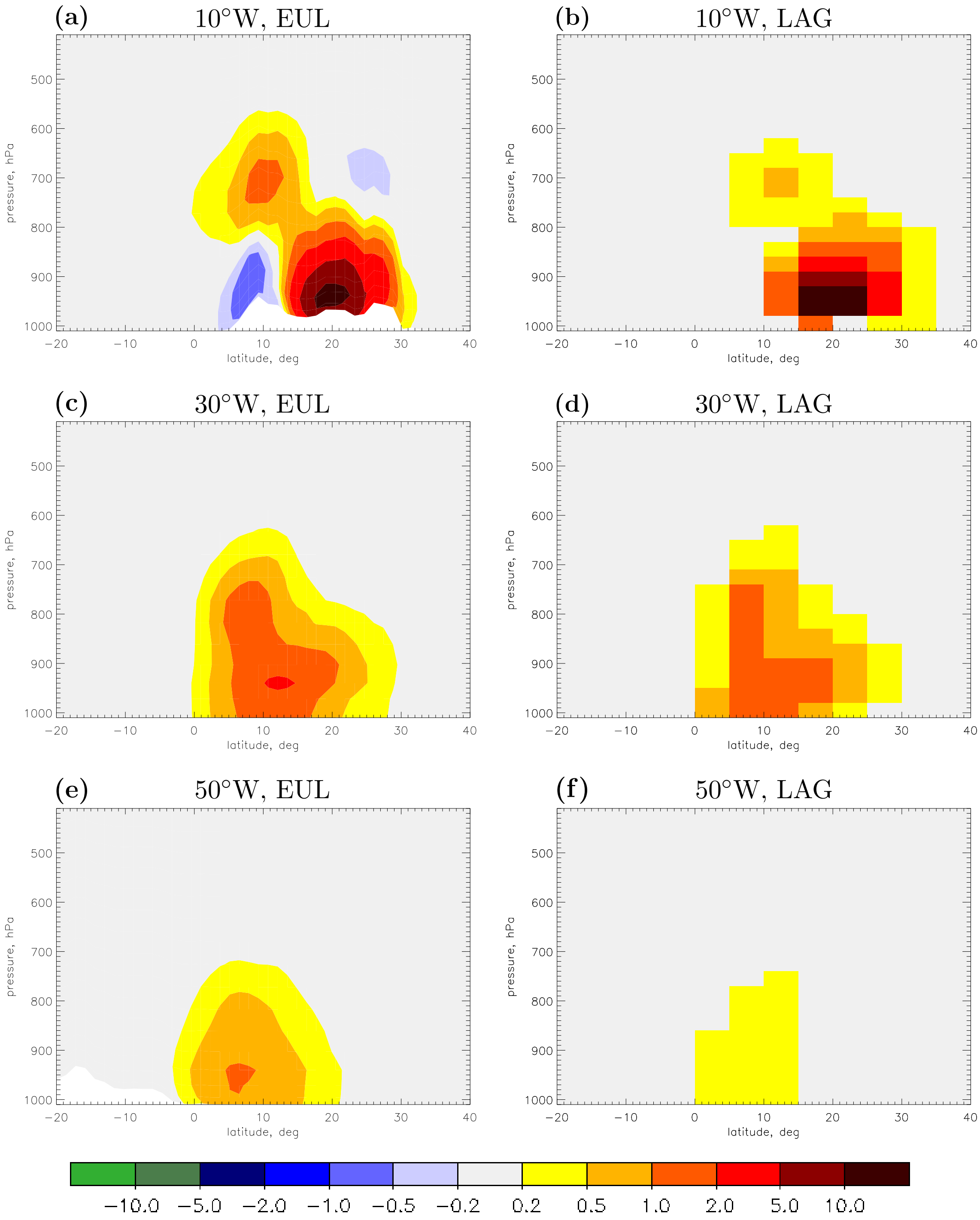

Fig. 4.10: Meridional cross sections of the MAM mean zonal dust flux of the Eulerian model output ($DU\_flux^{\mathrm{MAM}}_{\mathrm{EUL}}$ in kg m^{-2} per month according to Eq. 4.7, left column) and the Lagrangian trajectory data ($DU\_flux^{\mathrm{MAM}}_{\mathrm{LAG}}$ according to Eq. 4.8, right column) across 10°W (top), 30°W (middle), and 50°W (bottom). Positive (negative) values mark westward (eastward) fluxes. White areas at the bottom of panels (a) and (e) show the orography.

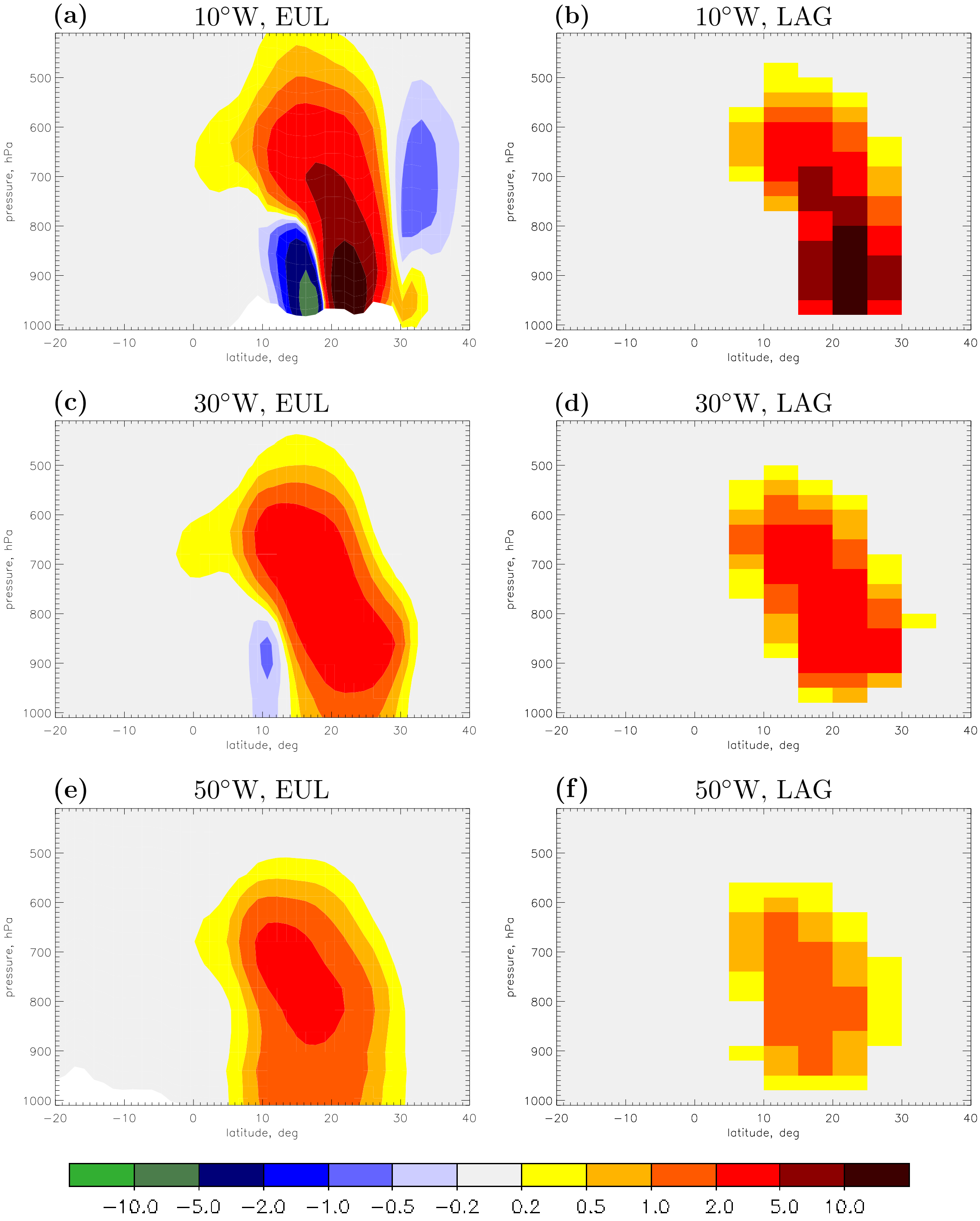

Fig. 4.11: Meridional cross sections of the JJA mean zonal dust flux of the Eulerian model output ($DU\_flux^{\mathrm{JJA}}_{\mathrm{EUL}}$ in kg m^{-2} per month according to Eq. 4.7, left column) and the Lagrangian trajectory data ($DU\_flux^{\mathrm{JJA}}_{\mathrm{LAG}}$ according to Eq. 4.8, right column) across 10°W (top), 30°W (middle), and 50°W (bottom). Positive (negative) values mark westward (eastward) fluxes. White areas at the bottom of panels (a) and (e) show the orography.

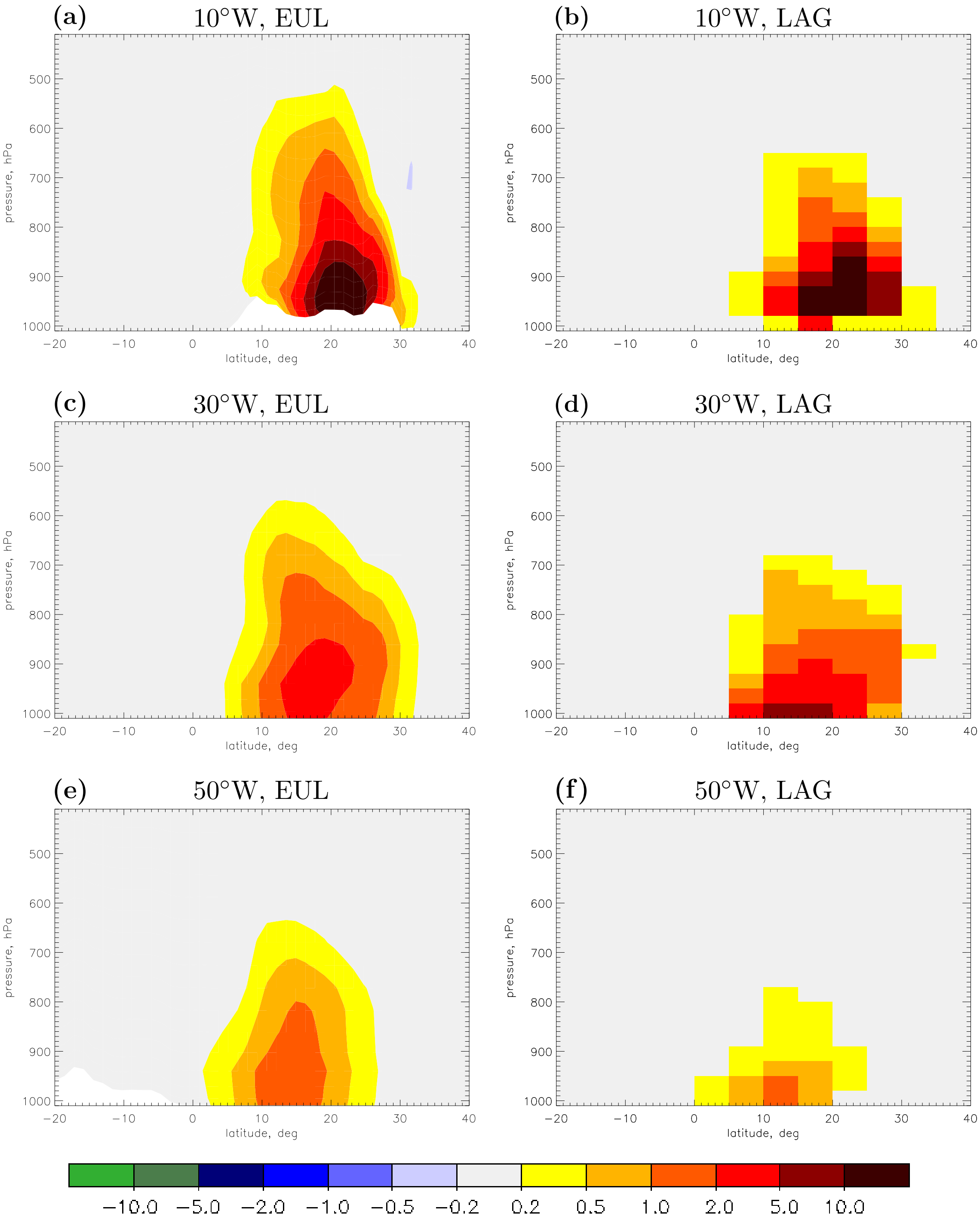

Fig. 4.12: Meridional cross sections of the SON mean zonal dust flux of the Eulerian model output ($DU\_flux^{\mathrm{SON}}_{\mathrm{EUL}}$ in kg m^{-2} per month according to Eq. 4.7, left column) and the Lagrangian trajectory data ($DU\_flux^{\mathrm{SON}}_{\mathrm{LAG}}$ according to Eq. 4.8, right column) across 10°W (top), 30°W (middle), and 50°W (bottom). Positive (negative) values mark westward (eastward) fluxes. White areas at the bottom of panels (a) and (e) show the orography.

	EUL	LAG	ratio $\frac{\text{LAG}}{\text{EUL}}$
10°W	278.1	422.7	1.5
20°W	239.7	272.9	1.1
30°W	174.2	155.1	0.9
40°W	132.1	83.8	0.6
50°W	93.6	45.0	0.5
60°W	63.4	22.9	0.4

Table 4.2: Annual westward zonal dust fluxes in Tg yr^{-1} across longitudes between 10 and 60°W. Results from Eulerian and Lagrangian data and the ratio thereof are listed.

over North Africa, the eastward transport back to the continent is underestimated. For example, no trajectories are considered that travel eastwards from the Atlantic Ocean towards the West African coast, gain dust in this region, travel further east and transport the dust back to the continent. This Lagrangian underrepresentation of the eastward dust flux can be nicely seen at 10°W in JJA (Figs. 4.11a,b). Between 10 and 20°N and up to 800 hPa the Eulerian eastward dust flux in the monsoon wind layer is on the same order of magnitude as the westward dust export further north. With the Lagrangian method the trade winds are not represented, explaining the higher Lagrangian zonal dust fluxes at 10 and 20°W (Table 4.2). Further west the Eulerian fluxes are higher than the Lagrangian values. Two processes, which are not represented by the trajectories, are responsible for this: First, dust particles sedimenting from higher levels can be gained by air masses below, which are potentially not captured by the trajectory approach, and transported further west. The second process is numerical diffusion, which increases the dust concentration in air parcels that are also not represented by the Lagrangian method. The overall fairly high agreement between Eulerian and Lagrangian results, however, legitimates the investigation of the transatlantic transport of dust with the trajectories considered here, when keeping in mind the processes that lead to differences between the two methods.

The distribution of the Eulerian and Lagrangian fluxes agree well at different longitudes and in all seasons (Figs. 4.9 – 4.12). The maxima are at the same latitudinal and vertical position. Also some finer structures are represented by the trajectories, like two maxima at 10°W in MAM at around 10°N, 700 hPa and at 20°N, 950 hPa (Figs. 4.10a,b) and the kind of L-shaped structure at 30°W in MAM (Figs. 4.10c,d). Some discrepancies occur in JJA when the main transatlantic transport takes place above 900 hPa. The Eulerian dust fluxes at 30 and 50°W (Figs. 4.11c,e) show large values from about 600 hPa down to the surface, while the Lagrangian ones are fairly low beneath 950 hPa. The explanation for this difference is that the settling of dust is visible in the Eulerian data. However, there are only few trajectories below 950 hPa causing low Lagrangian fluxes there. The maxima of the westward dust flux indeed coincide very well, while the minima at 10 and 30°W, i.e., the eastward dust fluxes, are only visible in the Eulerian data for the aforementioned reasons.

The cross sections illustrate the seasonal variation of the SAL. During NH-winter the transport mainly occurs below 850 hPa. The near-surface maximum shifts southward from around 20°N at 10°W (Figs. 4.9a,b) to 10°N at 50°W (Figs. 4.9e,f). In NH-spring the transport height rises up to 600 hPa and the southward displacement is similar to DJF (Fig. 4.10). The zonal transport in JJA occurs between 950 and 500 hPa and shows only little latitudinal variation (Fig. 4.11). In NH-autumn the southward shift increases again and the vertical extent of the SAL decreases with low fluxes above 650 hPa.

In summary, the meridional cross sections confirm that the trajectories represent the Eulerian transatlantic transport to the Americas very well. The vertical and latitudinal structure of the SAL significantly varies in the course of the year. During NH-winter the dust transport proceeds in the near-surface layers while it takes place in the lower free troposphere in NH-summer. These results of the T85TG five-year time slice simulation confirm findings of earlier studies on the seasonal variation of the SAL (e.g., Schepanski et al., 2009 and Ben-Ami et al., 2012), which were based on single-month model studies or satellite retrievals.

4.5.4 Dust gain and loss during the transport

The net dust emission flux ($\mathit{\Delta DU}$) is defined as dust emission minus deposition at one grid point. This parameter can be most easily obtained from Eulerian model output as the difference of the seasonal dust emission minus deposition. It can be compared to the respective Lagrangian value, which is calculated as follows (see also Eq. (4.9) and Fig. 4.13):

The net emission of dust along the trajectories ($\mathit{\Delta DU}$) is defined as the change in dust mixing ratio (DU in kg kg^{-1}) during the previous time step, multiplied with the trajectory mass m_T in kg, which is constant along the trajectory. $\mathit{\Delta DU}$ at the place of the trajectory at the time step t_x is thus defined as the dust mixing ratio at time t_x minus the mixing ratio at time t_{x-1} times m_T. t_x denotes the trajectory time steps in five-hour intervals from zero to 360 hours (i.e., 15 days). In the schematic example in Fig. 4.13 four trajectories are initialised above the orange grid point from the lowermost level (k_1) to the planetary boundary layer height (k_4 in this example). Only the trajectories denoted with T2, T3, and T4 contribute to $\mathit{\Delta DU}$, because T1 does not cross 30°W. So, $\mathit{\Delta DU}$ of the blue grid point is the sum of

$$\begin{aligned}
&[DU(\mathrm{T2}, t_2) - DU(\mathrm{T2}, t_1)] \cdot m_T(T2) + \\
&[DU(\mathrm{T3}, t_2) - DU(\mathrm{T3}, t_1)] \cdot m_T(T3) + \\
&[DU(\mathrm{T4}, t_2) - DU(\mathrm{T4}, t_1)] \cdot m_T(T4) \quad .
\end{aligned}$$

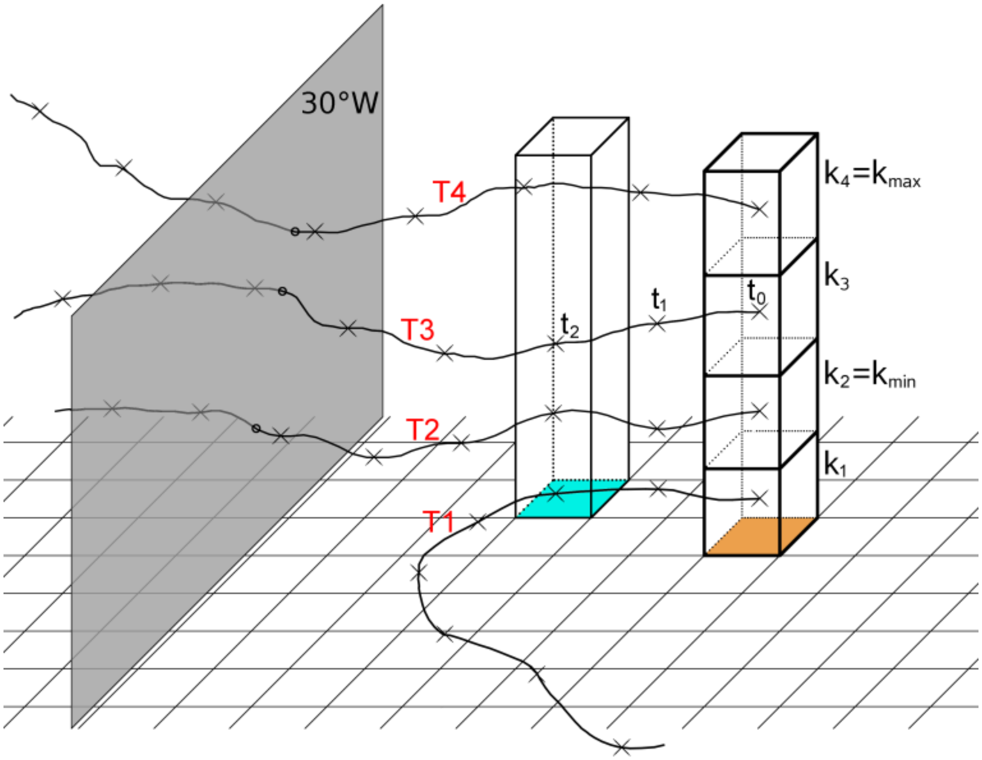

Fig. 4.13: Schematic example to explain the Lagrangian calculation of the net dust emission flux ΔDU according to Eq. (4.9). See text for further details.

There is a special treatment of the first trajectory time step: The net emission for t_1 is defined as the difference of the Eulerian surface dust emission flux (DEF) minus the deposition flux (DDF) at the starting grid point. This flux in mg m^{-2} s^{-1} is converted to the absolute mass of emitted dust by multiplication with the grid point area (A) in square meters and the number of seconds between two output time steps (i.e., 18 000 s = 5 hours). There is no information about the vertical distribution of freshly emitted dust to the model levels inside the boundary layer. Therefore, this procedure is done only once at each grid point where trajectories start, namely for the level k_{min}, where the lowermost trajectory is initialised that crosses 30°W. In Fig. 4.13 k_{min} is k_2, as the trajectory from the lowest level k_1 does not cross 30°W. For each grid point, i.e., $i \in (-180°W, +180°W)$ and $j \in (-90°N, +90°N)$, ΔDU is calculated for each season according to the following equation.

$$\Delta DU_{i,j,X} = \sum_{\text{Traj.}\in X} \begin{cases} (DEF_{t_x} - DDF_{t_x}) \cdot A_{i,j} \cdot 18\,000 & \text{, if } x = 1 \\ \left(DU_{t_x} - DU_{t_{x-1}}\right) \cdot m_T & \text{, if } x > 1 \end{cases} \tag{4.9}$$

$$\text{and if } lon_{t_x},\ lat_{t_x} \in GP_{i,j} \text{ (both cases)}$$

X denotes the season. For the correct positioning, the condition that the longitude (lon) and the latitude (lat) of the trajectory are located within the grid point $GP_{i,j}$

has to be fulfilled in both cases. With this method it is possible to obtain the net dust emission in kg per hectare and season from the Eulerian and the Lagrangian data, which is shown in Fig. 4.14.

First of all, due to the selection criteria for the trajectories, there are differences between the Eulerian and Lagrangian results in dust emission regions where no or only few trajectories pass, e.g., in Central Asia or South Africa. The focus, however, is on North Africa, the adjacent Atlantic Ocean, the northern part of South America, and the Caribbean. In these regions many Eulerian features are well represented by the trajectories. The horizontal distributions and absolute values of the Eulerian and Lagrangian data agree very well. The seasonal cycle is visible in both data sets, with dust reaching the southern part of the Amazon Basin south of the equator in DJF (Figs. 4.14a,b) and MAM (Figs. 4.14c,d) and the more zonal transport to the Caribbean in JJA (Figs. 4.14e,f) and SON (Figs. 4.14g,h). Also smaller scale features are comparable, like two "emission holes" in the central Sahara around 25°N, 5°E and 20°N, 15°E, which are best visible in JJA. These "holes" with negative net dust emission correspond to the Hoggar and the Tibesti Mountains where the soil conditions inhibit dust emission and dust from the surrounding source regions is deposited. The highest negative values are downstream of and fairly close to the prominent dust emission regions, showing the fast settling of large particles shortly after the emission. In all seasons the Lagrangian method slightly overestimates the dust deposition southwest of the Mali/Mauritania emission region. This indicates that dust, removed from the trajectories in this region, is gained by other air masses and transported further, which is not captured by the Lagrangian method. The distribution and absolute values of the dust emission at the Bodélé Depression and the deposition downstream coincide very well in the Eulerian and Lagrangian data. In DJF, MAM, and SON the dust is mainly transported to the south and southwest. In JJA the ITCZ is positioned north of the Bodélé Depression and dust emitted there is transported northwards to the Tibesti Mountains, causing the strong negative values there (Figs. 4.14e,f).

The Lagrangian westward zonal dust fluxes are higher than the Eulerian fluxes at 10 and 20°W, while they amount to only 40 to 50% of the Eulerian values at 50 and 60°W (Table 4.2). This underestimation of the Lagrangian dust transport to the Americas is also visible in the net dust emission fluxes in the Amazon Basin and the Caribbean. In addition to the numbers of trajectories reaching CAR and AMA, Table 4.3 lists the values of the dust deposition fluxes in these regions, derived with the different approaches.

The annual Lagrangian dust deposition represents 40% of the Eulerian deposition in the Caribbean and 38% in the Amazon Basin, which is consistent with the differences in the zonal dust fluxes between the two approaches (Table 4.2). The strongest relative difference occurs in the transport to the Caribbean during SON, when only

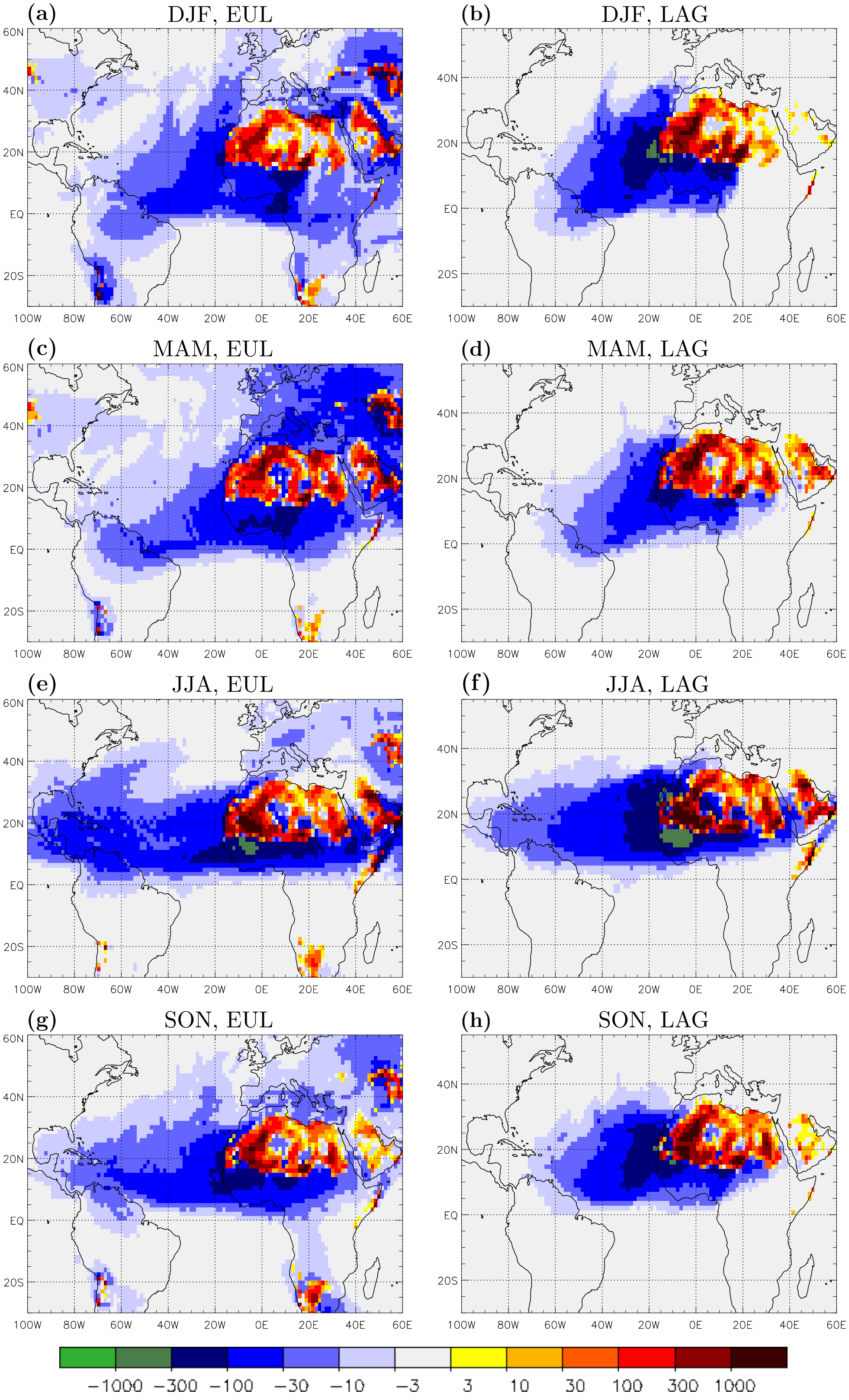

Fig. 4.14: Dust emission minus dust deposition in kg ha^{-1} per season from Eulerian data (left column) and Lagrangian data (ΔDU according to Eq. (4.9), right column) for DJF, MAM, JJA, and SON (from top to bottom).

	total #	CAR EUL	 LAG	 #	AMA EUL	 LAG	 #
DJF	152 357	1.8	0.7	21 556	8.9	4.9	100 387
MAM	102 534	2.1	0.9	20 437	9.1	2.8	54 355
JJA	257 403	21.1	10.0	140 809	8.5	2.4	64 973
SON	143 331	9.3	2.2	47 009	3.8	1.3	47 092
$\sum$	655 625	34.3	13.8	229 847	30.3	11.4	266 807

Table 4.3: Number of trajectories initialised and reaching CAR and AMA. The values in the EUL and LAG columns give the amount of dust in Tg that is deposited in the respective region and season, depending on the method.

24% of the Eulerian deposition is represented by the trajectories. The transport to the Amazon Basin in DJF is captured best; the Lagrangian deposition accounts for 55% of the Eulerian value then.

From the numbers of trajectories in Table 4.3, it is obvious that JJA is by far the most active season with regard to the transatlantic dust transport. About twice as many trajectories are initialised than in the other seasons. 55% of them reach the Caribbean and contribute 72% to the annual Lagrangian deposition in this region. During DJF 66% of the trajectories reach the Amazon Basin but they transport only 43% of the annual dust. MAM and JJA add another 20 to 25% each. Notice that the Amazon Basin extends to 10°N and that the dust is transported to the part north of the equator during NH-summer (Figs. 4.14e,f). Restricting the Amazon Basin to the part south of the equator – as in sections 4.3 and 4.4 – again generates a more distinct seasonality. The dust is not able to cross the ITCZ, either because it is not transported there but further north to the Caribbean or because it is washed out from the atmosphere due to the convective precipitation within the ITCZ. This leads to very low dust deposition in the southern part of the Amazon Basin during the second half of the year (Figs. 4.14e,f and g,h).

4.6 Source regions of dust reaching the Americas

Trapp et al. (2010) analysed the elemental composition of dust samples collected at Barbados and Miami over the NH-summers of 2003 and 2004 but they were not able to conclude on the source regions of the measured dust. Some studies, e.g., by Koren et al. (2006) or Tegen et al. (2006), assign a huge part of the dust reaching the Amazon Basin during NH-winter to emissions from the Bodélé Depression. Nevertheless, exact connections between African emission regions and the Americas do not exist.

In this section trajectories are exploited to identify the source regions of dust reaching the Americas. They are calculated in the following way: The loss of dust along the

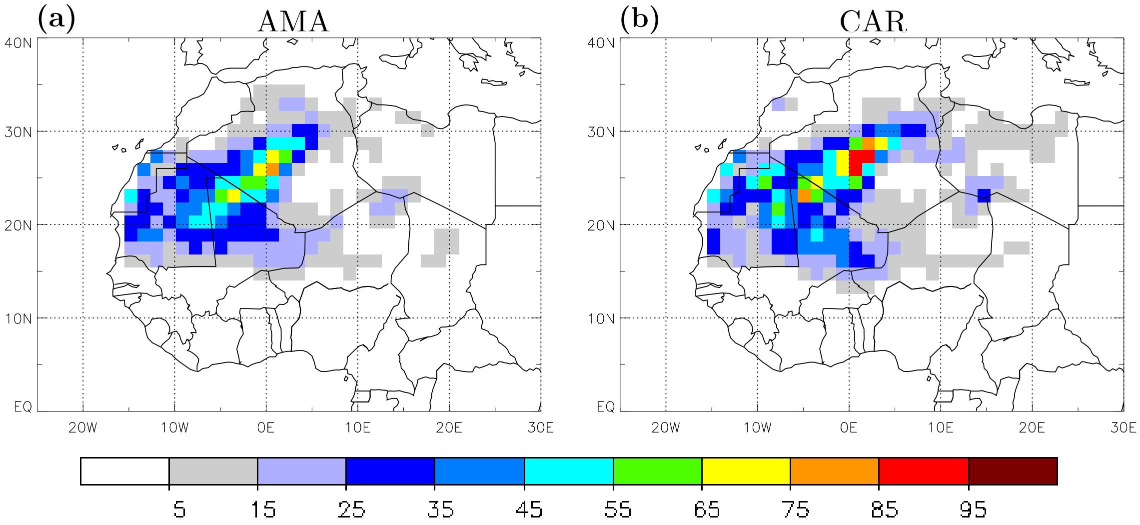

Fig. 4.15: Source regions of dust reaching the Americas. The amount of dust that one trajectory transports to AMA (a) and CAR (b) contributes to the field shown here at the grid points where the trajectories start. The unit is kg ha^{-1} yr^{-1}. See text for further details.

trajectories ΔDU is computed as described in section 4.5.4. For each trajectory time step t_x when the trajectory is inside one of the target regions, $\Delta DU(t_x)$ is added to the grid box where the trajectory starts. This is done separately for the Amazon Basin and the Caribbean. The sum over all trajectories of the fields derived in this way is shown in Fig. 4.15. Integrating over North Africa results in the values given in Table 4.3, i.e., 11.4 Tg yr^{-1} in AMA (Fig. 4.15a) and 13.8 Tg yr^{-1} in CAR (Fig. 4.15b). Keeping in mind that these Lagrangian values represent only about 40% of the Eulerian results (30.3 Tg yr^{-1} in AMA and 34.3 Tg yr^{-1} in CAR, see Table 4.3) in the respective regions, the dust deposition fluxes of the T85TG time slice simulation in these regions are on the same order of magnitude as earlier values in literature (Kaufman et al. (2005): 50 ± 15 Tg yr^{-1} in AMA, 50 ± 25 Tg yr^{-1} in CAR; Koren et al. (2006): 40 Tg yr^{-1} in AMA).

For both target regions the main area where trajectories start is limited to the dust source regions in Mali, Mauritania, and Algeria. Dust reaching the Amazon Basin mainly originates from a belt, stretching from Central Algeria at 30°N, 5°E to the eastern part of Mauritania at 20°N, 10°W. Most of the dust reaching the Caribbean is also emitted from the central and southwestern part of Algeria. The northern and eastern part of Mauritania and North Mali contribute a lot to the Caribbean dust as well.

It is remarkable that trajectories starting over the Bodélé Depression (around 16°N, 18°E) do not directly contribute to the dust transport to the Americas, which is in contradiction to earlier studies: Considering that the Bodélé Depression is the most active Saharan dust source region in DJF and with regard to the wind regimes, Schepanski et al. (2009) found the preconditions for long-range transport to South America to be best during the NH-winter season. Tegen et al. (2006) concluded from global model results for the year 1987 that "dust from the Bodélé Depression may play an important role for fertilizing the Amazon rain forest", and finally, based on satellite data and results of Kaufman et al. (2005), Koren et al. (2006) estimated that more than 50% of the annually deposited dust in the Amazon rain forest originate from the Bodélé Depression between November and March. Their approach is completely different from the method presented here. They estimated the mass column concentration for Saharan dust from MODIS and MISR (Multi-angle Imaging SpectroRadiometer) optical depth. Further assumptions to separate dust from marine aerosol and smoke were required to calculate the dust flux over the Atlantic Ocean. The transatlantic transport was then computed by applying westward reanalysis winds to the dust concentration (Koren et al. 2006).

In addition to the very different methodologies, the discrepancies between the current and prior studies listed above might be accounted for by a restriction of the approach presented here to identify the source regions for transatlantic dust transport. Namely, dust, emitted at one place, can be gained by trajectories starting at another place. This way, some source regions, e.g., the Bodélé Depression, could be obscured because dust emitted there can indeed be transported to the Americas, but by trajectories starting from different places. This, however, can be ruled out for the dust from the Bodélé Depression with a look at Fig. 4.16. It shows the number density of trajectories that are started from the Bodélé Depression (14–18°N, 16–20°E) and their net dust emission (as described in section 4.5.4). In NH-winter, when most of the dust that reaches the Amazon Basin is transported there, the Bodélé Depression trajectories travel southwestwards until they arrive at the Gulf of Guinea, from where they move further to the west (Fig. 4.16a). They have lost most of their dust on the way to the coast (Fig. 4.16c). If this dust were gained by other trajectories and carried across the Atlantic Ocean, many of the dusty trajectories crossing 30°W would have to pass the region southwest of the Bodélé Depression. The main pathway of the dusty trajectories, however, is located much further northwest (Fig. 4.8). In JJA the trajectories travel from the Bodélé Depression in all directions but mainly to the west and lose most of their dust within a radius of about 15° ($\cong$ 1 650 km) (Figs. 4.16b,d). A large portion of them contribute to the transatlantic transport and gain dust from the emission regions in Mali and Mauritania, which becomes obvious by the positive values in Fig. 4.16d over these countries.

This first objectively determined, Lagrangian connection between North African dust source regions and the Americas illustrates the importance of West African emission regions for the transatlantic transport of Saharan dust.

In the following, the contribution of dust emissions from the Bodélé Depression in Chad to the deposition in the Amazon Basin is analysed further. The averaged

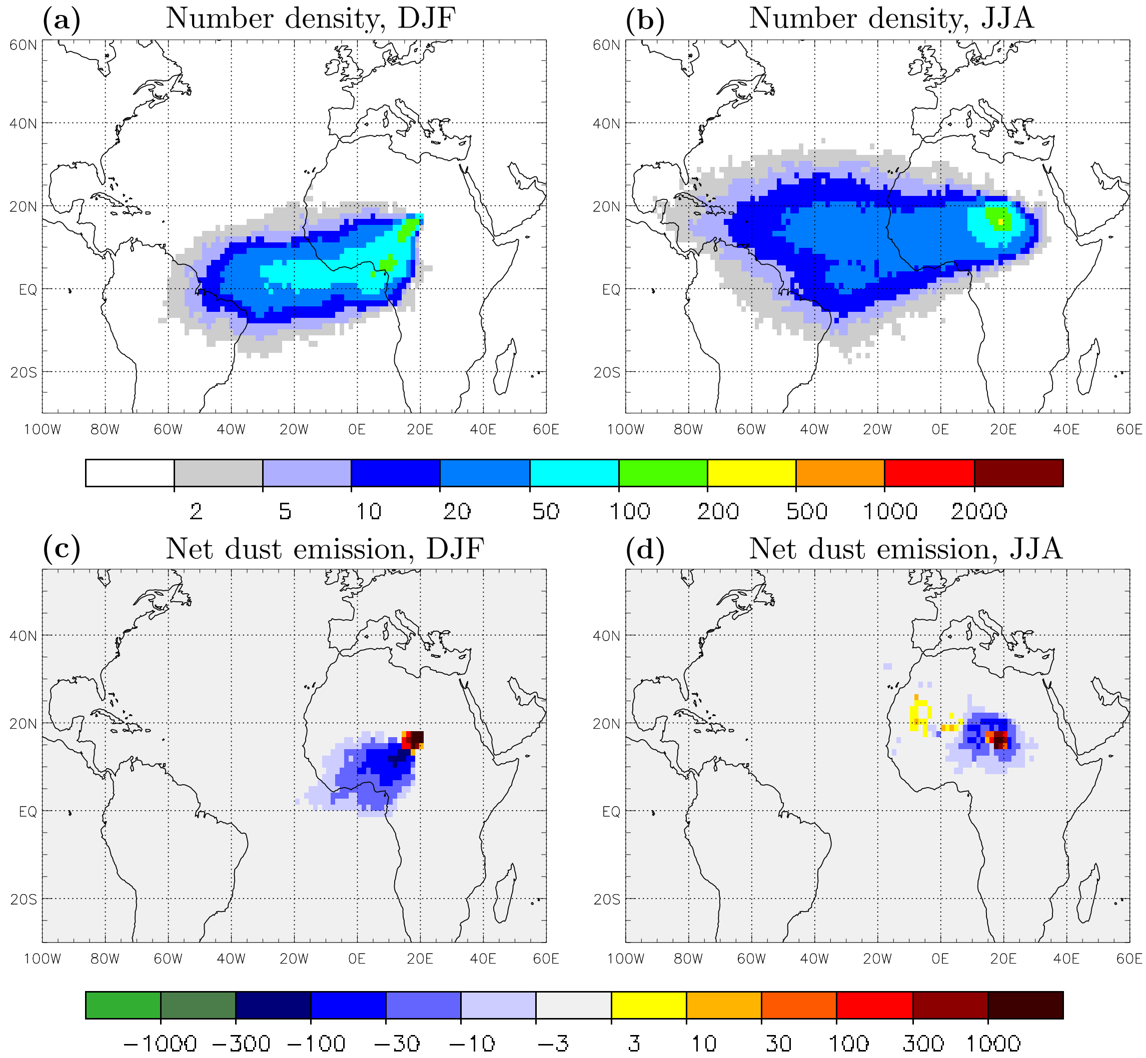

Fig. 4.16: Seasonal averaged number density (# per 10^4 km^2 per season) of trajectories initialised at the Bodélé Depression – (a) DJF, (b) JJA – and their net dust emission in kg ha^{-1} per season – (c) DJF, (d) JJA.

trajectory pathways in JJA, weighted with the reciprocal of the dust mixing ratio at 30°W (Fig. 4.8c), start in Chad while the dusty trajectories are initialised in the southwestern or central part of Algeria in each season. This is another hint that dust from the Bodélé Depression does only have a little share of the entire transport. Also the following Eulerian analysis supports this: The correlation of the dust emission time series from the Bodélé Depression and the time-lagged time series of the dust transport across 30°W is calculated - as described in the discussion of Fig. 4.4. This correlation does not indicate a physical relationship of these time series. The correlation coefficients vary around zero, occasionally and only in single seasons exceeding values of 0.2 (not shown).

Altogether, the robustness of the finding that the Bodélé Depression does not contribute a lot to the transatlantic dust transport is corroborated by very different methodological approaches. The main source regions of dust reaching the Caribbean and the Amazon rain forest are found to be the deserts in central and Southwest Algeria, Mauritania, and Mali.

4.7 Summary

The results in this chapter are based on two different methodologies, namely Eulerian and Lagrangian approaches. Eulerian results capture all physical processes (and potential numerical artifacts) that are included in the EMAC model and are based on the complete model output of the time slice simulation. The calculation and selection of trajectories from this model output allows for a complementary, more specific insight. The chosen trajectories, however, are not able to capture all processes that occur in the model. For instance, if dust is removed from one air parcel at one place, it is not necessarily deposited there (as assumed by the Lagrangian approach) but might be transported further by another air parcel that is not described by the chosen trajectories. This leads to differences between Eulerian and Lagrangian results, when looking at the deposition fluxes in the Amazon Basin and the Caribbean, for example. However, various comparisons of the two methods, such as the vertical distribution of the zonal dust flux, illustrate that the mean characteristics of the trajectories are representative for the complete dust cycle from the emission in North Africa, over the transatlantic transport, to the deposition in the Americas.

The shown results of the T85TG five-year time slice simulation reveal an episodic character of the transatlantic transport of dust with the maximum activity during NH-summer. The seasonality of the horizontal distribution of the transport is clearly visible. Following the annual cycle of the trade winds, the dust is transported to the Amazon Basin in South America mainly during DJF and to the Caribbean in NH-summer. MAM and SON show transitional characteristics, where MAM is closer to the DJF properties and SON is more related to JJA. Wet removal contributes most to the deposition of dust, as the main arrival seasons, i.e., DJF for the southern part of the Amazon Basin and JJA for the Caribbean, coincide with the rainy seasons in the respective region. The transport time that the dust needs from the source regions in North Africa across the Atlantic Ocean is on the order of 9 to 11 days. The transport to the Amazon Basin during NH-winter takes about one day less than the transport to the Caribbean in NH-summer.

The vertical distribution of the dust transport emphasises the strong seasonal cycle. In DJF the dust stays at low levels during the entire transatlantic transport, occasionally reaching heights above 800 hPa. In JJA the advection of denser air of the WAM from the south causes the lifting of dust-laden Saharan air. The resulting SAL then crosses the Atlantic Ocean at higher altitudes. At 50°W the maximum dust concentrations are still between 600 and 900 hPa. Closer to the source regions a certain amount of dust reaches levels even above 500 hPa. MAM and SON again show transitional characteristics.

The contribution of the different dust source regions in North Africa to the dust deposition in the Amazon Basin and the Caribbean is quantified with the Lagrangian data. In contrast to earlier publications (e.g., Kaufman et al., 2005, Koren et al., 2006, and Tegen et al., 2006), the Bodélé Depression in Chad is not found to make a major contribution to the dust that is deposited in South and Central America. Instead, the deserts in central and Southwest Algeria, Mauritania, and Mali are the main source regions of the dust that travels across the Atlantic Ocean and gets deposited in the Amazon Basin and the Caribbean. This systematic difference between the present and earlier studies suggests future improvements of the Lagrangian methods. One possibility is to refine the trajectory initialisation. If the removal of dust from one air parcel is higher than the deposition flux at the surface, the temporal evolution of the dust in surrounding grid boxes could be analysed. From grid boxes that gained dust, newly initialised forward trajectories can trace this dust further. Time slice simulations of a model system with a Lagrangian core might also offer a solution for this problem. Here, the question about the contribution of dust from the Bodélé Depression to the transatlantic transport cannot be finally clarified.

5

The mineral dust cycle during the Little Ice Age

5.1 Introduction

Several reconstructions and simulations of the climate of the past yield in parts quite different results. For the last millennium, for example, the range of global or northern hemispheric temperature before 1900 varies on the order of 0.5 to 1 K (Hegerl et al. 2006, Jungclaus et al. 2010, Christiansen and Ljungqvist 2012). Factors influencing the global climate, as the solar and volcanic forcing, are not yet fully understood (Gerber et al. 2003, Crowley et al. 2008). The impact of these parameters on atmospheric CO_2 concentrations, the feedback of the carbon cycle on the climate system and especially their role in generating the Medieval Warm Period (ca. 900–1250) and the LIA (ca. 1500–1850) are part of current research (e.g., Jungclaus et al. 2010). Better understanding of these mechanisms in the past is necessary to improve model systems for future climate projections.

In addition to the mentioned forcing factors (solar, volcanic, greenhouse gases), mineral dust influences the global climate. However, its direct and indirect impacts on the climate system are also fraught with uncertainty (IPCC, 2007). In order to improve understanding of the role of mineral dust in the climate system, it is essential to know about the characteristics of the dust cycle in different climate epochs. Reconstructions of the LGM (about 20 000 BP), revealed substantial differences in the mean dust emissions, concentrations, and deposition fluxes compared to recent climate. For instance, simulations by Mahowald et al. (1999) found a global dust load during the LGM that was 2.5 times higher than under present day conditions. The focus of this study is on a more recent and less intense cold anomaly, the LIA, which was the coldest period during the last millennium. The mean global temperature was about 0.5 to 1 K lower than today (Hegerl et al. 2006, Christiansen and Ljungqvist 2012). The temporal definition of the LIA is difficult and varies between the second half of the 13th century for the initiation and the end of the 19th century for the termination of this cold period (Grove 2001, Wang et al. 2006, Sirocko 2009, Jungclaus et al. 2010).

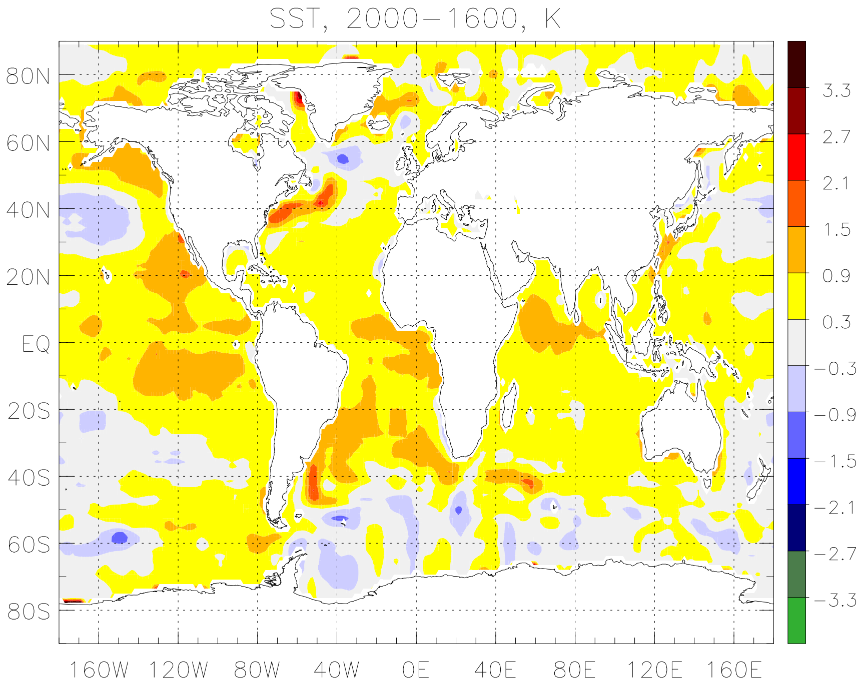

Fig. 5.1: Difference of the SST of the simulation in the recent climate minus the SST used in the simulation during the LIA, i.e., conditions for the year 2000 minus those for 1600.

The LIA was a time with extreme weather conditions in Europe, where winters were often extraordinary long and cold. However, there were strong climatic variations and besides cold and wet summers, there were also periods with unusually hot years (Sirocko 2009). The mean temperature in Europe was about 2 K below present day values (Sirocko 2009). The cooling was observed over the entire globe, but its intensity regionally varied. Figure 5.1 shows the difference of the SST used for the time slice simulation in the recent climate minus the SST for the LIA simulation. The global average of this difference amounts to 0.5 K. In places it reaches values of more than 2 K, e.g., east of North America around 40°N, and even 3 K in the Baffin Bay west of Greenland. On the other hand, there are also spots with negative values, indicating a warmer SST during the LIA, e.g., south of Greenland or in the South Atlantic Ocean.

In this chapter the simulation of the mineral dust cycle under LIA conditions is analysed. The therefore adapted parameters, e.g., the SST, and the entire model setup are specified in section 5.2. The performance of the model and the comparison with the simulation in the recent climate are then presented in section 5.3. Section 5.4 contains the summary.

5.2 Methodology

To adapt a climate model for another climate epoch, the forcing factors of the model have to be adjusted. These forcings are the boundary conditions of the model that change with time, namely SST, sea ice concentration (SIC), greenhouse gas (GHG) concentrations, volcanic aerosols, solar irradiance, ozone concentration, and land surface parameters. Reconstructions of these parameters for the LIA were provided from the Millennium project (Jonas Bhend, personal communication 2011, 2012, Jungclaus et al. 2010).

One problem with such extensive changes in the model setup is to assign the simulated differences to the responsible forcing factor(s). Therefore, the adaption of the model should be on the one hand as limited as possible, on the other hand large enough to reproduce the climatic conditions of the LIA. According to this approach, the land surface parameters are not changed for simulations during the LIA presented here. Hence, potential differences in the dust emissions can be ascribed to climatic changes enforced by the forcing factors listed above. If the surface parameters were changed as well, one could not conclude whether different dust emissions are caused by the global dynamics or by locally varied surface conditions.

5.2.1 Forcing factors for LIA simulations

The differences in the SST are depicted in Fig. 5.1 and described in the previous section. The SIC is adapted such that the ice covered parts of the oceans reach further south in the North Atlantic Ocean and somewhat further north in the oceans around Antarctica (Jonas Bhend, personal communication, 2011, not shown).

The GHG concentrations are fixed in all simulations. For the LIA, they are reduced to pre-industrial values. Compared to the present day simulations, the individual components are changed as follows: CO_2 from 348 to 276 ppmv, CH_4 from 1.65 to 0.69 ppmv, and N_2O from 306 to 269 ppbv. The concentrations of chlorofluorocarbons are set to zero.

Finally, the impact of volcanic stratospheric aerosol on the radiation budget is adapted. For this purpose, the optical thickness of the volcanic background is changed according to the reconstructions of past volcanic activity of Crowley et al. (2008), which was on average higher during the LIA than in the recent climate (Jonas Bhend, personal communication, 2011). This change is implemented as time-invariant, higher optical thickness in the LIA simulations, meaning that the long-term impact is considered, while episodic volcanic eruptions are not represented.

The other abovementioned boundary conditions are unchanged, so that all differences between the LIA and the recent simulations can be traced back to the combined effect of the variations of SST, SIC, GHG concentrations, and volcanic aerosol.

5.2.2 Setup of LIA simulations

The changes in the model setup compared to the present day simulation, described in the previous section, call for the investigation of the spin up and stability of simulations during the LIA. For this purpose, a five-year time slice simulation without chemistry is performed, called LIA_dyn from now on.

To compare the mineral dust cycle during the LIA with recent conditions, the chemistry has to be switched on in the LIA simulation after the 5-year spin up period. Therefore, the emissions of chemical species, required for the chemical setup, described in section 2, have to be adapted. These changes mainly consist in setting the emissions, e.g., biogenic and biomass burning emissions, to pre-industrial values (Andrea Pozzer, personal communication, 2011).

After the spin up of the LIA_dyn simulation, the output of LIA_dyn is used to initialise the five-year time slice simulation with chemistry, called LIA_chem in the following. The boundary conditions, as the SST, are identical for LIA_chem and for LIA_dyn. LIA_chem can then be compared with the T85TG simulation in the recent climate, hereafter denoted as REC_chem. For reasons of clarity, the simulations discussed in this chapter and their main characteristics are summarised here.

LIA_dyn	Five-year simulation without chemistry during the LIA for the dynamical spin up of the model.
LIA_chem	Five-year simulation with chemistry during the LIA, initialised from the final state of LIA_dyn.
REC_chem	Five-year simulation with chemistry in the recent climate, identical to T85TG (see chapters 3 and 4).

5.3 Results

The investigation of the dynamical behaviour of the model with the boundary conditions of the LIA is presented in section 5.3.1. Afterwards, the simulation with chemistry during the LIA is evaluated in section 5.3.2 and the results for the LIA are compared with the simulation in the recent climate. The focus of this comparison lies on the processes within the so called “dust belt” in section 5.3.3 and on the transatlantic transport in section 5.3.4.

5.3.1 Model spin up during the LIA (LIA_dyn – without chemistry)

The parameters used to evaluate the simulation with regard to the spin up and the stability are temperature on the lowest model layer, 10-m wind speed and soil moisture. The temperature is very important because many reconstructions of the climate of the past focus on this parameter. The other two parameters are considered because they control the mineral dust emissions. Different regions are investigated. Global averages and the mean over all land grid points give information about the overall behaviour of the model. Of special interest are the dust source regions, i.e., all grid points that potentially emit dust (abbreviated with EmiGP in the figures), and the grid points in the Sahara.

Figure 5.2 illustrates the temporal evolution of temperature on the lowest model layer during the five years of the LIA_dyn simulation. Due to the constant SST-forcing over the five years, the global near-surface temperature, which is dominated by the SST, is expected to have no long spin up and to vary only little from year to year. The simulation shows that the global annual mean temperature practically does not change during the five years and that the annual cycle is fairly constant. The annual mean values do not deviate more than 0.05 K from the five-year average. To gain insight into the impact of the implemented changes on the land surface, which is not directly controlled by the prescribed SST, the temperature on the lowest model layer averaged over all land grid point is shown in red in Fig. 5.2. About two-third of the land surface are in the northern hemisphere. Due to this hemispheric bias, the annual cycle of the land surface temperature has a stronger amplitude than the global average. There is also no trend in the annual mean temperature over land and single annual means do not deviate more than 0.15 K from each other. The behaviour in the dust source regions is very similar. Averaged over all grid points that potentially emit dust (EmiGP: orange in Fig. 5.2), and only those in the Sahara (blue in Fig. 5.2) the simulation produces stable conditions from the first year on. The smaller the considered regions, the larger is the interannual variation. The annual averages vary in a range of 0.39 K (0.45 K) for all dust emission grid points (grid points in the Sahara). In the Sahara some interannual variations of single seasons can be seen; e.g., the NH-winter between the first and the second year of the simulation is more than 1 K warmer than the following one.

The same analysis of the 10-m wind speed in these regions, i.e., global, land surface, dust source regions, and Sahara, yield similar results (see Fig. 5.3). There are some years with slightly higher or lower mean wind velocities than the five-year average but the time series contain no trend in any of the regions.

Somewhat differently behaves the soil moisture, as shown for the entire land surface, the dust source regions, and the Sahara in Fig. 5.4. The soil moisture is not defined over water. Thus, the average over the land surface yields the same results as the global mean, which is therefore not shown here. The annual mean of the first year over all land grid points is lower than the five-year average. The last four annual means are slightly larger. In the dust source regions and the Sahara there is an opposite temporal evolution. This indicates that the soil moisture was initialised too low, with respect to the entire land surface, and somewhat too high at the dust emitting grid points. The soil moisture is one of the parameters that requires

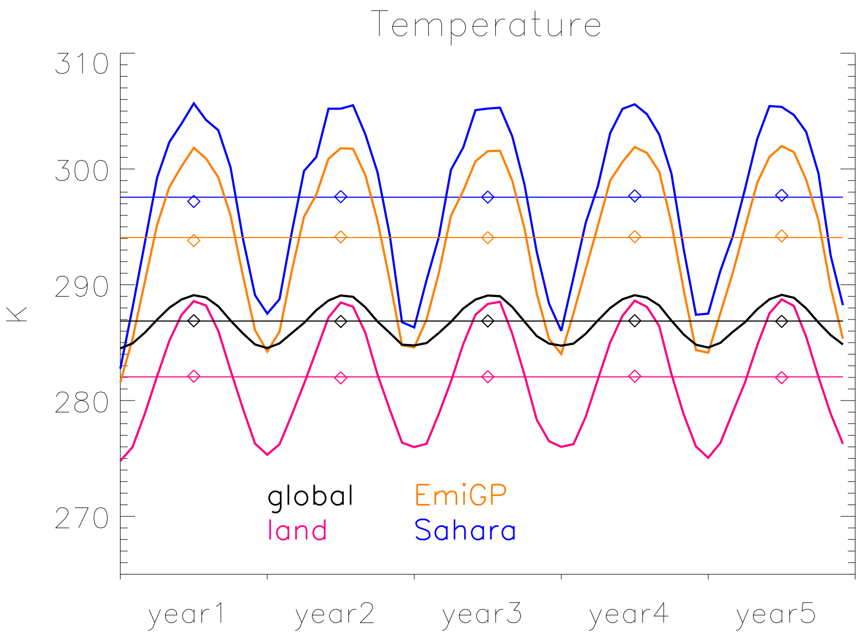

Fig. 5.2: Five-year time series of monthly mean temperature on the lowest model layer of the time slice simulation LIA_dyn without chemistry. Diamonds illustrate annual means and horizontal lines the five-year average. Results are shown for the entire globe (black), land grid points (red), the dust emitting grid points (orange), and the Sahara (blue). year1 to year5 denote the respective year of the simulation.

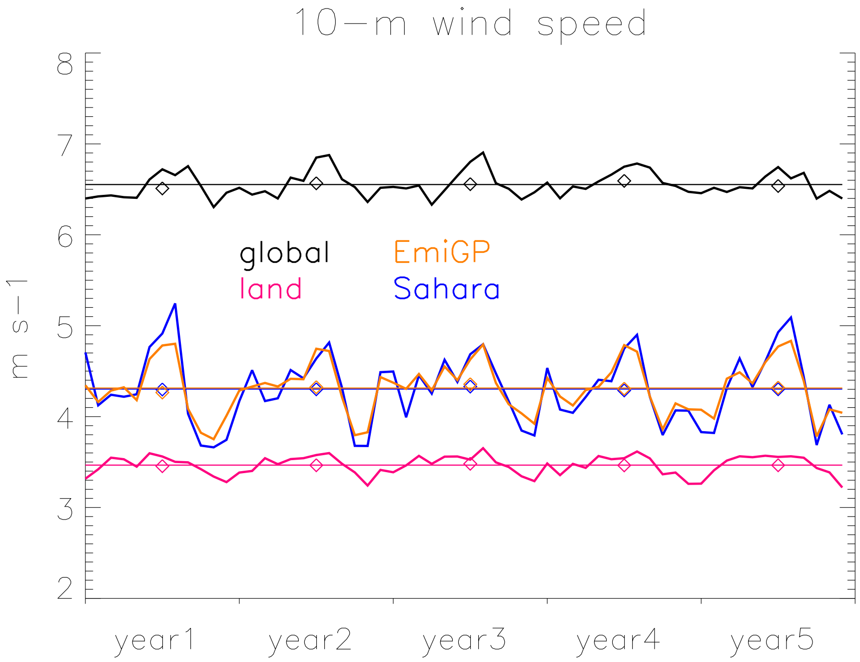

Fig. 5.3: Five-year time series of monthly mean 10-m wind speed of the time slice simulation LIA_dyn without chemistry. Diamonds illustrate annual means and horizontal lines the five-year average. Results are shown for the entire globe (black), land grid points (red), the dust emitting grid points (orange), and the Sahara (blue). year1 to year5 denote the respective year of the simulation.

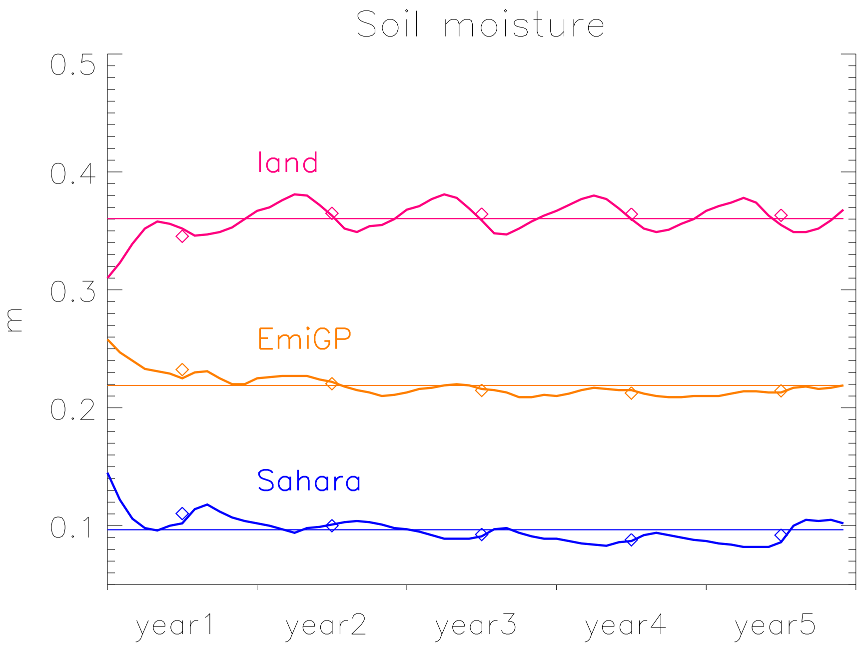

Fig. 5.4: Five-year time series of monthly mean soil moisture of the time slice simulation LIA_dyn without chemistry. Diamonds illustrate annual means and horizontal lines the five-year average. Results are shown for the entire globe (black), land grid points (red), the dust emitting grid points (orange), and the Sahara (blue). year1 to year5 denote the respective year of the simulation.

the longest time to spin up and the model takes one to two years to reach stable conditions with regard to this parameter.

5.3.2 Model evaluation (LIA_chem – with chemistry)

The analyses in the previous section revealed that the spin up of the model takes less than two years. The model output at the end of the five-year LIA_dyn simulation can therefore be used for the initiation of the LIA_chem simulation.

Many reconstructions of the climate of the past focus on surface temperature, which is chosen for a first evaluation of the LIA_chem simulation. To reduce the impact of the prescribed SST, the mean temperature on the lowest model layer is investigated. Because of the systematic difference between the temperature at the surface and on the lowest model layer, not the absolute values, but the temperature difference of the recent climate minus the LIA are compared.

The difference in the surface temperature between the recent climate and conditions about 400 years ago depends on the examined region. On the global scale, Frank et al. (2010) and Jungclaus et al. (2010) found a cooling during the LIA between 0.3 and 1.0 K compared to the recent climate. Gerber et al. (2003) summarised several reconstructions, yielding differences for the temperature in the northern hemisphere between 0.4 and 1.1 K. Further regionalisation reveals a cooling during the LIA of

	$T_{\mathrm{REC\_chem}}$, K	T_{LIA}, K		ΔT, K
		$T_{\mathrm{LIA\_chem}}$	$T_{\mathrm{LIA\_dyn}}$	
global	287.56	286.89	286.88	0.67
NH	288.48	287.71	287.75	0.77
NH, land only	284.45	283.55	283.63	0.90
30°–70°N, land only	278.10	277.20	277.28	0.90

Table 5.1: Annual mean temperature on the lowest model layer of the time slice simulations with chemistry during the recent climate ($T_{\mathrm{REC\_chem}}$) and the LIA ($T_{\mathrm{LIA\_chem}}$) and the difference thereof ($\Delta T = T_{\mathrm{REC\_chem}} - T_{\mathrm{LIA\_chem}}$). Also listed are the results of the LIA_dyn simulation.

about 0.75 K for the land surface in the northern hemisphere (Hegerl et al. 2006) and of circa 1.0 K for the land surface between 30°N and 70°N (Cook et al. 2004).

Table 5.1 lists the mean temperature on the lowest model layer of the simulations REC_chem, LIA_chem, the difference thereof, and the results of LIA_dyn. Depending on the considered region, the model produces a cooling during the LIA in the range of 0.67 to 0.90 K. The values of the global and the northern hemispheric cooling lie within the range of the aforementioned reconstructions. As the values of Hegerl et al. (2006) and Cook et al. (2004) do contain a considerable, but not exactly quantifiable, uncertainty range as well, the here simulated temperature decrease amounts to realistic values.

The differences between the LIA_chem and the LIA_dyn simulations are more than one order of magnitude smaller than the differences between LIA_chem and REC_chem. The slightly different results of the two simulations during the LIA are mainly caused by the different initialisations. Both represent five-year time slices for the year 1600, but LIA_chem is initialised with the meteorological conditions at the end of the LIA_dyn simulation. The small differences of less than 0.1 K show the impact of the initial conditions for these simulations. Longer time slices would reduce the differences further.

Figures 5.5 to 5.7 illustrate the seasonal cycle of various parameters of the REC_chem and the LIA_chem simulations. As in section 5.3.1, four different regions are considered, namely the entire globe, the land surface, the dust source regions, and the Sahara. Annual mean values and the differences between the two climate epochs are summarised in Table 5.2. The temperature on the lowest model layer (Fig. 5.5) shows the expected seasonal cycle in all regions. While on the global scale and over the entire land mass the differences between the two simulations are nearly constant over the whole year, the cooling in the LIA at the dust emitting grid points and in the Sahara is stronger during the NH-summer months than in the rest of the year.

The global mean 10-m wind speed (Fig. 5.6) amounts to about 6.5 m s^{-1} on average in both simulations, with a small maximum during NH-summer and slightly lower values during the rest of the year. The differences between REC_chem and LIA_chem

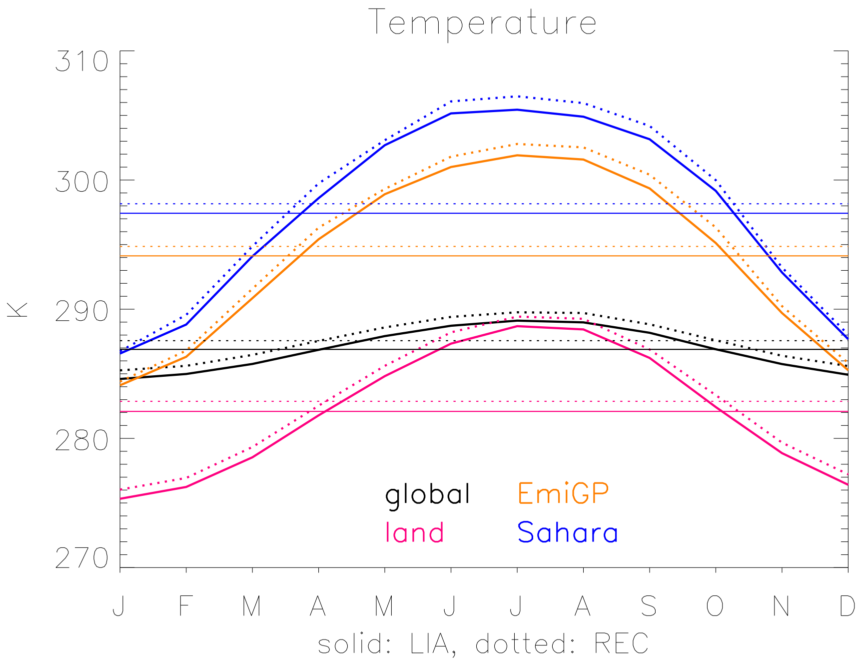

Fig. 5.5: Annual cycle of the temperature on the lowest model layer during the LIA (solid lines) and the recent climate (dotted lines). Horizontal lines give the annual mean values. Results are shown for the entire globe (black), land grid points (red), the dust emitting grid points (orange), and the Sahara (blue).

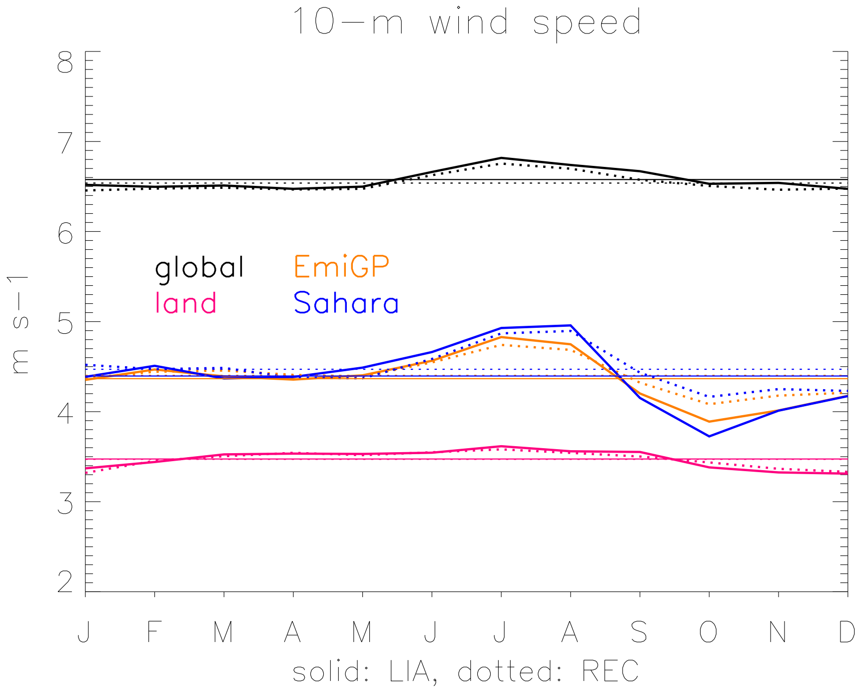

Fig. 5.6: Annual cycle of the 10-m wind speed during the LIA (solid lines) and the recent climate (dotted lines). Horizontal lines give the annual mean values. Results are shown for the entire globe (black), land grid points (red), the dust emitting grid points (orange), and the Sahara (blue).

		REC_chem	LIA_chem	$\Delta_{\text{REC-LIA}}$
T, K	global	287.56	286.89	0.67
	land	282.87	282.09	0.78
	EmiGP	294.86	294.13	0.73
	Sahara	298.16	297.43	0.73
$v_{\text{10-m}}$, m s^{-1}	global	6.54	6.58	-0.04
	land	3.47	3.47	0.00
	EmiGP	4.40	4.37	0.03
	Sahara	4.47	4.40	0.07
RR, kg m^{-2} per day	global	3.04	3.03	0.01
	land	2.62	2.55	0.07
	EmiGP	0.37	0.34	0.03
	Sahara	0.21	0.17	0.04
Dust emission, Tg per month	EmiGP	151.3	150.5	0.8
	Sahara	75.8	76.1	-0.3

Table 5.2: Mean temperature on the lowest model layer (T), 10-m wind speed ($v_{\text{10-m}}$), precipitation (RR), and dust emission in different regions during the recent and the LIA-climate. $\Delta_{\text{REC-LIA}}$ denotes the difference of REC_chem minus LIA_chem.

are marginal. Considering only the land surface yields similar results. At the dust source grid points and in the Sahara the 10-m wind speed is on average slightly higher in the recent climate (see Table 5.2). This difference is mainly caused by higher recent values in NH-autumn. Further regional differences between the simulations will be analysed in detail in the following section. In both simulations the wind speed reaches its maximum in NH-summer and the minimum in NH-autumn.

The precipitation differences between both simulations are negligible at the global scale and on the land surface, and the annual cycles are very weak (Fig. 5.7). The annual mean precipitation in the dust source regions and the Sahara is 10–20% higher in the recent climate. There are two remarkable differences between the two climate epochs: The first one is the maximum in the Sahara in the recent climate in May, which also dominates the precipitation at all dust emission grid points. The five-year time series of the precipitation in the Sahara in Fig. 5.8 shows the absolute maximum of the recent precipitation in May of the first year and local maxima in May of the remaining years. The five-year average is clearly dominated by the first year, suggesting that this is not a systematic difference between the two climate epochs. The second difference in the annual cycle is a shift of the maximum rainfall in the Sahara from August during the LIA to September in the recent climate (Fig. 5.7). These maxima during the second half of the year show the impact of the WAM, which also influences the annual cycle in the dust source regions, where the recent precipitation is higher than during the LIA in September and October. In LIA_chem the NH-summer maximum in the Sahara always occurs in August (Fig. 5.8). In the

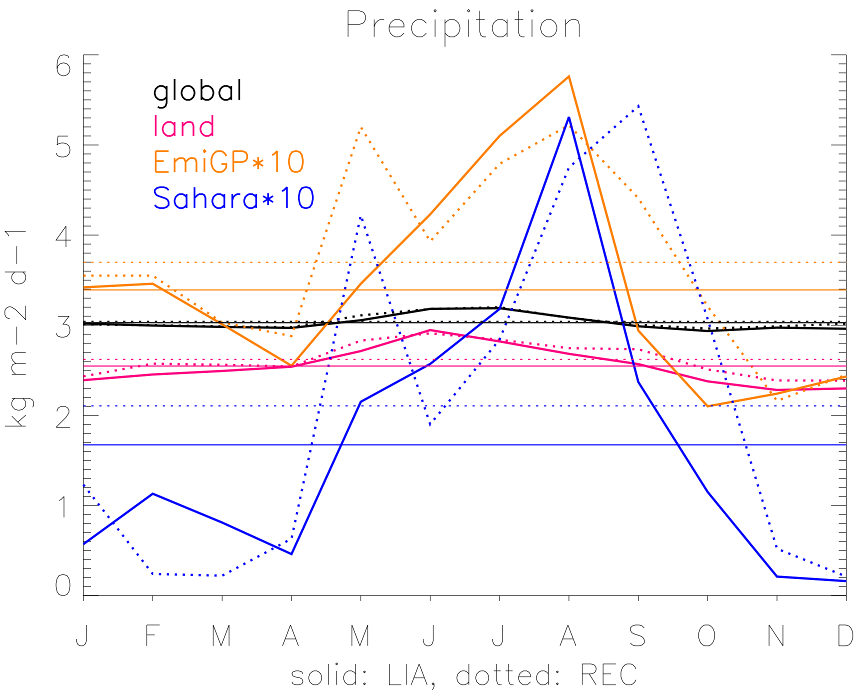

Fig. 5.7: Annual cycle of precipitation during the LIA (solid lines) and the recent climate (dotted lines). Horizontal lines give the annual mean values. Results are shown for the entire globe (black), land grid points (red), the dust emitting grid points (orange), and the Sahara (blue). The latter two are multiplied by a factor of 10.

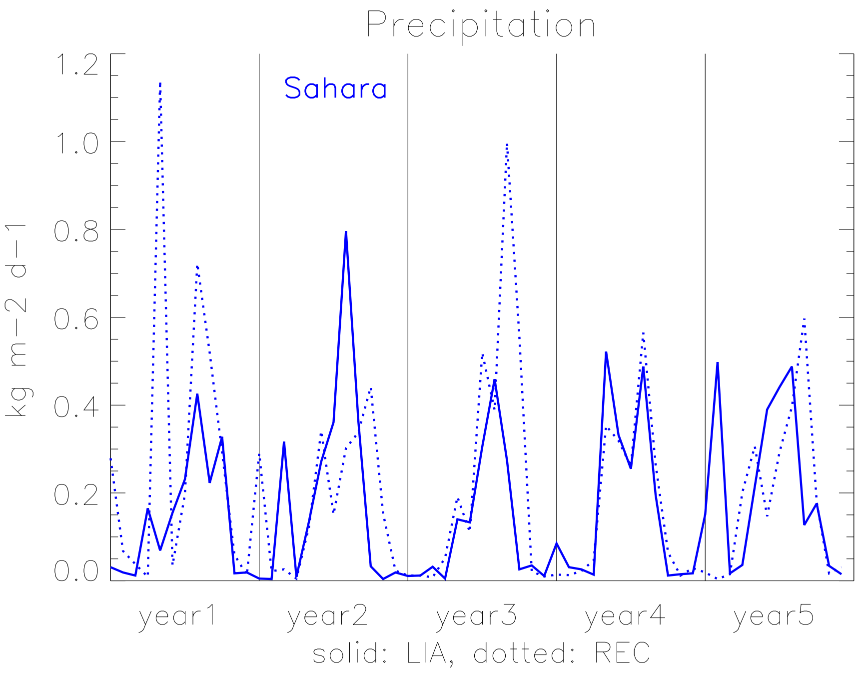

Fig. 5.8: Five-year time series of monthly mean precipitation during the LIA (solid lines) and the recent climate (dotted lines). Results are shown for the Sahara only. year1 to year5 denote the respective year of the simulations.

recent climate only the first and the fourth year have a maximum in August. In the third and fifth year it occurs in September, in the second year even in October. This indicates a systematic difference between REC_chem and LIA_chem with maximum monsoon activity later in the year in the recent climate.

During the LIA annual dust emissions, summed up over all dust emitting grid points and for the Sahara only, are nearly the same as in the recent climate (see Table 5.2). Furthermore, the global dust deposition, the atmospheric burden, and, consequently, the life time of dust differ less than 3% between REC_chem and LIA_chem. Sulphurous species are necessary for the ageing and scavenging of the dust particles (cf. section 2.5 on page 16). The similar life times of dust in both simulations demonstrate that there is still enough sulphuric acid in the atmosphere in the LIA_chem simulation, to transfer dust particles from the insoluble to the soluble modes, although emission and atmospheric load of sulphurous species are reduced by 75% compared to REC_chem.

Figure 5.9 shows that also the annual cycles of the dust emissions are comparable. As for the seasonality of precipitation, there is a shift of the Saharan dust emission peak, which occurs from June to August during the LIA and from July to September in the recent climate. This confirms a later onset of the WAM in the recent climate, compared to the LIA, because the monsoon season is accompanied by strong, dust raising winds (Pye 1987). Especially in the beginning of the WAM-season, when the soil is not yet wetted by monsoon-related precipitation, the dust emission is very effective (Formenti et al. 2011). The annual cycles show that maximum Saharan dust emissions (REC_chem: August, LIA_chem: June) occur one to two months prior to the maxima in precipitation (REC_chem: September, LIA_chem: August – cf. Fig. 5.7 and Fig. 5.9). In single years, however, this can be different. In the first and fourth year of each simulation the NH-summer maxima of Saharan dust emissions occur in August, coinciding with the maxima in precipitation. The month with the maximum dust emissions in LIA_chem is June (Fig. 5.9), which is dominated by the absolute maximum in the second year (Fig. 5.10). In REC_chem the maximum occurs in August of the third year. Also the emissions in August of the first year are fairly high, leading to the maximum in the annual cycle in August. The five-year time series of precipitation and dust emission in the Sahara show very high interannual variability, indicating that the illustrated seasonal cycles are not fully representative for the conditions in individual years in the Sahara.

In both climate epochs the Sahara contributes only about 40% to the global dust emissions in July. In most other months the percentage of Saharan dust emissions is larger than 50%. During NH-summer, especially in July, the dust emissions in the Thar Desert, which are initiated by the Indian Monsoon, dominate the global emissions. The following section provides regional and seasonal investigations of the dust emissions and parameters affecting them in more detail.

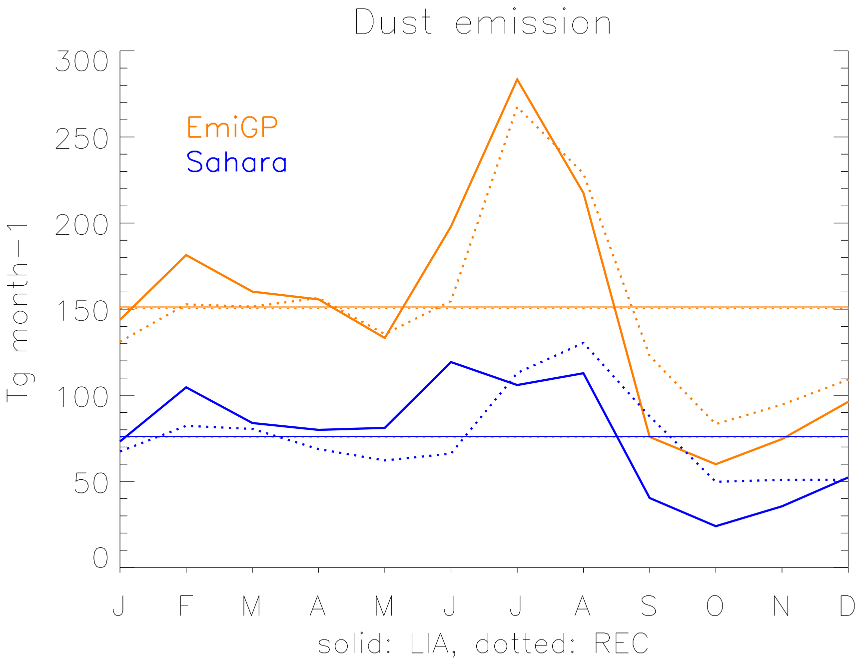

Fig. 5.9: Annual cycle of the dust emission during the LIA (solid lines) and the recent climate (dotted lines). Horizontal lines give the annual mean values. Results are shown for the dust emitting grid points (orange) and the Sahara (blue).

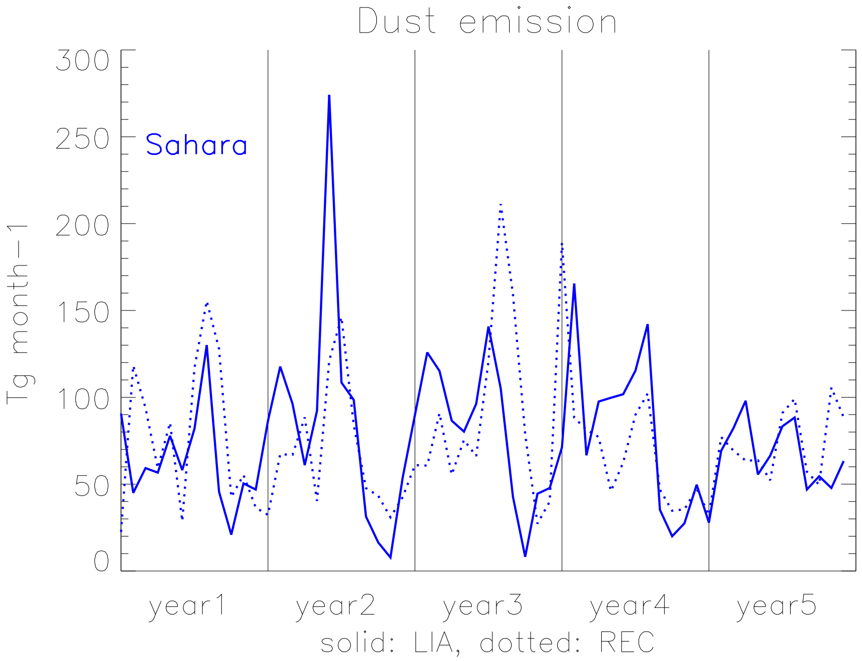

Fig. 5.10: Five-year time series of monthly mean dust emission during the LIA (solid lines) and the recent climate (dotted lines). Results are shown for the Sahara only. year1 to year5 denote the respective year of the simulations.

5.3.3 Climatic differences within the "dust belt"

Global annual dust emissions do not deviate much between the REC_chem (1 815 Tg yr^{-1}) and the LIA_chem (1 806 Tg yr^{-1}) simulation. However, there are some interesting differences in the global distribution of the emissions. In both climate epochs almost 90% of the global dust are emitted from the so called "dust belt" (0–50°N, 20°W–100°E, Prospero et al. 2002). The following analysis focusses on this region.

Differences of the annual mean dust emission and deposition fluxes in kg ha^{-1} yr^{-1} of the simulations REC_chem minus LIA_chem are illustrated in Fig. 5.11. Regions with today higher (lower) emission and deposition fluxes are shown with reddish (blueish) colours. In the recent climate the annual emissions are higher north and east of the Caspian Sea, in the Thar Desert, and in the southwestern part of Algeria. The highest negative values, i.e., higher emissions during the LIA, are found in Mali/Mauritania and on the Arabian Peninsula. The differences in other prominent dust source regions, as the Bodélé Depression and the Taklamakan Desert, indicate somewhat higher emissions in the recent climate (Fig. 5.11a).

The difference of the dust deposition fluxes (Fig. 5.11b, note the different and nonlinear colour bar) shows a more complex pattern. Downstream of the West African source regions, i.e., mainly to the west of them, the deposition flux of REC_chem is higher in the northern part and lower in the southern part, which is consistent with the dust emission difference pattern. Also in the area around the Caspian Sea both the emissions and the deposition fluxes are higher in the recent climate. Downstream of the Thar Desert one would expect higher dust deposition in the recent climate because of the much higher recent emissions there. However, the difference field shows the structure of a dipole in the monsoon dominated region on the windward side of the Himalayas. Adjacent to the Thar Desert the deposition is higher during the LIA, further east it becomes higher in the recent climate. These differences will be analysed in more detail for the different seasons later in this section.

The verification of differences in the dust cycle between the two climate epochs is complicated, as there are only very little comparison data sets for the LIA available. Information on dust concentration and deposition fluxes can be gained from ice and marine sediment cores. Unfortunately, most of these core data (cf. Mahowald et al. (1999) for the LGM) do not resolve the LIA. Three time series that resolve the LIA and provide information about mineral dust, are presented in Kaspari et al. (2007, Mt. Everest), Eichler et al. (2011, Central Asia), and Sigl et al. (in preparation, Alps).

Mt. Everest, 28°N, 87°E (Kaspari et al. 2007)

The drilling site of this ice core is located on the East Rongbuk glacier on the

(a) Dust emission

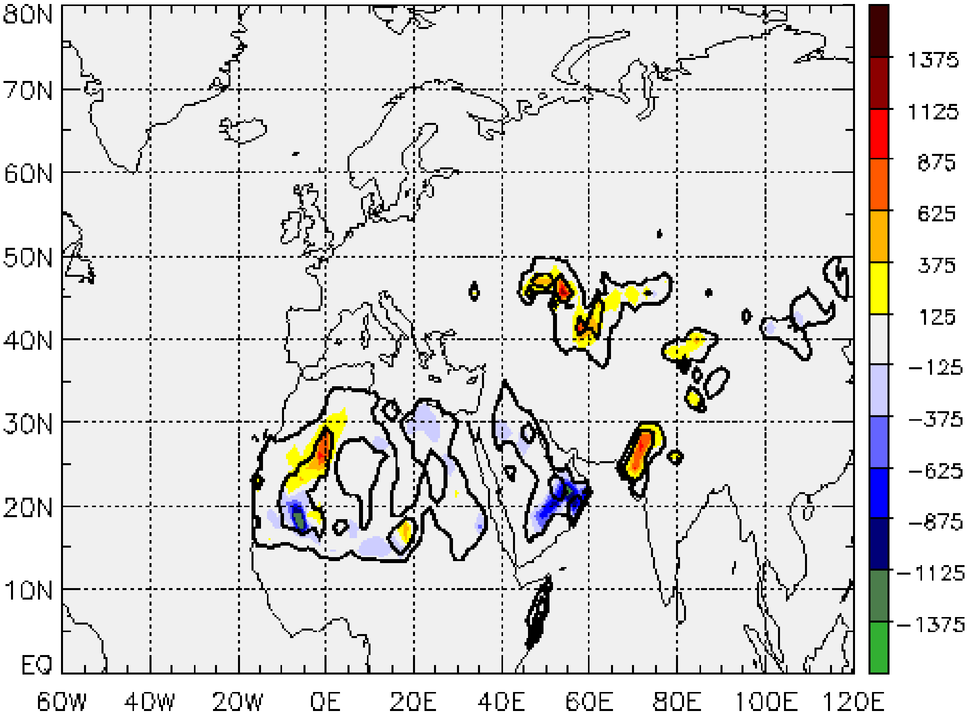

(b) Dust deposition

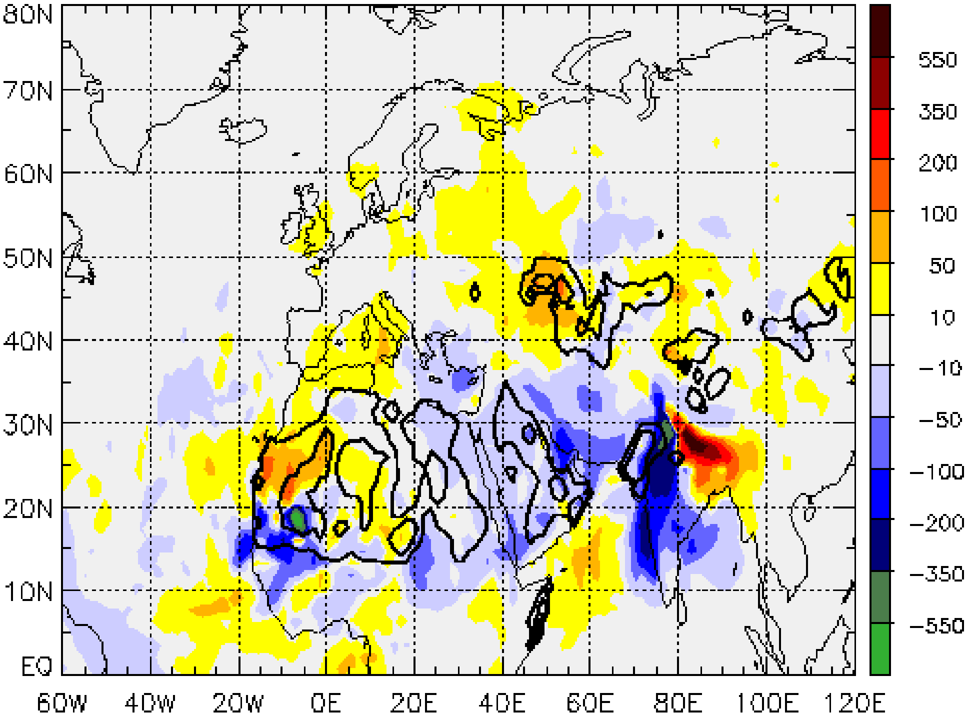

Fig. 5.11: Difference of the annual mean dust emission fluxes (a) and the dust deposition fluxes (b) in kg ha^{-1} yr^{-1} of the simulations REC_chem minus LIA_chem. Note the different and non-linear colour bar in (b). Bold black isolines (200, 2 000 kg ha^{-1} yr^{-1}) mark the regions where about 80% (20%) of the dust is emitted in the REC_chem simulation.

northeast ridge of Mt. Everest and the core was retrieved in 2002. Kaspari et al. (2007) found dustier conditions from AD 1400 on, compared to earlier times. However, no information was given about the difference between the LIA and recent conditions. The difference of the annual dust deposition fluxes in Fig. 5.11b shows that the drilling site is located in a border region. On the windward side of the Himalayas, south of the ridge, the dust deposition flux is higher in the REC_chem simulation. Further north the values are slightly higher in LIA_chem. Due to the relatively coarse horizontal resolution, it is not possible to precisely distinguish between grid boxes south and north of the Mt. Everest ridge. Conclusions on the correctness of the simulated differences in the dust deposition cannot be drawn from the data of a single ice core in this region.

Central Asia, 50°N, 87°E (Eichler et al. 2011)

This ice core was retrieved from the Belukha glacier in the Siberian Altai mountains in 2001. The authors found high dust concentrations between 1540 and 1600 and concluded on exceptional dry conditions in this time. Increased temperature around 1600 were thought to initiate a phase with increased forest-fire activity from 1600 to 1680. This proxy, however, is only analysed for the time until 1940, so that no conclusions on the differences to the recent climate can be drawn.

Alps, 46°N, 8°E (Sigl et al., in preparation)

In 2003 this ice core was received from the Colle Gnifetti glacier in the southern Central Alps. The dust concentrations derived from this core indicate that among the entire past millennium the dust transport to the Alps was never as intense as during the most recent 20 years. This is supported by the model results. The difference of the dust deposition fluxes is indeed very low directly in the Alpine region, but further south, over the Western Mediterranean and the Apennine Peninsula, the deposition fluxes are higher in the REC_chem simulation. Reasons why these differences are not simulated in the Alps might be a slight shift in the dust transport, or a too coarse horizontal resolution of the model.

All in all, the very limited availability of comparison data sets does not allow for an in-depth verification of the simulated dust cycle during the LIA.

In the following, a detailed analysis of the differences in single seasons and reasons therefore are provided, starting with JJA, which is the season with highest dust emissions. Secondly, the season SON will be investigated, because the difference of the dust emissions between REC_chem and LIA_chem is largest in this season (Fig. 5.9). Afterwards DJF and MAM are analysed. The following figures depict the differences of dust emission and deposition fluxes, mean sea level pressure (MSLP), temperature on the lowest model layer, 10-m wind velocity, and precipitation of the REC_chem minus the LIA_chem simulation. Interpreting these figures is easiest keeping the question in mind, how the shown parameters change from the LIA to the recent climate: positive values show, for example, that the recent climate is warmer or wetter, regions with negative values are today colder or drier than during the LIA.

- JJA

The total dust emission flux in the "dust belt" during JJA in the recent climate accounts for 652 Tg, which is about 7% lower than the emissions during the LIA (702 Tg). A similar difference of 9% occurs in the deposition fluxes (REC: 596 Tg, LIA: 658 Tg). In both climate epochs the deposition fluxes are 5–10% lower than the emission fluxes. This indicates a net transport of dust out of the depicted region on the order of 50 Tg per season. Considering the spatial distribution of the differences in the dust emissions in Fig. 5.12a, there are two regions with higher emissions in the recent climate, namely the northern part of the West African source regions and the Thar Desert. In the southern and eastern part of the Sahara, over the Arabian Peninsula, and east of the Caspian Sea the emissions are higher during the LIA. The different emissions lead to an interesting picture in the differences of the dust deposition (Fig. 5.12b). Downstream of the Thar Desert, there occurs a shift of the deposition flux, with recent depositions occurring further east than during the LIA. Close to the remaining source regions listed above, the deposition fluxes behave according to the emissions. North of the South American coast line the deposition is higher during the LIA. This will be analysed further when considering the transatlantic transport in section 5.3.4. Mentionable are also the spots of higher recent dust deposition along 10°N, which seem not to be directly connected to a region with higher recent emissions.

The land-sea pressure contrast, with high pressure over the Indian Ocean and low pressure over the southern Asian continent, is the driving factor of the Indian Monsoon (Fleitmann et al. 2004). While the differences in MSLP between the two climate epochs are smaller than ±0.5 hPa south of 10°N, the pressure further north is higher in the recent climate (Fig. 5.12c). This would imply a stronger pressure gradient and a stronger monsoon circulation during the LIA, indicated by more than 1 m s^{-1} higher 10-m wind velocities over the Arabian Sea and the Bay of Bengal (Fig. 5.12e). The assumption of a stronger Indian summer monsoon during the LIA is supported by Denniston et al. (2000). Analysing speleothems from a cave in central Nepal, they found moister and/or cooler conditions from 1550 to 1640, which also confirms the differences of temperature and precipitation in Figs. 5.12d,f. It is surprising that the wind speed over the Thar Desert and further east is higher in the recent climate. In this region the temperature difference is also most distinct, with values of more than 2 K (Fig. 5.12d). The warmer air might reduce the pressure, which

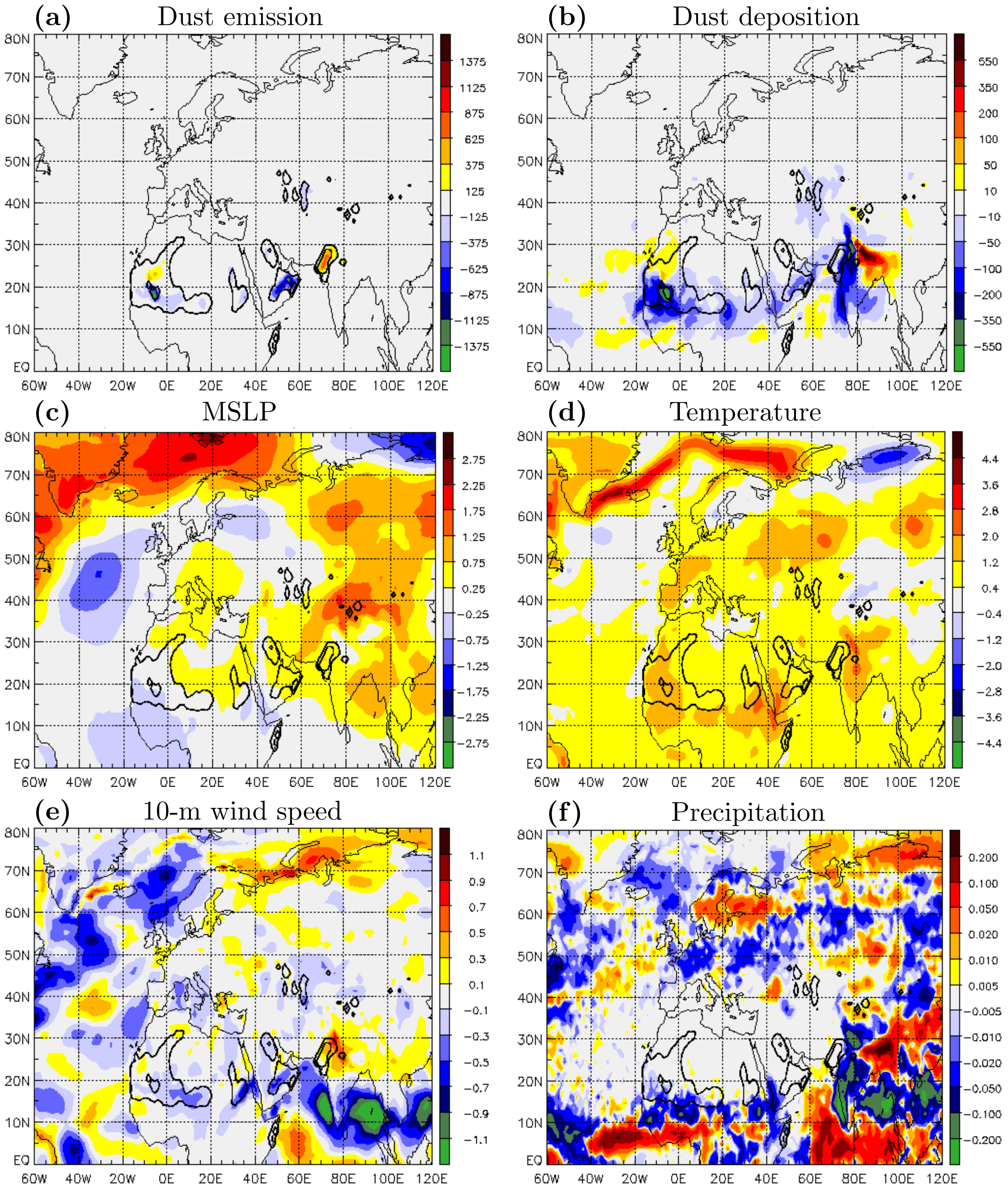

Fig. 5.12: Difference of the (a) dust emission in kg ha^{-1}, (b) dust deposition in kg ha^{-1}, (c) MSLP in hPa, (d) temperature on the lowest model layer in K, (e) 10-m wind velocity in m s^{-1}, and (f) precipitation in kg m^{-2} per hour during JJA of the simulations REC_chem minus LIA_chem. Bold black isolines (200, 2 000 kg ha^{-1} per season) mark the regions where about 80% (20%) of the dust is emitted in the REC_chem simulation.

is apart from that higher in the surroundings in the recent climate. This leads to an area northeast of the Thar Desert, where the MSLP is the same in both climate epochs. Together with higher pressure around this region, a circulation is enforced in the recent climate that induces higher wind speeds and therefore higher dust emissions in the Thar Desert. Higher wind velocity also means faster transport of the freshly emitted dust and longer travel distances in the recent climate. In combination with a shift in the precipitation pattern (Fig. 5.12f), this causes the eastward displacement of the dust deposition flux in the recent climate, compared to the LIA (Fig. 5.12b). The differences in the precipitation show similar features as the dust deposition: During the LIA both fields are enhanced adjacent to the Thar Desert, along the Western Indian coastline, and over the Bay of Bengal, while they are lower further east (Figs. 5.12b,f). This shows the strong impact of wet removal processes, associated with monsoon-related precipitation, on the total dust deposition in this region.

Stronger monsoon circulation over the Arabian Sea also causes higher 10-m winds and higher dust emissions over the Arabian Peninsula during the LIA (Figs. 5.12a,e). This dust is transported from Arabia across the Arabian Sea and contributes to the higher deposition fluxes over the western part of the Indian subcontinent during the LIA (Fig. 5.12b).

North African dust emissions are influenced by the WAM during NH-summer. The often large monsoon pressure gradient can cause strong, dust mobilising winds along the intertropical discontinuity, which separates the monsoon flow from Saharan air masses (Karam et al. 2008, Knippertz and Todd 2012). The leading edge of the WAM is located over the northern part of the Sahel between 15 and 20°N during NH-summer. The difference of the MSLP (Fig. 5.12c) shows slightly lower pressure in the recent climate south of the West African dust source regions, i.e., south of the intertropical discontinuity. To the north and northeast the MSLP is higher in the recent climate. The land-sea pressure gradient is therefore stronger during the LIA, inducing higher 10-m wind velocities in the Sahel and southern Sahara (Fig. 5.12e). The higher wind speeds during the LIA in JJA are responsible for higher dust emissions between 15 and 20°N, especially over South Mali and Mauritania (Fig. 5.12a). The stronger pressure gradient over West Africa also indicates a more intense summer monsoon activity during the LIA. This is corroborated by the differences in precipitation between the two climate epochs, showing more rainfall during the LIA north of 10°N and less precipitation further south (Fig. 5.12f). Nicholson and Webster (2007) analysed the interannual variability of rainfall in the Sahel. They found years with a stronger pressure gradient over West Africa to be associated with wet conditions in the Sahel and dry conditions over the Guinea coast. The node of this rainfall dipole was found to be located rather consistently around 10°N (Nicholson and Webster 2007), matching quite well with the pattern in Fig. 5.12f.

These differences in precipitation between the two climate epochs also influence the total dust deposition. In the recent climate the dust deposition south of 10°N and west of 0°E is higher than during the LIA (Fig. 5.12b), indicating that more dust is scavenged in this region due to more intense precipitation. Higher deposition fluxes north of 10°N during the LIA are caused by higher rain rates but also by higher dust emissions between 15 and 20°N.

Higher emissions in the recent climate over the northern parts of Mali and Mauritania are not connected to differences in the mean 10-m wind velocity and are of much smaller magnitude than the differences further south.

- SON

For several reasons, NH-autumn is an outstanding season: (1) The absolute emission (REC: 251 Tg, LIA: 157 Tg) and deposition fluxes (REC: 249 Tg, LIA: 161 Tg) are lowest, compared to the other seasons. (2) NH-autumn is the only season with on average higher fluxes in the recent climate than during the LIA. (3) Differences between the dust emission and the deposition in the "dust belt" are smaller ($< \pm 3\%$) than in the other seasons, and during the LIA there is more dust transported into this region than out of it, i.e., the deposition flux is higher than the emission flux.

Another interesting feature is that there are almost exclusively positive values in the difference fields of the emission and deposition fluxes (Figs. 5.13a,b), meaning that there are hardly any regions with higher emissions during the LIA. The largest differences in the emissions occur in the West African dust source regions. Close to and downstream of these regions, i.e., over the adjacent Atlantic Ocean, there are also the biggest differences in the deposition fluxes.

North African dust emissions during SON are mainly driven by northerly and northeasterly winds, triggered by a north-south pressure contrast with high pressure over Morocco, Algeria, Libya, and the Western Mediterranean and low pressure further south. The difference of the MSLP indicates that this pressure gradient is stronger in the recent climate, when pressure is higher in the north and lower in the south than during the LIA (Fig. 5.13c). This results in higher 10-m wind velocities over almost the entire North African continent (Fig. 5.13e) and higher dust emission fluxes in the recent climate (Fig. 5.13a).

The region around 15°N, 0°E, where the temperature is higher during the LIA, is very close to the strong positive signal in the precipitation located slightly further south (Fig. 5.13f). This region with higher precipitation in the recent climate extends to the east and west, showing higher rain rates within the ITCZ. This, again, also indicates stronger cloud cover in the recent climate, reducing direct solar radiation and causing the cooling in the Sahel region.

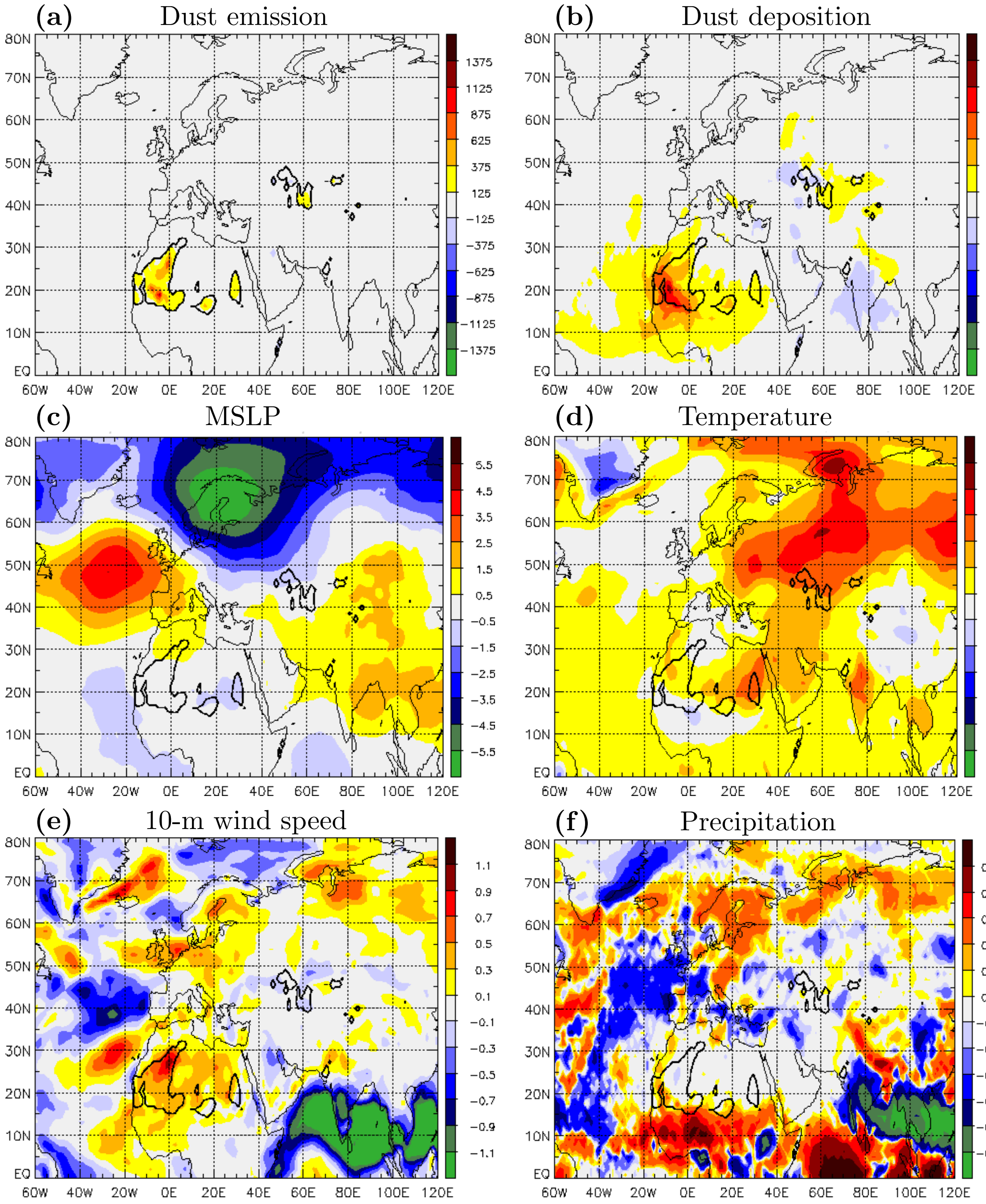

Fig. 5.13: Difference of the (a) dust emission in kg ha^{-1}, (b) dust deposition in kg ha^{-1}, (c) MSLP in hPa, (d) temperature on the lowest model layer in K, (e) 10-m wind velocity in m s^{-1}, and (f) precipitation in kg m^{-2} per hour during SON of the simulations REC_chem minus LIA_chem. Bold black isolines (200, 2 000 kg ha^{-1} per season) mark the regions where about 80% (20%) of the dust is emitted in the REC_chem simulation.

With regard to the difference fields, one has to mention the higher pressure in the recent climate over the North Atlantic Ocean west of Europe (+4 hPa) and the much lower pressure north of 60°N, especially over Northern Scandinavia, where the difference amounts to more than 5.5 hPa (Fig. 5.13c). This signal in the MSLP difference varies in its intensity from year to year, but the pattern is robust during the entire simulation periods of REC_chem and LIA_chem. There are also some spots in Russia where temperature in the recent climate is more than 3.6 K higher than during the LIA, while it is today about 2 K colder over Greenland (Fig. 5.13d). These differences, however, do not appear to directly impact the mineral dust cycle and therefore they are not analysed further in this study.

- DJF

The differences between the two climate epochs of the dust emission and deposition fluxes are relatively small during DJF (Figs. 5.14a,b). Integrated over the depicted region, the emission (deposition) flux of the REC_chem simulation amounts to 314 Tg (249 Tg), compared to 331 Tg (276 Tg) in LIA_chem. In both climate epochs the deposition is about 20% lower than the emission, showing that there is a net transport of dust out of this region. Despite this huge relative difference between emission and deposition fluxes, the total export of dust out of the "dust belt" in DJF is on the same order of magnitude (about 60 Tg per season) as in JJA. Recent emissions are slightly higher in the region north and east of the Caspian Sea and over the southeastern part of the Arabian Peninsula, while emissions during the LIA are higher in the North African source regions, especially the Bodélé Depression, and in the northern part of Arabia. The deposition fluxes of the LIA_chem simulation are higher in a belt stretching from the Atlantic Ocean off the West African coast across North Africa towards the Middle East. Close to the Caspian Sea and in Eastern Arabia the dust deposition is higher in the recent climate, due to the higher emissions there.

The higher emission in the Caspian Sea region in the recent climate can be explained with a displacement of the Siberian High between the REC_chem and the LIA_chem simulation. The positive values in the difference of MSLP (Fig. 5.14c), centred around 55°N, 65°E, and the negative values around 65°N, 95°E indicate a westward shift of the anticyclone in the recent climate. This pattern is mirrored in the temperature difference, but with opposite sign. The regions with higher pressure in the respective climate epoch might involve more frequent low-level stratus clouds, leading to the observed temperature differences over Siberia in Fig. 5.14d. The more western position of the Siberian High in the recent climate causes a stronger pressure gradient and higher 10-m wind velocities (Fig. 5.14e) over the dust source regions around the Caspian Sea, inducing higher dust emission fluxes there.

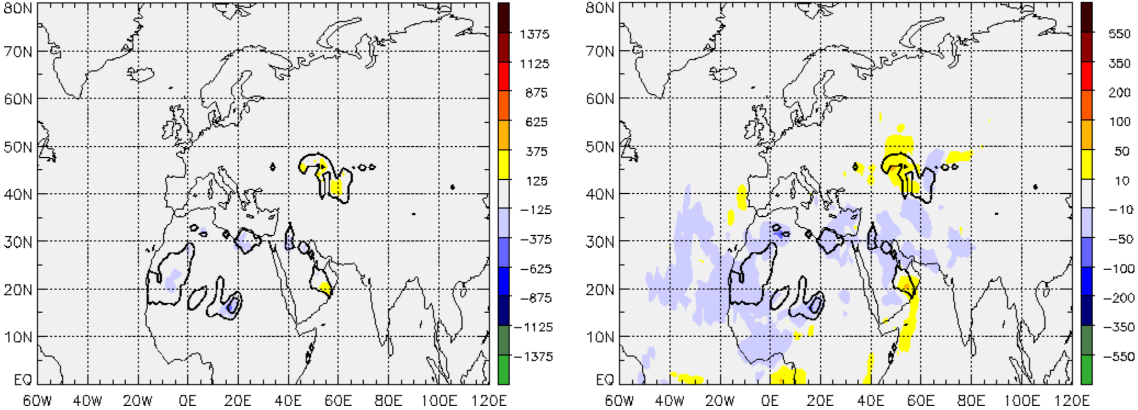
(a) Dust emission

(b) Dust deposition

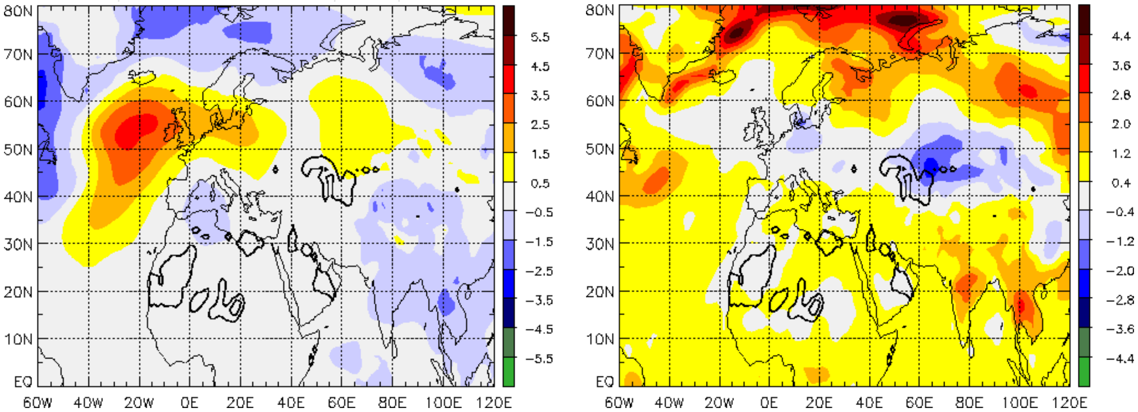
(c) MSLP

(d) Temperature

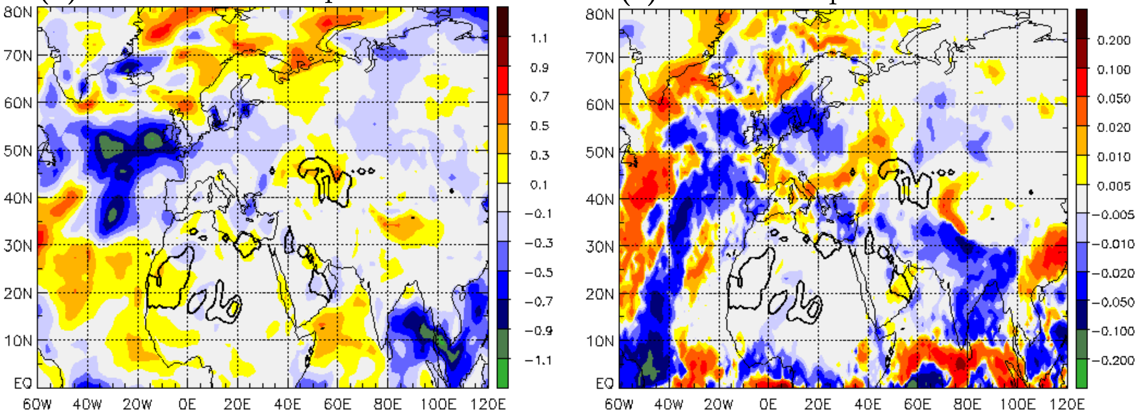
(e) 10-m wind speed

(f) Precipitation

Fig. 5.14: Difference of the (a) dust emission in kg ha^{-1}, (b) dust deposition in kg ha^{-1}, (c) MSLP in hPa, (d) temperature on the lowest model layer in K, (e) 10-m wind velocity in m s^{-1}, and (f) precipitation in kg m^{-2} per hour during DJF of the simulations REC_chem minus LIA_chem. Bold black isolines (200, 2 000 kg ha^{-1} per season) mark the regions where about 80% (20%) of the dust is emitted in the REC_chem simulation.

The most striking feature in the MSLP difference is higher pressure in the recent climate over the eastern North Atlantic Ocean, west of Great Britain, extending in the southern direction to the Azores and to the east towards the Baltic Sea (Fig. 5.14c). This difference causes a weaker pressure gradient and lower 10-m wind speed in the REC_chem simulation between the Azores High and the Icelandic Low. South of the Azores High the MSLP is almost the same in both simulations, meaning that the pressure gradient there is higher in the recent climate, resulting in higher wind velocities (Fig. 5.14e). The MSLP over the Western Mediterranean, Tunisia, and adjacent regions is higher in the LIA_chem simulation, while differences over the remaining North African continent are negligible. The difference of the 10-m wind speed shows an ambiguous behaviour, with positive and negative values in North Africa. For example, the mean 10-m wind over the Bodélé Depression is higher in the recent climate, but the dust emission flux is higher during the LIA. This suggests the more frequent occurrence of episodic, short-term events with strong winds and high dust emission fluxes during the LIA, leading to on average higher emissions but having only minor influence on the mean 10-m wind speed.

Precipitation, which indirectly affects the dust emission via the soil moisture, does not significantly change in any of the dust source regions (Fig. 5.14f).

- MAM

As in DJF, total dust emission and deposition fluxes in the “dust belt” in the recent climate (emission: 431 Tg, deposition: 371 Tg) are quite similar to those during the LIA (emission: 440 Tg, deposition: 374 Tg). The deposition corresponds to about 85% of the emission, implying again a net transport of dust out of the depicted domain of around 60 Tg per season. However, there are some regions where the local fluxes show distinct differences (Figs. 5.15a,b). North and east of the Caspian Sea and in the Bodélé Depression the emissions are higher in the recent climate. During the LIA the dust emission flux is higher in the West African source regions in Mali and Mauritania. Downstream of these emission regions, i.e., west and northwest of the Caspian Sea, west of the Bodélé Depression, and southwest of West Africa, the deposition fluxes behave according to the dust emissions.

Comparing the results of both simulations, one has to mention the huge difference in the MSLP over the North Atlantic Ocean and over Greenland (Fig. 5.15c). Higher pressure in the north and lower pressure in the south in the recent climate imply a weaker pressure gradient between the Azores High and the Icelandic Low. This causes weaker 10-m wind velocities over the North Atlantic Ocean between Newfoundland and Great Britain in the recent climate (Fig. 5.15e).

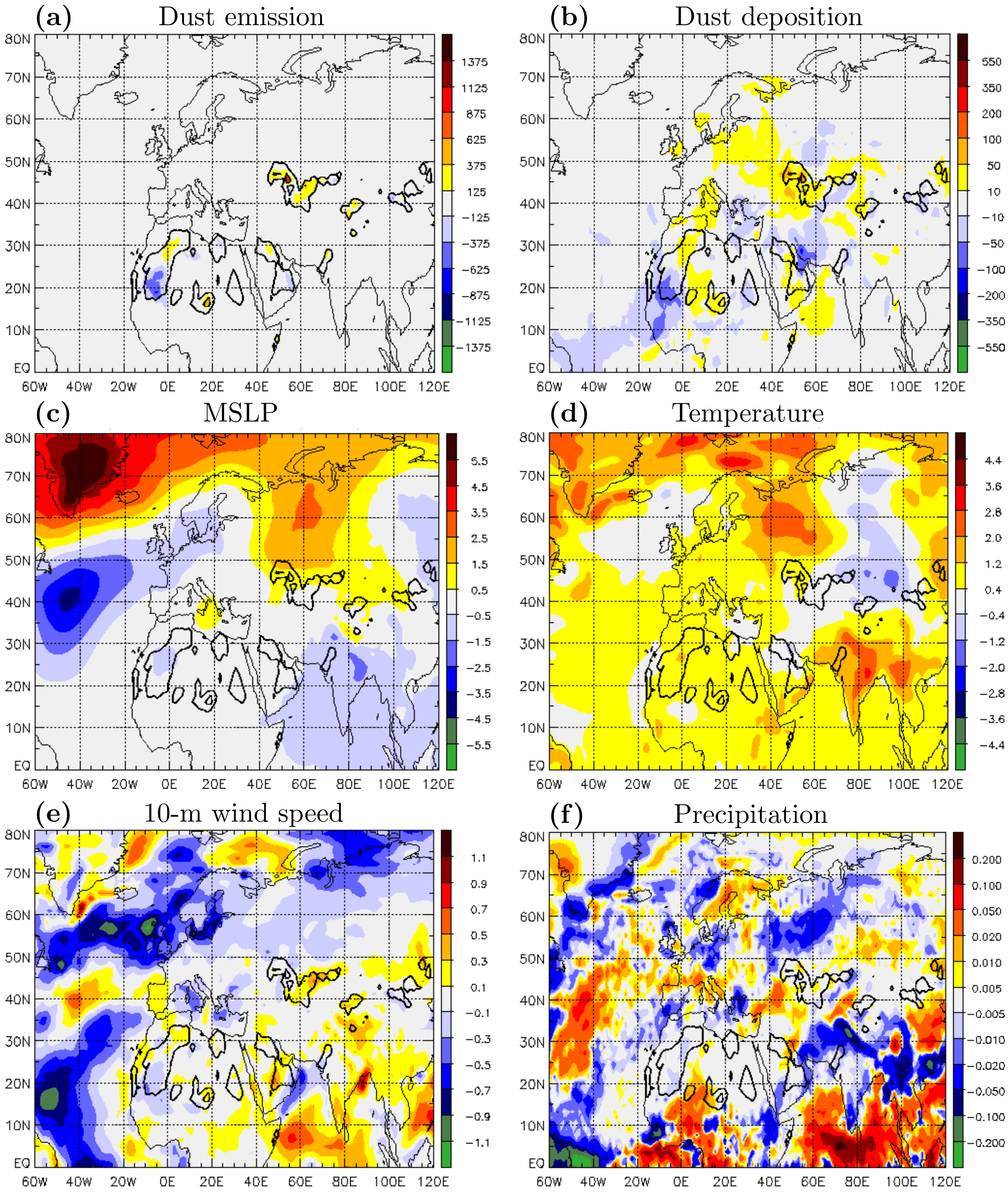

Fig. 5.15: Difference of the (a) dust emission in kg ha^{-1}, (b) dust deposition in kg ha^{-1}, (c) MSLP in hPa, (d) temperature on the lowest model layer in K, (e) 10-m wind velocity in m s^{-1}, and (f) precipitation in kg m^{-2} per hour during MAM of the simulations REC_chem minus LIA_chem. Bold black isolines (200, 2 000 kg ha^{-1} per season) mark the regions where about 80% (20%) of the dust is emitted in the REC_chem simulation.

The ridge over Central Asia is more distinct in the recent climate, visible in the positive signal in Fig. 5.15c over Siberia. This causes a stronger southerly flow on the back side and a stronger northerly flow on the front side of the ridge in the REC_chem simulation, resulting in cooler temperature in the recent climate at the front side due to advection (Fig. 5.15d). The more distinct ridge suppresses precipitation in the region around 55°N, 60°E in the recent climate (Fig. 5.15f). In the dust source region (40–50°N, 60–80°E) the recent 10-m wind speed is higher than during the LIA (Fig. 5.15e), inducing slightly higher dust emissions there (Fig. 5.15a). Emissions are also higher further west, especially at 45°N, 55°E, but neither the 10-m winds nor the precipitation do show any distinct difference there.

The differences of the 10-m wind are patchy over North Africa. In regions with today higher winds, e.g., over the Bodélé Depression, the dust emissions are also higher, while higher wind velocities during the LIA, e.g., over the southern part of the West African source regions, cause stronger emissions in the LIA_chem simulation (Figs. 5.15a,e). Because of many small-scale signals in the 10-m wind and because of the non-geostrophic character of the flow at these latitudes, the connections between pressure, temperature, and wind speed are difficult to analyse. Warmer temperature over the Sahara in the recent climate (Fig. 5.15d) might be one reason for reduced pressure values (Fig. 5.15c). Lower 10-m wind velocities coincide with less dust emission in the recent climate over the southern part of the West African dust source regions.

Another region with remarkable differences that, however, do not affect the dust emissions, is the Indian subcontinent, where the temperature is up to 3 K higher in the REC_chem simulation (Fig. 5.15d), causing a lower MSLP in the recent climate (Fig. 5.15c).

So far, the analyses of the LIA_dyn and LIA_chem time slice simulations revealed the ability of the model to reproduce stable climatic conditions with near-surface temperature on average 0.5 to 1 K cooler than in the recent climate. The annual global characteristics of the mineral dust cycle are comparable with the recent climate, however, there are notable differences on the seasonal and regional scale. Largest differences in dust emission and deposition fluxes occur in JJA and SON. Intensification of the Indian Monsoon and earlier onset of the WAM during the LIA explain some of the differences. Other signals can also be traced back to differences in the regional dynamics between the two climate epochs.

Interannual variability of precipitation and dust emissions in the Sahara is very high, and the question arises, how representative the results of the LIA_dyn and LIA_chem simulations are. The LIA spans a range of about 500 years and the five-year time slice simulations discussed here cannot represent the entire climate epoch. Time slices covering longer periods than five years might yield more robust results. However, the simulated cooling in LIA_dyn and LIA_chem suggests that the model reproduces conditions that are "typical" for the LIA. This is confirmed by the comparison with various other reconstructions of temperature during the LIA.

5.3.4 Climatic differences of the transatlantic transport

The analysis of the transatlantic transport of dust from North Africa to the Americas in section 4 revealed the importance of source regions in Algeria, Mauritania, and Mali. The differences of dust emission and deposition fluxes in Fig. 5.11 suggest interesting variations of the dust transport between the two climate epochs. The following analyses are based on Eulerian considerations and trajectory calculations for the LIA. The trajectories are initialised in analogy to those in the recent climate (see section 4.2.2), but of course from the emission grid points of the LIA_chem simulation. The results are compared to the findings for the recent climate (cf. section 4).

Amount of emitted, transported, and deposited dust

A first overview about differences in the transatlantic transport of mineral dust is given by Fig. 5.16, which shows the Eulerian net dust emission flux, i.e., the emission minus the deposition flux, for the different seasons in the recent climate and during the LIA. The differences between both climate epochs are not obvious at first sight. In DJF (Figs. 5.16a,b) and in MAM (Figs. 5.16c,d) the emissions from the West African source regions are slightly higher during the LIA and so are the deposition fluxes in the Amazon Basin. In NH-summer the deposition in the Sahel is higher during the LIA, but no clear signal appears in the Caribbean or the Amazon Basin. As mentioned in the previous section, the dust emission during NH-autumn from West African sources is higher in the recent climate, which can also be seen in Figs. 5.16g,h. This leads to higher recent dust deposition over the Atlantic Ocean and in the Caribbean.

The differences are quantified in Table 5.3. It lists the dust emission (EMI), deposition (DEP), and the net emission (net EMI) over the North African continent, as well as the deposition in the Caribbean (CAR) and the Amazon Basin (AMA)[1] for the recent climate, the LIA, and the absolute and the relative differences between the two climates. Annual values do not deviate much between the REC_chem and the LIA_chem simulations. The biggest relative, albeit statistically not significant, difference occurs in the deposition in the Amazon Basin, which is about 5% higher during the LIA. In single seasons, however, the results show remarkable differences. In DJF all values except the deposition in the Caribbean are 12–15% higher during the LIA. The climatic differences of the net emission in North Africa and of the

---

[1] See Fig. 4.1 on page 47 for the definition of the regions.

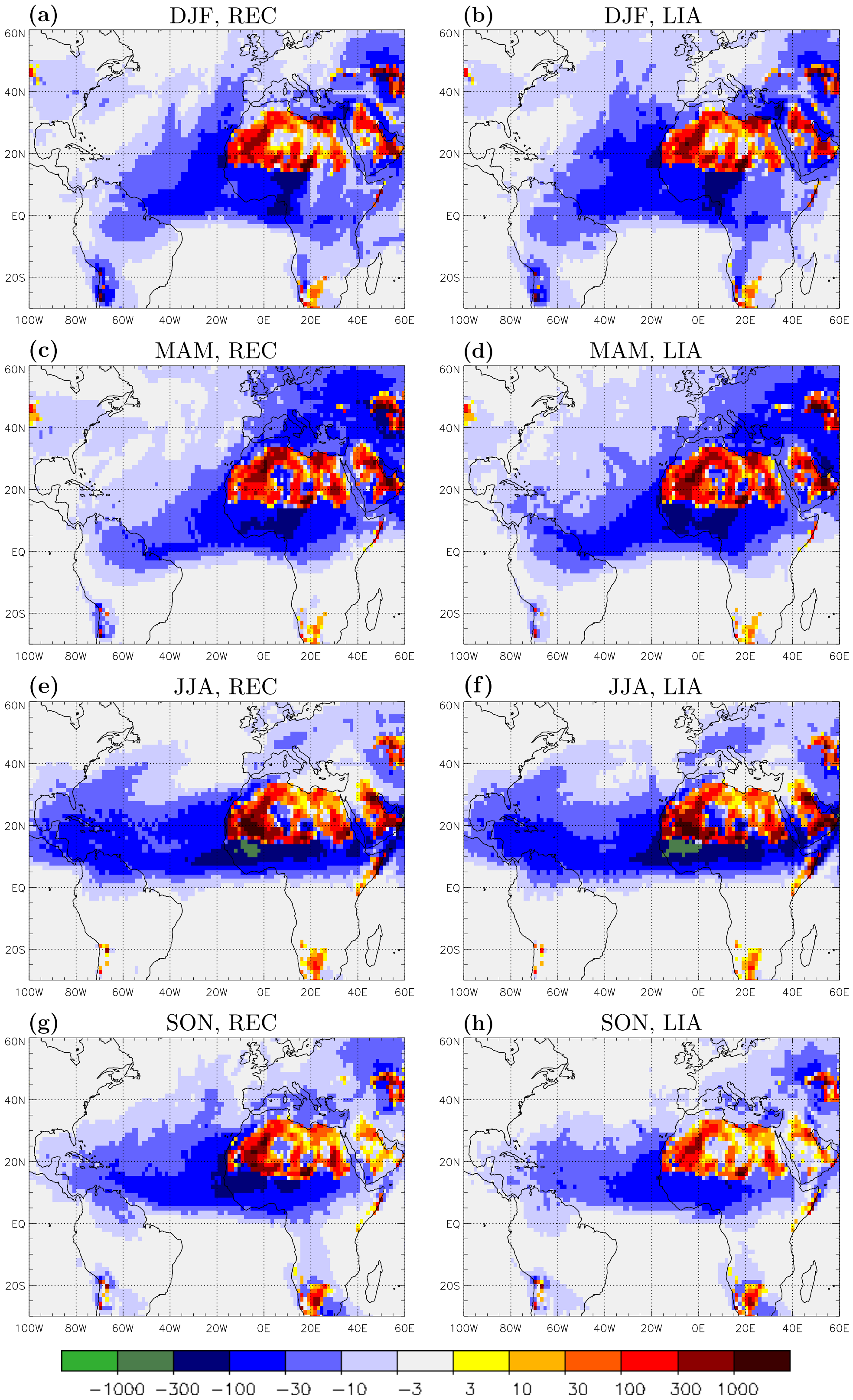

Fig. 5.16: Dust emission minus dust deposition in kg ha^{-1} per season from Eulerian data in the recent climate (REC_chem: left column) and during the LIA (LIA_chem: right column) for DJF, MAM, JJA, and SON (from top to bottom).

			REC	LIA	$\mathit{\Delta}_{\text{REC-LIA}}$	P, %
DJF	North Africa	EMI	205.2	234.2	-29.0	-14
		DEP	98.6	111.8	-13.2	-13
		net EMI	106.6	122.4	-15.8	-15
	CAR	DEP	1.8	1.6	0.2	+11
	AMA	DEP	8.9	10.0	-1.1	-12
MAM	North Africa	EMI	225.0	259.8	-34.8	-15
		DEP	131.4	139.5	-8.1	-6
		net EMI	93.6	120.3	-26.7	-29
	CAR	DEP	2.1	4.4	-2.3	-110
	AMA	DEP	9.1	11.6	-2.5	-27
JJA	North Africa	EMI	361.0	390.3	-29.3	-8
		DEP	199.7	243.4	-43.7	-22
		net EMI	161.3	146.9	14.4	+9
	CAR	DEP	21.1	22.8	-1.7	-8
	AMA	DEP	8.5	7.6	0.9	+11
SON	North Africa	EMI	196.8	108.0	88.8	+45
		DEP	122.7	64.8	57.9	+47
		net EMI	74.1	43.1	31.0	+42
	CAR	DEP	9.3	5.6	3.7	+40
	AMA	DEP	3.8	2.6	1.2	+32
annual	North Africa	EMI	988.0	992.3	-4.3	±0
		DEP	552.4	559.5	-7.1	-1
		net EMI	435.6	432.7	2.9	+1
	CAR	DEP	34.3	34.4	-0.1	±0
	AMA	DEP	30.3	31.8	-1.5	-5

Table 5.3: Seasonal and annual fluxes in Tg per season and in Tg yr^{-1}, respectively, of dust emission (EMI), deposition (DEP), and net emission (net EMI, i.e., EMI minus DEP) over North Africa, and of the deposition in the Caribbean (CAR) and the Amazon Basin (AMA). Listed are results for the recent climate, the LIA, the difference thereof ($\mathit{\Delta}_{\text{REC-LIA}}$), and the difference in percent of the recent values P, i.e., $\frac{\mathit{\Delta}_{\text{REC-LIA}}}{\text{REC}} \cdot 100$.

deposition in the Amazon Basin are even higher in MAM and amount to almost 30%. Only a small fraction of the annual dust deposition in the Caribbean occurs during MAM, but during the LIA it is more than twice of the recent value. In JJA the emission and especially the deposition (22%) over North Africa are also higher during the LIA. The higher deposition fluxes are mainly located in the Sahel (Figs. 5.16e,f). This again is in agreement with wetter conditions in the Sahel due to an intensified WAM in the NH-summer months during the LIA, causing higher wet deposition rates (cf. section 5.3.3). During the LIA, the deposition in the Caribbean is increased by 8%, while it is decreased by 11% in the Amazon Basin. The biggest relative differences over North Africa occur in NH-autumn, when the fluxes in the recent climate are higher by 40–50%. This also goes together with the temporal shift of the WAM, which is more intense during SON in the recent climate (cf. section 5.3.3), causing higher dust emissions. Correspondingly, the differences in the Caribbean and the Amazon Basin deposition amount to 40% and 32%, respectively. The higher fluxes in the recent climate during SON compensate the differences in the rest of the year, leading to relatively small annual variations between the two climate epochs.

Transport time scales

The same method as previously used for the recent climate (see section 4.4) is applied here for determining the transport time of dust from the source regions to the Americas during the LIA. Again, the time series of dust transport across 30°W (TRA) is considered, as well as dust concentrations arriving (ARR) and deposition fluxes (DEP) in the Caribbean and the Amazon Basin.

The correlation of the TRA time series against the time lagged ARR time series and of ARR against DEP reveals similar results as in the recent climate (cf. Figs. 5.17 and 4.4). For the transport to the Caribbean during NH-summer, the contrast between single seasons (solid black lines in Fig. 5.17b) and the time series over the entire five years (dotted black line) is more distinct than in the recent climate. The same reason is responsible for the lower (higher) correlation between TRA and ARR (ARR and DEP) over the five years compared to the single seasons: The dust transport through 30°W is relatively constant over the year, but the dust mainly

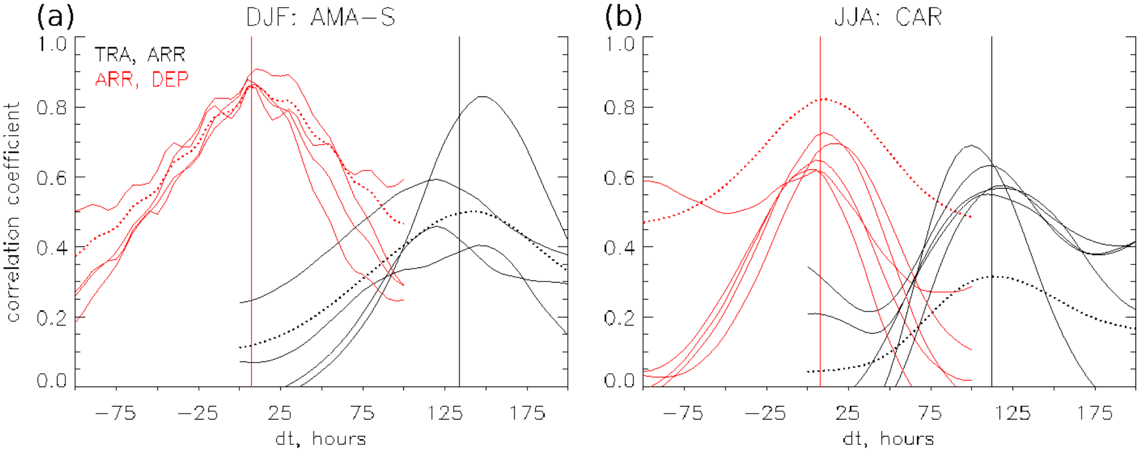

Fig. 5.17: Time lagged correlations of the time series TRA and ARR (black) and ARR and DEP (red) during the LIA. Solid lines show single seasons, i.e., DJF of year1/year2, ..., DJF of year4/year5 in (a) and JJA of year1, ..., JJA of year5 in (b). year1 to year5 denote the respective year of the LIA_chem time slice simulation. Dotted lines illustrate the time series of the entire five years from year1 to year5. Vertical lines mark the time shift of the maximum correlation, averaged over the the single seasons.

	$\bar{\tau}_{30^\circ\mathrm{W}}$		$\bar{\tau}_{\mathrm{CAR}} - \bar{\tau}_{30^\circ\mathrm{W}}$		$\bar{\tau}_{\mathrm{AMA\text{-}S}} - \bar{\tau}_{30^\circ\mathrm{W}}$		$\bar{\tau}_{\mathrm{CAR}}$		$\bar{\tau}_{\mathrm{AMA\text{-}S}}$	
	REC	LIA	REC	LIA	REC	LIA	REC	LIA	REC	LIA
DJF	4.62	4.80	3.56	2.89	4.71	4.78	8.18	7.69	9.33	9.58
MAM	7.25	6.38	3.99	4.45	3.39	3.58	11.24	10.83	10.64	9.96
JJA	6.63	6.65	3.66	3.73	4.32	4.37	10.29	10.38	10.95	11.02
SON	5.79	5.74	4.34	4.30	5.16	5.36	10.13	10.04	10.95	11.10

Table 5.4: Transport time (in days) of dust from North African source regions to 30°W ($\bar{\tau}_{30^\circ\mathrm{W}}$), from there to the target regions CAR and AMA-S, and the total time from North Africa to CAR ($\bar{\tau}_{\mathrm{CAR}}$) and AMA-S ($\bar{\tau}_{\mathrm{AMA\text{-}S}}$) in the recent climate and during the LIA. All values are calculated with the Lagrangian method.

reaches the Caribbean during NH-summer, which reduces the correlation of the five-year time series. When no or only little dust is transported to the Caribbean in DJF, MAM, and SON, ARR and DEP are both low. This increases the correlation between these parameters, when considering the entire five years compared to single seasons. The duration of the transport from 30°W to the region AMA-S in DJF is 5.57 days, which is slightly shorter than in the recent climate (5.73 days). The transport to the Caribbean in NH-summer is more than half a day faster during the LIA (4.67 days) than in the recent climate (5.25 days).

Lagrangian calculations of the transport times for the recent climate and the LIA are summarised in Table 5.4. The results for the two different climate epochs are quite similar. To reach the southern part of the Amazon Basin in DJF during the LIA, the dust requires $4.80 + 4.78 = 9.58$ days (REC: $4.62 + 4.71 = 9.33$ days). The difference in the transport times to the Caribbean during JJA is even less (LIA: $6.65 + 3.73 = 10.38$ days, REC: $6.63 + 3.66 = 10.29$ days). In MAM the climatic differences are most distinct. The time from the source regions to 30°W is almost one day shorter during the LIA. Although the further transport to the target regions is slightly faster in the recent climate, the overall transport time from North Africa to the Caribbean and the Amazon Basin is shorter during the LIA. To the Caribbean it takes $6.38+4.45 = 10.83$ days (REC: $7.25+3.99 = 11.24$ days) and to the Amazon Basin $6.38 + 3.58 = 9.96$ days (REC: $7.25 + 3.39 = 10.64$ days). This accelerated transatlantic transport during the LIA causes higher deposition fluxes in MAM in the Caribbean and in the Amazon region during the LIA (see Table 5.3), because during the shorter transport time less dust can be removed by sedimentation (and potentially by wet removal) over the Atlantic Ocean.

Horizontal and vertical distribution of the dust transport

Again, the mean pathways of the dusty trajectories has been calculated by averaging the characteristics of all trajectories, weighted with the dust mixing ratio at 30°W (cf. section 4.5.2 on page 57). Results for the individual seasons of both climate epochs are shown in Fig. 5.18. In DJF the source region and the initial dust mix-

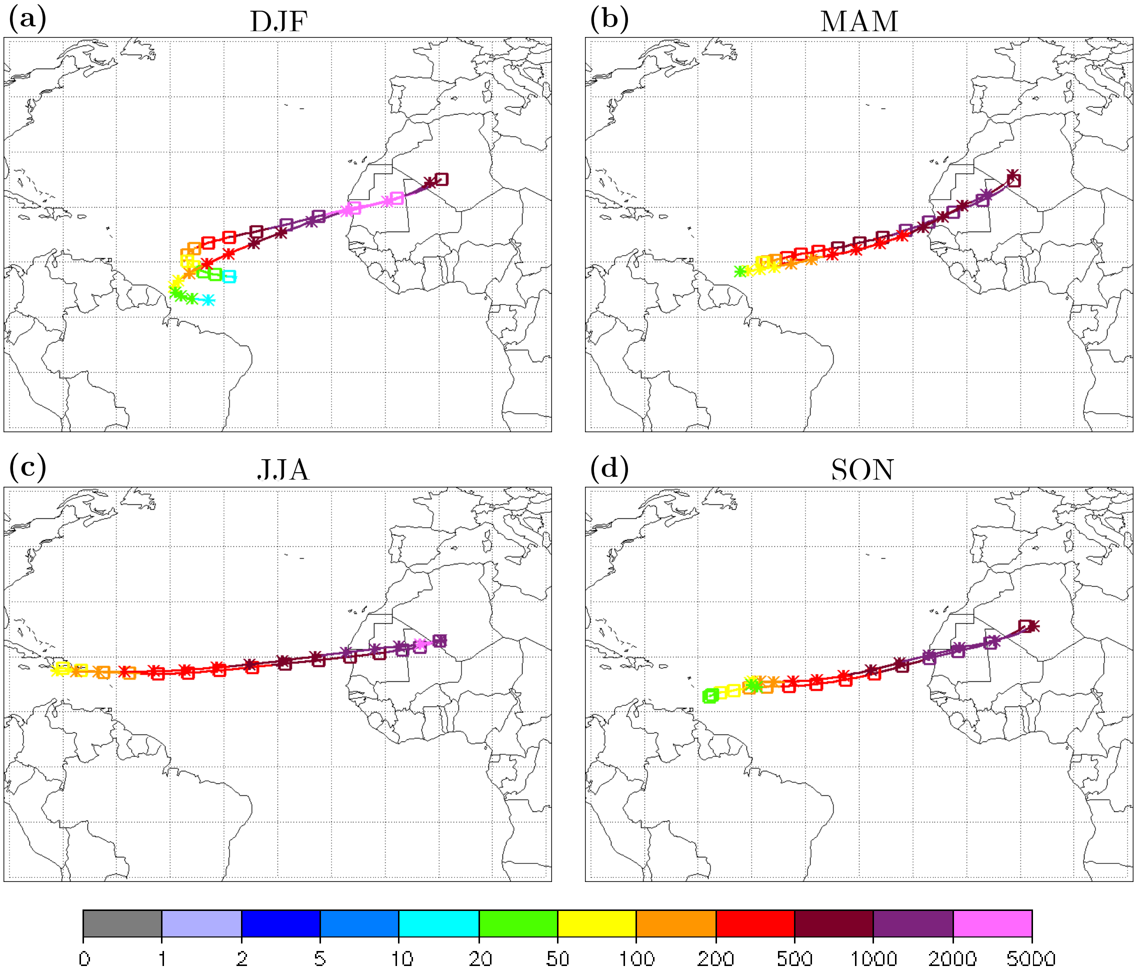

Fig. 5.18: Seasonal variation of the pathways of the dusty trajectories. A symbol along the trajectories is drawn every 25 hours. "∗" symbols denote results for the recent climate and "□" for the LIA. The coloured variable along the trajectories is the dust mixing ratio in µg kg^{-1}.

ing ratio are very similar for the recent climate and the LIA. About 50 hours after initialisation, the pathways begin to diverge. In the recent climate the trajectories reach on average positions further south and further west than during the LIA (Fig. 5.18a). This is surprising because the dust deposition in the Amazon Basin in DJF is 12% higher during the LIA, suggesting that episodic events of intense dust transport to and deposition in the Amazon region occur during the LIA, which have only a minor influence on the mean pathway. The pathways in MAM are quite similar in both climate periods (Fig. 5.18b). About 100 hours after initialisation, the mean pathway in the recent climate is located slightly further south and the final position is around 500 km further southwest, closer to the coast of Guyana, than during the LIA. Some differences also occur in the dust mixing ratio along the trajectories, which is higher during the LIA along the entire pathway. Higher initial dust concentrations, together with the faster transport (see previous paragraph), cause the higher deposition fluxes in the Caribbean and the Amazon Basin during the LIA in MAM. The differences in the mean pathways between the two climate epochs are marginal in NH-summer (Fig. 5.18c). The start and end points are almost identical, but during the transport there is a southward shift of 1–2° during the LIA. The dust mixing ratio remains longer on a high level in the recent climate. However, when reaching the Caribbean, the values for the two climate epochs converge. The situation in NH-autumn is opposite to the one in NH-winter. Although the deposition fluxes in the target regions are higher in the recent climate, the trajectories reach on average further west during the LIA (Fig. 5.18d). This indicates again that single, strong events of transatlantic dust transport are important, but in SON they occur more frequently and/or are more intense in the recent climate.

Despite these seasonal differences, the annually integrated zonal dust fluxes at various longitudes do not deviate more than 5% between both climate epochs (Table 5.5). Nevertheless, there are again some seasonal variations in the vertical distribution of the zonal dust flux, which is illustrated for the recent climate and the LIA at 10°W, 30°W, and 50°W in Figs. 5.19 – 5.22. In DJF the zonal transport across 10°W is higher during the LIA, especially south of 10°N (Figs. 5.19a,b). Across 30°W, there are higher values during the LIA close to the surface around 15°N (Figs. 5.19c,d), while at 50°W the zonal fluxes look almost equal (Figs. 5.19e,f). This indicates that between 30°W and 50°W more dust is deposited during the LIA, in accordance with higher deposition in the Amazon Basin during the LIA (see Table 5.3). Also in NH-spring zonal fluxes are generally higher during the LIA (Fig. 5.20). At 10°W the differences are especially visible close to the surface around 20°N and in the elevated layer around 10°N between 600 and 800 hPa (Figs. 5.20a,b). In addition to the generally higher fluxes, there is a structural difference at 30°W, where a certain amount of the transport during the LIA also occurs north of 25°N and shows a local maximum between 800 and 1 000 hPa around 29°N (Figs. 5.20c,d). The long-range transport through 30°W and 50°W reveals no marked differences between REC_chem and LIA_chem in JJA (Figs. 5.21c,d and e,f). Also the deposition fluxes in the target regions are quite similar with differences of about 10%

	REC	LIA
10°W	278.1	277.6
20°W	239.7	239.3
30°W	174.2	179.0
40°W	132.1	136.1
50°W	93.6	93.2
60°W	63.4	60.5

Table 5.5: Annually integrated zonal dust fluxes in Tg yr^{-1} across longitudes between 10 and 60°W in the recent climate and during the LIA.

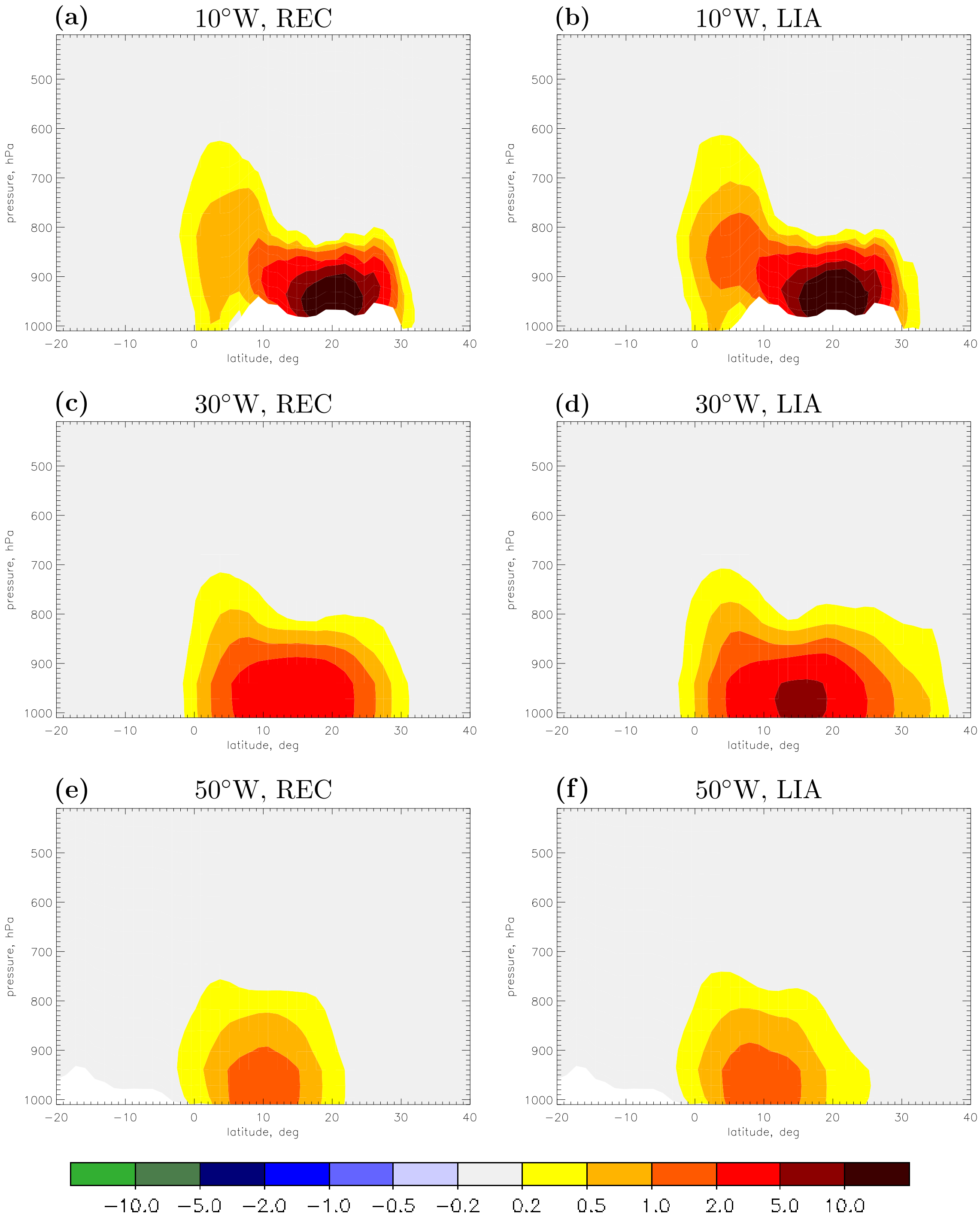

Fig. 5.19: Meridional cross sections of the DJF mean zonal dust flux of the Eulerian model output in kg m^{-2} per month of the REC_chem simulation (left column) and the LIA_chem simulation (right column) through 10°W (top), 30°W (middle), and 50°W (bottom). White areas at the bottom of panels (a), (b), (e), and (f) show the orography.

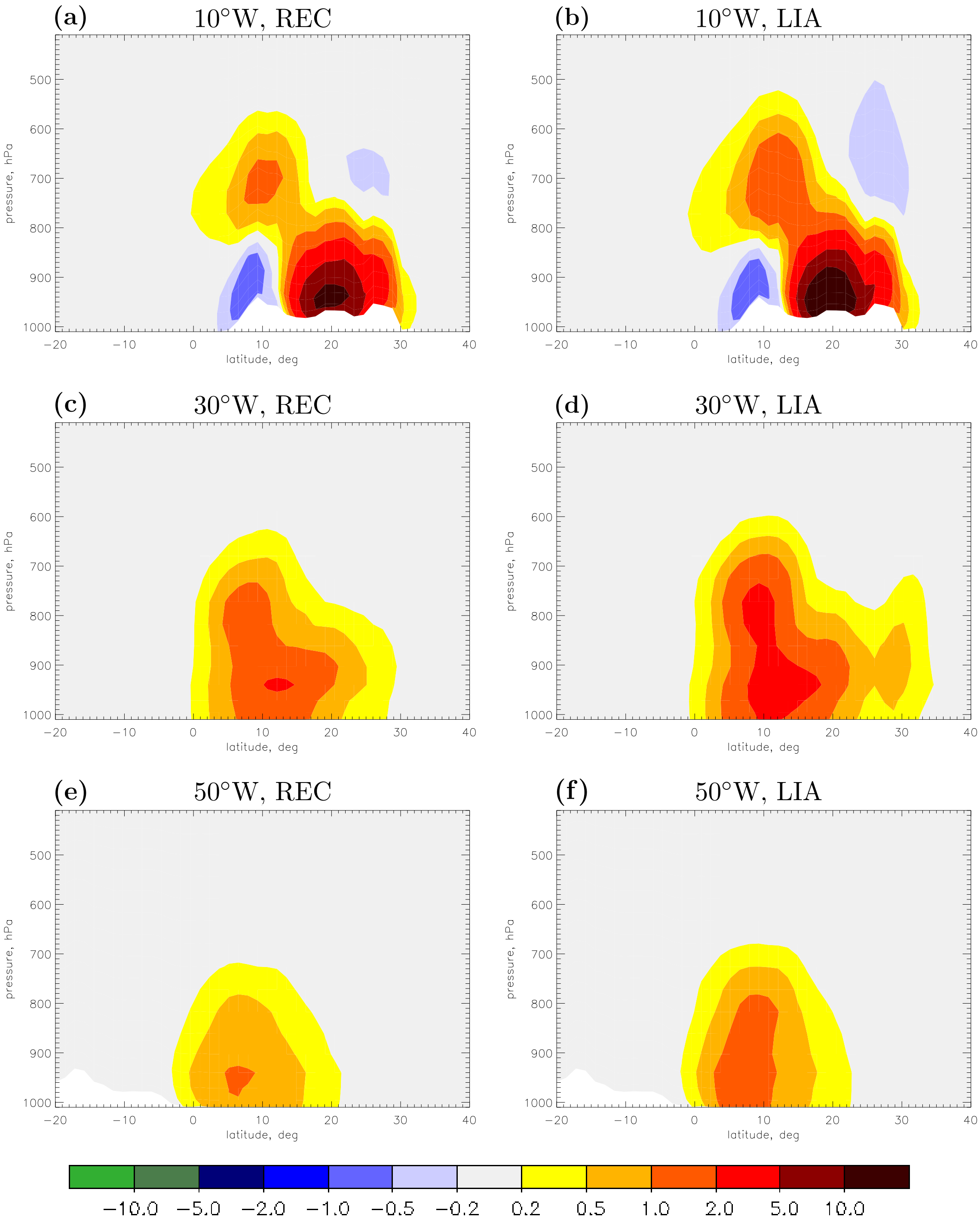

Fig. 5.20: Meridional cross sections of the MAM mean zonal dust flux of the Eulerian model output in kg m^{-2} per month of the REC_chem simulation (left column) and the LIA_chem simulation (right column) through 10°W (top), 30°W (middle), and 50°W (bottom). White areas at the bottom of panels (a), (b), (e), and (f) show the orography.

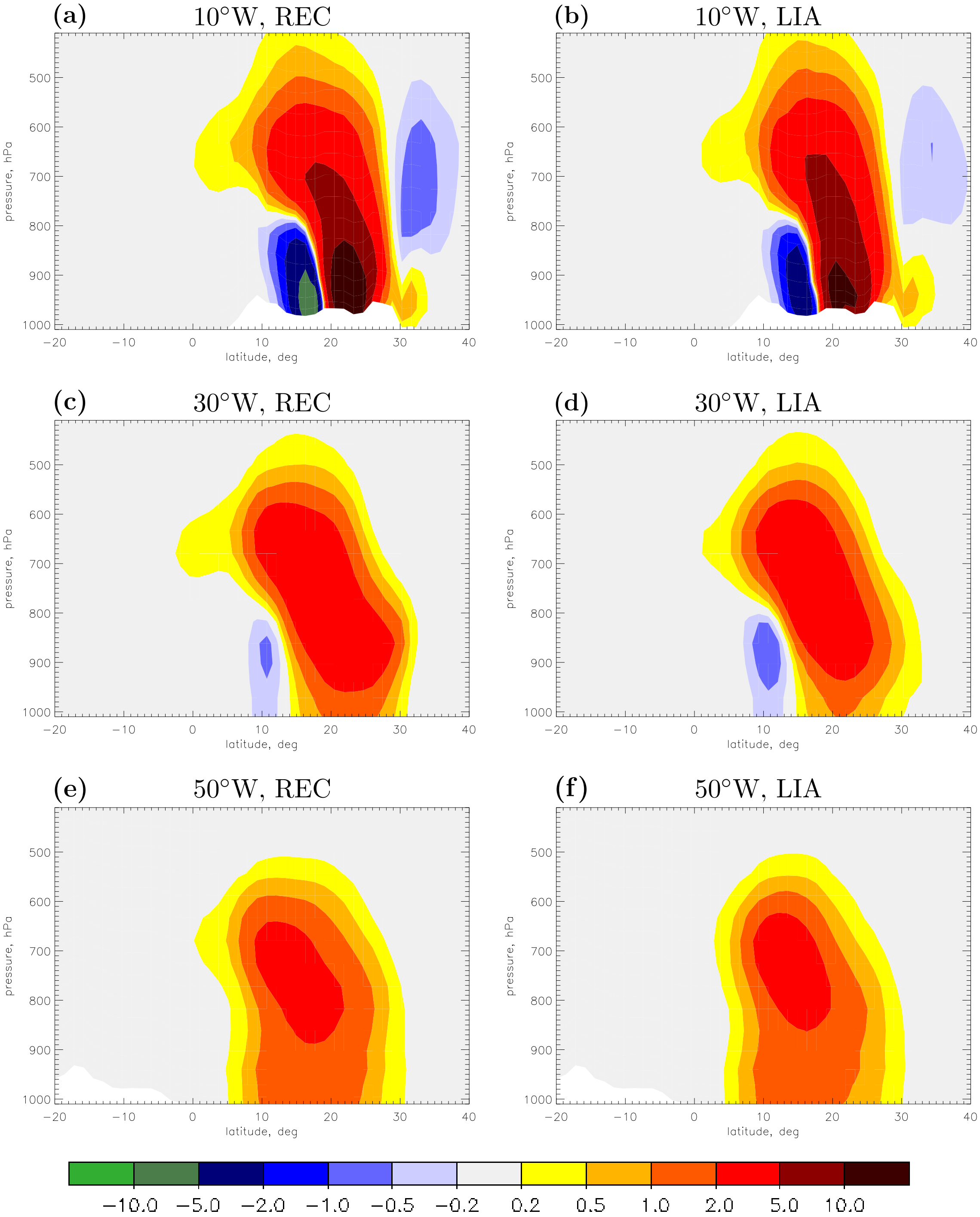

Fig. 5.21: Meridional cross sections of the JJA mean zonal dust flux of the Eulerian model output in kg m^{-2} per month of the REC_chem simulation (left column) and the LIA_chem simulation (right column) through 10°W (top), 30°W (middle), and 50°W (bottom). White areas at the bottom of panels (a), (b), (e), and (f) show the orography.

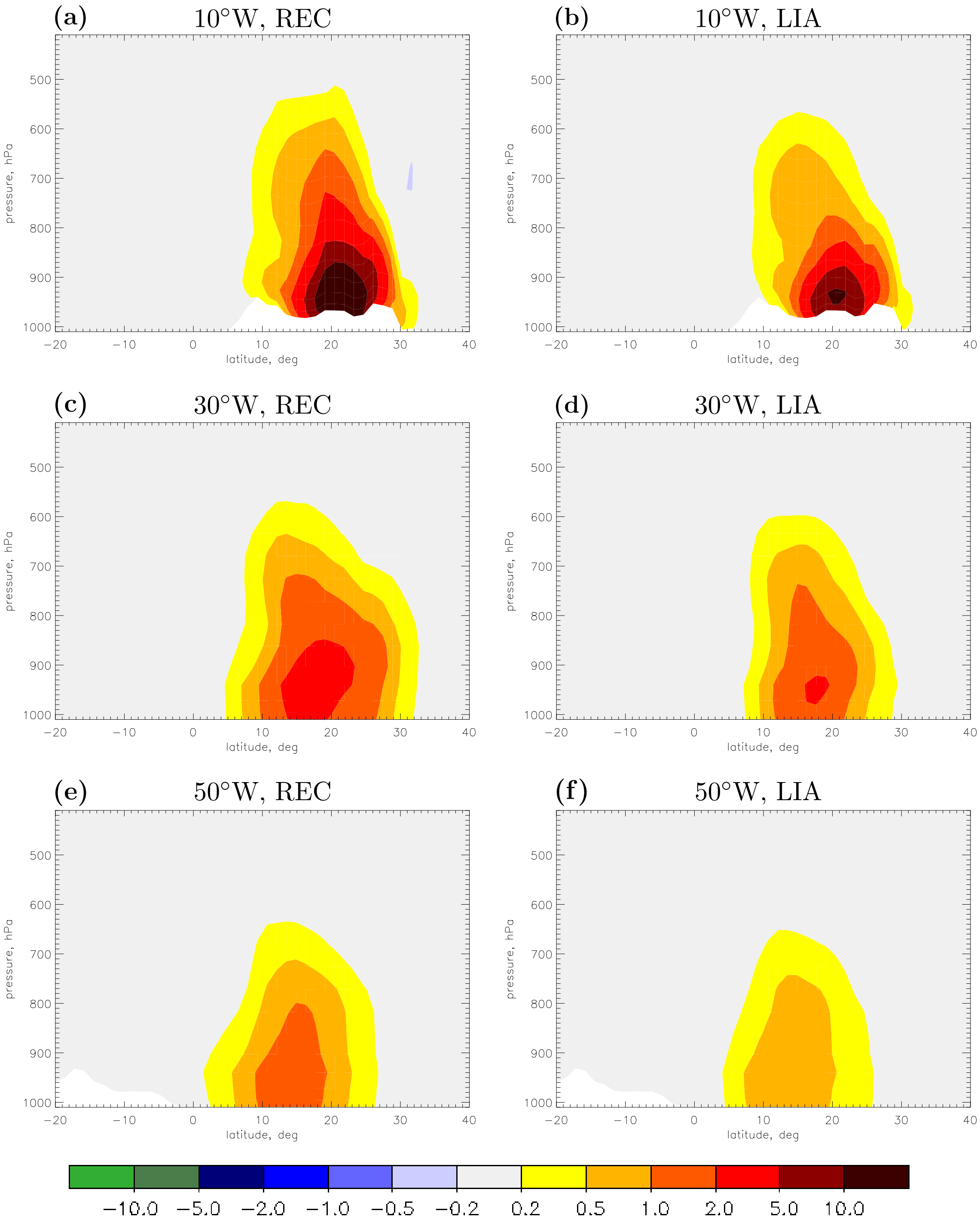

Fig. 5.22: Meridional cross sections of the SON mean zonal dust flux of the Eulerian model output in kg m^{-2} per month of the REC_chem simulation (left column) and the LIA_chem simulation (right column) through 10°W (top), 30°W (middle), and 50°W (bottom). White areas at the bottom of panels (a), (b), (e), and (f) show the orography.

(Table 5.3). At 10°W the maximum fluxes in the lower troposphere are higher in the recent climate. This is true for the westward fluxes north of 20°N and for the eastward fluxes between 10 and 20°N (Figs. 5.21a,b). Higher emissions in the recent climate in NH-autumn (see section 5.3.3) cause higher westward zonal dust fluxes at all illustrated longitudes (Fig. 5.22). The vertical structure of the transport, however, does not differ a lot between the two climate epochs in SON.

Source regions of dust reaching the Americas

The Lagrangian investigation of the explicit source regions in North Africa that contribute most to the transatlantic dust transport in the recent climate revealed the importance of the dust sources in central and Southwest Algeria, Mali, and Mauritania (see Fig. 4.15). Following the same approach (cf. section 4.6 on page 70) the source regions are calculated for the trajectories of the LIA_chem simulation. The differences of both climate epochs (recent climate minus LIA) are shown for dust reaching the Amazon Basin and the Caribbean in Figs. 5.23a,b, respectively. The annual dust deposition in the Amazon Basin during the LIA is about 5% higher than in the recent climate (Table 5.3). The main source regions, namely Algeria, Mauritania, and Mali (centred around 25°N, 5°W), are the same in both climate epochs but their intensity is higher during the LIA (Fig. 5.23a). The contribution of source regions in Niger is also stronger during the LIA, while the importance of dust sources north of 30°N is slightly higher in the recent climate (Fig. 5.23a).

The annual dust deposition in the Caribbean is almost equal in both climate epochs (Table 5.3), meaning that the positive and negative differences in Fig. 5.23b cancel.

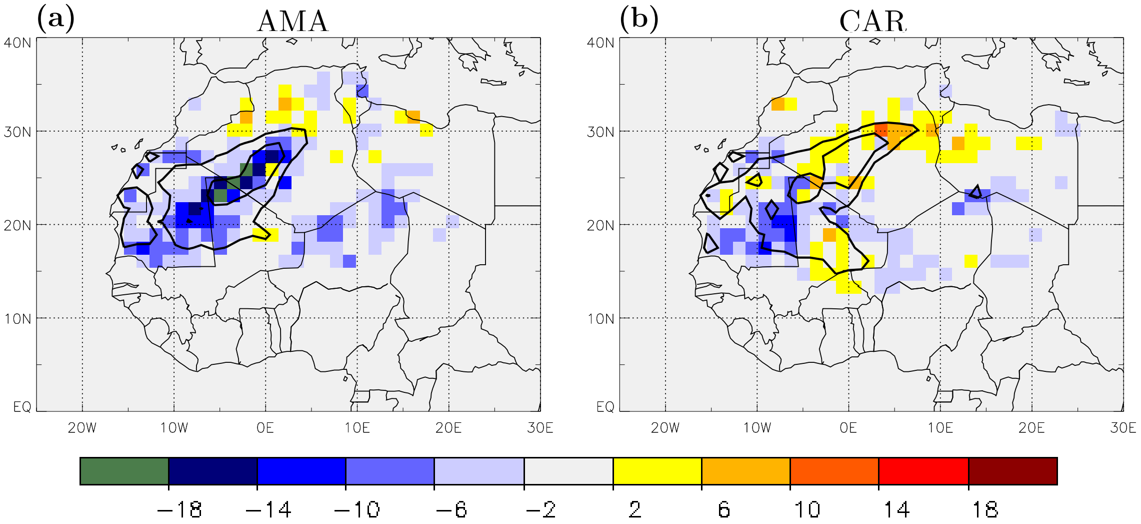

Fig. 5.23: Source regions of dust reaching the Amazon Basin (a) and the Caribbean (b). The shading shows the difference of the recent climate minus the LIA in kg ha^{-1} yr^{-1} and bold black isolines (25 and 50 kg ha^{-1} yr^{-1}) mark the absolute values of the recent climate.

The differences in the regions contributing most to the Caribbean dust, indicated by the interior bold black isoline, are quite small. However, there is a southwestward shift in the source regions from the recent climate to the LIA, visible in the blueish colours around 20°N, 7°W and the reddish colours at 30°N, 5°E. This is consistent with the difference of the annual dust emission fluxes between the recent climate and the LIA (Fig. 5.11), which also shows a dipole pattern over West Africa, with higher recent emissions north of about 22°N and higher emissions during the LIA further south, induced by the more intense WAM.

5.4 Summary

With boundary conditions representing the year AD 1600, the model requires one to two years to spin up and produce stable conditions. Changes in the model setup are restricted to the SST, SIC, GHG concentrations and volcanic stratospheric aerosol. The model reproduces a "Little Ice Age" with a cooling of 0.67 K on the global scale and 0.9 K on the northern hemispheric land surface, compared to recent conditions. With respect to the global annual dust cycle, the differences between the two climate epochs are quite small. Nevertheless, there are some interesting regional and seasonal discrepancies.

Asian source regions are more active in the recent climate. Strong warming over the northern part of India in JJA induces a regional pressure contrast and a circulation that leads to higher dust emissions in the Thar Desert in the recent climate. The Indian Monsoon, however, is stronger during the LIA, causing higher dust emissions in the eastern part of the Arabian Peninsula. Together with a shift in the precipitation pattern, this causes higher dust deposition fluxes over the western part of the Indian subcontinent during the LIA, while further east more dust is deposited in the recent climate.

An intensification of the WAM during the LIA generates wetter conditions in the Sahel and stronger dust emissions from the southern source regions in West Africa in JJA. In NH-autumn an increased pressure gradient over North Africa in the recent climate induces higher 10-m winds and dust emissions over almost the entire continent. Compared to the differences in JJA and SON, the effects are smaller during the rest of the year. The Bodélé Depression, the world's most active dust source region, shows only slightly higher emissions during the LIA in DJF and higher recent emissions on the same order of magnitude in MAM.

On the annual scale the transatlantic dust transport shows no distinct differences between the LIA_chem and the REC_chem simulations. The location of the source regions of dust that reaches the Amazon Basin is mainly the same in both climate epochs, i.e., Southwest Algeria, Mauritania, and North Mali. Slightly stronger emissions during the LIA cause a 5% increase in the annual deposition fluxes in the

Amazon region. The largest contribution to this difference occurs during MAM, when stronger emissions in North Africa and a faster transport across the Atlantic Ocean lead to higher dust deposition fluxes in the Americas. In the Caribbean, however, seasonal differences between the climate epochs change sign during the year and compensate each other, with the result that annual dust deposition in the Caribbean during the LIA is almost the same as in the recent climate. In both climate epochs the dust source regions in Algeria, Mauritania, and Mali contribute most to the dust that is deposited in the Caribbean. During the LIA, however, the activity is increased in Mali, while the contribution of Algerian sources is higher in the recent climate.

One must consider that REC_chem and LIA_chem use identical surface parameters, which affect the dust emissions. Adapting these parameters for the LIA would influence the differences in the mineral dust cycle between both climate epochs.

6

Conclusion

The effects of airborne mineral dust particles on the regional and global climate are not yet fully understood. With an atmospheric life time of several days dust particles are able to travel distances of thousands of kilometres. On their way they potentially influence the atmospheric state, the weather, and ultimately the climate through their direct and indirect impacts on clouds and precipitation, radiation, and the dynamics. The deposited dust fertilises oceans and rain forests, sometimes far away from the dust source regions. Additionally, the impact of changed climatic conditions on the dust cycle and possible feedback mechanisms have not been studied in detail so far.

This thesis provides the first systematic, climatological investigation of the global mineral dust cycle as simulated with the GCCM EMAC. The objectives of the present study involve the analysis of the performance of various model setups and the determination of the most appropriate one with regard to the dust cycle. Moreover, results from the simulation with this setup form the basis for further investigations of characteristics of the transatlantic dust transport such as the seasonality and the duration of the transport and the localisation of the main source regions. Another focus is on the reconstruction of the dust cycle under climatic conditions of the LIA and the question if there are systematic differences between this cold anomaly and the recent climate.

6.1 Discussion of the results

Sensitivity studies target the influence of the chemical setup and the choice of the dust emission scheme and the spectral model resolution on the dust cycle. They show the necessity of including a basic sulphur chemistry in order to capture the ageing of dust particles and dust removal processes in a realistic way. Disproportionally high dust emissions from the Thar Desert in India, corroborating results of Stier et al. (2005), have been identified as a problematic aspect of the dust emission scheme of Balkanski et al. (2004). The scheme by Tegen et al. (2002) produces a more reliable global distribution of dust emission fluxes and is therefore preferred for the detailed dust cycle investigations in the present study. The spectral resolutions T42 and T63 are found to generate erroneous dust emission fluxes in important dust source regions as the Bodélé Depression (underestimation) and the Tarim Basin (overestimation). Such resolution-induced deficiencies might also arise in simulations of the mineral dust cycle with other model systems, independent of the dust emission scheme. In comparison with in-situ measurements of dust concentrations and deposition fluxes, the T85 spectral resolution yields a more realistic global dust cycle than the T106 resolution.

In conclusion, it is found that the most appropriate setup for simulating the global mineral dust cycle with EMAC comprises a basic sulphur chemical mechanism, the spectral resolution T85, and the dust emission scheme described by Tegen et al. (2002). This setup is recommended for future simulations of the dust cycle with the EMAC model system.

The transport of dust from North Africa across the Atlantic Ocean to the Americas is investigated in the second part of this thesis, gaining new insights into the source regions of the dust. For the first time, a combination of Eulerian and Lagrangian approaches is used to climatologically analyse the transatlantic dust transport based on results of a five-year time slice simulation. The main North African source regions of the dust that reaches the Americas are found to be located in Algeria, Mauritania, and Mali. Very surprising, because in marked contrast to earlier studies, e.g., by Kaufman et al. (2005) and Koren et al. (2006), is the result that the contribution of dust from the Bodélé Depression is quite low. To verify this finding, it is investigated in detail with different methodologies, each of them corroborating the new result. Because of the inconsistency with previous knowledge, this issue has to be further scrutinised in the future, as particularly discussed in the outlook in section 6.2.

Largely in line with prior studies are other aspects of the transatlantic dust transport. The model results show an annual variation of the transport, which is zonally oriented towards the Caribbean during NH-summer, while it reaches South America during NH-winter. The transport in boreal spring and autumn shows transitional characteristics. This seasonal shift is well known and documented, e.g., by Ben-Ami et al. (2012) and citations therein. These earlier studies used satellite retrievals, ground-based measurements, or relatively short-term model simulations, which are now corroborated by the continuous five-year time slice simulation presented here. The solstice seasons also differ in the vertical extent of the transport. In NH-winter dust crosses the Atlantic Ocean in the lower troposphere, below 800 hPa. The transport mainly occurs at higher levels between 600 and 900 hPa in NH-summer. Carlson and Prospero (1972) introduced the now commonly used term SAL for this dusty air layer, which suggests a more or less continuous dust transport from North

Africa westwards during NH-summer. In fact, however, there are single, well separated events of Saharan dust outbreaks, described, e.g., by Prospero (1999) and verified here by five-year time series.

Based on the five-year model output, dust is traced by forward trajectories from its African source regions to the deposition regions across the Atlantic Ocean, allowing for unprecedented accuracy in determining the transport time. On average, the dust takes about nine days in NH-winter and ten days in NH-summer from Africa to the Amazon Basin and the Caribbean, respectively. First estimates of the transport time from the African coast to the Caribbean were based on the arrival time differential between three dust measurement stations (Sal Island/Cape Verde, Barbados, and Miami) during the NH-summer of 1974 and amounted to five to seven days (Prospero and Carlson 1981). Similar results were obtained by Engelstaedter et al. (2009), initialising backward trajectories at Barbados on days in June between 1980 and 1992. The difference of three to four days between these studies and results presented here matches the time that the dust takes from its emission regions to the African coast, which was not considered by Prospero and Carlson (1981) and Engelstaedter et al. (2009). Thus, their findings can be corroborated by the Lagrangian investigation of the five-year time slice simulation.

The third part of this thesis deals with the changes in the mineral dust cycle under the climatic conditions during the LIA in the middle of the past millennium. Previous palaeoclimatic reconstructions, focussing on mineral dust, are restricted to simulations of the LGM, about 20 000 years ago. The present study gives insight into the impact of climatic changes on the dust cycle on time scales of few centuries. Sea surface temperature, sea ice concentration, greenhouse gas concentrations, and volcanic stratospheric aerosols are adapted in the model to represent the climate of the year AD 1600.

The simulated cooling is on the order of 0.5 to 1 K and thus similar to other reconstructions of this time (e.g., Jungclaus et al. 2010). Accompanied dynamical changes influence the dust cycle on regional and seasonal scale, while the annual global dust budget shows no significant response. The verification of the simulation with regard to the dust cycle is problematic because only few ice or marine sediment cores provide information on dust concentrations or deposition fluxes during the LIA. Further limitations concern the representativity of the five-year time slice simulation, which only covers a short period of the LIA, lasting from the 13th to the 19th century. Moreover, the changes in the model setup do not consider surface parameters as land use and vegetation, and thus the roughness length. These parameters, however, influence the soil moisture and near-surface wind speed and they are therefore crucial for the dust emission. Mulitza et al. (2010), for example, described increased dust emissions from West Africa during the last two centuries and discussed a causal relation to agricultural activities in the Sahel, which modified the surface properties there. The aforementioned aspects, i.e., unchanged surface parameters, the length of the time slices, and the shortage of comparison data sets, offer large potential for improvements, as described in the subsequent outlook.

Despite these potential elements of uncertainty, the comparison of the simulations during the LIA and in the recent climate reveals interesting climatic differences. Intensification of the Indian summer monsoon during the LIA is consistent with findings by Denniston et al. (2000). As a consequence, dust emissions from the Arabian Peninsula are increased due to higher near-surface wind velocities. The WAM circulation is intensified during the LIA as well, involving on average higher dust emissions from North African source regions during NH-summer and wetter conditions in the Sahel.

6.2 Outlook

The general performance of GCMs in simulating the global mineral dust cycle holds potential for future improvements. Wide ranges of simulated surface dust fluxes and atmospheric dust burden, depending on the model system and setup, show the uncertainties that the simulations of the dust cycle are fraught with. To reduce these uncertainties, it is essential to improve our knowledge about the real dust cycle. There are only few measurement sites recording surface dust concentrations, deposition fluxes, and aerosol optical thickness. Additionally, most of these stations are quite far away from the main dust source regions in the large deserts. Therefore, the measurements are very sparse in those regions where the information would be most valuable and extensions of the measuring network would improve the understanding of the dust cycle. Furthermore, refinements of retrieval algorithms could increase the accuracy of satellite-based estimates of the dust column mass, which might be the most appropriate parameter for comparisons between satellite and model data. Evaluation and tuning of models with such improved satellite products and with extended ground-based measurements would narrow the wide range of simulated dust parameters, reducing the uncertainty of the models.

On the other hand, the representation of emission, ageing, and atmospheric removal of dust particles in numerical models might be improved by gaining further insight into these processes with the aid of experimental studies. However, limiting factors will remain, even if there would be “perfect” parametrisations for these processes. For example, global maps of surface parameters and soil properties can always be more detailed and accurate. Moreover, the computational cost of improved and potentially more complex parametrisations must stay within reason to be applicable for global simulations.

New findings presented in this thesis are based on free running five-year time slice simulations with the GCCM EMAC. Many examples of simulations with different model systems show the dependency of various model results on the horizontal resolution (see section 3.1). It is obvious that the dependency of the dust cycle on the resolution occurs not only in EMAC but in other GCMs as well. To investigate this and also the dependency on the dust emission scheme with different model systems, e.g., those participating in the AEROCOM project (Huneeus et al. 2011), might be a fruitful future study. This would answer the question if the resolution- and emission scheme-dependent results found here are model specific or generally valid. Another topic, worthwhile to look at, concerns the impact of the nudging, as Timmreck and Schulz (2004) described significant differences in the dust cycle between nudged and free-running simulations with the ECHAM4 model system.

Furthermore, the length of time slice simulations influences the results of a model. Simulations longer than five years would enhance the statistical significance of the discussed findings. This might especially make the climatic differences between the simulations during the LIA and in the recent climate more conclusive. Moreover, changed surface parameters and their influence on the dust emission may be considered in future investigations of the mineral dust cycle during different climate epochs. The present study, neglecting land surface changes, could serve as basic reference for such more sophisticated studies. Existing ice and marine sediment cores comprise valuable information on the palaeoclimatic dust cycle (Mahowald et al. 1999). A higher time resolution of such core data could provide an excellent opportunity for evaluating the mineral dust cycle in simulations during the past millennium. This, in turn, would increase our understanding of the climate variablity on the time scale of centuries and potentially improve future climate projections.

The major controversy, this thesis raises, concerns the Bodélé Depression, which is the most outstanding dust source region in the world. Dust from this hot spot was assumed to constitute a large proportion of the total transatlantic dust transport but this is not corroborated by results presented here. Refinements of the Lagrangian methods are required to analyse this issue in even greater detail. It needs to be investigated wheather and to what extent the Bodélé Depression contributes to the dust transport from North Africa across the Atlantic Ocean, which stays an open question here.

Appendix

A

MECCA reaction tables

A complete list of references and further information on this chemical mechanism is available in the electronic supplement “The Basic Sulphur Chemical Mechanism of MECCA” of Gläser et al. (2012b).

Table A.1: Gas phase reactions.

#	reaction	rate coefficient
`G1000`	O_2 + O1D → O3P + O_2	`3.3E-11*EXP(55./temp)`
`G1001`	$O_2 + O(^3P) \rightarrow O_3$	`6.E-34*((temp/300.)**(-2.4))*cair`
`G1002a`	$O_3 + O(^1D) \rightarrow 2\ O_2$	`1.2E-10`
`G1003a`	$O_3 + O(^3P) \rightarrow 2\ O_2$	`8.E-12*EXP(-2060./temp)`
`G2100`	$H + O_2 \rightarrow HO_2$	`k_3rd(temp,cair,4.4E-32,1.3,4.7E-11,0.2,0.6)`
`G2104`	$OH + O_3 \rightarrow HO_2 + O_2$	`1.7E-12*EXP(-940./temp)`
`G2105`	$OH + H_2 \rightarrow H_2O + H$	`2.8E-12*EXP(-1800./temp)`
`G2107`	$HO_2 + O_3 \rightarrow OH + 2\ O_2$	`1.E-14*EXP(-490./temp)`
`G2109`	$HO_2 + OH \rightarrow H_2O + O_2$	`4.8E-11*EXP(250./temp)`
`G2110`	$HO_2 + HO_2 \rightarrow H_2O_2 + O_2$	`kHO2_HO2`
`G2111`	$H_2O + O(^1D) \rightarrow 2\ OH$	`1.63E-10*EXP(60./temp)`
`G2112`	$H_2O_2 + OH \rightarrow H_2O + HO_2$	`1.8E-12`
`G3101`	$N_2 + O(^1D) \rightarrow O(^3P) + N_2$	`2.15E-11*EXP(110./temp)`
`G3103`	$NO + O_3 \rightarrow NO_2 + O_2$	`3.E-12*EXP(-1500./temp)`
`G3106`	$NO_2 + O_3 \rightarrow NO_3 + O_2$	`1.2E-13*EXP(-2450./temp)`
`G3108`	$NO_3 + NO \rightarrow 2\ NO_2$	`1.5E-11*EXP(170./temp)`
`G3109`	$NO_3 + NO_2 \rightarrow N_2O_5$	`k_NO3_NO2`
`G3110`	$N_2O_5 \rightarrow NO_2 + NO_3$	`k_NO3_NO2/(2.7E-27*EXP(11000./temp))`
`G3201`	$NO + HO_2 \rightarrow NO_2 + OH$	`3.5E-12*EXP(250./temp)`

– continued on next page –

– continued from previous page –

#	reaction	rate coefficient
G3202	$NO_2 + OH \rightarrow HNO_3$	`k_3rd(temp,cair,1.8E-30,3.0,2.8E-11,0.,0.6)`
G3203	$NO_2 + HO_2 \rightarrow HNO_4$	`k_NO2_HO2`
G3204	$NO_3 + HO_2 \rightarrow NO_2 + OH + O_2$	`3.5E-12`
G3206	$HNO_3 + OH \rightarrow H_2O + NO_3$	`k_HNO3_OH`
G3207	$HNO_4 \rightarrow NO_2 + HO_2$	`k_NO2_HO2/(2.1E-27*EXP(10900./temp))`
G3208	$HNO_4 + OH \rightarrow NO_2 + H_2O$	`1.3E-12*EXP(380./temp)`
G4101	$CH_4 + OH \rightarrow CH_3O_2 + H_2O$	`1.85E-20*EXP(2.82*log(temp)-987./temp)`
G4102	$CH_3OH + OH \rightarrow HCHO + HO_2$	`2.9E-12*EXP(-345./temp)`
G4103	$CH_3O_2 + HO_2 \rightarrow CH_3OOH + O_2$	`4.1E-13*EXP(750./temp)`
G4104	$CH_3O_2 + NO \rightarrow HCHO + NO_2 + HO_2$	`2.8E-12*EXP(300./temp)`
G4105	$CH_3O_2 + NO_3 \rightarrow HCHO + HO_2 + NO_2$	`1.3E-12`
G4106a	$CH_3O_2 + CH_3O_2 \rightarrow 2\ HCHO + 2\ HO_2$	`9.5E-14*EXP(390./temp)/(1.+ 1./26.2*EXP(1130./temp))`
G4106b	$CH_3O_2 + CH_3O_2 \rightarrow HCHO + CH_3OH + O_2$	`9.5E-14*EXP(390./temp)/(1.+26.2*EXP(-1130./temp))`
G4107	$CH_3OOH + OH \rightarrow .7\ CH_3O_2 + .3\ HCHO + .3\ OH + H_2O$	`k_CH3OOH_OH`
G4108	$HCHO + OH \rightarrow CO + H_2O + HO_2$	`9.52E-18*EXP(2.03*log(temp)+ 636./temp)`
G4109	$HCHO + NO_3 \rightarrow HNO_3 + CO + HO_2$	`3.4E-13*EXP(-1900./temp)`
G4110	$CO + OH \rightarrow H + CO_2$	`(1.57E-13+cair*3.54E-33)`
G9200	$SO_2 + OH \rightarrow H_2SO_4 + HO_2$	`k_3rd(temp,cair,3.3E-31,4.3,1.6E-12,0.,0.6)`
G9400a	$DMS + OH \rightarrow CH_3SO_2 + HCHO$	`1.13E-11*EXP(-253./temp)`
G9400b	$DMS + OH \rightarrow DMSO + HO_2$	`k_DMS_OH`
G9401	$DMS + NO_3 \rightarrow CH_3SO_2 + HNO_3 + HCHO$	`1.9E-13*EXP(520./temp)`
G9402	$DMSO + OH \rightarrow .6\ SO_2 + HCHO + .6\ CH_3O_2 + .4\ HO_2 + .4\ CH_3SO_3H$	`1.E-10`
G9403	$CH_3SO_2 \rightarrow SO_2 + CH_3O_2$	`1.9E13*EXP(-8661./temp)`
G9404	$CH_3SO_2 + O_3 \rightarrow CH_3SO_3$	`3.E-13`
G9405	$CH_3SO_3 + HO_2 \rightarrow CH_3SO_3H$	`5.E-11`

Notes:

- Rate coefficients for three-body reactions are defined via the function `k_3rd`(T, M, k_0^{300}, n, k_{inf}^{300}, m, f_c). In the code, the temperature T is called `temp` and the concentration of "air molecules" M is called `cair`. Using the auxiliary variables $k_0(T)$, $k_{\mathrm{inf}}(T)$, and k_{ratio}, `k_3rd` is defined as:

$$k_0(T) = k_0^{300} \times \left(\frac{300\ \mathrm{K}}{T}\right)^n \tag{A.1}$$

$$k_{\mathrm{inf}}(T) = k_{\mathrm{inf}}^{300} \times \left(\frac{300\ \mathrm{K}}{T}\right)^m \tag{A.2}$$

$$k_{\mathrm{ratio}} = \frac{k_0(T)M}{k_{\mathrm{inf}}(T)} \tag{A.3}$$

$$\mathtt{k\_3rd} = \frac{k_0(T)M}{1+k_{\mathrm{ratio}}} \times f_\mathrm{c}^{\left(\frac{1}{1+(\log_{10}(k_{\mathrm{ratio}}))^2}\right)} \tag{A.4}$$

- `EXP`(y) $\equiv e^{\mathrm{y}}$
- x.Ey $\equiv \mathrm{x} \cdot 10^{\mathrm{y}}$
- `C(ind_X)`: concentration of `X` in molecules cm^{-3}
- `k_HO2_HO2 = (1.5E-12EXP(19./temp)+1.7E-33*EXP(1000./temp)*cair)* (1.+1.4E-21*EXP(2200./temp)*C(ind_H2O))`
- `k_NO3_NO2 = k_3rd(temp,cair,2.E-30,4.4,1.4E-12,0.7,0.6)`
- `k_NO2_HO2 = k_3rd(temp,cair,1.8E-31,3.2,4.7E-12,1.4,0.6)`
- `k_HNO3_OH = 2.4E-14*EXP(460./temp)+1./(1./(6.5E-34*EXP(1335./temp)* cair)+1./(2.7E-17*EXP(2199./temp)))`
- `k_CH3OOH_OH = 3.8E-12*EXP(200./temp)`
- `k_DMS_OH = 1.E-39*EXP(5820./temp)*C(ind_O2)/(1.+5.E-30* EXP(6280./temp)*C(ind_O2))`

Table A.2: Photolysis reactions.

#	reaction	rate coefficient
`J1000`	$O_2 + h\nu \rightarrow O(^3P) + O(^3P)$	`jx(ip_O2)`
`J1001a`	$O_3 + h\nu \rightarrow O(^1D)$	`jx(ip_O1D)`
`J1001b`	$O_3 + h\nu \rightarrow O(^3P)$	`jx(ip_O3P)`
`J2101`	$H_2O_2 + h\nu \rightarrow 2\ OH$	`jx(ip_H2O2)`
`J3101`	$NO_2 + h\nu \rightarrow NO + O(^3P)$	`jx(ip_NO2)`
`J3103a`	$NO_3 + h\nu \rightarrow NO_2 + O(^3P)$	`jx(ip_NO2O)`
`J3103b`	$NO_3 + h\nu \rightarrow NO$	`jx(ip_NOO2)`
`J3104a`	$N_2O_5 + h\nu \rightarrow NO_2 + NO_3$	`jx(ip_N2O5)`
`J3201`	$HNO_3 + h\nu \rightarrow NO_2 + OH$	`jx(ip_HNO3)`
`J3202`	$HNO_4 + h\nu \rightarrow .667\ NO_2 + .667\ HO_2 + .333\ NO_3 + .333\ OH$	`jx(ip_HNO4)`
`J4100`	$CH_3OOH + h\nu \rightarrow HCHO + OH + HO_2$	`jx(ip_CH3OOH)`
`J4101a`	$HCHO + h\nu \rightarrow H_2 + CO$	`jx(ip_COH2)`
`J4101b`	$HCHO + h\nu \rightarrow H + CO + HO_2$	`jx(ip_CHOH)`

Notes:

The rate coefficients (J-values) are calculated in the MESSy submodel JVAL and then supplied to the MECCA chemistry.

B

MESSy submodels used in this thesis

Submodel name	Reference and short description referring to http://www.messy-interface.org.
CLOUD	contains the original cloud process and cover routines from ECHAM5 in a modularised, MESSy-conform structure and calculates the cloud cover as well as cloud microphysics including precipitation (Jöckel et al. 2006).
CONVECT	calculates the process of **convect**ion. It consists of an interface to choose different convection schemes and the calculations themselves. Currently, the original ECHAM5 convection routines with all three closures (Nordeng, Tiedtke, Hybrid), including an update for positive definite tracers, are implemented. Additionally two different convection schemes are selectable (Tost et al. 2010). In this thesis the Tiedtke scheme with the Nordeng closure is used, which is the default convection parametrisation.
CVTRANS	stands for **c**on**v**ective tracer **trans**port and calculates the transport of tracers due to convection. It uses a monotonic, positive definite and mass conserving algorithm following the bulk approach (Tost 2006a).
DRYDEP	calculates gas phase and aerosol tracer **dry dep**osition according to the ‘big leaf approach’ (Kerkweg et al. 2006a).
JVAL	provides online calculations of photolysis rate coefficients (**J-val**ues) using cloud water and ice content and cloudiness, calculated by the basemodel, as well as climatological aerosol and ozone. A delta-twostream-method is used for 8 spectral intervals in the UV and visible spectrum together with pre-calculated effective crosssections (partially temperature and pressure dependent) for more than 50 tropospheric and stratospheric species (Jöckel et al. 2006).

LNOX	contains a parametrisation to calculate the $\mathbf{NO}_X$ production resulting from **l**ightning activity (Tost et al. 2007).
M7	is a dynamical aerosol model that redistributes number and mass between **7** **m**odes and from the gas to the aerosol phase (for each mode), by nucleation, condensation and coagulation (Kerkweg et al. 2008).
MECCA	stands for **M**odule **E**fficiently **C**alculating the **C**hemistry of the **A**tmosphere and calculates tropospheric and stratospheric chemistry (Sander et al. 2011). More information on the chemical setup are provided in section 2.5 and appendix A.
OFFLEM	stands for **offl**ine **em**issions and reads emission fluxes in 2D, i.e., surface emissions and 3D, e.g., aircraft emissions from netCDF-files and updates the tracer tendencies accordingly (Kerkweg et al. 2006b).
ONLEM	stands for **onl**ine-calculated **em**issions and calculates 2D surface emission fluxes for gas-phase tracers, which depend on prognostic variables, and updates the tracer tendencies accordingly. In addition, aerosol source functions are calculated (Kerkweg et al. 2006b). Details about the emission of mineral dust, that is calculated within this submodel, are provided in section 2.3.
RAD4ALL	is a re-implementation of the ECHAM5 radiation code (ECHAM version 5.3.01) according to the MESSy standard. New and extended features are: (1) Choice between standard ECHAM5 radiation and RAD4ALL is done via namelist. (2) All input quantities are now controlled by namelist. (3) Online coupling of radiation with trace gases. (4) All input quantities (except aerosols in the current version) can be read from external climatologies (Jöckel et al. 2006).
SCAV	stands for **scav**enging and simulates the processes of wet deposition as well as liquid and ice phase chemistry in precipitation fluxes. It considers gas-phase and aerosol species in large-scale as well as in convective clouds and precipitation events (Tost et al. 2006b).
SEDI	calculates **sedi**mentation of aerosol particles and their components (Kerkweg et al. 2006a).
TNUDGE	stands for **t**racer **nudg(e)**ing and is used for nudging user-defined tracers with arbitrary user-defined fields (Kerkweg et al. 2006b).

TROPOP	calculates the **tropop**ause height according to various definitions (WMO, PV) and other diagnostics as the planetary boundary layer height (Jöckel et al. 2006). The latter is used for defining criteria for trajectory initialisation in this thesis (see section 4.2.2).

C

Dust measurements

Table C.1: List of dust deposition measurements.

Latitude	Longitude	$\frac{g}{m^{-2}\ yr^{-1}}$	Latitude	Longitude	$\frac{g}{m^{-2}\ yr^{-1}}$
Ginoux et al. (2001)			Tegen et al. (2002)		
52.92	174.06	0.60	-64.93	-2.59	0.52
45.50	6.50	2.10	5.37	-85.58	4.80
41.80	2.30	5.30	50.00	-144.98	0.30
28.20	-177.35	0.60	-20.07	9.17	5.80
25.75	-80.25	1.62	-20.05	9.16	2.50
21.30	-157.6	0.42	-20.05	9.16	3.80
11.30	162.30	0.44	-35.52	161.00	1.24
3.90	-159.30	0.09	-17.76	154.83	0.40
-0.53	166.95	0.23	-12.99	155.99	0.73
-14.25	-170.60	0.15	0.00	175.00	0.92
-21.25	-159.75	0.21	0.00	175.16	0.73
-22.15	167.00	0.37	1.22	160.57	0.84
-29.08	167.98	0.64	5.01	138.83	0.57
-34.50	172.75	0.14	12.02	134.29	0.11
40.00	85.00	450.00	30.00	175.00	3.00
32.00	34.50	30.00	34.42	177.74	3.25
			37.40	174.95	8.77
Mahowald et al. (2009)			40.00	145.43	7.32
42.00	9.0	15.43	46.12	175.03	4.09
-69.52	170.6	0.002	46.82	162.12	0.86
-75.00	-170.6	0.003	10.00	65.00	1.50
-76.45	-175.5	0.003	14.48	64.77	4.30
-64.60	140.3	0.001	15.47	68.75	7.40
-64.88	141.0	0.001	15.98	61.50	4.50

– continued on next page –

– continued from previous page –

Latitude	Longitude	$\frac{g}{m^{-2}\ yr^{-1}}$	Latitude	Longitude	$\frac{g}{m^{-2}\ yr^{-1}}$
-64.97	141.4	0.001	16.25	60.47	6.10
-64.93	141.2	0.001	17.40	58.80	12.40
-65.57	74.9	0.002	-2.18	-9.90	1.20
-64.90	75.0	0.003	1.79	-11.13	4.30
-66.12	75.3	0.002	11.48	-21.02	22.62
-66.30	75.7	0.002	18.50	-21.08	18.74
-70.57	76.9	0.002	19.00	-20.17	21.55
-73.43	76.2	0.002	20.92	-19.75	21.92
-74.90	74.5	0.001	20.92	-19.74	27.20
-75.85	71.5	0.001	20.92	-19.74	11.39
-66.77	112.8	0.001	21.15	-20.68	19.70
29.52	34.9	5.83	21.15	-20.69	20.48
43.10	141.3	5.20	21.15	-31.17	3.73
31.50	35.3	44.57	21.93	-25.23	6.70
32.70	35.5	285.71	24.55	-22.83	5.21
35.20	24.8	21.26	28.00	-21.98	2.40
43.50	4.8	11.31	29.11	-15.45	4.15
43.60	7.3	1.80	31.55	-24.67	2.36
36.30	-5.4	22.80	32.08	-64.25	1.90
54.42	-7.2	2.09	33.15	-21.98	1.76
54.30	-8.6	1.57	33.82	-21.02	4.75
43.60	7.3	32.00	47.72	-20.87	3.10
			47.83	-19.50	2.80

Table C.2: List of dust concentration measurements.

Latitude	Longitude	$\frac{\mu g}{m^{-3}}$	Latitude	Longitude	$\frac{\mu g}{m^{-3}}$
Stier et al. (2005)			Mahowald et al. (2009)		
-34.3	18.5	2.20	-21.5	165.0	0.18
-62.2	-58.3	0.52	-28.2	-177.4	0.84
-67.6	62.5	0.10	21.3	-157.7	0.66
-64.8	-64.1	0.35	11.3	-162.3	0.31
-22.1	167.0	0.17	3.9	159.3	0.06
-8.5	-179.2	0.19	43.1	141.3	1.20
-0.5	166.9	0.10	37.9	139.1	0.75
-29.1	168.0	0.84	52.7	174.0	0.86

– continued on next page –

– continued from previous page –

Latitude	Longitude	$\frac{\mu\text{g}}{\text{m}^{-3}}$	Latitude	Longitude	$\frac{\mu\text{g}}{\text{m}^{-3}}$
-21.2	-159.8	0.11	30.0	-176.0	0.91
-14.2	-170.6	0.16	21.5	-158.0	0.74
28.2	-177.4	0.72	11.5	162.0	0.28
21.3	-157.7	0.66	3.9	-159.3	0.11
33.5	126.5	14.14	-0.5	166.9	0.11
26.9	128.2	8.37	-13.5	-172.5	0.02
3.9	-159.3	0.10	-21.5	165.0	0.18
11.3	162.3	0.24	-29.0	168.0	0.44
13.2	-59.4	14.48	13.2	-59.4	8.74
28.3	-16.5	30.18	32.3	-64.9	3.45
32.3	-64.9	3.36	-40.7	144.7	0.51
53.3	-9.9	1.00	16.7	-22.9	76.87
25.8	-80.2	4.59	33.5	126.5	4.15
			-8.5	179.2	0.17
			26.9	128.3	4.76
			28.3	-16.5	22.27
			53.3	-9.9	0.51
			27.8	-80.3	5.57

D

Abbreviations and units

Abbreviations

AD	Anno Domini
AEROCOM	Aerosol Comparisons between Observations and Models
AIRS	Advanced Infrared Radiation Sounder
AMA	Amazon region
AMA-S	Amazon region south of the equator
ASE	Advection from southeast
BK scheme	Dust emission parametrisation from Balkanski et al. (2004)
BP	Before present
BSC-DREAM	Barcelona Supercomputing Center-Dust REgional Atmospheric Model
CAR	Caribbean
DC	Density current
DJF	December, January, February
DP	Dust phase
ECHAM	is composed of European Centre and Hamburg
ECHAM5	ECHAM model version 5.3.02
ECMWF	European Centre for Medium-range Weather Forecasts
EMAC	ECHAM5/MESSy Atmospheric Chemistry
EmiGP	Grid points that potentially emit dust
ERA-40	ECMWF 40-year Re-analysis data set
EUL	Eulerian
EUMETSAT	European Organisation for the Exploitation of Meteorological Satellites
GCCM	Global Chemistry Climate Model
GCM	Global Circulation Model
GHG	Greenhouse gas

GMI CTM	Global Modeling Initiative, Chemistry Transport Model
IFS	Integrated Forecasting System of the ECMWF
IN	Ice nuclei
IP	Intermediate phase
IPCC	Intergovernmental Panel on Climate Change
IPSL	Institut Pierre Simon Laplace
ITCZ	Intertropical convergence zone
JJA	June, July, August
LAG	Lagrangian
LAGRANTO	LAGRangian ANalysis TOol
LGM	Last Glacial Maximum
LIA	Little Ice Age
LM-MUSCAT	Lokal Modell - MUlti-Scale Chemical Aerosol Transport
MAM	March, April, May
MESSy	Modular Earth Submodel System
MISR	Multiangle Imaging SpectroRadiometer
MODIS	Moderate Resolution Imaging Spectroradiometer
MPI-MET	Max Planck Institute for Meteorology
MSG	Meteosat Second Generation
MSLP	Mean sea level pressure
NAO	North Atlantic Oscillation
NH	Northern hemispheric
NWP	Numerical weather prediction
PM_{10}	Particles smaller than 10 μm
RGB	Red–green–blue
SAL	Saharan Air Layer
SAMUM	Saharan Mineral Dust Experiment
SEVIRI	Spinning Enhanced Visible and InfraRed Imager
SIC	Sea ice concentration
SON	September, October, November
SST	Sea surface temperature
TG scheme	Dust emission parametrisation from Tegen et al. (2002)
TOMS	Total Ozone Mapping Spectrometer
TSP	Total suspended particle matter
WAM	West African Monsoon

Units

g	gramme
ha	hectare
hPa	hectopascal
K	kelvin
kg	kilogramme
km	kilometre
l	litre
m	metre
mg	milligramme
µg	microgramme
µm	micrometre
ppbv	parts per billion by volume
ppmv	parts per million by volume
s	second
Tg	teragramme
yr	year

References

Aquila, V., Hendricks, J., Lauer, A., Riemer, N., Vogel, H., Baumgardner, D., Minikin, A., Petzold, A., Schwarz, J. P., Spackman, J. R., Weinzierl, B., Righi, M., and Dall'Amico, M.: MADE-in: a new aerosol microphysics submodel for global simulation of insoluble particles and their mixing state, Geosci. Model Dev., 4, 325–355, doi:10.5194/gmd-4-325-2011, 2011.

Balkanski, Y., Schulz, M., Claquin, T., Moulin, C., and Ginoux, P.: Emission of Atmospheric Trace Compounds, chap. Global Emissions of Mineral Aerosol: Formulation and Validation using satellite Imagery, pp. 239–267, Kluwer, 2004.

Ben-Ami, Y., Koren, I., Rudich, Y., Artaxo, P., Martin, S. T., and Andreae, M. O.: Transport of North African dust from the Bodélé depression to the Amazon Basin: a case study, Atmos. Chem. Phys., 10, 7533–7544, doi:10.5194/acp-10-7533-2010, 2010.

Ben-Ami, Y., Koren, I., Altaratz, O., Kostinski, A., and Lehahn, Y.: Discernible rhythm in the spatio/temporal distributions of transatlantic dust, Atmos. Chem. Phys., 12, 2253–2262, doi:10.5194/acp-12-2253-2012, 2012.

Bencardino, M., Sprovieri, F., Cofone, F., and Pirrone, N.: Variability of Atmospheric Aerosol and Ozone Concentrations at Marine, Urban, and High-Altitude Monitoring Stations in Southern Italy during the 2007 Summer Saharan Dust Outbreaks and Wildfire Episodes, J. Air Waste Manage. Assoc., 61, 952–967, doi:10.1080/10473289.2011.599279, 2011.

Bian, H., Chin, M., Rodriguez, J. M., Yu, H., Penner, J. E., and Strahan, S.: Sensitivity of aerosol optical thickness and aerosol direct radiative effect to relative humidity, Atmos. Chem. Phys., 9, 2375–2386, 2009.

Brindley, H., Knippertz, P., Ryder, C., and Ashpole, I.: A critical evaluation of the ability of the Spinning Enhanced Visible and Infrared Imager (SEVIRI) thermal infrared red-green-blue rendering to identify dust events: Theoretical analysis, J. Geophys. Res.-Atmos., 117, D07 201, doi:10.1029/2011JD017326, 2012.

Carlson, T. N. and Prospero, J. M.: The Large-Scale Movement of Saharan Air Outbreaks over the Northern Equatorial Atlantic, J. Appl. Meteor., 11, 283–297, doi:10.1175/1520-0450(1972)011⟨0283:TLSMOS⟩2.0.CO;2, 1972.

Chadwick, O. A., Derry, L. A., Vitousek, P. M., Huebert, B. J., and Hedin, L. O.: Changing sources of nutrients during four million years of ecosystem development, Nature, 397, 491–497, 1999.

Chen, Y. S., Sheen, P. C., Chen, E. R., Liu, Y. K., Wu, T. N., and Yang, C. Y.: Effects of Asian dust storm events on daily mortality in Taipei, Taiwan, Environ. Res., 95, 151–155, doi:10.1016/j.envres.2003.08.008, 2004.

Cheng, T., Peng, Y., Feichter, J., and Tegen, I.: An improvement on the dust emission scheme in the global aerosol-climate model ECHAM5-HAM, Atmos. Chem. Phys., 8, 1105–1117, 2008.

Christiansen, B. and Ljungqvist, F. C.: The extra-tropical Northern Hemisphere temperature in the last two millennia: reconstructions of low-frequency variability, Clim. Past., 8, 765–786, doi:10.5194/cp-8-765-2012, 2012.

Cook, E. R., Esper, J., and D'Arrigo, R. D.: Extra-tropical Northern Hemisphere land temperature variability over the past 1000 years, Quat. Sci. Rev., 23, 2063–2074, doi:10.1016/j.quaascirev.2004.08.013, 2004.

Criado, C. and Dorta, P.: An unusual 'blood rain' over the Canary Islands (Spain). The storm of January 1999, J. Arid. Environ., 55, 765–783, doi:10.1016/S0140-1963(02)00320-8, 2003.

Crowley, T. J., Zielinski, G., Vinther, B., Udisti, R., Kreutz, K., Cole-Dai, J., and Castellano, J.: Volcanism and the Little Ice Age, PAGES Newsletter, 16, 22–23, 2008.

Cziczo, D. J., Murphy, D. M., Hudson, P. K., and Thomson, D. S.: Single particle measurements of the chemical composition of cirrus ice residue during CRYSTAL-FACE, J. Geophys. Res.-Atmos., 109, doi:10.1029/2003JD004032, 2004.

Delany, A. C., Parkin, D. W., Griffin, J. J., Goldberg, E. D., and Reimann, B. E. F.: Airborne Dust Collected At Barbados, Geochim. Cosmochim. Acta, 31, 885–&, doi:10.1016/S0016-7037(67)80037-1, 1967.

DeMott, P. J., Cziczo, D. J., Prenni, A. J., Murphy, D. M., Kreidenweis, S. M., Thomson, D. S., Borys, R., and Rogers, D. C.: Measurements of the concentration and composition of nuclei for cirrus formation, Proc. Natl. Acad. Sci. U. S. A., 100, 14 655–14 660, doi:10.1073/pnas.2532677100, 2003a.

DeMott, P. J., Sassen, K., Poellot, M. R., Baumgardner, D., Rogers, D. C., Brooks, S. D., Prenni, A. J., and Kreidenweis, S. M.: African dust aerosols as atmospheric ice nuclei, Geophys. Res. Lett., 30, doi:10.1029/2003GL017410, 2003b.

Denniston, R. F., Gonzalez, L. A., Asmerom, Y., Sharma, R. H., and Reagan, M. K.: Speleothem evidence for changes in Indian summer monsoon precipitation over the last similar to 2300 years, Quat. Res., 53, 196–202, doi:10.1006/qres.1999.2111, 2000.

Eichler, A., Tinner, W., Brusch, S., Olivier, S., Papina, T., and Schwikowski, M.: An ice-core based history of Siberian forest fires since AD 1250, Quat. Sci. Rev., 30, 1027–1034, doi:10.1016/j.quascirev.2011.02.007, 2011.

ElFandy, M. G.: Dust - An Active Meteorological Factor In the Atmosphere of Northern Africa, J. Appl. Phys., 20, 660–666, doi:10.1063/1.1698451, 1949.

Engelstaedter, S., Washington, R., and Mahowald, N.: Impact of changes in atmospheric conditions in modulating summer dust concentration at Barbados: A back-trajectory analysis, J. Geophys. Res.-Atmos., 114, D17 111, doi:10.1029/2008JD011180, 2009.

Fécan, F., Marticorena, B., and Bergametti, G.: Parametrization of the increase of the aeolian erosion threshold wind friction velocity due to soil moisture for arid and semi-arid areas, Ann. Geophys., 17, 149–157, 1999.

Fleitmann, D., Burns, S. J., Neff, U., Mudelsee, M., Mangini, A., and Matter, A.: Palaeoclimatic interpretation of high-resolution oxygen isotope profiles derived from annually laminated speleothems from Southern Oman, Quat. Sci. Rev., 23, 935–945, doi:10.1016/j.quascirev.2003.06.019, 2004.

Formenti, P., Rajot, J. L., Desboeufs, K., Saïd, F., Grand, N., Chevaillier, S., and Schmechtig, C.: Airborne observations of mineral dust over western Africa in the summer Monsoon season: spatial and vertical variability of physico–chemical and optical properties, Atmos. Chem. Phys., 11, 6387–6410, doi:10.5194/acp-11-6387-2011, 2011.

Frank, D. C., Esper, J., Raible, C. C., Buntgen, U., Trouet, V., Stocker, B., and Joos, F.: Ensemble reconstruction constraints on the global carbon cycle sensitivity to climate, Nature, 463, 527–U143, doi:10.1038/nature08769, 2010.

Geng, H., Park, Y., Hwang, H., Kang, S., and Ro, C. U.: Elevated nitrogen-containing particles observed in Asian dust aerosol samples collected at the marine boundary layer of the Bohai Sea and the Yellow Sea, Atmos. Chem. Phys., 9, 6933–6947, 2009.

Gerber, S., Joos, F., Brügger, P., Stocker, T. F., Mann, M. E., Sitch, S., and Scholze, M.: Constraining temperature variations over the last millennium by comparing simulated and observed atmospheric CO2, Clim. Dyn., 20, 281–299, doi:10.1007/s00382-002-0270-8, 2003.

Ginoux, P., Chin, M., Tegen, I., Prospero, J., Holben, B., Dubovik, O., and Lin, S. J.: Sources and distributions of dust aerosols simulated with the GOCART model, J. Geophys. Res.-Atmos., 106, 20 255–20 273, 2001.

Ginoux, P., Prospero, J. M., Torres, O., and Chin, M.: Long-term simulation of global dust distribution with the GOCART model: correlation with North Atlantic Oscillation, Environ. Modell. Softw., 19, 113–128, doi:10.1016/S1364-8152(03)00114-2, 2004.

Gläser, G., Knippertz, P., and Heinold, B.: Orographic Effects and Evaporative Cooling along a Subtropical Cold Front: The Case of the Spectacular Saharan Dust Outbreak of March 2004, Mon. Wea. Rev., 140, 2520–2533, doi:10.1175/MWR-D-11-00315.1, 2012a.

Gläser, G., Kerkweg, A., and Wernli, H.: The Mineral Dust Cycle in EMAC 2.40: sensitivity to the spectral resolution and the dust emission scheme, Atmos. Chem. Phys., 12, 1611–1627, doi:10.5194/acp-12-1611-2012, 2012b.

Grove, J. M.: The initiation of the “Little Ice Age” in regions round the North Atlantic, Clim. Change, 48, 53–82, doi:10.1023/A:1005662822136, 2001.

Habib, G., Venkataraman, C., Chiapello, I., Ramachandran, S., Boucher, O., and Reddy, M. S.: Seasonal and interannual variability in absorbing aerosols over India derived from TOMS: Relationship to regional meteorology and emissions, Atmos. Environ., 40, 1909–1921, doi:10.1016/j.atmosenv.2005.07.077, 2006.

Haywood, J. M., Francis, P. N., Glew, M. D., and Taylor, J. P.: Optical properties and direct radiative effect of Saharan dust: A case study of two Saharan dust outbreaks using aircraft data, J. Geophys. Res.-Atmos., 106, 18 417–18 430, 2001.

Hegerl, G. C., Crowley, T. J., Hyde, W. T., and Frame, D. J.: Climate sensitivity constrained by temperature reconstructions over the past seven centuries, Nature, 440, 1029–1032, doi:10.1038/nature04679, 2006.

Heinold, B., Knippertz, P., Marsham, J. H., Fiedler, S., Dixon, N. S., Schepanski, K., Laurent, B., and Tegen, I.: The role of deep convection and low-level jets for dust emis in West Africa, J. Geophys. Res., 2012, submitted.

Heintzenberg, J.: The SAMUM-1 experiment over Southern Morocco: overview and introduction, Tellus Ser. B-Chem. Phys. Meteorol., 61, 2–11, doi:10.1111/j.1600-

0889.2008.00403.x, 2009.

Huang, J., Zhang, C., and Prospero, J. M.: African dust outbreaks: A satellite perspective of temporal and spatial variability over the tropical Atlantic Ocean, J. Geophys. Res.-Atmos., 115, D05 202, doi:10.1029/2009JD012516, 2010.

Huneeus, N., Schulz, M., Balkanski, Y., Griesfeller, J., Prospero, J., Kinne, S., Bauer, S., Boucher, O., Chin, M., Dentener, F., Diehl, T., Easter, R., Fillmore, D., Ghan, S., Ginoux, P., Grini, A., Horowitz, L., Koch, D., Krol, M. C., Landing, W., Liu, X., Mahowald, N., Miller, R., Morcrette, J. J., Myhre, G., Penner, J., Perlwitz, J., Stier, P., Takemura, T., and Zender, C. S.: Global dust model intercomparison in AeroCom phase I, Atmos. Chem. Phys., 11, 7781–7816, doi: 10.5194/acp-11-7781-2011, 2011.

IPCC: Climate Change 2007: The Physical Science Basis. Contribution of Working Group I to the Fourth Assessment Report of the Intergovernmental Panel on Climate Change, edited by: Solomon, S., Qin, D., Manning, M., Chen, Z., Marquis, M., Averyt, K.B., Tignor, M. and Miller, H.L., Cambridge University Press, Cambridge, UK and New York, NY, USA, 2007.

Janjic, Z. I.: The Step-Mountain Eta Coordinate Model: Further Developments of the Convection, Viscous Sublayer, and Turbulence Closure Schemes, Mon. Weather Rev., 122, 927–945, 1994.

Jickells, T. D., An, Z. S., Andersen, K. K., Baker, A. R., Bergametti, G., Brooks, N., Cao, J. J., Boyd, P. W., Duce, R. A., Hunter, K. A., Kawahata, H., Kubilay, N., laRoche, J., Liss, P. S., Mahowald, N., Prospero, J. M., Ridgwell, A. J., Tegen, I., and Torres, R.: Global iron connections between desert dust, ocean biogeochemistry, and climate, Science, 308, 67–71, doi:10.1126/science.1105959, 2005.

Jöckel, P., Sander, R., Kerkweg, A., Tost, H., and Lelieveld, J.: Technical note: The Modular Earth Submodel System (MESSy) - a new approach towards Earth System Modeling, Atmos. Chem. Phys., 5, 433–444, 2005.

Jöckel, P., Tost, H., Pozzer, A., Brühl, C., Buchholz, J., Ganzeveld, L., Hoor, P., Kerkweg, A., Lawrence, M. G., Sander, R., Steil, B., Stiller, G., Tanarhte, M., Taraborrelli, D., Van Aardenne, J., and Lelieveld, J.: The atmospheric chemistry general circulation model ECHAM5/MESSy1: consistent simulation of ozone from the surface to the mesosphere, Atmos. Chem. Phys., 6, 5067–5104, 2006.

Jöckel, P., Kerkweg, A., Pozzer, A., Sander, R., Tost, H., Riede, H., Baumgaertner, A., Gromov, S., and Kern, B.: Development cycle 2 of the Modular Earth Submodel System (MESSy2), Geosci. Model Dev., 3, 717–752, doi:

10.5194/gmd-3-717-2010, 2010.

Jung, T., Gulev, S. K., Rudeva, I., and Soloviov, V.: Sensitivity of extratropical cyclone characteristics to horizontal resolution in the ECMWF model, Q. J. R. Meteorol. Soc., 132, 1839–1857, doi:10.1256/qj.05.212, 2006.

Jungclaus, J. H., Lorenz, S. J., Timmreck, C., Reick, C. H., Brovkin, V., Six, K., Segschneider, J., Giorgetta, M. A., Crowley, T. J., Pongratz, J., Krivova, N. A., Vieira, L. E., Solanki, S. K., Klocke, D., Botzet, M., Esch, M., Gayler, V., Haak, H., Raddatz, T. J., Roeckner, E., Schnur, R., Widmann, H., Claussen, M., Stevens, B., and Marotzke, J.: Climate and carbon-cycle variability over the last millennium, Clim. Past., 6, 723–737, doi:10.5194/cp-6-723-2010, 2010.

Junge, C. E.: Recent Investigations In Air Chemistry, Tellus, 8, 127–139, 1956.

Kandler, K., Schütz, L., Deutscher, C., Ebert, M., Hofmann, H., Jäckel, S., Jaenicke, R., Knippertz, P., Lieke, K., Massling, A., Petzold, A., Schladitz, A., Weinzierl, B., Wiedensohler, A., Zorn, S., and Weinbruch, S.: Size distribution, mass concentration, chemical and mineralogical composition and derived optical parameters of the boundary layer aerosol at Tinfou, Morocco, during SAMUM 2006, Tellus Ser. B-Chem. Phys. Meteorol., 61, 32–50, doi:10.1111/j.1600-0889.2008.00385.x, 2009.

Kang, J.-Y., Yoon, S.-C., Shao, Y., and Kim, S.-W.: Comparison of vertical dust flux by implementing three dust emission schemes in WRF/Chem, J. Geophys. Res.-Atmos., 116, doi:10.1029/2010JD014649, 2011.

Karam, D. B., Flamant, C., Knippertz, P., Reitebuch, O., Pelon, J., Chong, M., and Dabas, A.: Dust emissions over the Sahel associated with the West African monsoon intertropical discontinuity region: A representative case-study, Q. J. R. Meteorol. Soc., 134, 621–634, doi:10.1002/qj.244, 2008.

Karanasiou, A., Moreno, N., Moreno, T., Viana, M., de Leeuw, F., and Querol, X.: Health effects from Sahara dust episodes in Europe: Literature review and research gaps., Environ. Int., 47, 107–14, 2012.

Kaspari, S., Mayewski, P., Kang, S., Sneed, S., Hou, S., Hooke, R., Kreutz, K., Introne, D., Handley, M., Maasch, K., Qin, D., and Ren, J.: Reduction in northward incursions of the South Asian monsoon since approximate to 1400 AD inferred from a Mt. Everest ice core, Geophys. Res. Lett., 34, doi:10.1029/2007GL030440, 2007.

Kaufman, Y. J., Koren, I., Remer, L. A., Tanré, D., Ginoux, P., and Fan, S.: Dust transport and deposition observed from the Terra-Moderate Resolution Imaging Spectroradiometer (MODIS) spacecraft over the Atlantic ocean, J. Geophys. Res.-

Atmos., 110, doi:10.1029/2003JD004436, 2005.

Kerkweg, A., Buchholz, J., Ganzeveld, L., Pozzer, A., Tost, H., and Jöckel, P.: Technical note: An implementation of the dry removal processes DRY DEPosition and SEDImentation in the modular earth submodel system (MESSy), Atmos. Chem. Phys., 6, 4617–4632, 2006a.

Kerkweg, A., Sander, R., Tost, H., and Jöckel, P.: Technical note: Implementation of prescribed (OFFLEM), calculated (ONLEM), and pseudo-emissions (TNUDGE) of chemical species in the Modular Earth Submodel System (MESSy), Atmos. Chem. Phys., 6, 3603–3609, 2006b.

Kerkweg, A., Jöckel, P., Pozzer, A., Tost, H., Sander, R., Schulz, M., Stier, P., Vignati, E., Wilson, J., and Lelieveld, J.: Consistent simulation of bromine chemistry from the marine boundary layer to the stratosphere - Part 1: Model description, sea salt aerosols and pH, Atmos. Chem. Phys., 8, 5899–5917, 2008.

Klein, H., Nickovic, S., Haunold, W., Bundke, U., Nillius, B., Ebert, M., Weinbruch, S., Schütz, L., Levin, Z., Barrie, L. A., and Bingemer, H.: Saharan dust and ice nuclei over Central Europe, Atmos. Chem. Phys., 10, 10 211–10 221, doi:10.5194/acp-10-10211-2010, 2010.

Knippertz, P. and Fink, A. H.: Synoptic and dynamic aspects of an extreme springtime Saharan dust outbreak, Q. J. R. Meteorol. Soc., 132, 1153–1177, doi:10.1256/qj.05.109, 2006.

Knippertz, P. and Todd, M. C.: Mineral Dust Aerosols Over the Sahara: Meteorological Controls On Emission and Transport and Implications For Modeling, Rev. Geophys., 50, RG1007, doi:10.1029/2011RG000362, 2012.

Knippertz, P., Deutscher, C., Kandler, K., Müller, T., Schulz, O., and Schütz, L.: Dust mobilization due to density currents in the Atlas region: Observations from the Saharan Mineral Dust Experiment 2006 field campaign, J. Geophys. Res.-Atmos., 112, doi:10.1029/2007JD008774, 2007.

Knippertz, P., Ansmann, A., Althausen, D., Müller, D., Tesche, M., Bierwirth, E., Dinter, T., Müller, T., Von Hoyningen-Huene, W., Schepanski, K., Wendisch, M., Heinold, B., Kandler, K., Petzold, A., Schütz, L., and Tegen, I.: Dust mobilization and transport in the northern Sahara during SAMUM 2006 - a meteorological overview, Tellus Ser. B-Chem. Phys. Meteorol., 61, 12–31, doi:10.1111/j.1600-0889.2008.00380.x, 2009.

Kocha, C., Lafore, J. P., Tulet, P., and Seity, Y.: High-resolution simulation of a major West African dust-storm: comparison with observations and investigation of dust impact, Q. J. R. Meteorol. Soc., 138, 455–470, doi:10.1002/qj.927, 2012.

Koren, I., Kaufman, Y. J., Washington, R., Todd, M. C., Rudich, Y., Martins, J. V., and Rosenfeld, D.: The Bodélé depression: a single spot in the Sahara that provides most of the mineral dust to the Amazon forest, Environ. Res. Lett., 1, 014 005, doi:10.1088/1748-9326/1/1/014005, 2006.

Kwon, H. J., Cho, S. H., Chun, Y., Lagarde, F., and Pershagen, G.: Effects of the Asian dust events on daily mortality in Seoul, Korea, Environ. Res., 90, 1–5, doi:10.1006/enrs.2002.4377, 2002.

Lambert, F., Bigler, M., Steffensen, J. P., Hutterli, M., and Fischer, H.: Centennial mineral dust variability in high-resolution ice core data from Dome C, Antarctica, Clim. Past., 8, 609–623, doi:10.5194/cp-8-609-2012, 2012.

Laskin, A., Iedema, M. J., Ichkovich, A., Graber, E. R., Taraniuk, I., and Rudich, Y.: Direct observation of completely processed calcium carbonate dust particles, Faraday Discuss., 130, 453–468, doi:10.1039/b417366j, 2005.

Lee, Y. H., Chen, K., and Adams, P. J.: Development of a global model of mineral dust aerosol microphysics, Atmos. Chem. Phys., 9, 2441–2458, 2009.

Lushine, J. B.: Dust Layer In Eastern Caribbean, Mon. Weather Rev., 103, 454–455, doi:10.1175/1520-0493(1975)103⟨0454:ADLITE⟩2.0.CO;2, 1975.

Maher, B. A., Prospero, J. M., Mackie, D., Gaiero, D., Hesse, P. P., and Balkanski, Y.: Global connections between aeolian dust, climate and ocean biogeochemistry at the present day and at the last glacial maximum, Earth Sci. Rev., 99, 61–97, doi:10.1016/j.earscirev.2009.12.001, 2010.

Mahowald, N., Kohfeld, K., Hansson, M., Balkanski, Y., Harrison, S. P., Prentice, I. C., Schulz, M., and Rodhe, H.: Dust sources and deposition during the last glacial maximum and current climate: A comparison of model results with paleodata from ice cores and marine sediments, J. Geophys. Res.-Atmos., 104, 15 895–15 916, doi:10.1029/1999JD900084, 1999.

Mahowald, N. M., Baker, A. R., Bergametti, G., Brooks, N., Duce, R. A., Jickells, T. D., Kubilay, N., Prospero, J. M., and Tegen, I.: Atmospheric global dust cycle and iron inputs to the ocean, Glob. Biogeochem. Cycle, 19, GB4025, doi: 10.1029/2004GB002402, 2005.

Mahowald, N. M., Engelstaedter, S., Luo, C., Sealy, A., Artaxo, P., Benitez-Nelson, C., Bonnet, S., Chen, Y., Chuang, P. Y., Cohen, D. D., Dulac, F., Herut, B., Johansen, A. M., Kubilay, N., Losno, R., Maenhaut, W., Paytan, A., Prospero, J. A., Shank, L. M., and Siefert, R. L.: Atmospheric Iron Deposition: Global Distribution, Variability, and Human Perturbations, Annu. Rev. Mar. Sci., 1, 245–278, doi:10.1146/annurev.marine.010908.163727, 2009.

Mangold, A., De Backer, H., De Paepe, B., Dewitte, S., Chiapello, I., Derimian, Y., Kacenelenbogen, M., Léon, J.-F., Huneeus, N., Schulz, M., Ceburnis, D., O'Dowd, C., Flentje, H., Kinne, S., Benedetti, A., Morcrette, J. J., and Boucher, O.: Aerosol analysis and forecast in the European Centre for Medium-Range Weather Forecasts Integrated Forecast System: 3. Evaluation by means of case studies, J. Geophys. Res.-Atmos., 116, doi:10.1029/2010JD014864, 2011.

Marsham, J. H., Knippertz, P., Dixon, N. S., Parker, D. J., and Lister, G. M. S.: The importance of the representation of deep convection for modeled dust-generating winds over West Africa during summer, Geophys. Res. Lett., 38, L16 803, doi:10.1029/2011GL048368, 2011.

Marti, O., Braconnot, P., Dufresne, J. L., Bellier, J., Benshila, R., Bony, S., Brockmann, P., Cadule, P., Caubel, A., Codron, F., de Noblet, N., Denvil, S., Fairhead, L., Fichefet, T., Foujols, M. A., Friedlingstein, P., Goosse, H., Grandpeix, J. Y., Guilyardi, E., Hourdin, F., Idelkadi, A., Kageyama, M., Krinner, G., Lévy, C., Madec, G., Mignot, J., Musat, I., Swingedouw, D., and Talandier, C.: Key features of the IPSL ocean atmosphere model and its sensitivity to atmospheric resolution, Clim. Dyn., 34, 1–26, doi:10.1007/s00382-009-0640-6, 2010.

Marticorena, B. and Bergametti, G.: Modeling the Atmospheric Dust Cycle .1. Design of A Soil-derived Dust Emission Scheme, J. Geophys. Res.-Atmos., 100, 16 415–16 430, doi:10.1029/95JD00690, 1995.

Martin, J. H. and Fitzwater, S. E.: Iron deficiency limits phytoplankton growth in the north-east Pacific subarctic, Nature, 331, 341–343, 1988.

Min, Q. . L., Li, R., Lin, B., Joseph, E., Wang, S., Hu, Y., Morris, V., and Chang, F.: Evidence of mineral dust altering cloud microphysics and precipitation, Atmos. Chem. Phys., 9, 3223–3231, 2009.

Mulitza, S., Heslop, D., Pittauerova, D., Fischer, H. W., Meyer, I., Stuut, J. B., Zabel, M., Mollenhauer, G., Collins, J. A., Kuhnert, H., and Schulz, M.: Increase in African dust flux at the onset of commercial agriculture in the Sahel region RID E-5044-2011, Nature, 466, 226–228, doi:10.1038/nature09213, 2010.

Nicholson, S. E. and Webster, P. J.: A physical basis for the interannual variability of rainfall in the Sahel, Q. J. R. Meteorol. Soc., 133, 2065–2084, doi:10.1002/qj.104, 2007.

Nickovic, S., Kallos, G., Papadopoulos, A., and Kakaliagou, O.: A model for prediction of desert dust cycle in the atmosphere, J. Geophys. Res.-Atmos., 106, 18 113–18 129, 2001.

Nowottnick, E., Colarco, P., da Silva, A., Hlavka, D., and McGill, M.: The fate of saharan dust across the atlantic and implications for a central american dust barrier, Atmos. Chem. Phys., 11, 8415–8431, doi:10.5194/acp-11-8415-2011, 2011.

Pan, W. Y., Wu, L. G., and Shie, C. L.: Influence of the Saharan Air Layer on Atlantic Tropical Cyclone Formation during the Period 1–12 September 2003, Adv. Atmos. Sci., 28, 16–32, doi:10.1007/s00376-010-9165-5, 2011.

Pérez, C., Nickovic, S., Baldasano, J. M., Sicard, M., Rocadenbosch, F., and Cachorro, V. E.: A long Saharan dust event over the western Mediterranean: Lidar, Sun photometer observations, and regional dust modeling, J. Geophys. Res.-Atmos., 111, doi:10.1029/2005JD006579, 2006a.

Pérez, C., Nickovic, S., Pejanovic, G., Baldasano, J. M., and Özsoy, E.: Interactive dust-radiation modeling: A step to improve weather forecasts, J. Geophys. Res.-Atmos., 111, doi:10.1029/2005JD006717, 2006b.

Petit, J. R., Jouzel, J., Raynaud, D., Barkov, N. I., Barnola, J. M., Basile, I., Bender, M., Chappellaz, J., Davis, M., Delaygue, G., Delmotte, M., Kotlyakov, V. M., Legrand, M., Lipenkov, V. Y., Lorius, C., Pépin, L., Ritz, C., Saltzman, E., and Stievenard, M.: Climate and atmospheric history of the past 420,000 years from the Vostok ice core, Antarctica, Nature, 399, 429–436, 1999.

Pierangelo, C., Chédin, A., Heilliette, S., Jacquinet-Husson, N., and Armante, R.: Dust altitude and infrared optical depth from AIRS, Atmos. Chem. Phys., 4, 1813–1822, 2004.

Prenni, A. J., Petters, M. D., Kreidenweis, S. M., Heald, C. L., Martin, S. T., Artaxo, P., Garland, R. M., Wollny, A. G., and Pöschl, U.: Relative roles of biogenic emissions and Saharan dust as ice nuclei in the Amazon basin, Nature Geoscience, 2, 401–404, doi:10.1038/NGEO517, 2009.

Prospero, J. M.: Long-term measurements of the transport of African mineral dust to the southeastern United States: Implications for regional air quality, J. Geophys. Res.-Atmos., 104, 15 917–15 927, 1999.

Prospero, J. M. and Carlson, T. N.: Saharan Air Outbreaks Over the Tropical North-Atlantic, Pure Appl. Geophys., 119, 677–691, doi:10.1007/BF00878167, 1981.

Prospero, J. M., Bonatti, E., Schubert, C., and Carlson, T. N.: Dust In Caribbean Atmosphere Traced To An African Dust Storm, Earth Planet. Sci. Lett., 9, 287–&, doi:10.1016/0012-821X(70)90039-7, 1970.

Prospero, J. M., Landing, W. M., and Schulz, M.: African dust deposition to Florida: Temporal and spatial variability and comparisons to models, J. Geophys. Res.-

Atmos., 115, D13 304, doi:10.1029/2009JD012773, 2010.

Prospero, J. M., Ginoux, P., Torres, O., Nicholson, S. E., and Gill, T. E.: Environmental characterization of global sources of atmospheric soil dust identified with the Nimbus 7 Total Ozone Mapping Spectrometer (TOMS) absorbing aerosol product, Rev. Geophys., 40, doi:10.1029/2000RG000095, 2002.

Pye, K.: Aeolian Dust and Dust Deposits, Academic Press, Orlando Florida, 334 pp, 1987.

Ramos, A. G., Martel, A., Codd, G. A., Soler, E., Coca, J., Redondo, A., Morrison, L. F., Metcalf, J. S., Ojeda, A., Suárez, S., and Petit, M.: Bloom of the marine diazotrophic cyanobacterium Trichodesmium erythraeum in the Northwest African upwelling, Mar. Ecol.-Prog. Ser., 301, 303–305, doi:10.3354/meps301303, 2005.

Remer, L. A., Kaufman, Y. J., Tanré, D., Mattoo, S., Chu, D. A., Martins, J. V., Li, R. R., Ichoku, C., Levy, R. C., Kleidman, R. G., Eck, T. F., Vermote, E., and Holben, B. N.: The MODIS aerosol algorithm, products, and validation, J. Atmos. Sci., 62, 947–973, doi:10.1175/JAS3385.1, 2005.

Richardson, M. S., DeMott, P. J., Kreidenweis, S. M., Cziczo, D. J., Dunlea, E. J., Jimenez, J. L., Thomson, D. S., Ashbaugh, L. L., Borys, R. D., Westphal, D. L., Casuccio, G. S., and Lersch, T. L.: Measurements of heterogeneous ice nuclei in the western United States in springtime and their relation to aerosol characteristics, J. Geophys. Res.-Atmos., 112, doi:10.1029/2006JD007500, 2007.

Roeckner, E., Bäuml, G., Bonaventura, L., Brokopf, R., Esch, M., Giorgetta, M., Hagemann, S., Kirchner, I., Kornblueh, L., Manzini, E., Rhodin, A., Schlese, U., Schulzweida, U., and Tompkins, A.: The atmospheric general circulation model ECHAM5: Part I, Tech. Rep. 349, Max Planck Institut für Meteorologie, 2003.

Roeckner, E., Brokopf, R., Esch, M., Giorgetta, M., Hagemann, S., Kornblueh, L., Manzini, E., Schlese, U., and Schulzweida, U.: Sensitivity of simulated climate to horizontal and vertical resolution in the ECHAM5 atmosphere model, J. Clim., 19, 3771–3791, 2006.

Sander, R., Baumgaertner, A., Gromov, S., Harder, H., Jöckel, P., Kerkweg, A., Kubistin, D., Regelin, E., Riede, H., Sandu, A., Taraborrelli, D., Tost, H., and Xie, Z.: The atmospheric chemistry box model CAABA/MECCA-3.0, Geosci. Model Dev., 4, 373–380, doi:10.5194/gmd-4-373-2011, 2011.

Sassen, K., DeMott, P. J., Prospero, J. M., and Poellot, M. R.: Saharan dust storms and indirect aerosol effects on clouds: CRYSTAL-FACE results, Geophys. Res. Lett., 30, doi:10.1029/2003GL017371, 2003.

Schepanski, K., Tegen, I., and Macke, A.: Saharan dust transport and deposition towards the tropical northern Atlantic, Atmos. Chem. Phys., 9, 1173–1189, 2009.

Seinfeld, J. and Pandis, S.: Atmospheric Chemistry and Physics. From Air Pollution to Climate Change, Wiley-Interscience, 1997.

Shao, Y. and Raupach, M. R.: Effect of saltation bombardment on the entrainment of dust by wind, J. Geophys. Res.-Atmos., 98, 12 719–12 726, 1993.

Shao, Y., Fink, A. H., and Klose, M.: Numerical simulation of a continental-scale Saharan dust event, J. Geophys. Res.-Atmos., 115, doi:{10.1029/2009JD012678}, 2010.

Sirocko, F.: Wetter, Klima, Menschheitsentwicklung - Von der Eiszeit bis ins 21. Jahrhundert, Wissenschaftliche Buchgesellschaft, Darmstadt, 280 pp, 2009.

Skonieczny, C., Bory, A., Bout-Roumazeilles, V., Abouchami, W., Galer, S. J. G., Crosta, X., Stuut, J. B., Meyer, I., Chiapello, I., Podvin, T., Chatenet, B., Diallo, A., and Ndiaye, T.: The 7–13 March 2006 major Saharan outbreak: Multiproxy characterization of mineral dust deposited on the West African margin, J. Geophys. Res.-Atmos., 116, D18 210, doi:10.1029/2011JD016173, 2011.

Smith, R. S. and Gregory, J.: The last glacial cycle: transient simulations with an AOGCM, Clim. Dyn., 38, 1545–1559, doi:10.1007/s00382-011-1283-y, 2012.

Sodemann, H., Palmer, A. S., Schwierz, C., Schwikowski, M., and Wernli, H.: The transport history of two Saharan dust events archived in an Alpine ice core, Atmos. Chem. Phys., 6, 667–688, 2006.

Stier, P., Feichter, J., Kinne, S., Kloster, S., Vignati, E., Wilson, J., Ganzeveld, L., Tegen, I., Werner, M., Balkanski, Y., Schulz, M., Boucher, O., Minikin, A., and Petzold, A.: The aerosol-climate model ECHAM5-HAM, Atmos. Chem. Phys., 5, 1125–1156, 2005.

Sultan, B., Labadi, K., Guegan, J. F., and Janicot, S.: Climate drives the meningitis epidemics onset in West Africa, Plos Med., 2, e6, doi:10.1371/journal.pmed.0020006, 2005.

Swap, R., Garstang, M., Greco, S., Talbot, R., and Kallberg, P.: Saharan dust in the Amazon Basin, Tellus Ser. B-Chem. Phys. Meteorol., 44, 133–149, 1992.

Takemura, T., Egashira, M., Matsuzawa, K., Ichijo, H., O'ishi, R., and Abe-Ouchi, A.: A simulation of the global distribution and radiative forcing of soil dust aerosols at the Last Glacial Maximum, Atmos. Chem. Phys., 9, 3061–3073, 2009.

Tegen, I., Heinold, B., Todd, M., Helmert, J., Washington, R., and Dubovik, O.: Modelling soil dust aerosol in the Bodélé depression during the BoDEx campaign, Atmos. Chem. Phys., 6, 4345–4359, 2006.

Tegen, I., Harrison, S. P., Kohfeld, K., Prentice, I. C., Coe, M., and Heimann, M.: Impact of vegetation and preferential source areas on global dust aerosol: Results from a model study, J. Geophys. Res.-Atmos., 107, doi:10.1029/2001JD000963, 2002.

Textor, C., Schulz, M., Guibert, S., Kinne, S., Balkanski, Y., Bauer, S., Berntsen, T., Berglen, T., Boucher, O., Chin, M., Dentener, F., Diehl, T., Easter, R., Feichter, H., Fillmore, D., Ghan, S., Ginoux, P., Gong, S., Grini, A., Hendricks, J., Horowitz, L., Huang, P., Isaksen, I., Iversen, T., Kloster, S., Koch, D., Kirkevåg, A., Kristjansson, J. E., Krol, M., Lauer, A., Lamarque, J. F., Liu, X., Montanaro, V., Myhre, G., Penner, J., Pitari, G., Reddy, S., Seland, O., Stier, P., Takemura, T., and Tie, X.: Analysis and quantification of the diversities of aerosol life cycles within AeroCom, Atmos. Chem. Phys., 6, 1777–1813, 2006.

Thorncroft, C. D. and Blackburn, M.: Maintenance of the African easterly jet, Q. J. R. Meteorol. Soc., 125, 763–786, doi:10.1256/smsqj.55501, 1999.

Timmreck, C. and Schulz, M.: Significant dust simulation differences in nudged and climatological operation mode of the AGCM ECHAM, J. Geophys. Res.-Atmos., 109, doi:10.1029/2003JD004381, 2004.

Todd, M. C., Washington, R., Raghavan, S., Lizcano, G., and Knippertz, P.: Regional model simulations of the Bodélé low-level jet of northern Chad during the Bodélé Dust Experiment (BoDEx 2005), J. Clim., 21, 995–1012, doi: {10.1175/2007JCLI1766.1}, 2008.

Tost, H.: Global Modelling of Cloud, Convection and Precipitation Influences on Trace Gases and Aerosols, Ph.D. thesis, Rheinische Friedrich-Wilhelms-Universität Bonn, Germany, 2006a.

Tost, H., Jöckel, P. J., and Lelieveld, J.: Lightning and convection parameterisations - uncertainties in global modelling, Atmos. Chem. Phys., 7, 4553–4568, 2007.

Tost, H., Lawrence, M. G., Brühl, C., and Jöckel, P.: Uncertainties in atmospheric chemistry modelling due to convection parameterisations and subsequent scavenging, Atmos. Chem. Phys., 10, 1931–1951, doi:10.5194/acp-10-1931-2010, 2010.

Tost, H., Jöckel, P., Kerkweg, A., Sander, R., and Lelieveld, J.: Technical note: A new comprehensive SCAVenging submodel for global atmospheric chemistry modelling, Atmos. Chem. Phys., 6, 565–574, 2006b.

Trapp, J. M., Millero, F. J., and Prospero, J. M.: Temporal variability of the elemental composition of African dust measured in trade wind aerosols at Barbados and Miami, Mar. Chem., 120, 71–82, doi:10.1016/j.marchem.2008.10.004, 2010.

Vignati, E., Wilson, J., and Stier, P.: M7: An efficient size-resolved aerosol microphysics module for large-scale aerosol transport models, J. Geophys. Res.-Atmos., 109, doi:10.1029/2003JD004485, 2004.

Wang, N. L., Yao, T. D., Pu, J. C., Zhang, Y. L., and Sun, W. Z.: Climatic and environmental changes over the last millennium recorded in the Malan ice core from the northern Tibetan Plateau, Sci. China Ser. D, 49, 1079–1089, doi: 10.1007/s11430-006-1079-9, 2006.

Wang, S. H., Hsu, N. C., Tsay, S. C., Lin, N. H., Sayer, A. M., Huang, S. J., and Lau, W. K. M.: Can Asian dust trigger phytoplankton blooms in the oligotrophic northern South China Sea?, Geophys. Res. Lett., 39, L05 811, doi: 10.1029/2011GL050415, 2012.

Washington, R., Todd, M., Middleton, N. J., and Goudie, A. S.: Dust-storm source areas determined by the total ozone monitoring spectrometer and surface observations, Ann. Assoc. Am. Geogr., 93, 297–313, 2003.

Wernli, H. and Davies, H. C.: A Lagrangian-based analysis of extratropical cyclones .1. The method and some applications, Q. J. R. Meteorol. Soc., 123, 467–489, 1997.

Wernli, H., Hofmann, C., and Zimmer, M.: Spatial Forecast Verification Methods Intercomparison Project: Application of the SAL Technique, Weather Forecast., 24, 1472–1484, doi:10.1175/2009WAF2222271.1, 2009.

Wiegand, L., Twitchett, A., Schwierz, C., and Knippertz, P.: Heavy Precipitation at the Alpine South Side and Saharan Dust over Central Europe: A Predictability Study Using TIGGE, Weather Forecast., 26, 957–974, doi:10.1175/WAF-D-10-05060.1, 2011.

Winckler, G., Anderson, R. F., Fleisher, M. Q., Mcgee, D., and Mahowald, N.: Covariant glacial-interglacial dust fluxes in the equatorial Pacific and Antarctica, Science, 320, 93–96, doi:10.1126/science.1150595, 2008.

Zhao, X. J., Zhuang, G. S., Wang, Z. F., Sun, Y. L., Wang, Y., and Yuan, H.: Variation of sources and mixing mechanism of mineral dust with pollution aerosol - revealed by the two peaks of a super dust storm in Beijing, Atmos. Res., 84, 265–279, doi:10.1016/j.atmosres.2006.08.005, 2007.

Zuberi, B., Bertram, A. K., Cassa, C. A., Molina, L. T., and Molina, M.: Heterogeneous nucleation of ice in (NH4)(2)SO4-H2O particles with mineral dust immersions, Geophys. Res. Lett., 29, doi:10.1029/2001GL014289, 2002.

Danksagung

Hier möchte ich nun allen Menschen danken, die mich während der vergangenen Jahre begleitet und so zum erfolgreichen Abschluss dieser Arbeit beigetragen haben.

Aus Gründen des Datenschutzes muss auf die namentliche Nennung dieser Personen verzichtet werden.

Allen, die sich angesprochen fühlen, sage ich an dieser Stelle: Vielen Dank!